

Structure-Property Relationship of Binder Jetted Fused Silica Preforms to Manufacture
Ceramic-Metallic Interpenetrating Phase Composites

by

Kyle Myers

Submitted in Partial Fulfillment of the Requirements

for the Degree of

Doctor of Philosophy

in the

Materials Science and Engineering

Program

YOUNGSTOWN STATE UNIVERSITY

May, 2016

Structure-Property Relationship of Binder Jetted Fused Silica Preforms to Manufacture
Ceramic-Metallic Interpenetrating Phase Composites

Kyle Myers

I hereby release this dissertation to the public. I understand that this dissertation will be made available from the OhioLINK ETD Center and the Maag Library Circulation Desk for public access. I also authorize the University or other individuals to make copies of this thesis as needed for scholarly research.

Signature:

Kyle Myers, Student Date

Approvals:

Dr. Pedro Cortes, Dissertation Advisor Date

Dr. Brett Conner, Committee Member Date

Dr. Tim Wagner, Committee Member Date

Dr. Donald Priour, Committee Member Date

Brian Hetzel, Committee Member Date

Dr. Salvatore A. Sanders, Dean of Graduate Studies Date

ABSTRACT

Additive manufacturing (AM) is an area of high interest due to its rapid prototyping and high complexity abilities. Powder based AM techniques allow for a wide variety of materials to be studied. Here, the binder jetting of fused silica (SiO_2) powders were investigated as precursor materials for subsequent molten metal infiltration and the manufacturing of metal-ceramic interpenetrating phase composites (IPCs). The structure-property relationship of cured, sintered, and infiltrated states were correlated to the variables powder size, spread speed, binder saturation, layer thickness, and sintering temperature.

The process parameters of the X1-Lab printer were optimized to manufacture the strongest SiO_2 ceramic body with the highest density. The printed parts were subsequently infiltrated with molten aluminum to create unique $\text{Al}/\text{Al}_2\text{O}_3$ IPCs. The parameters of 48 μm powders, 0.5 mm/sec spread speed, 60% binder saturation, 100 μm layer thickness, and 1500°C sintering temperature resulted in the highest density and compression strength of both the sintered and composite states. It was also found, that the mechanical investigation of the composite materials exhibited a strain-rate dependency that was observed by the split Hopkinson testing. In addition to the aforementioned outcomes, it was found that further densification of the printed parts is required to achieve the full potential of additive manufacturing on synthesizing IPCs for structural applications. A homogenization technique was also carried out via Matlab, and it showed to be a quick and reliable simulation technique to predict the elastic modulus of a two-phase composite system. Finally, alternative processing techniques were explored to create dense printed and infiltrated parts. It was shown that the agglomeration of small

particles and the addition of external pressure during the infiltration stage appear to be promising routes for increasing the density of IPCs manufactured via binder jetting.

Acknowledgements

I would first like to thank my dissertation advisor Dr. Pedro Cortes. Without your mentorship and guidance, I would not be where I am today. Thanks for everything Dr. Cortes.

I would like to thank my committee members Dr. Brett Conner, Dr. Tim Wagner, and Dr. Donald Priour. Thanks for the opportunity and knowledge to fulfil and exceed the requirements for this degree.

I would also like to thank Mark Peters, Brian Hetzel, Walt Whitman, and Eddie Stride thank Fireline Inc. Brian, you have been a great role model and friend.

All of the graduate students at Youngstown State that I have met through my four years here. I am truly thankful for our long lasting friendship and memories, as well as the beers at Inner Circle. Cheers.

Lastly, I would like to thank my family and wonderful girlfriend Traci. Thanks for all the love and support. I love you all.

Table of Contents

Title Page	i
Abstract	iii
Acknowledgements	v
Table of Contents	vi
List of Figures	ix
List of Tables	xii

Chapter 1 Introduction.....1

Chapter 2 Literature Review	15
2.1 Ceramics	15
2.1.1 Crystal Structures	16
2.1.2 Mechanical Properties	21
2.1.3 Manufacturing Techniques	22
2.1.3.1 Casting	23
2.1.3.2 Forming	24
2.1.3.3 Pressing	26
2.2 Metals	28
2.2.1 Mechanical Properties	30
2.2.2 Manufacturing Techniques	33
2.2.2.1 Casting	33
2.2.2.2 Deformation	35
2.2.2.3 Subtraction	36
2.3 Composites	38
2.4 Ceramic-Metallic Composites	40
2.4.1 Manufacturing Techniques	41
2.4.2 Reactive Metal Penetration	46
2.4.3 Applications	51
2.4.3.1 Ballistics	52
2.4.3.2 Automotive and Aerospace	55
2.4.4 Mechanical Property Characterization	58
2.5 Additive Manufacturing	63
2.5.1 Computer Assisted Design (CAD)	64
2.5.2 Vat Polymerization	66
2.5.3 Sheet Lamination	68
2.5.4 Powder Bed Fusion	70
2.5.5 Material Extrusion	73
2.5.6 Directed Energy Deposition	75
2.5.7 Binder Jetting	77
2.5.7.1 Introduction	77
2.5.7.2 Process Parameters	80
2.5.7.3 Infiltration of Printed Ceramic Structures	85

Chapter 3 Experimental	118
3.1 Binder Jetting of Ceramic Precursors	118
3.1.1 Powder Feeding Systems	119
3.1.2 Printhead Systems	120
3.1.3 CAD File	122
3.1.4 Curing and Sintering	122
3.2 Reactive Metal Penetration of Printed Silica Parts	123
3.3 Optical and Analytical Characterization of the Printed Ceramic and Composite Materials	124
3.3.1 Grinding and Polishing	125
3.3.2 Optical Microscopy	126
3.3.3 X-ray Diffraction	126
3.3.4 Scanning Electron Microscopy	129
3.3.5 Energy Dispersive Spectroscopy	133
3.4 Mechanical Testing	134
3.4.1 Compression Testing	135
3.4.2 Flexural Testing	137
3.4.3 High Strain Rate Compression Testing	138
 Chapter 4 Mechanical Property Simulation	 142
4.1 Mechanical Property Simulation Techniques for Composites.....	142
4.2 Homogenization Technique	150
4.3 Simulation Work	152
4.4 Experimental	156
4.5 Results and Discussion	156
4.6 Homogenization Conclusions	162
 Chapter 5 Binder Jetting Results and Discussion	 166
5.1 Fused Silica Powder Investigation	166
5.2 Optimization of Printing Parameters and Sintering Temperature to Maximize Density and Compression Strength of Sintered Ceramic Structures.....	172
5.2.1 Binder Saturation	173
5.2.2 Layer Thickness	176
5.2.3 Sintering Temperature	179
5.2.4 Printing Parameters	185
5.3 Investigation of the Infiltration Process of Sintered Silica Parts for the Manufacturing of Metal-Ceramic Interpenetrating Phase Composites (IPCs).....	190
5.4 Effect of the Sintering Temperature on the Compressive Strength of Composites Manufactured from the 48 μm Powder	193
5.5 Dimensional Accuracy and Reproducibility	202
5.6 Investigation of Physical and Mechanical Isotropic Properties of Sintered Parts	206
5.7 High Strain Rate Compression Testing of Composite Parts	211
5.8 Manufacturing of Scaled-Up Parts for Industrial Purposes	216
5.9 Densification Techniques.....	220
5.9.1 Redesigning of Parts	220
5.9.2 External Pressure	223

5.9.3 Agglomerated Powder	228
5.10 Cured State Mechanical Properties	230
Chapter 6	237

List of Figures

Figure 1.1 – Microstructure of MMC brake rotor.....	2
Figure 1.2 – Market analysis of MMCs of current and future years.....	2
Figure 1.3 – Image of fused silica glass preform and infiltrated Al ₂ O ₃ /Al composite.....	4
Figure 1.4 – 2D and 3D microstructure of interpenetrating phase composites.....	5
Figure 1.5 – Schematic of binder jet printing process.....	8
Figure 1.6 – Microstructure of stainless steel/bronze IPC.....	9
Figure 2.1 – Schematic of the seven possible unit cells.....	17
Figure 2.2 – Illustration of common ceramic crystal structures.....	21
Figure 2.3 – Schematic of slip casting manufacturing technique of ceramics.....	24
Figure 2.4 – Schematic of jiggering manufacturing technique of ceramics.....	25
Figure 2.5 – Schematic of extrusion manufacturing technique of ceramics.....	26
Figure 2.6 – Schematic of die pressing manufacturing technique of ceramics.....	27
Figure 2.7 – Schematic for cold and hot isostatic pressuring technique.....	28
Figure 2.8 – Illustration of the nucleation process of metal grains.....	30
Figure 2.9 – Relationship of material properties of common materials.....	33
Figure 2.10 – Schematic of sand mold casting of metals.....	34
Figure 2.11 – Representation of bulk metal deformation processes.....	36
Figure 2.12 – Representation of the three different types of composite materials.....	39
Figure 2.13 – Plot of the strength to weight ratio at different temperatures of different engineered materials.....	41
Figure 2.14 – Illustration of the nucleation process of metal grains with ceramic particles.....	43
Figure 2.15 – Schematic of different metal infiltration processes.....	44
Figure 2.16 – Plot of Gibbs energy and specific volume of different ceramics.....	49
Figure 2.17 – Schematic of good and bad wetting conditions.....	50
Figure 2.18 – Relationship of pore size and pressure for infiltration of molten Al in porous Al ₂ O ₃ parts.....	51
Figure 2.19 – Trends of specific modulus and specific strength of engineered materials.....	52
Figure 2.20 – Images of armor piercing round stopped by a metal-ceramic composite.....	54
Figure 2.21 – Image of layered ballistic system including an IPC.....	55
Figure 2.22 – SEM image of Al/SiC composite system.....	57
Figure 2.23 – Images of a CAD drawing and its tessellated form.....	65
Figure 2.24 – Classifications of different additive manufacturing techniques.....	66
Figure 2.25 – Schematic for the vat polymerization AM technique.....	68
Figure 2.26 – Schematic for the laminated object AM technique.....	69
Figure 2.27 – Schematic for the powder bed fusion AM technique.....	71
Figure 2.28 – Schematic for the fused deposition modeling AM technique.....	73
Figure 2.29 – Schematic for the directed energy deposition AM technique.....	76
Figure 2.30 – Schematic for the binder jet AM technique.....	78
Figure 2.31 – SEM image of stainless steel/bronze IPC.....	79
Figure 2.32 – SEM images of composites that were manufactured by binder jetting of ceramic bodies with subsequent metal infiltration.....	87
Figure 3.1 – Images of X1-Lab and M-Flex binder jetting printers manufactured by Ex One.....	119
Figure 3.2 – Schematic of the powder feeding systems of the X1-Lab and M-Flex.....	120

Figure 3.3 – Schematic of continuous stream and droplet on demand deposition methods..	121
Figure 3.4 – Schematic of a piezoelectric nozzle	121
Figure 3.5 – CAD drawing of the shapes printed for testing.....	122
Figure 3.6 – Image of kilns used for the infiltration process of printed SiO ₂ parts	124
Figure 3.7 – Image of the D8 Bruker PXRD	127
Figure 3.8 – Schematic of Bragg-Brentano goniometer used in the PXRD	127
Figure 3.9 – Schematic of diffraction showing Bragg’s law	128
Figure 3.10 – Image of JEOL JIB 4500 and JEOL JSM-IT 300 SEMs.....	130
Figure 3.11 – Schematic of an electron beam column in a SEM.....	131
Figure 3.12 – Representation of electron interaction during SEM analysis	132
Figure 3.13 – Representation of electron interactions for EDS analysis	134
Figure 3.14 – Image of Instron machine shown in the compression testing set up	135
Figure 3.15 – Schematic of a three wire quarter bridge.....	137
Figure 3.16 – Image of Instron machine showing the flexural testing set up.....	137
Figure 3.17 – Representation of the wave propagation during split Hopkinson testing.....	139
Figure 4.1 – Schematic of a microstructure used for a basic self-consistent model.....	144
Figure 4.2 – Unit cell representation of stainless steel/bronze composite.....	145
Figure 4.3 – Unit cell representation of a multiphase composite system	146
Figure 4.4 – Voxel unit cell representation of a two phase composite	147
Figure 4.5 – Unit cell representation of an interpenetrating phase composite.....	148
Figure 4.6 – Simulated stress contours of an Al/SiC composite.....	149
Figure 4.7 – Microstructure and converted binary image of Al/Al ₂ O ₃ composite	154
Figure 4.8 – Optical micrograph images of Al/Al ₂ O ₃ composite used in homogenization technique.....	157
Figure 4.9 – Stress-strain relationship of simulated and experimental results	159
Figure 4.10 – Optical micrograph images of three different planes of an Al/Al ₂ O ₃ composite.....	160
Figure 4.11 – Optical micrograph images of Sample 2 in the homogenization simulation...161	161
Figure 4.12 – Optical micrograph images of Al/Al ₂ O ₃ composite highlighting the binary conversion of porosity in a sample	162
Figure 5.1 – SEM images of four different SiO ₂ powders.....	168
Figure 5.2 – Diagram showing the printing direction of cylinder shapes.....	169
Figure 5.3 – Images of the 8 μm powder showing large porosity gaps	170
Figure 5.4 – Cured densities using different spread speeds.....	171
Figure 5.5 – Sintered densities using different binder saturation levels	174
Figure 5.6 – Image of printed cylinders showing barrel deformation of high binder saturation prints.....	175
Figure 5.7 – Compression strength of sintered parts using different binder saturations	176
Figure 5.8 – Sintered densities using different layer thicknesses	177
Figure 5.9 – Compression strength of sintered parts using different layer thicknesses.....	178
Figure 5.10 – Sintered densities using different sintering temperatures.....	180
Figure 5.11 – Image of sintered parts showing warping.....	180
Figure 5.12 – Compression strength using different sintering temperatures	181
Figure 5.13 – PXRD analysis of sintered parts at different sintering temperatures	183
Figure 5.14 – Magnified PXRD analysis of cristobalite phase.....	184
Figure 5.15 – SEM images of SiO ₂ part sintered at 1450°C showing micro-cracking.....	184

Figure 5.16 – Temperature and pressure phase diagram of SiO ₂	185
Figure 5.17 – Summary of densities and compression strengths of all tests	186
Figure 5.18 – SEM images of SiO ₂ parts sintered at different temperatures	189
Figure 5.19 – SEM images of the infiltrated 65 μm printed part.....	190
Figure 5.20 – SEM images of the infiltrated 48 μm printed part.....	191
Figure 5.21 – Special fixture used for infiltration of multiple parts	194
Figure 5.22 – Image of the cross-cut section of the infiltrated parts sintered at different temperatures.....	196
Figure 5.23 – SEM images of infiltrated parts showing a porous layer	197
Figure 5.24 – SEM images of infiltrated parts sintered at 1300°C.....	198
Figure 5.25 – SEM images of the edge of the infiltrated parts sintered at 1500°C	199
Figure 5.26 – SEM images of the center of the infiltrated parts sintered at 1500°C	199
Figure 5.27 – Optical micrograph image of infiltrated part showing random porosity	201
Figure 5.28 – Optical micrograph image of fully dense infiltrated binder jet printed composite	202
Figure 5.29 – Schematic of the layering of parts printed in different directions	208
Figure 5.30 – Image of sintered parts which were printed in different directions after compression testing.....	209
Figure 5.31 – Schematic of the crack propagation of sintered parts which were printed in different directions	213
Figure 5.32 – Impulse data from split Hopkinson testing.....	214
Figure 5.33 – Elastic modulus analysis using split Hopkinson testing.....	216
Figure 5.34 – Image of infiltrated parts after split Hopkinson testing.....	218
Figure 5.35 – Image of large plates printed on a M-Flex	219
Figure 5.36 – Image of large plates after sintering	220
Figure 5.37 – Schematic of taper design for high temperature sintering.....	221
Figure 5.38 – Image of part sintered at 1650°C designed with 5-degree taper	222
Figure 5.39 – SEM image of infiltrated part sintered at 1650°C	223
Figure 5.40 – Image of pressure chamber used for pressure infiltrations.....	226
Figure 5.41 – Optical micrograph image of pressure infiltrated SiO ₂ with Al.....	227
Figure 5.42 – SEM image of pressure infiltrated SiC with Al.....	228
Figure 5.43 – SEM image of agglomerated SiO ₂ powder	229

List of Tables

Table 1.1 – Advantages and disadvantages of different ceramic manufacturing techniques	6
Table 2.1 – Cation/anion radius ratio for specific crystal structures	18
Table 2.2 – Crystal structures from common ceramic materials	20
Table 2.3 – List of additives for traditional manufacturing techniques for ceramics	23
Table 2.4 – Mechanical properties for engineering metals.....	32
Table 2.5 – Subtraction manufacturing techniques for metals	37
Table 2.6 – Mechanical properties of metal-ceramic properties.....	59
Table 2.7 – Advantages and disadvantages of vat polymerization.....	67
Table 2.8 – Advantages and disadvantages of sheet lamination.....	70
Table 2.9 – Advantages and disadvantages of powder bed fusion	72
Table 2.10 – Advantages and disadvantages of material extrusion.....	75
Table 2.11 – Advantages and disadvantages of directed energy deposition.....	77
Table 2.12 – Advantages and disadvantages of binder jetting.....	80
Table 3.1 – Procedure for grinding and polishing samples for microscopy	125
Table 4.1 – Simulated mechanical properties of binder jetted Al ₂ O ₃ /Al composite	161
Table 5.1 – Particle size distribution of investigated SiO ₂ powders.....	167
Table 5.2 – List of parameters used for binder saturation, layer thickness, and sintering temperature	173
Table 5.3 – Initial results of sintering 65 and 48 μm printed parts.....	187
Table 5.4 – Initial results of infiltrating 65 and 48 μm sintered parts	192
Table 5.5 – Properties of 48 μm parts sintered at different temperatures.....	195
Table 5.6 – Dimensional accuracy results from 65 and 48 μm printed powders.....	205
Table 5.7 – Shrinkage measurements of sintering 65 and 48 μm parts sintered at 1500°C ..	206
Table 5.8 – Isotropic testing results of 48 μm parts sintered at 1500°C.....	209
Table 5.9 – Quasi-static and dynamic compression results of 48 μm parts sintered at 1400 and 1500°C	216
Table 5.10 – Compression results of 48 μm tapered parts sintered at 1650°C.....	222
Table 5.11 – Results of hot isostatic pressing from 48 μm printed parts.....	224
Table 5.12 – Summary of properties of the 48 μm printed parts in the cured state.....	231

Chapter 1 Introduction

Ceramic matrix composites (CMCs) and metal matrix composites (MMCs) are systems based on a ceramic and metal material, respectively, as the matrix phase while having either whiskers, particulates or another material as interpenetrating network, as the reinforcement phase (see Figure 1.1). These systems have attracted considerable interest due to their desired lightweight, thermal and mechanical properties at high temperatures [1]. The applications of these composites include cutting tools, forming dies, gas turbine parts, high pressure heat exchangers, and ballistic armor among many others [2]. CMCs are commonly reinforced with another ceramic, such as alumina (Al_2O_3) matrix with Nextel 720 ($\text{Al}_2\text{O}_3\text{-SiO}_2$) whiskers [3], and in these cases, the presence of the reinforcement phase deflects cracks upon formation allowing the material to display superior mechanical properties than the matrix material itself. Currently, CMCs are making a great impact in the aerospace industry. General Electric (GE) is currently researching CMCs to increase the efficiency of turbine engines, and has recently opened a plant dedicated to CMC research [4]. A study titled “Ceramic Matrix Composites Market in the US 2015-2019” shows that the GE Aviation will be a major driving force for the growth of the CMC market with a backlog of \$161 billion in orders for jet engine parts components [5]. The study also projects the market for ceramic matrix composites in the United States to grow at a compound annual growth rate of 11.45% from 2014 to 2019. This projection agrees with the market analysis carried out by the US DOD *et al.* [6] by estimating an increase of volume production of 49% from 2012 to

2019 (see Figure 1.2). These trends clearly show the interest of MMCs in different industrial sectors, especially the ground transportation sector.

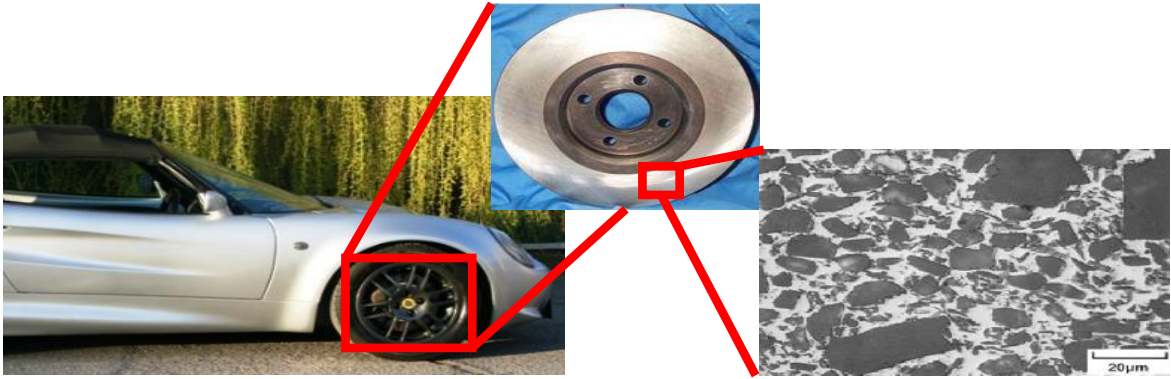


Figure 1.1. The Lotus Elise MMC brake rotor and a micrograph of an MMC microstructure.

Indeed, market studies have shown that approximately half of all manufactured MMCs are used in the ground transportation [7]. This is due to the production of aluminum based MMCs, which features low densities, excellent heat dissipation, and great wear resistance, making them attractive for the automotive industry [8].

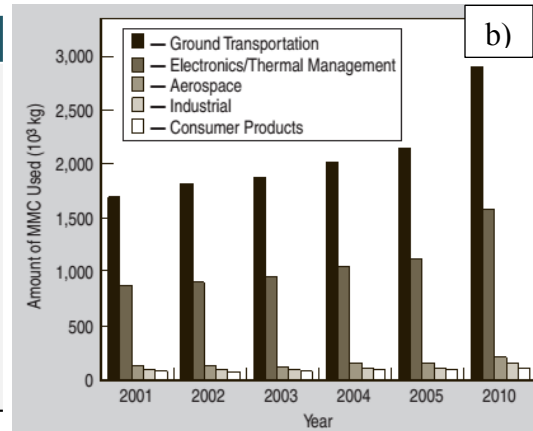
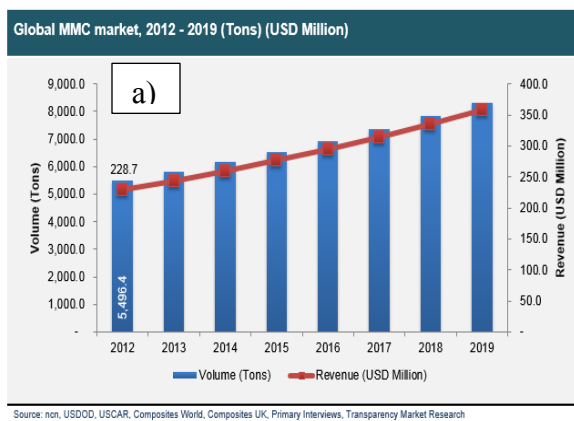
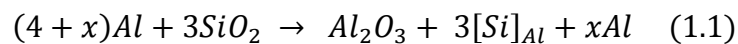


Figure 1.2. Market analysis of MMCs projecting the volume production and annual revenue in the current and future years (a), and a reported production analysis of the use of MMCs in the different industrial sectors (b) [6-7].

Evidently, there is a niche market for MMCs and therefore the continuous improvement on their performance and manufacturing process is an important aspect for their growth and application on diverse sectors. On these improvement terms, it is possible to have two materials that are both individually continuous through the composite. In this case both materials are considered to be a matrix material, and are appropriately called an interpenetrating phase composite (IPC) [9]. Typically IPCs have at least one the interpenetrating material as the metallic phase due to the ability of the molten metal to flow into a porous structure. One of the most common IPC systems studied is the Al_2O_3/Al IPC system due to its lightweight high strength properties. The Al_2O_3/Al IPCs can be manufactured through a large number of processing techniques which include: the Lanxide process of directed metal oxidation (DIMOX), using a sacrificial oxide displacement reaction, also known as the reactive metal penetration (RMP) process, squeeze casting, gas pressure infiltration, and self-propagating high-temperature synthesis (SHS) [10-14]. From these techniques, the RMP process has been highly used on producing MMCs since it takes advantage of a naturally occurring reduction reaction between a molten metal (typically aluminum) and a ceramic material (typically silica, SiO_2). The general chemical reaction between the molten aluminum and silica can be seen in Equation 1.1 [15]:



where x , is the excess amount of aluminum that surrounds the ceramic silica precursor. The RMP process was first studied and patented by Michael Breslin at The Ohio State University [16]. Breslin's process involved the submersion of silica-based ceramics under molten aluminum and aluminum alloys. The final $\text{Al}_2\text{O}_3/\text{Al}$ co-continuous ceramic composite created through Breslin's process was appropriately named C4. The RMP process is a 'near net-shape' technique that allows the final composite to keep its initial ceramic dimensions by up to 99% [17] (see Figure 1.3).

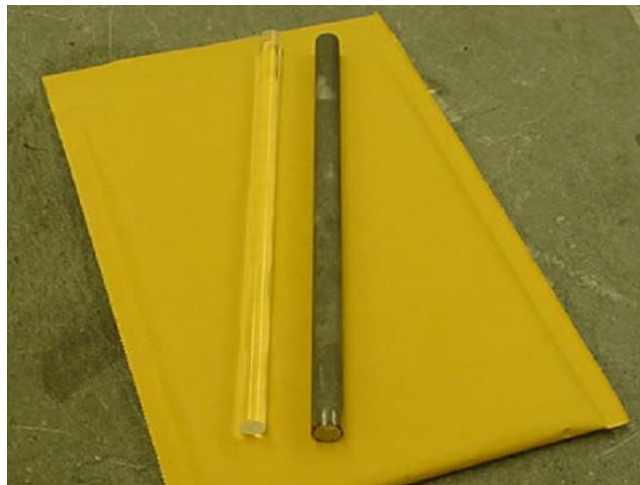


Figure 1.3. Fused quartz silica glass rod (left) and an $\text{Al}_2\text{O}_3/\text{Al}$ IPC (right) manufactured by the RMP process of fused quartz silica with aluminum [18].

Microscopic analysis of IPC composites in two dimensions commonly shows a random distribution of both phases, this distribution is actually a random network of both ceramic and metallic phases, which run continuously in all three directions (see Figure 1.4). This phase distribution can slightly be controlled by the density of the ceramic precursor. Indeed, by varying the amount of sacrificial oxide and porosity present in the ceramic precursor, the phase distribution of Al and Al_2O_3 in the composite can be controlled [19]. As expected, the IPCs thermal and mechanical properties will strongly depend on the

phase distribution of both phases. The properties of the IPC can also be controlled by using specific sacrificial oxides that will create desired phases such as spinel ($MgAl_2O_4$) and/or by using different aluminum alloys [18, 20-21]. Hence, the ceramic precursor material used in the synthesis of CMCs is a crucial aspect for determining their final mechanical and thermal properties, and therefore, the chemical nature of the precursor and the way the precursor is manufactured play an important role in the final outcome.

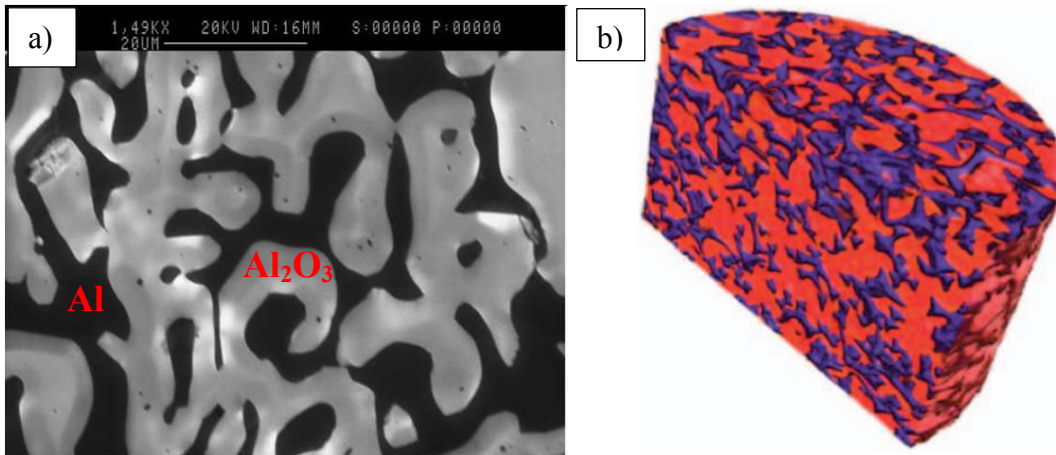


Figure 1.4. Microstructural analysis of an IPC material. a) 2D microstructure of Al_2O_3/Al IPC created by RMP. b) 3D CT-scan of an Al_2O_3/Cu IPC where the blue phase is Cu and the red phase is Al_2O_3 [18, 22].

A regional company with an extensive expertise in the manufacturing process of Al_2O_3/Al composites, is Fireline Inc. (located in Youngstown, OH). Fireline specializes in creating Al_2O_3/Al based composites via the RMP process, which is unique based on the ceramic precursors and aluminum alloy bath used. Fireline's RMP based composites are typically made from silica based ceramic precursors and inert silicon carbide (SiC) particulates, which are submerged under an aluminum-silicon alloy. These high performance IPCs are typically used for high temperature applications, but have recently sparked interest in the ballistic armor and brake rotor fields.

The shape of the ceramics used in the creation of the MMCs can be manufactured through different routes, such as slip casting, extrusion, dry pressing, wet pressing, hot pressing, isostatic pressing, jiggering, and injection molding. A list of the advantages and the disadvantages of each manufacturing technique can be seen in Table 1.1 [23].

Table 1.1. Advantages and disadvantages of ceramic manufacturing techniques [23].

Process	Advantages	Disadvantages
Slip Casting	Large parts; complex shapes; low equipment cost	Low production rate; limited dimensional accuracy
Extrusion	Hollow shapes and small diameters; high production rate	Parts have constant cross section; limited thickness
Dry Pressing	Close tolerances; high production rate with automation	Density variation in parts with high length-to-diameter ratios; high cost equipment; dies require high abrasive-wear resistance
Wet Pressing	Complex shapes; high production rate	Limited part size and dimensional accuracy; high tooling costs
Hot Pressing	Strong high-density parts	Protective atmosphere required; short die life
Isostatic Pressing	Uniform density distribution	Equipment can be costly
Jiggering	High production rate with automation; low tooling cost	Limited to axisymmetric parts; limited dimensional accuracy
Injection Molding	Complex shapes; high production rate	High tooling costs

Commonly, the manufacturing process of ceramic structures for their further transformation into a ceramic-metallic IPC is performed via slip casting. Slip casting involves the mixing of ceramics with water and other additives to create a slurry, or “slip”. This slip is then poured into a plaster mold and left to dry. The mold then draws out most of the water in the ceramic, leaving a part strong enough for handling. The

ceramic part is then sintered in order to achieve a final ceramic part [23]. Although slip casting has a lot of benefits, not all ceramic materials (such as magnesia) can be easily slip casted. Also, it is difficult to create a complex mold for very intricate parts. Therefore, the incorporation of Additive Manufacturing (AM) on ceramic precursor could be the missing link in the creation of IPCs to fit virtually any design. AM is the process of creating a part in a layer-by-layer fashion. The part is built up by the deposition process of material based off of a digital file describing a 3D object, which is created by a Computer Assisted Drafting (CAD) software. AM is often interchanged with the term of 3D printing. Since the inception of 3D printing in the 1980s, many processes have been created to expand the materials that can be printed. Most 3D printing processes locally melt the material which is being printed to induce bonding of layers, therefore, the local melting is all dependent on the material's melting temperature. However, the ability to locally melt metals and ceramics require a substantial amount of energy. The main energy source to print metals and ceramics are typically lasers or electron beams [24]. An alternative way to 3D printing is to locally glue the material together, which can be achieved by the binder jetting technology [25].

Binder jetting is a type of AM by which the part is built by laying down binder droplets onto a bed of evenly spread powder material (see Figure 1.5). The binder material is a liquid based polymer system that upon curing will turn into a solid adhesive. Subsequently, the printed part is sintered and the polymer binder burns off, leaving a solid ceramic part for its further transformation into an IPC.

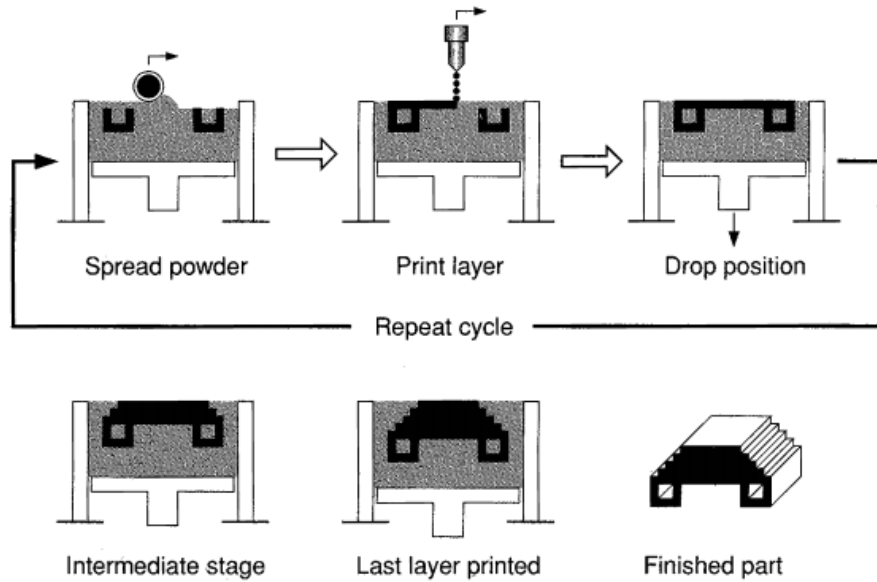


Figure 1.5. Schematic of the binder jetting process. The process is accomplished by rolling powder flat and dropping binder in the position of the part being created. The process is repeated until the part is complete [26].

However, one drawback from the binder jetting process is the porosity left in the sintered part. Here, the binder itself takes up space in the printed part leaving the ceramic particles too far apart to achieve an appropriate sintering stage. Typically a sintered part will achieve a density around 50-60% depending on the processing parameters and particle shape [27]. On the other hand, the drawback of porosity in a printed body ceramic, can be taken as advantage during the transformation process of the printed part by infiltrating it with metal and yielding the aforementioned IPC. The leading vendor of binder jetting printers, Ex One™, sells their equipment to print 316 stainless steel. In this case, Ex One achieves a fully dense part by taking advantage of naturally occurring wicking process between stainless steel and molten bronze. Here, the bronze fills the porosity of the stainless steel part, leaving a stainless steel/bronze IPC (Figure 1.6).

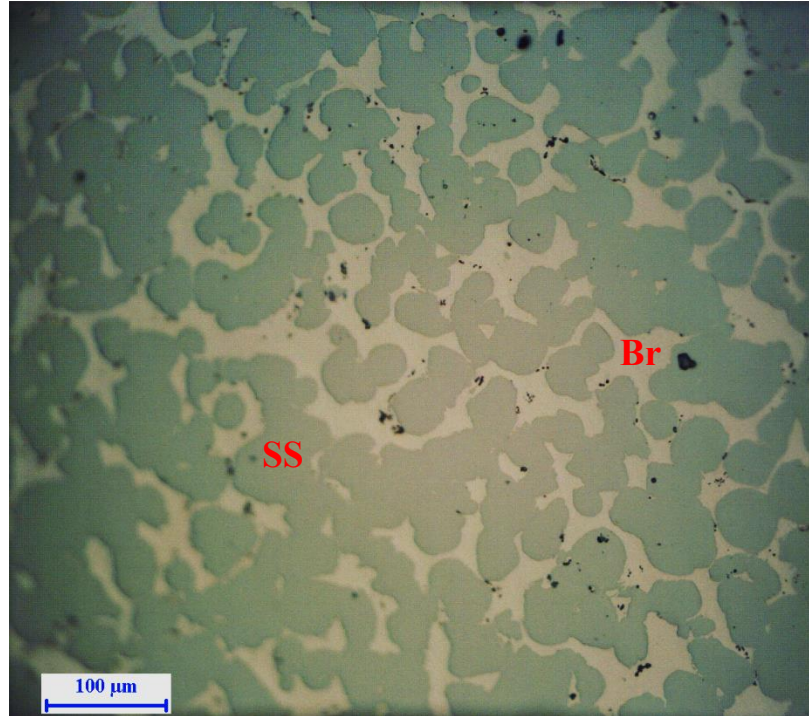


Figure 1.6. Optical micrograph of a stainless steel/bronze IPC manufactured from the infiltration of a binder jetted stainless steel backbone which was infiltrated with bronze.

The lighter phase is bronze (Br) and the darker phase is stainless steel (SS).

The concept of manufacturing IPCs with binder jetting has been studied for years due to its ability to create a composite with any unique dimensions or geometry, which is not possible with any other manufacturing technique. This concept has led to the subject of this research work: the study of the structure-property relationship of ceramic-metallic IPCs, manufactured via binder jetting.

Objectives

The main objective of this research program is to investigate the process of forming ceramic-metallic IPCs via the RMP process using a binder jetting 3D printed ceramic precursor. Here, silica based ceramics will be printed, cured, sintered, and infiltrated with aluminum to create the ceramic-metallic composite.

Additional specific objectives are to:

- Characterize the physical and mechanical properties of the cured, sintered, and composite structures.
- Investigate the process settings for binder jetting which optimize the physical and mechanical properties of the IPCs.
- To use a homogenization simulation technique to model the elastic modulus of a binder jetted two-phase IPC.

Organization

This study is divided into 6 chapters:

- Chapter 1 presents the information needed to show the reasoning of this study.
- Chapter 2 presents the literature review of metals, ceramics, composites, and all of their manufacturing processes and corresponding mechanical properties. It also includes the background of all AM techniques.
- Chapter 3 describes the experimental procedure used in the binder jetting process, the metal infiltration technique, and the mechanical testing used in this study.
- Chapter 4 includes the mathematical description of a homogenization simulation technique for predicting the elastic modulus of manufactured-printed MMCs.
- Chapter 5 displays the results and discussion of all the data found.
- Chapter 6 concludes and summarizes the present research work.

References

1. Moya, J. S., Lopez-Esteban, S., & Pecharroman, C. (2007). The challenge of ceramic/metal microcomposites and nanocomposites. *Progress in Materials Science*, 52(7), 1017-1090.
2. De Garmo, E. P., Black, J. T., & Kohser, R. A. (2011). *DeGarmo's materials and processes in manufacturing*. John Wiley & Sons.
3. Wannaparhun, S., Seal, S., & Desai, V. (2002). Surface chemistry of Nextel-720, alumina and Nextel-720/alumina ceramic matrix composite (CMC) using XPS—A tool for nano-spectroscopy. *Applied surface science*, 185(3), 183-196.
4. "Ceramic Matrix Composites | GE Global Research." *GE Global Research*. Accessed: 09 Nov. 2015. <http://www.geglobalresearch.com/innovation/ceramic-matrix-composites-improve-engine-efficiency>.
5. TechNavio, "Ceramic Matrix Composites Market in the US 2015-2019", July 2015. <http://www.technavio.com/report/ceramic-matrix-composites-market-in-the-us-2015-2019>.
6. Transparency Market Research "Metal Matrix Composites (MMC) Market for Ground Transportation, Electronics/Thermal Management, Aerospace and Other End-users - Global Industry Analysis, Size, Share, Growth, Trends and Forecast, 2013 – 2019" May 2014. <http://www.transparencymarketresearch.com/metal-matrix-composites.html>.
7. Chawla, N., & Chawla, K. K. (2006). Metal-matrix composites in ground transportation. *The Journal of The Minerals, Metals & Materials Society*, 58(11), 67-70.

8. Macke, A., Schultz, B. F., Rohatgi, P. K., & Gupta, N. (2013). Metal matrix composites for automotive applications. *Advanced Composite Materials for Automotive Applications: Structural Integrity and Crashworthiness*, 311-344.
9. Clarke, D. R. (1992). Interpenetrating phase composites. *Journal of the American Ceramic Society*, 75(4), 739-758.
10. Breval, E., Aghajanian, M. K., & Luszcz, S. J. (1990). Microstructure and composition of alumina/aluminum composites made by directed oxidation of aluminum. *Journal of the American Ceramic Society*, 73(9), 2610-2614.
11. Breslin, M. C., Ringnalda, J., Xu, L., Fuller, M., Seeger, J., Daehn, G. S., Otani, T., & Fraser, H. L. (1995). Processing, microstructure, and properties of co-continuous alumina-aluminum composites. *Materials Science and Engineering: A*, 195, 113-119.
12. Feng, H. J., & Moore, J. J. (1995). In situ combustion synthesis of dense ceramic and ceramic-metal interpenetrating phase composites. *Metallurgical and Materials Transactions B*, 26(2), 265-273.
13. Lange, F. F., Velamakanni, B. V., & Evans, A. G. (1990). Method for Processing Metal-Reinforced Ceramic Composites. *Journal of the American Ceramic Society*, 73(2), 388-393.
14. Prielipp, H., Knechtel, M., Claussen, N., Streiffer, S. K., Müllejans, H., Rühle, M., & Rödel, J. (1995). Strength and fracture toughness of aluminum/alumina composites with interpenetrating networks. *Materials Science and Engineering: A*, 197(1), 19-30.

15. La Vecchia, G. M., Badini, C., Puppo, D., & D'Errico, F. (2003). Co-continuous Al/Al₂O₃ composite produced by liquid displacement reaction: Relationship between microstructure and mechanical behavior. *Journal of materials science*, 38(17), 3567-3577.
16. Breslin, M. C. (1993). *U.S. Patent No. 5,214,011*. Washington, DC: U.S. Patent and Trademark Office.
17. Fahrenholtz, W. G., Ewsuk, K. G., Ellerby, D. T., & Loehman, R. E. (1996). Near-Net-Shape Processing of Metal-Ceramic Composites by Reactive Metal Penetration. *Journal of the American Ceramic Society*, 79(9), 2497-2499.
18. Paul, R. M. (2007). *Microstructural and Chemical Characterization of Interpenetrating Phase Composites as Unique Refractory Materials Produced Via Reactive Metal Penetration* (Master's Thesis, Youngstown State University).
19. Fahrenholtz, W. G., Ellerby, D. T., Ewsuk, K. G., & Loehman, R. E. (2000). Forming Al₂O₃-Al composites with controlled compositions by reactive metal penetration of dense aluminosilicate preforms. *Journal of the American Ceramic Society*, 83(5), 1293-1295.
20. Yurcho, A. M. (2011). *Microstructural Investigation of Al/Al-Fe alloy-Al₂O₃ Interpenetrating Phase Composites Produced by Reactive Metal Penetration* (Master's Thesis, Youngstown State University).
21. Myers, K. M. (2012). *Investigation of Novel Precursor Routes for Incorporation of Titanium Alloys and Nano-Sized Features into Ceramic-Metallic Composites Formed via the TCON Process* (Master's Thesis, Youngstown State University).

22. Poniznik, Z., Salit, V., Basista, M., & Gross, D. (2008). Effective elastic properties of interpenetrating phase composites. *Computational Materials Science*, 44(2), 813-820.
23. Kalpakjian, S., Schmid, S. R., & Kok, C. W. (2008). *Manufacturing processes for engineering materials*. Pearson-Prentice Hall.
24. Gibson, I., Rosen, D. W., & Stucker, B. (2010) Additive manufacturing technologies: rapid prototyping to direct digital manufacturing.
25. Sachs, E., Cima, M., Williams, P., Brancazio, D., & Cornie, J. (1992). Three dimensional printing: rapid tooling and prototypes directly from a CAD model. *Journal of Manufacturing Science and Engineering*, 114(4), 481-488.
26. Jee, H. J., & Sachs, E. (2000). A visual simulation technique for 3D printing. *Advances in Engineering Software*, 31(2), 97-106.
27. Yoo, J., Cima, M. J., Khanuja, S., & Sachs, E. M. (1993). Structural ceramic components by 3D printing. In *Solid Freeform Fabrication Symposium*, 40-50.

Chapter 2 Literature Review

The composites studied in this research work are made of two basic materials: a ceramic and a metal. The unique thermal and mechanical properties of these systems stem from the individual materials that constitute the composite. An introduction to ceramic and metal materials and their mechanical properties, and manufacturing techniques is initially given in this chapter to provide an understanding of the benefits that each material provides to the composite. Also, an introduction to general composites is given to display the unique characteristics of these systems. A more detailed description of aluminum-based composites as well as their applications for lightweight materials is subsequently presented. Finally, a basic description and the advantages and disadvantages of each additive manufacturing technique is presented, with the biggest insight on the binder jet printing process and the printing of ceramic materials for molten metal infiltration.

2.1 Ceramics

The word “ceramic” is derived from the Greek word “keramikos”, which means “burnt stuff”. The terminology infers that ceramics must be heated to high temperatures to manufacture a shape [1]. Ceramics are inorganic materials typically consisting of at least two elements. The atomic bonding in ceramics is predominately ionic, where a positively charged cation will attract a negatively charged anion to balance the compound’s overall charge, which creates a crystal structure [2]. Indeed, most ceramic materials have ionic bonding, but some ceramics can exhibit a degree of covalent bonding. These ceramics contain elements that typically have covalent characteristics such as carbon (C). An example of a covalently bonded ceramic would be silicon carbide (SiC) [3]. The type of

bonding and elements that are in a ceramic material play a big roll on how the ceramic is constructed at the elemental level.

2.1.1 Crystal Structures

The mechanical and thermal properties of all materials can be described by how each material is bonded and arranged on an atomic level, or crystal structure. The crystal structure is defined by its smallest repeating volume, or unit cell. Each unique repeating unit can vary by its length (a, b, and c) and angle (α , β , and γ) in all three dimensions (see Figure 2.1) [4]. There are seven basic unit cell structures that can be formed: cubic, tetragonal, orthorhombic, monoclinic, triclinic, hexagonal, and trigonal. A few of these unit cells can have variations, which are function of the translation of the unit vector of each individual unit cell. These variations are called Bravais lattices. In three dimensions there are 14 distinct Bravais lattices which can be seen in Figure 2.1 [4].

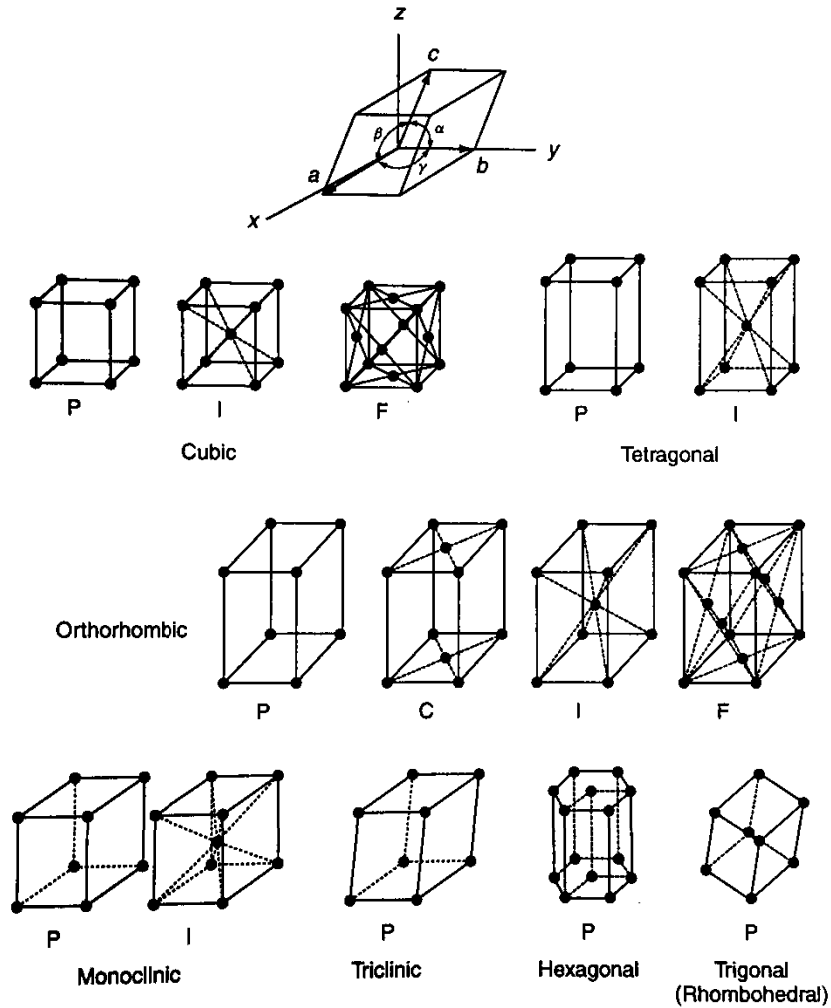


Figure 2.1. Representation of a unit cell (top) showing the variables of a , b , c , α , β , and γ .

Below are the 14 Bravais lattices in three dimensions, where P = primitive, I = body centered, F = face centered, and C = base centered [4].

The ionic character of the bonds created in the unit cell is mostly dependent on the electronegativities of all the atoms present. A crystal will form when the electrical charge of the ions is net neutral. When the crystal is net neutral, the placement of each atom is dependent on two characteristics: the magnitude of the electrical charge of each individual atom and the radius of each ion [5]. The magnitude of the charge for the

cation-anion relationship will determine the ratio of how many cations are present in the unit cell compared to anions. The second criterion involves the ratio of the cation/anion radius', r_c/r_a . This radius ratio determines the geometrical orientation of all atoms (see Table 2.1) [6].

Table 2.1. The cation/anion radius ratio with their corresponding coordination numbers and geometry for ceramic crystal structures.

Coordination Number	Geometry	Cation/Anion Radius Ratio r_c/r_a
8	Cube	1-0.732
6	Octahedron	0.732-0.414
4	Tetrahedron	0.414-0.225
3	Planar Triangle	0.225-0.155
2	Linear	< 0.155

For ceramics, the most common crystal structures will have coordination numbers 4, 6, and 8. These systems typically have atomic ratios AX, A_mX_p , and $A_mB_nX_p$, where A is the cation, and X is the anion. There are three common crystal structures that are related to the AX system. One is the “sodium chloride” (NaCl), which has a coordination number of 6. This unit cell is a face-centered cubic structure (FCC), where the cation/anion ratio is 0.56. The second common AX crystal lattice is named the “cesium chloride” (CsCl) unit cell. This unit cell has a coordination number of 8 ($r_c/r_a = 0.96$), but is not considered a body centered cubic (BCC) crystal structure because the cation and anion are interchangeable at each of the coordination positions. Therefore, the crystal structure is considered to be two primitive cubic crystal structures that are offset to each other. The third common crystal for AX systems is called “zinc blende” or “sphalerite”. The term zinc blende comes from the mineralogical term for zinc sulfide (ZnS). The ion radius

ratio for ZnS is 0.40 which gives it a coordination number of 4. The crystal structure is a FCC structure which has a sulfur at all 8 corner positions, as well as at the 4 face positions. Another common ceramic that has the zinc blende crystal structure is SiC [3] The crystal structures of rock salt, cesium chloride and zinc blende can be seen in Figure 2.2 [7].

For ions that are not equal in charge, a chemical formula will result with an A_mX_p form, where m and/or p is greater than 1. One of the more common chemical structures of this nature is called the “fluorite” crystal structure. The fluorite structure is most commonly associated with calcium fluoride (CaF_2). The r_c/r_a ratio for CaF_2 is equal to 0.75, which gives the systems a coordination number of 8. To achieve the chemical formula of CaF_2 , calcium is only present in half of the eight cubes (see Figure 2.2) [7]. Other common ceramics that have the fluorite crystal structure are uranium oxide (UO_2) and thorium oxide (ThO_2) [6].

It is also possible to form ceramics with two different cations in the molecular formula. These ceramics will have the chemical formula of $A_mB_nX_p$. The two most common ceramic formulas are ABX_3 and AB_2X_4 , which are known as the “perovskite” and “spinel” crystal structures respectively. For instance, calcium titanium oxide ($CaTiO_3$) has the perovskite structure (FCC), where the Ca^{+2} ions are at the corner of the cubic lattice, the Ti^{+4} ion is at the center, and the O^{-2} at every face of the cube (see Figure 2.2). Some other compounds that have the perovskite crystal structure include barium titanate ($BaTiO_3$), strontium stannate ($SrSnO_3$), and strontium zirconate ($SrZrO_3$) [8]. The spinel crystal structure is also a FCC system where the B cation is at the corners of the cubic system as well as at the octahedral sites throughout the repeating unit cell. Here, the

A-cations will be in the tetrahedral positions and the X anion will fill in between the bonds of the octahedral and tetrahedral positions (see Figure 2.2). Some of the common spinel ceramics are MgAl_2O_4 , FeAl_2O_4 , and MgCr_2O_4 [6]. A summary of the typical crystal structure data for ceramics can be seen in Table 2.2.

Table 2.2. Summary of the crystal structures for ceramic materials [6]

System	Unit Cell	Crystal Structure	Coordinate Number	Common Compound
AX	Sodium Chloride	FCC	6	NaCl, MgO, LiF
AX	Cesium Chloride	BCC	8	CsCl, CsBr, CsI
AX	Zinc Blend	FCC	4	ZnS, SiC, ZnTe
A_mX_p	Fluorite	BCC	8, 4	CaF_2 , UO_2 , ThO_2
$A_mB_nX_p$	Perovskite	FCC	12, 6, 2	CaTiO_3 , SrZrO_3 , MgTiO_3
$A_mB_nX_p$	Spinel	FCC	6, 4, 6	MgAl_2O_4 , FeAl_2O_4 , MgCr_2O_4

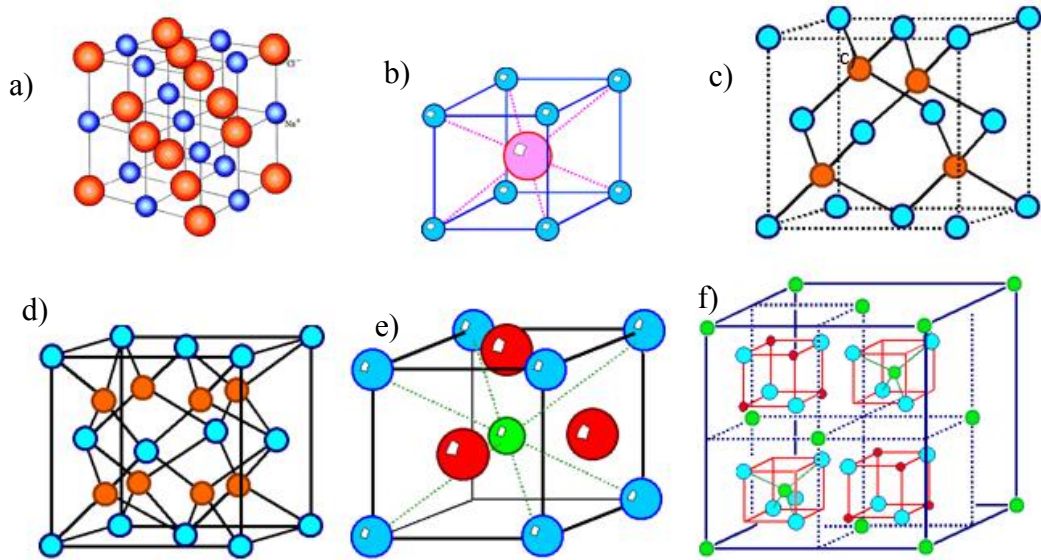


Figure 2.2. Common crystal structures of ceramic materials, a) rock salt, b) cesium chloride, c) zinc blende, d) fluorite, e) perovskite, and f) spinel [7].

2.1.2 Mechanical Properties

It is well known that the ions present in a specific crystal structure have some relationship to the mechanical strength of the ceramic, although the strength is mostly influenced by the particle size or grain structure [9]. Typically, ceramics are a brittle material that can break very easily under a tensile stress. The brittleness of a ceramic is due to existence of micro cracking and dislocations in the material. Micro-cracking is typically caused by a mismatch in strains from the different surrounding particles as the ceramic cools from typical manufacturing techniques. Any non-cubic crystal system will have an inherent anisotropic thermal expansion. The crack growth will typically follow specific crystallographic planes that correspond to planes with a high atomic density [10].

These micro cracks in can limit their tensile mechanical applications due to the potential of a catastrophic failure. Although ceramic materials do not have a high strength under tension, they are excellent at absorbing energy under compression conditions. Compressive stresses do not get amplified due to the micro cracks, and the stresses can be ten times higher than that of the tensile strength [11]. Since ceramic materials do not perform well under tension, they are typically tested using a 3 or 4 point flexural testing. In the 3 point bending test, a rectangular sample, with a length:width ratio of at least 16:1, is placed on a two support stands, and a load is applied in the center of the span. The sample is then bent until fracture occurs [12]. Typically, the maximum stress that is applied until the failure stage is reported, and it is called flexural strength or modulus of rupture.

Along with micro cracking, porosity (which is a common feature in ceramics), plays a large role in their strength. For instance, the elastic modulus can be diminished depending on the amount of porosity in the sample. A general model for the elastic modulus as a function porosity was given by Mackenzie in 1950 [13]:

$$E = E_o(1 - 1.9P + 0.9P^2) \quad (2.1)$$

where E , is the elastic modulus of the porous material, E_o , is the ideal elastic modulus of the material with no porosity, and P , is the porosity volume fraction of the material. Equation 2.1 is a valid approximation for a material that has a porosity lower than 50%. Also, for relatively low amounts of porosity the quadratic term can be ignored [14].

2.1.3 Manufacturing Techniques

There are several techniques to manufacture ceramic parts. Although each technique is different, there are a few steps that each technique has in common. Each technique involves grinding the raw materials to very fine particle sizes, mixing the ground particles with additives, shaping, drying, and firing to create the final part [15]. The additives that are mixed with the particles can be any of the following (see Table 2.3):

Table 2.3. List of additives used during the mixing of ceramic particles [15]

Additive	Purpose
Binder	Bonding of ceramic particles
Lubricant	Used for mold release and to reduce internal friction between particles
Wetting agent	Improves mixing
Plasticizer	Improves plasticity of mix and makes it more formable
Deflocculent	Makes the ceramic particles mix more evenly in solvent
Foaming agent	Helps to not create a foam on top of mix
Sintering aid	Helps to sinter ceramic material

The firing (or sintering) stage of manufacturing ceramic parts is a crucial step for creating a dense and strong final part. Here, the porous compact, which involve small particles, are bonded together into a dense part by solid state diffusion. It is commonly known for the sintering of ceramic parts, increasing the surface area: volume ratio of the compacted particles, will increase the density of the fired part [8]. Ceramic manufacturing can be generalized into three basic techniques: casting, forming, and pressing. These three techniques are described below.

2.1.3.1 Casting

Casting is the most commonly used manufacturing technique for ceramics. For casting, the ceramic powder is mixed with a solvent, typically water, to create a slip. The slip is then poured into a mold with a designed shape (see Figure 2.3) [1]. The mold is made of plaster of paris, which is used to absorb the water out of the slip. Once the outer edge of the ceramic is semi-solid, the rest of the slip is poured out. After the part is completely dried, the mold is removed and the ceramic can then be fired. During drying, the ceramic will shrink and, this shrinkage is taken into account when designing a part. At the drying stage, the part is considered to be in the “green” state. In the green state, the ceramic can be shaped or machined very easily to achieve precise dimensions or details. Finally, the part is fired to bond the ceramic particles together to make a final solid part [5].

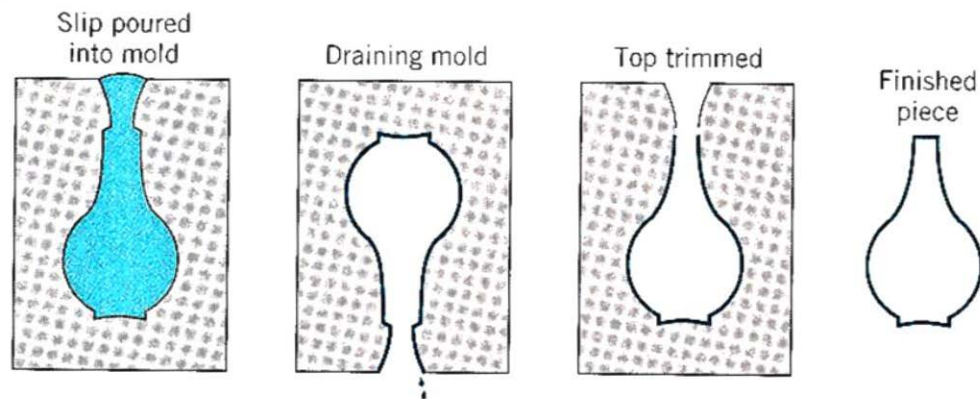


Figure 2.3. Schematic of the production of ceramic parts using a slip casting technique.

The diagram shows pouring, removal of excess slip, removal of mold, drying, and the final part [1].

2.1.3.2 Forming

The techniques that are considered to be forming are extrusion, injection molding, and jiggering. These manufacturing techniques can be performed with ceramics that are dry, wet, or plasticized. Plastic forming will take sheets of plasticized ceramic material and lay them either on the top of each other, or inside of a mold [16]. If multiple layers are used, the final part will have anisotropic properties due to the layering effect. The process of jiggering also can have anisotropic properties due to the layering effect. During jiggering, a clay slug is placed on a mold, and it is pressed down on top of the mold. A jiggering tool is used as the mold turns on a pottery wheel to shape the clay. The process is repeated until the final dimensions are achieved [16].

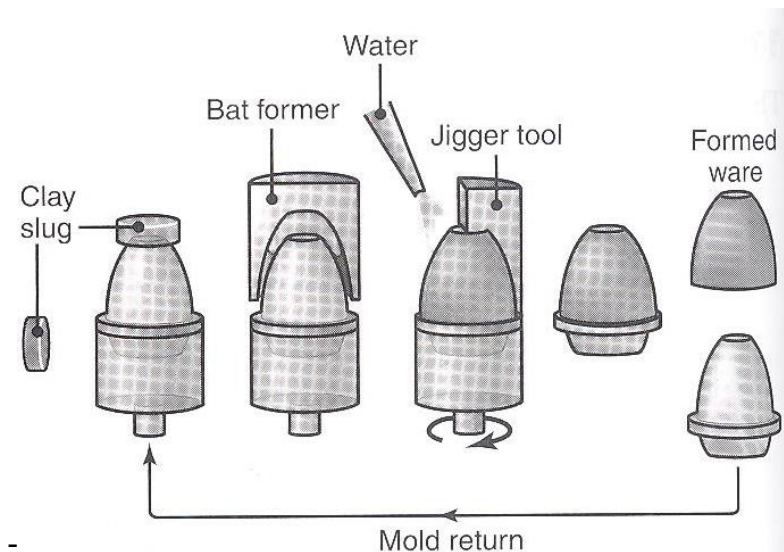


Figure 2.4. Schematic of jiggering (forming) process. A clay slug is placed on top of a mold base and then compressed to fit the mold. Subsequently, the jiggering tool is used to shape the final part. The process is repeated until the part reaches its final shape and thickness [15].

The processes of extrusion and injection molding do not use a layering technique. During both of these processes, the ceramic is in a wet form. For extrusion, the ceramic will have 20-30% water and binder. The ceramic is pushed through a die that will hold the final shape and length (see Figure 2.5) [17]. The process of extrusion allows for production of large sections of the final part, while the injection molding does not, due to the geometrical constraints of the mold. Injection molding of ceramic materials is typically used for precision parts in rocket engines. Similarly to extrusion, injection molding uses water and binder to flow the ceramic particles into a mold. After either the extrusion or the injection molding, drying and firing steps are needed to achieve a dense part [17].

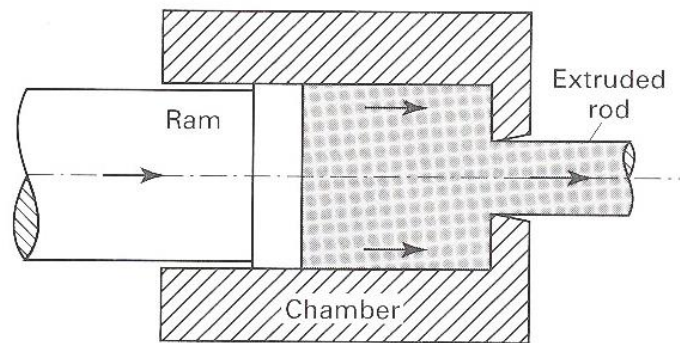


Figure 2.5. Schematic of the extrusion manufacturing technique. A ram or screw pushes the material through a die to create the desired shape. Similar to extrusion, injection molding uses the same technique to flow material, with the difference of having a mold at the end of the chamber [17].

2.1.3.3 Pressing

The manufacturing technique of pressing involves the flow of a wet or dry ceramic material into a mold. After filling the mold, a die presses down the material

unidirectionally. Due to the non-uniform pressure on the material, the molds tend to be basic in shape. The density of the pressed material tends not to be uniform throughout due to the uneven pressing. If the density variation is not suitable for a specific application or mold, a double-action press can be used to help create a more uniform sample (see Figure 2.6) [15]. In the double action press, two or more dies can apply pressure from the same or opposite side. The strength of the final part is directly related to the compressibility of powder. The more tightly packed the powder is, the higher the elastic modulus will be achieved after sintering [16].

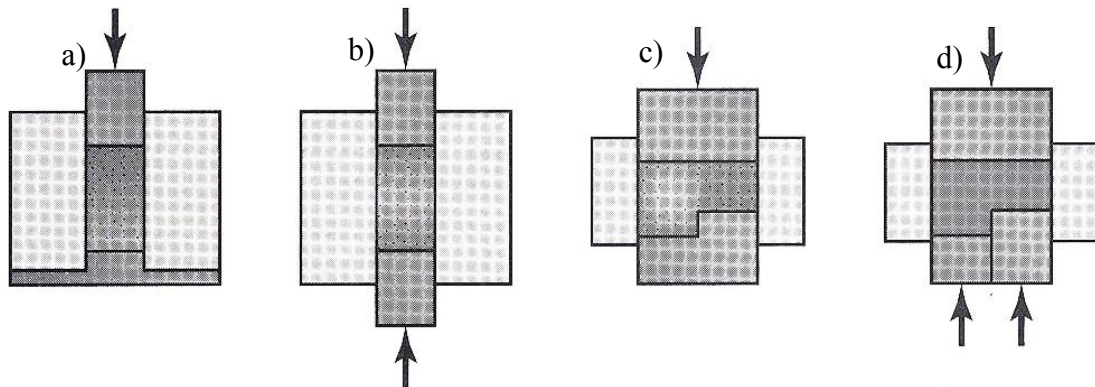


Figure 2.6. Schematic of die pressing process where a) and c) are single die presses with uniform and non-uniform shapes respectively. In contrast, images b) and d) show a double and multi-action press that are used to achieve a more uniform density of the pressed part [15].

One method used to achieve the maximum density of a pressed part is to apply uniform pressure in all directions upon the component. Isostatic pressing accomplishes this by taking advantage of surrounding the powder with a rubber mold that can compress without fracturing. The rubber mold is then placed into a pressure chamber that can reach over 400 MPa (60 ksi) [3]. The pressure chamber is back filled with water or an inert gas

to create the uniform pressure around the rubber mold (see Figure 2.7). If the compression is performed at room temperature, the process is called cold isostatic pressing (CIP). Following a CIP process, a secondary sintering process is needed to achieve the final part. In order to achieve this, the pressure chamber will need to be filled with an inert gas. On the other hand, the compression can be performed under hot isostatic pressing (HIP) conditions. The HIP process typically goes up to pressures of 100 MPa (15 ksi) and temperatures of 1100°C (2000°F). After HIPing, the part is fully dense (99-100%) and needs no secondary post processing [3].

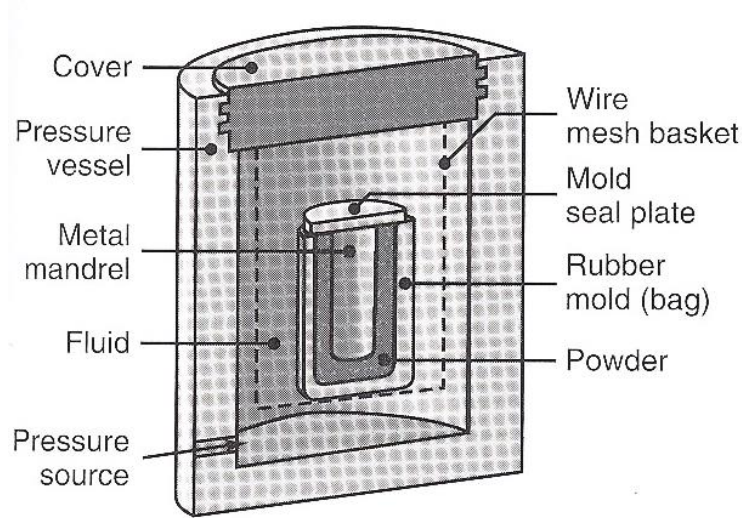


Figure 2.7. Schematic of the CIPing process. The process for HIPing is similar to CIP, with the addition of heating coils in the pressure chamber and the use of metal mold instead of a rubber mold [15].

2.2 Metals

The term “metal” originates from the Greek word “métallon” which means mine or quarry. Unlike ceramics, metals typically form crystal structures as a single atom system, where each atom has no atomic charge. Although metals can form in any crystal

structure, they are mostly body center cubic (bcc), face centered cubic (fcc), and hexagonal close packed (hcp) [9]. This is due to the packing efficiency that is associated with each crystal structure. The packing efficiency is measured by calculating the space in the crystal structure that is occupied by the atoms using the cell dimensions and the radius of the element. The packing efficiency for the bcc, fcc, and hcp lattices are 68, 74, and 74% respectively [3]. In metals, the atoms are bound together by a sharing of electrons that is similar to covalent bonding, but unlike covalent bonding, the valence electrons are shared universally, not locally. This means that the valence electrons are free to move around the material in an electron cloud or electron gas. The free movement of electrons is the cause for high electrical and thermal conductivity which is found in metals [18].

Metals are formed by melting a bulk material and then recrystallizing it. During the recrystallization, crystal structures begin to form at a point called the nucleus. At the nucleus, the atoms will continue solidifying by forming the repeating crystal structure, which is known as the grain. While the metal is solidifying, multiple grains are being grown simultaneously. The grains will eventually grow large enough until they meet each other and create boundaries (see Figure 2.8) [8]. The size of the grains greatly influences the mechanical strength of metal materials. Smaller grains in metals result in higher yield strengths due to the larger number of grain boundaries present in the system. The yield strength is defined at the point between the elastic and plastic deformation zone [9].

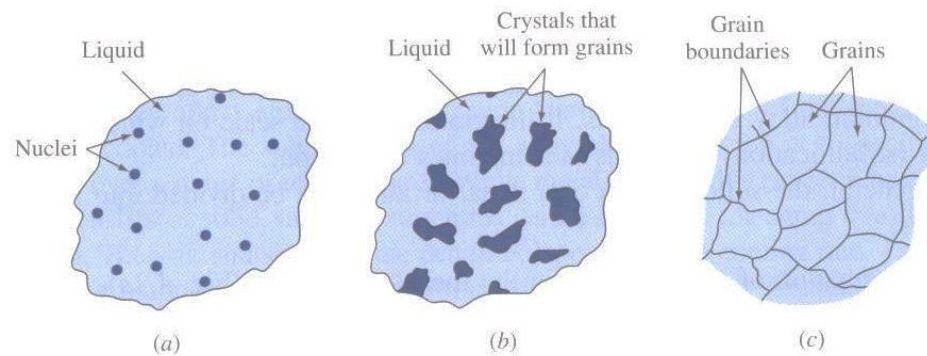


Figure 2.8. Schematic of the nucleation process during the solidification of metals. The process starts after the cooling of a molten metal, when a) a crystal structure is locally formed as multiple nuclei, b) the crystal structures extend to form grains, and c) the grains grow into each other and form grain boundaries [8].

The mechanical properties of metals can be tailored by controlling the grain structure. This can be accomplished by changing the cooling rate of the molten metal, creating more defects in the system by plastically deforming the metal, or by using heat treatments [19].

2.2.1 Mechanical Properties

The mechanical response of metals under stress is typically opposite to that observed in ceramics. While ceramics are brittle and can fracture under small loads, metals elongate and deform. Metals are considered to be ductile, where ductility is the measurement of the strain of a specimen before fracture. Due to the ductile nature of metals, their strength is typically tested under tension conditions [20].

Metals can be engineered into alloys in order to create stronger materials than the base constituents. Alloyed metals are divided into two categories: iron based or ferrous metals and nonferrous metals. Approximately 90% by weight of metallic materials used are ferrous alloys. Steel can contain anywhere between 0.05-2.0 wt. % of C, while cast iron is between 2.0-4.5 wt. % C. Additionally, other elements such as Mn, P, Si, Cr, Ni, or Mo are mixed to create steel alloys [5].

Nonferrous metals are abundant, but have different applications due to their mechanical and physical strengths. Aluminum based alloys are the most commonly nonferrous metals due to their low density and corrosive resistance. Aluminum is typically doped with Cu, Mn, Si, Mg, and Zn. Aluminum alloys are becoming more prevalent in the automotive industry for frames and structure parts [21]. Magnesium alloys have an even lower density than aluminum and are being used as structural materials in aerospace designs. Titanium based alloys are unique because they can retain strength at moderate temperatures, allowing them to be used in skin materials for high speed aircrafts [1]. On the other hand, copper alloys, such as brasses and bronzes, have great electrical properties and nickel super alloys have great high temperature strengths and resistance to plastic deformation due to a solid-solution formation of intermetallic phases [1]. A summary of the mechanical properties of commonly manufactured ferrous and nonferrous metals can be seen in Table 2.4 [11].

Table 2.4. Summary of the mechanical properties for commonly used ferrous and nonferrous engineered metals [11].

Material	Elastic Modulus (GPa)	Yield Strength (MPa)	Ultimate Strength (MPa)
Cast Iron A536	159	334	448
AISI 1020 Steel	203	260	441
ASTM A514, T1 Structural Steel	208	724	807
AISI 4142 Steel	200	1619	2450
AISI 4142 Steel 205°C Temper	207	1688	2240
AISI 4142 Steel 370°C Temper	207	1584	1757
AISI 4142 Steel 450°C Temper	207	1378	1413
18 Ni Maraging Steel (250)	186	1791	1860
SAE 308 Cast Aluminum	70	169	229
2024-T4 Aluminum	73.1	303	476
7075-T6 Aluminum	71	469	578
AZ91C-T6 Cast Magnesium	40	113	137

The applications of ceramic and metal materials are directly related to their mechanical and physical properties. A visual representation of the relationship between the density and elastic modulus, as well as the strength and service temperatures of common metal and ceramic materials can be seen in Figure 2.9 [22]. The figures show that the strength of ceramic materials is typically higher than that of metals and alloys. Although, ceramics tend to be lighter and serviceable at higher temperatures than metals, metals have the ability to plastically deform and not have a catastrophic failure.

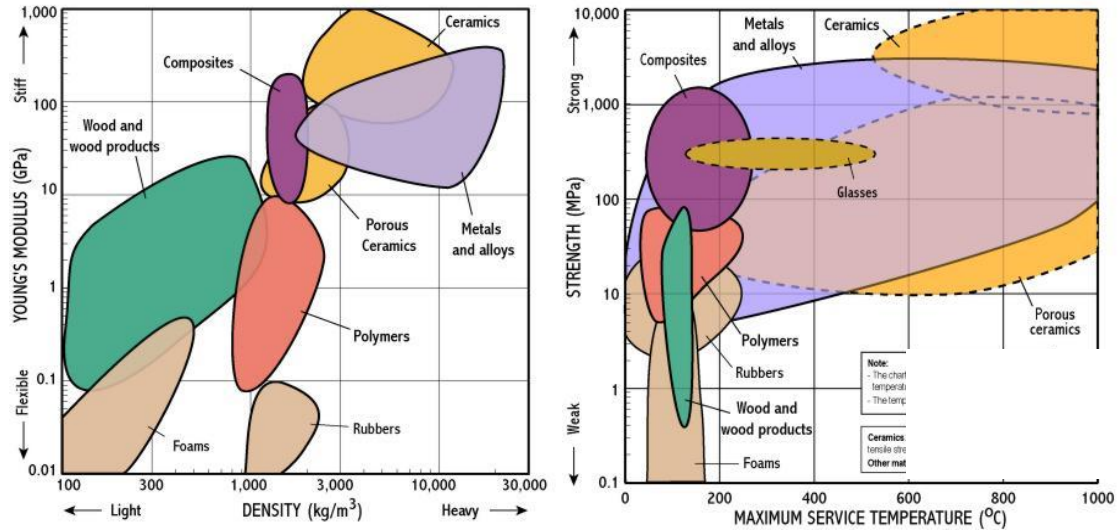


Figure 2.9. Relationship of Young's modulus versus density (a) and strength versus maximum service temperature for common materials (b) [22].

2.2.2 Manufacturing Techniques

Similar to ceramics, metals are manufactured by three main processes which are casting, deformation, and subtraction. The following section describes the manufacturing techniques used to create bulk metal parts.

2.2.2.1 Casting

Casting of metals is very similar to that of casting ceramics, with the significant difference is that metals are cast in the liquid state. Casting occurs at temperatures that are over the metal's melting point. For example, aluminum needs to be cast at over 660°C. The mold that is used for metal casting must be able to support high temperatures. The molds are typically made of silica sand that is naturally bonded (bank sand) or synthetic (lake sand) [16]. Metal molds are made of two parts which are split horizontally

(see Figure 2.10) [17]. Here, the mold cavity is filled with molten metal via the runner, which was filled through the pouring cup.

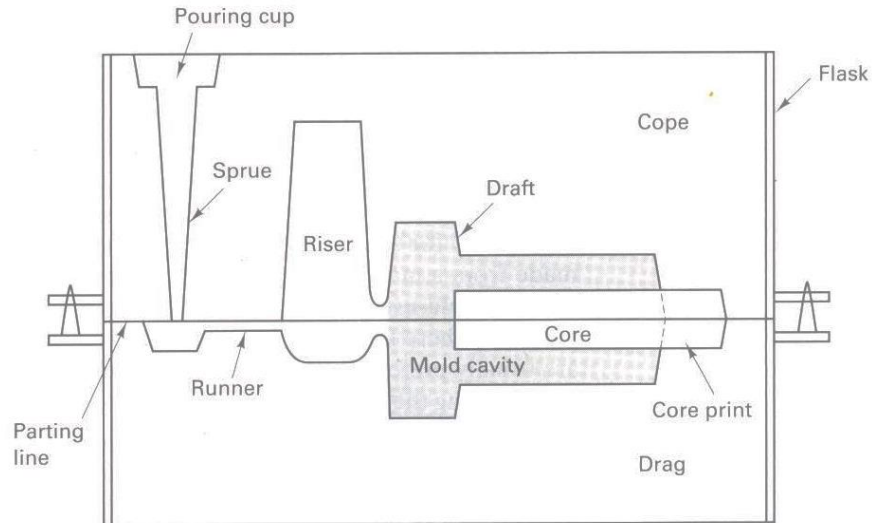


Figure 2.10. Schematic of a sand mold for metal casting. The metal is poured into the pouring cup and it travels through the runners to finally reach the mold cavity. The mold itself is a two-part sand mold which splits the final part down the center horizontally [17]. The metal mold shown in Figure 2.10 displays a riser, which is an extra source of molten metal to fill the mold cavity as it begins to solidify and shrink. By design, the riser will be the last to solidify and will contain all the shrinkage voids. After solidification the mold can be removed to recover the final part. The final part will have a parting line that is made from the two-piece mold [17].

Metal parts can also be formed using the same powder techniques as ceramics. Powder metallurgy (P/M) is defined as a manufacturing process that uses fine metal powders pressed into a mold, which can be hot or cold, to create a part. The powders can also be mixed into a slurry with binders. After compaction of the powder, the part is

sintered to create the final part. 70% of the P/M products are produced for the automotive market. [21].

2.2.2.2 Deformation

Deformation processes are those techniques that subject a solid piece of metal (generally casted) to plastic deformation under forces applied through a die or tooling. Deformation can be performed in cold, warm, or in hot atmospheres. Forging, rolling, extrusion, and pulling are bulk deformation techniques that are commonly used. Although all of the deformation techniques are similar, they differ by the degree of plastic deformation applied. For forging, the deformation is carried out with compression forces [15]. Here, a bulk piece of metal is placed between two dies and is compressed to fit a mold. During rolling, metal is pushed through two rolling pins to create a final part. The rolling technique is typically used to make plates, bars, rods, pipes, and I-beams. Extrusion and pulling are similar manufacturing techniques, which consist on deforming a metal, by pushing or pulling it through a die to create a shape. The only difference is that extrusion pushes the material through a die creating compressive deformation, whereas the pulling manufacturing creates a tension deformation [15]. A schematic of all of the deformation manufacturing techniques can be seen in Figure 2.11.

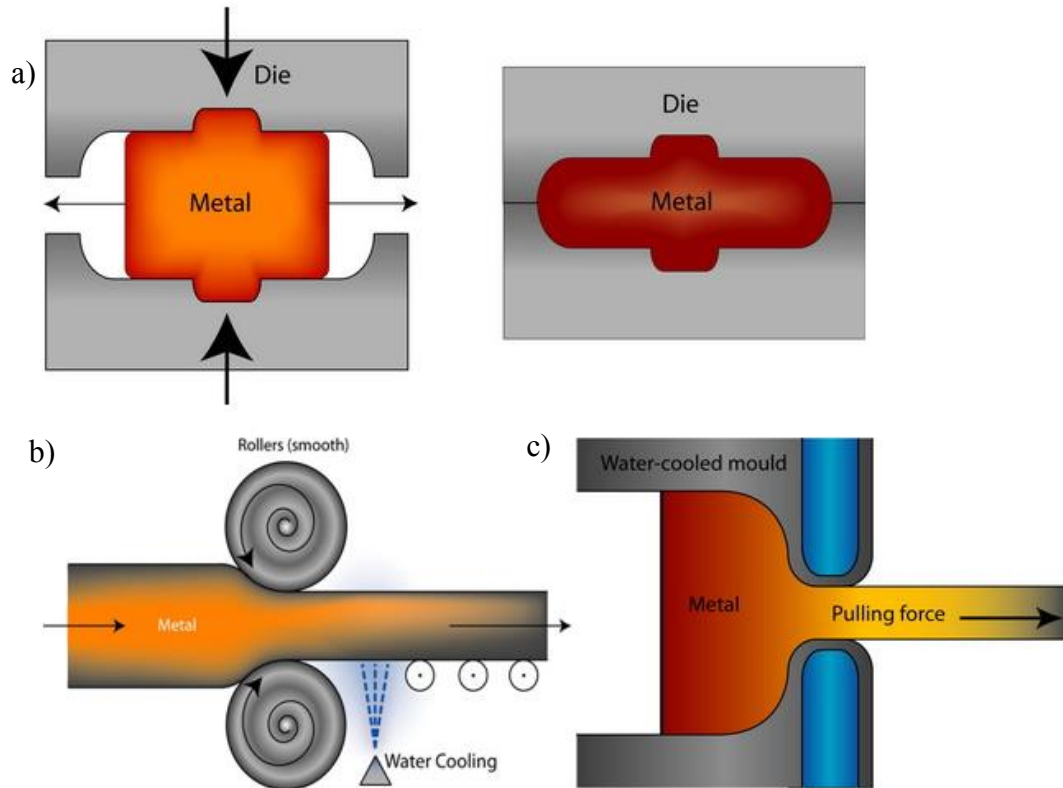


Figure 2.11. Schematics of bulk deformation processes for metal manufacturing: a) forging, where metal is compressed between two dies, b) rolling, where metal is pushed through rolling pins, and c) pulling, where the metal is pulled through a die. Image c) can also represent extrusion if the force is pushing the metal through the die [23].

2.2.2.3 Subtraction

Most parts manufactured using the previously mentioned techniques will not meet the dimensional accuracy or surface quality needed in the final part. These parts need further processing to reach these goals. Hence, material can be removed from a variety of different physical techniques which include: sawing, boring, turning, drilling, tapping, milling, grinding, lapping, and ultrasonic machining. A summary of all subtractive manufacturing techniques can be seen in Table 2.5 [17]. Other techniques such as

electricity, chemicals, heat, high pressure water, and optical sources of energy (high powered lasers) can also be used as advanced machining processes [15].

Table 2.5. Summary of subtraction manufacturing processes including raw material form, production rate and recommended material choice [17]

Process	Raw Material Form	Production Rate	Material Choice
Turning (Engine Lathes)	Cylinder preforms, casting forging	1-10 parts/hour	All ferrous and nonferrous material considered machinable
Turning (CNC)	Bar, rod, tube preforms	1-2 parts/minute to 1-4 parts/hour	Any material with good machinability rating
Turning (Automatic Screw Machine)	Bar, rod	10-30 parts/minute	Any material with good machinability rating
Turning (Swiss Automatic Machining)	Rod	12-30 parts/minute	Any material with good machinability rating
Boring (Vertical)	Casting, preforms	2-20 hours/piece	All ferrous and nonferrous
Milling	Bar, plate, rod, tube	1-100 parts/hour	Any material with good machinability rating
Hobbing (Milling Gears)	Blanks, preforms, rods	1 part/min	Any material with good machinability rating
Drilling	Plate, bar, preforms	2-20 second/hole after setup	Any unhardened material; carbides for some case hardened parts
Sawing	Bar, plate, sheet	3-30 parts/hour	Any nonhardened material
Broaching	Tube, rod, bars, plate	300-400 parts/minute	Any material with good machinability rating
Grinding	Plate, rod, bars	1-1000 pieces/hour	Nearly all metallic materials plus many nonmetallic
Shaping	Bar, plate, casting	1-4 parts/hour	Low-to-medium carbon steels and nonferrous metals, no hardened parts
Planing	Bar, plate, casting	1 part/hour	Low-to-medium carbon steels and nonferrous metals
Gear Shaping	Blanks	1-60 part/hour	Any material with good machinability rating

2.3 Composites

Composites are heterogeneous systems consisting of two or more materials that are bound together as one part [24]. They can be made from a mixture of different materials such as metals, ceramics, and plastics, which can also be a combination of these three as well. Typically, composites are identified by geometry of phases involved in the final part. The three commonly manufactured composites are laminar or layered, particulates, and fiber-reinforced [8]. Laminar or layered composites have two different materials which are bonded to each other. A common example of a layered composite is plywood. Here, layers of veneer wood are glued together with angles of the grains differing to improve the strength and fracture resistance. It should also be noted that these composites are anisotropic in nature. The transversal direction perpendicular to the layers will be weaker than the others [25]. Particulate and fiber-reinforced composites have two main phases in them. The matrix is the bulk material which is continuous through the whole part, whereas the reinforcement is the phase embedded into the matrix, which provides structural strength, wear resistance, and toughness. The distinction between particulate and fiber reinforced composites comes from the geometry of the reinforcement phase. Particulate composites have random shapes as well as random orientation throughout the matrix material. These composites can be isotropic in nature due to the random orientation of the particulates. The phase distribution and particle size will affect the final mechanical and thermal properties of the composite. The fiber-reinforced composites are generally made with fibers with high aspect ratios. The fibers can be oriented randomly or unidirectional and can also be continuous or discontinuous. Similar to the particle composites, randomly oriented fiber composites can be isotropic in

nature. The unidirectional fibers will make the composite anisotropic, where the strongest direction follows the length of the fibers [9]. A schematic of the main three composite types previously mentioned can be seen in Figure 2.12.

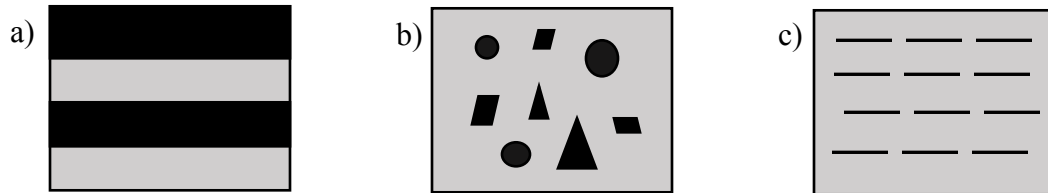


Figure 2.12. Representation of the three types of composite materials. The black and gray colors represent two different phases. Part a) is the laminate or layered structure where the two materials are glued together, b) is the particulate structure where the reinforcement materials have random size, shape and orientation, and c) the fiber-reinforced composite with long-thin reinforcement particles.

An alternative class of composite systems are those based on ceramic and metal materials. These composites are typically made with a metal matrix and a ceramic reinforcement. A smaller, unique class of high-performance ceramic-metal composites are the interpenetrating phase composites (IPCs), where both the ceramic and metal constituents are continuous throughout the entire composite. The process of creating these composite materials and their corresponding mechanical properties follows a large number of manufacturing techniques. For the focus of this research work, the manufacturing process and mechanical properties of two these phase ceramic-metallic based composites will be reviewed in more detail in the following sections.

2.4 Ceramic-Metallic Composites

The term ceramic-metallic composite refers to a two phase system where one phase is made of metal and the other of ceramic. In most cases, the metal component is the matrix of the composite, and the ceramic is the reinforcement. The addition of the ceramic phase in the composite, results in a higher strength to weight ratio system, in comparison to the metal matrix phase by itself (see Figure 2.13). The increased strength to weight ratio allows the metal matrix composites (MMCs) to have similar applications as high strength alloys and super alloys [26]. Typically, MMCs are used as structural components, automotive parts, aerospace equipment, and tooling [27]. Indeed, their application is dependent on their material constitution, and how much of each component are present in the final phase distribution of the composite. A special type of MMC, is a system known as interpenetrating phase composite (IPC), which is a composite constituted by a more even phase distribution of ceramic through the body. This equal phase configuration results in ceramic and metallic phases being continuous throughout the whole composite without isolated phases. Since both phases are continuous and interpenetrating, the mechanical strength of the IPCs are superior to those shown by common MMCs [28].

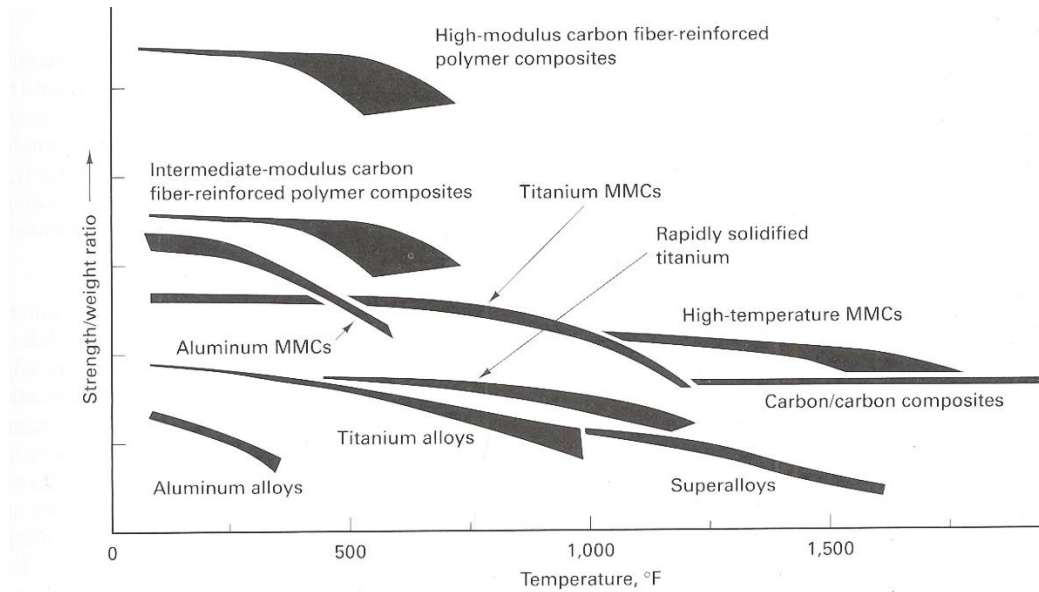


Figure 2.13. A plot of the strength to weight ratio versus temperature of metals, and their corresponding MMCs. The composite material shows a higher strength/weight ratio than the plain matrix at all reported temperatures [17].

Currently, there are several techniques to manufacture composites that are made of ceramics and metals. The constituents and the technique used for manufacturing these composites affect its final mechanical properties.

2.4.1 Manufacturing Techniques

The majority of metal-ceramic composites are created while the metal phase is in the molten state. Typically, the molten metal does not wet the ceramic phase; therefore, wetting agents are commonly added to the melt or to the ceramic particles to increase wetting. Molten or “wet” manufacturing process of composites can be performed in several ways [27]:

- Mixing ceramic particles in molten metal and casting a part.

- Melt infiltration into a ceramic body.
- Oxidation of the melt.

In the case of mixing ceramic particles in molten metal, several processing aspects need to be considered such as achieving a uniform distribution of the reinforcement material, adding the proper wetting agents to create a wetting effect between the particles and the molten metal, creating porosity from air bubbles during casting, and considering a possible reaction that may occur between the ceramic particulate and the molten metal [29]. Creating a part with uniform ceramic distribution through this technique is relatively difficult to achieve. The mixing blade and its design can have an influence on the distribution of the particulates. The blade must be able to move the particles around the molten system and also keep them in suspension to avoid agglomeration at the bottom [30]. It was found by Thomas [31] that particles below 10 μm will be carried by the liquid, and will remain suspended. When the particles are that small, the gravitational forces are negligible, creating a uniform distribution. The time of stirring and speed of the mixing blade can also affect the particle distribution. Prabu *et al.* [32] found that when mixing SiC in an Al-11Si alloy using a speed of 600 rpm, and a time of 10 minutes, it seems to have resulted in an appropriate ceramic particle distribution, which led to a high hardness value of the cast composite. The study was performed at different mixing speeds (500, 600, and 700 rpm) and mixing times (5, 10, and 15 minutes). Following mixing, the metal is casted into a mold, and as the metal solidifies, the metal begins to nucleate creating a grain structure. In this process, the particles are rejected by the grain growth, ending up in between the grains of the metal matrix (see Figure 2.14) [33].

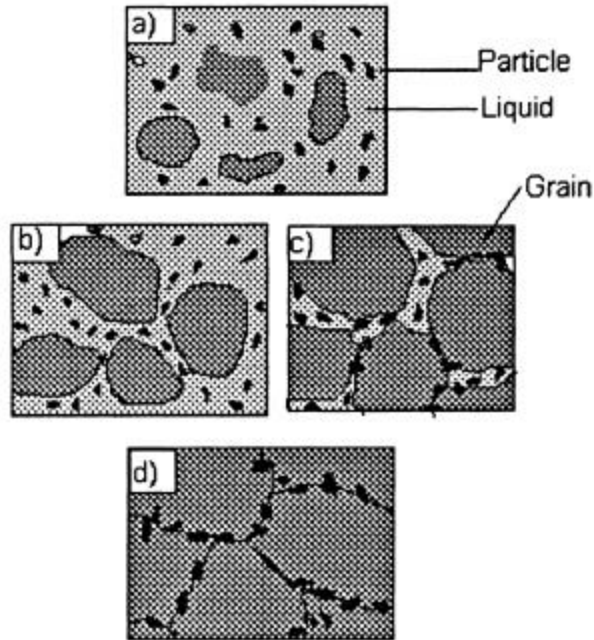


Figure 2.14. Schematic of the different steps of solidification of a metal within ceramic particles where: a) grain growth is random in the metal, b) there is interaction between the particles and the grains, c) particles are forced in between all of the grains, and d) the final microstructure of the MMC [33].

As mentioned before, the addition of ceramic particles to metals will increase the mechanical strength of the base material. One example of this was demonstrated by McDanel [34], where an aluminum alloy (Al-6061) was combined with varying amounts of SiC. He found that the tensile strength of the base aluminum alloy was 290 MPa, whereas the addition of 15, 20, and 30% SiC by volume resulted in strengths of 340, 410, and 435 MPa, respectively.

The other wet manufacturing technique relies on the infiltration of molten metal into a ceramic body [35]. Typically, metal is placed on top of a porous ceramic body and then is heated to temperatures above the melting point of the metal. The metal infiltrates into the

porosity of the ceramic perform creating a composite system. For instance, Binner *et al.* [36] was able to infiltrate an Al_2O_3 ceramic perform with an Al-Mg alloy. This pressureless infiltration can leave porosity in the final composite. To avoid porosity in the composite, external forces can be applied on the molten metal in the form of a mechanical die [37] or through an inert gas [38] like argon (Ar) (See Figure 2.15). Here, the external pressure forces the molten metal into the ceramic with little to no porosity left in the composite. Although pressurized infiltration systems will lead to less porosity, they can be expensive to build.

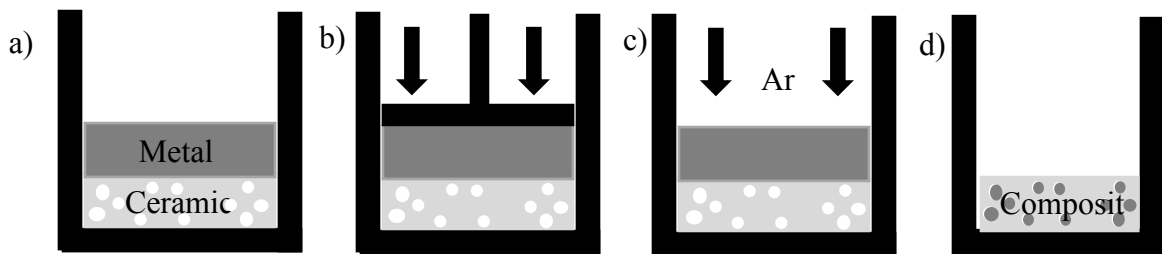


Figure 2.15. Schematic of infiltration techniques: a) pressureless infiltration where the metal infiltrates by a capillary effect, b) pressure infiltration, where a die forces the metal into the ceramic, c) pressure infiltration, where an inert gas (argon) forces the metal into the ceramic, and d) the final composite showing both the metal and ceramic phases.

The $\text{Al}_2\text{O}_3/\text{Al}$ IPC is widely studied for its impressive strength/weight ratio and high temperature properties. It can be formed by oxidizing molten aluminum, a process commonly called directed metal oxidation (DIMOX). Here, the metal is typically oxidized at 1400-1600 K in air, and at the surface, the aluminum is oxidized to form Al_2O_3 grains. Molten aluminum continues to follow the growth of oxide layer with veins on the size of 20 nm to 1 μm in width [39]. The composite will keep growing upwards, and fill out the area of the crucible or the mold. The DIMOX process can also be

performed using different aluminum alloys such as Al-Si-Mg alloys [40]. The oxidation of magnesium (Mg) will form magnesia (MgO), which is a precursor of spinel (MgAl_2O_4). At the beginning of this process, a thin layer of Al_2O_3 and MgO forms on the surface of the metal. Subsequently, the $\text{Al}_2\text{O}_3/\text{Al}$ network begins to grow upward away from the melt, and a $\text{MgAl}_2\text{O}_4/\text{Al}$ network begins to grow at the surface of the original melting zone. The rate of the spinel growth is dependent of the concentration of Mg present in the alloy [41].

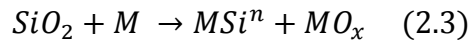
Another method to manufacture MMCs is to mix the ceramic and metal powders together, then compact the powders similarly to powder metallurgy. The powders can be dry or wet mixed, and compacted into a specific shape [42]. The compacted component is then dried, and subsequently sintered to achieve the final composite. This process typically results in some form of porosity in the final composite. Shamsudden *et al.* [43] mixed Al_2O_3 , chromium (Cr), and iron (Fe) powders together at different volume percentages. The mixtures were all uni-axially pressed at 750 MPa and subsequently sintered at 1100°C under vacuum. The final composites all had porosity ranging from 10-20%. In order to remove porosity, the mixtures were hot pressed and extruded through a die [44]. The MMCs manufactured by Mazen and Ahmed were found to have a tensile strength of up to 155 MPa when using Al and 5% Al_2O_3 . The authors claimed that there is a 64-100% tensile strength improvement compared to pure aluminum.

The manufacturing of an $\text{Al}_2\text{O}_3/\text{Al}$ composite can also be accomplished with a reaction based infiltration. An example of this process, would be the infiltration of silica (SiO_2) with molten Al. As the aluminum infiltrates the ceramic, it reacts with silica to form alumina [45]. The process can be performed in three dimensions and the reaction will

continue from all sides until the reaction fronts meet in the center [46]. The final composite results in an Al/Al₂O₃ IPC. This process is known as reactive melt penetration (RMP).

2.4.2 Reactive Metal Penetration

The original discovery of this process took place in the 1950's when Henri George received a patent for composite materials created from the reaction of molten metal with SiO₂ and silica based ceramics [47]. The general reaction can be summarized as:



where silica can react with any reducing metal (M) to form an oxide and a metal-silicon alloy. The patent claims that this reaction can be performed with the following reducing metal: Al, Mg, Na, K, Li, Ca, Ba, and Sr. George described that this reaction works best with Al and Al alloys at a temperature range of 700-900°C, but can happen at higher temperatures with larger Al₂O₃ grain growth. It is stated that the final composite will keep the shape of SiO₂ preform, with a phase distribution of approximately 80% Al₂O₃ and 20% Al.

This process was not utilized until 1993 when Michael Breslin [48] patented the synthesis process of Al₂O₃/Al ceramic-metal composites by reacting a sacrificial ceramic material with aluminum based alloys. The patent extended past silica based ceramics, and claimed that it will work with other ceramics such as MgO, SiC, SiN, ZrC, and ZrN. His patent also claims to work with aluminum alloys composed with one or more of the

following elements: Fe, Co, Mg, Ti, Ta, W, Y, Nb, Zr, and Hf. This RMP process has a reaction rate of approximately 8 cm/day while the DIMOX process is 2.5-3.8 cm/day [48]. Breslin *et al.* [45] also reported the development of a co-continuous ceramic-metal composite ($\text{Al}_2\text{O}_3/\text{Al}$), otherwise known as C^4 , which was created by the immersion of fused quartz glass in pure aluminum at temperature ranges of 700-1300°C. This composite was reported with a phase distribution of 65% alumina and 35% aluminum. It was found that the reaction rate increased dramatically, by increasing the temperature of the reaction. At 1000°C, the composite can infiltrate 6 mm in approximately 6 hours, but at 1300°C it only takes approximately 50 minutes. Breslin *et al.* also reported that the composites created through the aforementioned process had an average modulus of rupture of 470 MPa.

The RMP process allows the metal from the sacrificial oxide to remain in the metal matrix as an alloy or intermetallic phase. For example, reacting SiO_2 with Al will leave silicon pools throughout the metal matrix [49]. Additionally, many efforts have been made to create an $\text{Al}_2\text{O}_3/\text{Al}$ -Ti composite system using TiO_2 [50-54]. This composite can be created by reacting titanium based ceramics such as Al_2TiO_2 [52], MgTiO_3 [55], TiSiO_4 [55], and TiMg_2O_4 [56]. When reacting these materials, it is possible to form TiAl_3 , TiAl , and spinel MgAl_2O_4 in the case of the magnesium based ceramics. Spinel is also a desired phase because of its cubic crystal structure. In a $\text{MgAl}_2\text{O}_4/\text{Al}$ composite, there will be a cubic/cubic grain boundary where there is less chance to form dislocations ($\text{Al}_2\text{O}_3/\text{Al}$ composites are based on rhombohedral/cubic systems) [57]. Other systems that have been investigated are $\text{SrFe}_{12}\text{O}_{19}$ [55], NiO [52], NiAl_2O_4 [52], $\text{Mg}_2\text{Al}_4\text{Si}_5\text{O}_{18}$ [58], $\text{Al}_6\text{Si}_2\text{O}_{13}$ [49], $\text{SrMgAl}_{10}\text{O}_{17}$ [56], and $\text{SrNiAl}_{10}\text{O}_{17}$ [56]. It has also been found that

reacting molten aluminum with nickel based oxides will leave areas of pure Ni and in some cases NiAl [52]. Additionally, it has been shown that the sacrificial oxides of $\text{SrFe}_{12}\text{O}_{19}$ and $\text{Mg}_2\text{Al}_4\text{Si}_5\text{O}_{18}$, produced $\text{SrAl}_{12}\text{O}_{19}$ and MgAl_2O_4 , respectively; in small amounts in the final composite [55, 58]. In contrast, the oxides investigated by Loiacono only produced the typical Al/ Al_2O_3 composite with no evidence of Ni, Sr, or Mg in the composite.

In 1996 all of the published work on the RMP process corresponded to infiltration of aluminum alloys on silica based ceramics. Therefore, Liu and Köster [59] published a work on the criteria needed to form an oxide/metal composites using different sacrificial oxides than the silica based ones claimed on the Breslin patent [48]. Liu and Köster proposed that two criteria must be met in order to achieve an IPC. The first criterion was that the oxide to be formed must be more thermodynamically stable at the reaction temperature. In other words, the Gibbs free energy of formation of the created oxide must be more negative than the sacrificial oxide. The second criterion is that the volume of the crystal lattice which is being formed must be smaller than that of the sacrificial oxide. This must take place in order to create a pathway for the molten metal to continue propagating through the sacrificial oxide. These two criteria can be summarized in Figure 2.16, where the Gibbs free energy is plotted against the specific volume of multiple oxide systems. An internal blue box was added to the plot to show the oxides that in theory would react with molten aluminum to form alumina at 1000°C. Although the criteria described by Liu and Köster [59] was accurate, there is another aspect that was not considered, which is the wetting effect between the ceramic and metal material [50]. For instance, based on Figure 2.16, it could be assumed that TiO_2 should react with molten

aluminum. However, it has been found that molten aluminum does not wet TiO_2 at 1000°C [50]. The act of wetting can then be classified in two broad categories: physical wetting and chemical wetting [60].

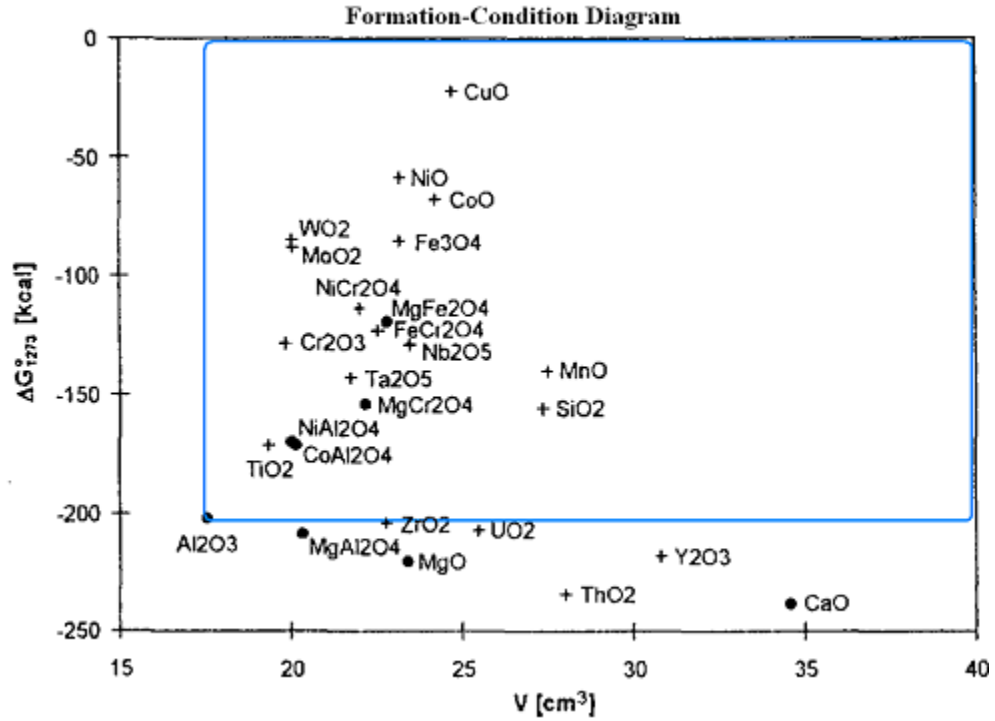


Figure 2.16. A plot of Gibbs free energy against the specific volume of several oxides.

All of the ceramics found inside the blue box represent materials that can be used as sacrificial oxides with molten aluminum to form an $\text{Al}_2\text{O}_3/\text{Al}$ composite [59].

Physical wetting is described as the physical force, such as van der Waals and dispersion forces that provide the attractive energy to disperse a liquid [60]. In contrast, chemical wetting is a process that involves a chemical reaction. A liquid is considered to have good wetting characteristics when its contact angle θ is less than 90° . Here, θ is the angle measured between the vectors of γ_{lv} and γ_{sl} , which can be seen in Figure 2.17. The γ_{sv} , γ_{lv}

and γ_{sl} vectors shown in Figure 2.17, represent the surface energy between the solid/vapor, liquid/vapor, and solid/liquid states respectively.

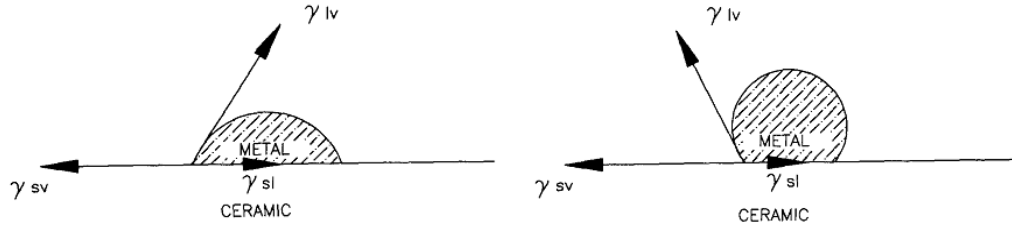


Figure 2.17. Schematic of good and bad wetting conditions between a drop of molten metal and a ceramic body. The left image shows good wetting with $\theta < 90^\circ$ and the right image shows poor wetting with $\theta > 90^\circ$ [60].

Sobczak *et al.* [50] found that at 1000°C molten aluminum has a wetting angle of 80° with TiO_2 . Indeed, this angle is less than the “good” limit of 90° , but is not close to wetting angle as that observed in SiO_2 , 53° , at 1000°C . Avraham and Kaplan [51] found that the spreading of aluminum on TiO_2 was governed by an activation energy barrier, and although TiO_2 may not react well with molten aluminum at 1000°C , it has been shown to fully react at temperatures of 1400°C and above [52].

It is widely known that molten aluminum has poor wetting conditions with ceramic materials. Typically, a non-wetting metal is infiltrated using external pressures [38, 61-62]. In non-wetting systems, a threshold pressure must be met to initiate a capillary infiltration. This pressure is described as P_0 which is a function of the wetting angle θ , the surface tension σ_s , and the hydraulic radius r_h , as described below:

$$P_0 = \frac{\sigma_s}{r_h} \cos \theta \quad (2.4)$$

The surface tension of pure aluminum is reported between 850-1100 mJ/m² [63]. Using these values, Mattern *et al.* [61] constructed a plot of the relationship between external pressure and infiltrated pore diameter of the aluminum/alumina system, which can be seen in Figure 2.18. The figure shows an inverse relationship between pore diameter and infiltration pressure, where a threshold pressure of MPa is needed to fill a pore on the size of a few μm . The relationship shows that larger pressures of about 100 MPa are needed to fill pores around 20 nm in size [61]. It is important to note that aluminum will fill the smaller pores following the ceramic matrix due to the reaction with the silica preform.

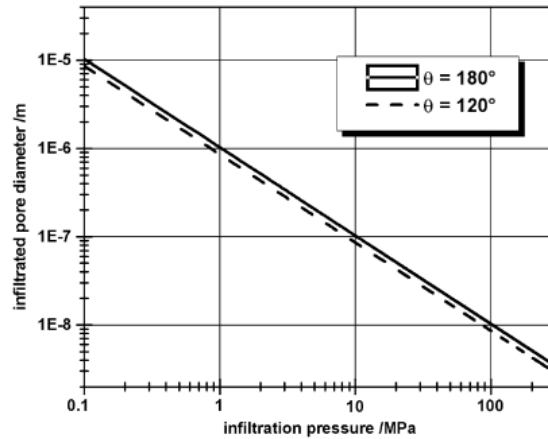


Figure 2.18. Relationship of infiltrated pore diameter and infiltration pressure for molten aluminum into ceramic pores [61].

2.4.3 Applications

Composites that have both metal and ceramic components have a wide variety of applications due to the unique properties of both constituents. The ability to change the materials and their phase distribution within the composite allows the tailoring of specific properties such as high specific strength and stiffness, high hardness and wear resistance, low coefficients of friction and thermal expansion, high thermal conductivity, and high

energy absorption and dampening [64]. Figure 2.19 shows the specific modulus and strength of different engineering materials, describing the wide range of mechanical values and consequently applications that they can cover. Based on the mechanical performance of the MMCs, they are currently used in automotive, aerospace, and military applications [65]. The lightweight and high strength capability of MMCs make them great candidates to replace higher density materials.

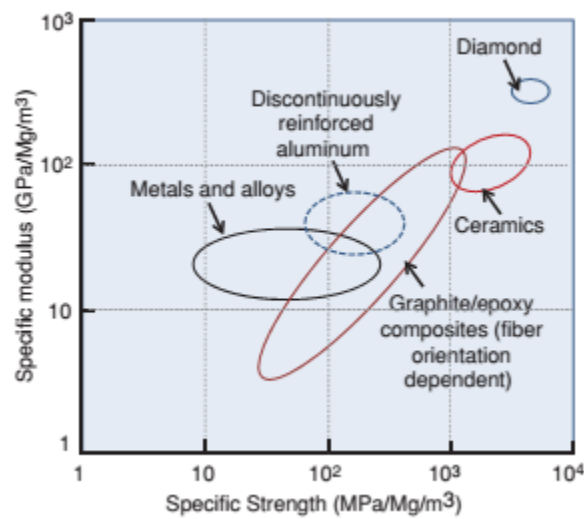


Figure 2.19. Trends in specific modulus and specific strength for engineering materials. The yield strength and compression strength are used for the metal and ceramic materials respectively [66].

2.4.3.1 Ballistics

Metal matrix composites and metal-ceramic IPCs are being investigated as ballistic materials on lighter, faster, and more fuel efficient vehicles. Ballistic materials must be able to absorb and dissipate energy and as well as able to stop a projectile. Currently, there are three main types of armor materials: metal [67], ceramic [68], and composite materials [69]. Typically, materials such as steel, high strength

aluminum alloys, Al_2O_3 , SiC, and TiB_2 are used for standalone metal or ceramic armors. Metallic armor has the benefits of easy machining, low cost, and survival of several ballistic impacts, but can become problematic when stopping larger caliber ammunition and can add considerable excessive weight. In contrast, ceramic armor is light-weight with a high strength substitute, but its high cost, difficult machinability, low toughness and limited capability to stop multiple shots due to its brittle nature makes ceramics not worthy of a standalone ballistic material [70]. On the other hand, composite materials have been used to help bridge the gap between the metal and ceramic materials. The composite materials can be MMCs, CMCs and polymer matrix composites (PMCs) or a layered system where different materials are bound together as a laminate system. Laminated systems can be backed with materials such as Kevlar® [71].

The current literature discusses MMCs manufactured with ceramic particles such as Al_2O_3 , SiC, TiB_2 , and B_4C for ballistic applications [70, 72-74]. The most commonly studied MMC has been the Al/SiC system [72-73, 75-78]. Vaziri *et al.* [77] found that with the addition of SiC to aluminum 6061-T6, the depth of penetration of the projectile decreased in comparison to the unreinforced matrix material. It was also found that the depth of penetration decreased with the addition of more SiC (15 to 30%) in the matrix material, even when increasing the impact speed. Karamis *et al.* [73] found that the type of projectile and the backing condition of the MMC greatly influences the damage formation. Karamis *et al.* [72] also studied an aluminum matrix composite with 20% alumina by volume. It was found that damaging or breaking the tip of the projectile decreased its penetration. The projectile tip was broken by the addition of hard ceramics that dug into the projectile tip, which caused deceleration of the bullet. The damaging of

projectile tips was also shown by Zhou *et al.* [70] who investigated an Al/B₄C MMC, where the post-fired retrieved projectile was found to have ceramic particles in it (see Figure 2.20). The projectile shows a spalling throughout the broken area due to the ceramic particles. The ceramic particles can also create furrows in the projectile showing a deceleration mechanism.

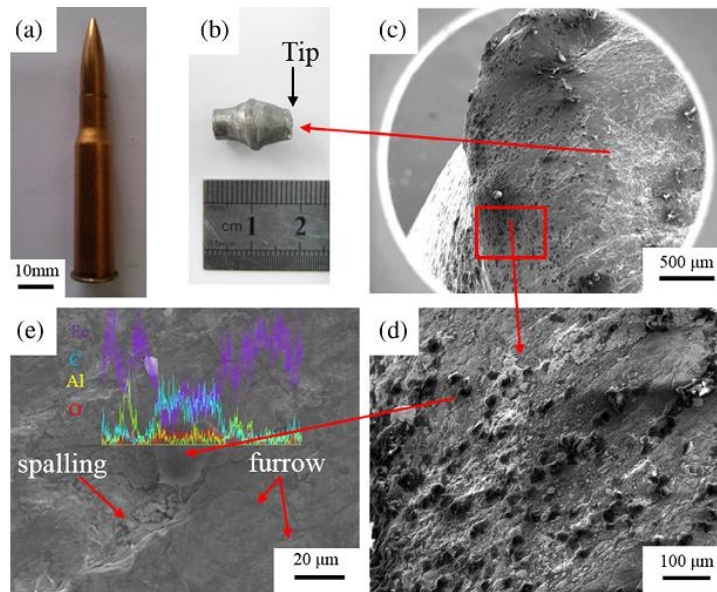


Figure 2.20. Images of (a) the armor piercing round, (b) the retrieved projectile after impact, (c) and (d) SEM image of the impacted projectile, and (e) the EDS analysis of the tested projectile including the ceramic particles [70].

IPCs have also been investigated as ballistic materials because of their enhanced mechanical strengths due to their interpenetrating network. Chang *et al.* [79-80] has investigated an Al/Al₂O₃ IPC that was created by infiltrating Al₂O₃ foam materials. The IPC was tested as a standalone ballistic material as well as part of a layered system. In the case of the layered system, the IPC was bonded to a dense Al₂O₃ plate (see Figure 2.21).

It was found that the IPC itself was not suitable to stop armor piercing rounds, but the layer system had showed promising results as a graded armor system.

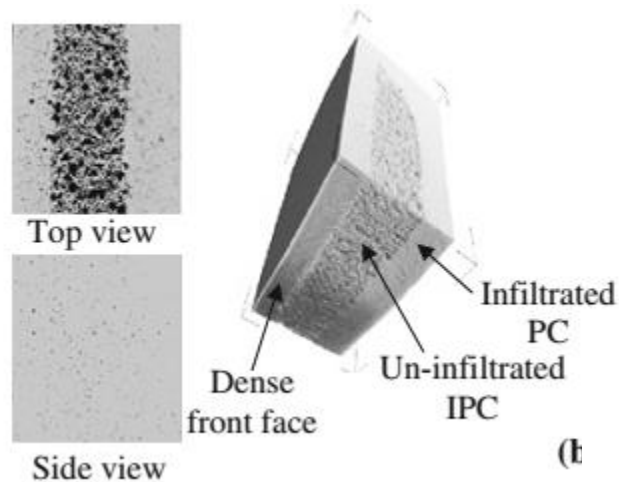


Figure 2.21. Layered ballistic system consisting of an IPC and a fully dense ceramic. The dense ceramic is used as the striking face [79].

2.4.3.2 Automotive and Aerospace

One of the most important properties of MMCs in the automotive industry is the high stiffness to weight ratio, which can result in fuel saving by reducing the overall vehicle weight (OVW). This weight reduction can come from replacing heavy steel components with MMCs, such as: powertrain, cylinder liner, piston, connecting rod, bearings, crank shaft, valvetrain, drivetrain, suspension, transmission housing, mount, impact zone, electronics, and batteries, all of which has been proposed by Macke *et al.* [66]. Indeed, reducing the OVW affords the potential to require less fuel consumption per distance traveled. This offers a cascade effect: reducing the fuel requirements provides the potential to reduce the size of the fuel tank, whose weight savings could in turn allow for a reduction in the size of the engine, which would further reduce the OVW [66].

Currently, companies such as Lotus, Ferrari, Plymouth, Corvette, Porsche, Toyota, Nissan, and Honda all have automobiles using MMC parts [26, 81].

The part that is getting the most attention for replacements by MMCs is the brake rotor. Aluminum based MMCs are highly attractive due to their low density, excellent heat dissipation, and great wear resistance [66]. Recent studies have shown that the amount of MMCs used in the automotive industry have increased steadily over the past 10 years, and are projected to increase through the year 2019 [26,82]. Significant research has went into the development of aluminum based MMCs as brake rotor materials, characterization and optimization of the MMCs, the testing apparatus, and analysis and comparison with cast iron brake systems have been widely studied [83-97]. The results show that MMCs have better wear resistance than cast iron, but finding the appropriate matching pad material can be challenging for creating an appropriate friction coefficient. IPC materials have also been tested as possible brake rotor materials. Al based IPCs with ceramic phases such as Al_2O_3 , SiC , TiB_2 , Si_3N_4 have been investigated, showing that the IPCs have similar or better wear resistance than cast iron [98-100].

The aerospace industry also has similar considerations for engineering materials on planes and space craft vehicles. The ability to manufacture lightweight and high strength materials will also continue to be a necessity in the automotive and aerospace industries due to increasing fuel prices [101]. The necessity of a higher strength material was first realized in 1954 when three Comet jet airplanes crashed due to premature fatigue failure of the pressurized fuselage. The failure was associated to stress concentrations at windows in hatches that were manufactured from 7075-type aluminum alloys [102]. Since then, numerous composite materials have been studied to replace

metal parts in airplanes and spaceships. Composites with an aluminum, titanium, or polymer matrix have been the most studied systems. It was found that aluminum based materials are not suitable for any skin material for a vehicle traveling faster than mach 2. At this point the aluminum matrix will fail due to the high temperatures created at that speed [101]. For higher temperature applications, more ceramic based composites are required. For instance, Yan *et al.* [103] developed a novel process for pressure-less infiltration of SiC to create a high volume SiC/Al composite (see Figure 2.22). The phase distribution of the final composite is typically between 55-57% SiC.

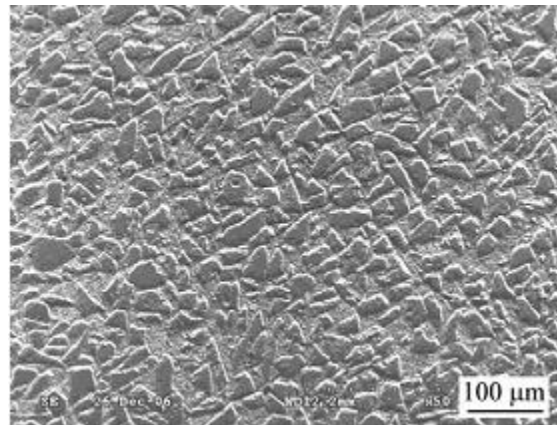


Figure 2.22. SEM image of the high volume SiC/Al composite developed by Yan *et al.* for potential aerospace applications [103].

The SiC/Al composite has a Young's modulus as high as 220 GPa and a specific modulus that is three times higher than Al, Ti, and steel alloys. Yan *et al.* also showed that the material can be welded together to create large frame objects. Other applications for higher content ceramic composites include propulsion and exhaust structures and thermal protection systems [104]. Pure ceramic composite such as alumina fiber reinforced aluminosilicate matrix composites are also being created for exhaust nozzles applications

in commercial aircrafts [105]. Other CMCs are being manufactured for thermal protection systems and high temperature structures [106-114].

2.4.4 Mechanical Property Characterization

Metal matrix composites have shown benefits as structural materials for the military, automotive, and aerospace industries. The mechanical properties of composite systems can change drastically depending on how it is manufactured, the materials used in the composite, and their phase distribution. For example, an Al/Al₂O₃ composite manufactured by reactive metal penetration has a flexural strength of 470 MPa [45]. A similar Al/Al₂O₃ composite manufactured via cold isostatic pressing of an Al₂O₃ body, and subsequently infiltrated using a hot press was found to have a flexural strength of 710 MPa [38]. The external pressure added into the system was able to create a fully dense composite leading to a stronger system. The phase distribution can also have an effect on the composites' mechanical strength. Gunther *et al.* [115] created two different Nb-16Al/Al₂O₃ composites that had phase distributions of 46/54 and 30/70. Both composites were manufactured by mixing Nb, Al, and Al₂O₃ powders in the appropriate amounts, powder compaction into a mold, and pressureless sintering. The addition of more metal to the composite led to a stronger composite system. Chen *et al.* [116] also showed a composite strengthening when creating Al-alloy/SiC composites. The tensile strength of the Al-10Mg/SiC was found to be higher than Al-5Mg-5Si/SiC, which was 226 and 178 MPa respectively. Both composites were manufactured the same way and with a phase distribution of 90/10.

Structural materials can be tested in a quasi-static or dynamic nature. Typically for quasi-static mechanical property testing, the Young's modulus is always tested. The fracture mechanics of the composite system will determine how the material is characterized. Ductile materials will be characterized using tension testing, reporting the yield strength and ultimate tensile strength. In contrast, brittle materials are subjected to flexural and compression testing, where the break strength is reported [11]. Table 2.6 was constructed to show the reported material properties of metal-ceramic composites showing their relationship to the manufacturing method, the material selection, and the phase distribution.

Table 2.6. Summary of research work on the mechanical properties of metal-ceramic composites.

Metal	Ceramic	Phase Distribution (M-C)	Manufacturing Method	Flexural Strength (MPa)	Compressive Tensile Strength (MPa)	Young's Modulus (GPa)	Reference
Si	SiC	51-49	Binder Jetting - Pressureless Infiltration	208	-	256	117
Si	SiC	79-21	Binder Jetting - Pressureless Infiltration	96	-	183	117
Cu-Alloy	Al ₂ O ₃	36-64	Binder Jetting - Pressureless Infiltration	236	-	204	118
Cu-Alloy	Al ₂ O ₃	29-71	Pressed Powder - Pressureless Infiltration	325	-	313	119
Cu-Alloy	Al ₂ O ₃	44-56	Binder Jetting - Pressureless Infiltration	245	-	204	120
TiSi ₂	Ti ₃ SiC ₂ -SiC-TiC	22-78	Binder Jetting - Pressureless Infiltration	293	-	-	121
TiAl ₃ -TiSi ₃	Ti ₃ SiC ₂ -SiC-TiC	25-75	Binder Jetting - Pressureless Infiltration	328	-	-	122
TiAl ₃ -	Ti ₃ AlC ₂ -	40-60	Binder Jetting -	320	-	184	123

Al	Al ₂ O ₃ - TiC		Pressureless Infiltration				
Al	Al ₂ O ₃	30-70	Extrusion Printing - Pressureless Infiltration	-	700-C	-	124
Al- 5Si- 5Mg	SiC	90-10	Pressed Powder - Pressureless Infiltration	-	178-T	-	116
Al- 10Mg	SiC	90-10	Pressed Powder - Pressureless Infiltration	-	226-T	-	116
Al- 10Si- 8Mg	SiC	35-65	Pressed Powder - Pressureless Infiltration	340	-	200	125
Al-Si- Mg	SiC	40-60	Pressed Powder - Pressureless Infiltration	298	-	206	126
Al	SiC	45-55	Pressed Powder - Pressureless Infiltration	405	-	220	103
Al	Al ₂ O ₃	11-89	Directed Metal Oxidation	250	1910-C	304	127
Al	Al ₂ O ₃	35-65	Reactive Metal Penetration	470	-	215	45
Fe-Cr- Ni	MgO	17-83	Mixed Powders - Hot Pressing	412	-	-	128
Ag	Al ₂ O ₃	10-90	Mixed Powders - Sintered	475	-	-	42
Ni	Al ₂ O ₃	35-65	Mixed Powders - Hot Pressing	613	-	292	129
MoSi ₂	Al ₂ O ₃	18-82	Mixed Powders - Reactive Hot Pressing	467	-	382	130
Fe	Al ₂ O ₃	22-78	Mixed Powders - Reactive Hot Pressing	520	-	332	131
Cr	Al ₂ O ₃	22-78	Mixed Powders - Reactive Hot Pressing	550	-	-	132
Ti- 10Al- 4V	Al ₂ O ₃	50-50	Compressed Powders - Sintered	527	-	-	115
Ti- 10Al- 4Nb	Al ₂ O ₃	50-50	Compressed Powders - Sintered	524	-	-	115
Nb- 16Al	Al ₂ O ₃	46-54	Compressed Powders - Sintered	1393	-	-	115
Nb- 16Al	Al ₂ O ₃	30-70	Compressed Powders - Sintered	1135	-	-	115

TiAl ₃	Ti ₃ AlC ₂ - Al ₂ O ₃	34-66	Pressed Powder - Pressureless Infiltration	288	-	-	133
Cu-Ni	TiB ₂	19-81	Pressed Powder - Pressureless Infiltration	844	-	-	134
Al	Al ₂ O ₃	37-63	Reactive Metal Penetration	280	773-C	202	135
Al-6Si	Al ₂ O ₃	35-65	Reactive Metal Penetration	320	-	300	136
NiAl (Si)	Al ₂ O ₃	38-62	Reactive Metal Penetration	194	-	207	137
Al 7075	MgAl ₂ O ₄ - Al ₂ O ₃	-	Reactive Metal Penetration	120	-	149	138
Al-Si	MgAl ₂ O ₄ - Al ₂ O ₃	-	Reactive Metal Penetration	186	-	157	139
Al	Al ₂ O ₃	-	Reactive Metal Penetration	281	-	202	139
Al	Al ₂ O ₃	25-75	Compressed Powders - Pressure Infiltration	710	-	-	38
AlSi ₉ Cu ₃	Al ₂ O ₃	48-52	Compressed Powders - Pressure Infiltration	-	830-C	155	140
Fe-Cr- Ni	Al ₂ O ₃	-	Mixed Powders - Reactive Hot Pressing	1100	-	-	141
Steel- Ti	Al ₂ O ₃	40-60	Pressed Powder - Pressureless Infiltration	450	-	278	142
Al	Al ₂ O ₃	-	Reactive Metal Penetration	293	-	-	143

On the other hand, the dynamic properties of materials are found to convey the materials response under impact situations. High strain rate testing can be performed by several methods including split Hopkinson pressure bar (SHPB), and high and low velocity impact testing. The SHPB is a testing set-up that produces a stress-strain relationship for a material that is being strained around 10^3 s^{-1} [144]. The impact testing typically analyzes the energy absorption of the material before rupture. The low velocity testing can be achieved by the use of the drop test method. In this method a steel impactor

with known weight is dropped onto the material of interest from a known distance [145]. The potential energy given from the known mass and height is recorded as the absorbed energy. The high velocity impact testing can be achieved by using a pressurized gas gun that fires steel rods or spheres as projectiles [146]. Any testing of ballistic grade materials involves impact testing which is carried out with bullets or armor piercing ammunition [76]. Materials that are not being tested with ballistic grade ammunition, are typically manufactured as part of a fiber laminate system [146]. The gas gun and drop test methods are typically performed with an all fiber laminate system [147-149], but recently foam materials have also been studied as core materials to the laminate system [150-153]. These materials are considered for leading edge components on aircrafts that are subjected to high velocity impacts from hail or birds [154].

High strength ballistic materials are frequently mechanically tested using the split Hopkinson pressure bar (SHPB) alongside of ballistic impact testing. Aluminum based MMCs have been extensively tested over the past years by SHPB. Chichili *et al.* [155] found that Al_2O_3 particle reinforced 6061-T6 Al had a brittle failure during dynamic testing, although the microstructure did show a ductile failure in the aluminum phase. The authors hypothesized that the failure process involved the cracking of the reinforcement particles, partial debonding of the particles, resulting in voids in the matrix material, and the growth of voids in the matrix resulting in the failure of the composite. Marchi *et al.* [156] found that the flow stress of Al_2O_3 particle reinforced pure Al is greater than the plain matrix material. They also showed that the increase of composite flow stress with strain rate was due to the thermally activated dislocations in the matrix. Marchi *et al.* also noticed that the largest particles would show the highest amount of

damage until it reached a plateau value. At this plateau value, the particle-particle interactions will dominate the fracture of the reinforcement. Owolabi *et al.* [157] investigated the adiabatic shear bands of Al 6061-T6 and its Al₂O₃ particle reinforced analogous. It was found that the particles would agglomerate in the shear bands preventing the grain elongation that is shown in the monolithic alloy. Similar results have been found in several other aluminum based MMCs with reinforcements including SiC, B₄C, and TiB₂ [158-162].

2.5 Additive Manufacturing

This section will include a summary of the seven types of additive manufacturing (AM) processes designated by the ASTM standards. The section will also include the history of the creation of additive manufacturing. This will include a description of the technological advances needed in the AM field, as well as the materials used in AM along with their advantages and disadvantages.

The term additive manufacturing simply means creating a product by the addition of material in a layer-by-layer fashion. This technology has many synonyms, but it is mostly connected with the terms of rapid prototyping (RP) and three dimensional (3D) printing. The term RP was used because this technology was mostly used to make prototype models. With further advancements, this technology was able to produce end line products needing little or no post processing steps [163]. This led to the formation of a committee within the ASTM International to agree on a new terminology for this technology. They agreed on the term of additive manufacturing. Even more recently, the committee also decided to break the AM technology into the following seven unique processes: binder jetting, directed energy deposition, material extrusion, material jetting,

powder bed fusion, sheet lamination, and vat photopolymerization [164]. Each process differs based on the way the material is bound together. They are all similar in the fact that each process adds material in layers based on a thin cross section of a computer aided design (CAD) object. Certainly, AM would not be possible without the existence of the CAD software.

2.5.1 Computer Assisted Design (CAD)

CAD software helps engineers to build anything from sky scrapers to nano-sized processors for electronics. Some CAD software allows the input of material properties to understand their effects on the structural, electrical, thermal, dynamic and static properties of the design. Computer aided manufacturing (CAM) systems were initially used in robotic manufacturing techniques, such as computer numerical controlled (CNC) subtractive manufacturing. Here, the CAM system produce the code for the CNC machinery by adding the coordinate data and trigger the cutting tools. Similar, AM processes use the CAM technology to accurately print a design. The main difference between the two technologies is that AM needs the surface of the object in the CAD model to be fully enclosed, while CAM does not. This is achieved by the CAD software, through the use of non-uniform rational basis-splines (NURBS) to precisely define the areas and curvatures that are on the surface. Additionally, the CAD object must also be sliced to generate data for each layer [165]. This was achieved by 3D Systems (USA) through the creation of a generic algorithm that every CAD software can use to slice 3D objects. In fact, 3D Systems was the first company to commercialize an AM system based on their stereolithography technology. This led them to create their slicing algorithm with a file extension of “STL”. The STL is also named after the process of

standard tessellation language. A tessellation of an object for AM will represent the 3D structure in terms of triangles with no overlaps or gaps (see Figure 2.23). Each triangle has three vertices with the normal vector pointing inside the object [17]. The STL file extension can be used in all types of AM machines.

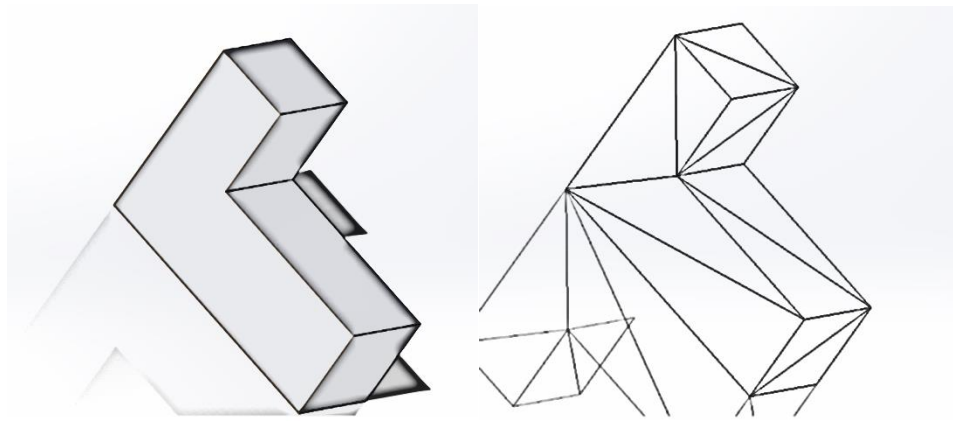


Figure 2.23. A CAD drawing (left) and its tessellated STL file (right).

The first “3D printer” was developed by Charles W. Hull in 1986. He patented his stereolithography apparatus and then commercialized it by founding 3D Systems. This system used focused ultraviolet light to cure a photopolymer. The light beam focused onto a vat of liquid photopolymer, to which the light hardens the polymer. Since the invention of the stereolithography, many unique variations to the concept of additive manufacturing have been implemented. Previously, printing technologies were grouped together by the binding mechanism or by the type of material being printed. However, these broad descriptions overlapped, and a new description was needed. Pham and Gault [166], described printing technologies by whether the material was deposited in one dimension or in two dimensions, along with the physical state of the material printed.

This was later extended by Gibson *et al.* [167] (Figure 2.24). Thus, the most recent description of the different AM technologies is presented in the following figure.

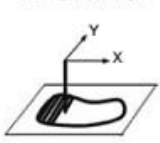
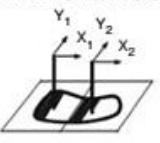
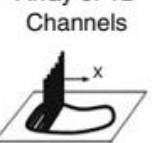
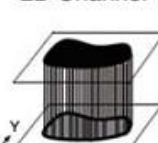
	1D Channel	2x1D Channels	Array of 1D Channels	2D Channel
Liquid Polymer				
Discrete Particles	SLA (3D Sys)	Dual beam SLA (3D Sys)	Objet	Envisiontech MicroTEC
Molten Mat.	SLS (3D Sys), LST (EOS), LENS Phenix, SDM	LST (EOS)	3D Printing	DPS
Solid Sheets	FDM, Solidscape		ThermoJet	
	Solido PLT (KIRA)			

Figure 2.24. Classifications of AM techniques [167].

2.5.2 Vat Polymerization

The process of vat polymerization is based on curing a liquid photopolymer, using an ultra-violet (UV) source which chemically reacts with the liquid photopolymer to become solid. Photopolymers were originally developed in the 1960s, and initially used in the coating and printing industries. They have photo-initiators, reactive diluents, flexibilizers, stabilizers, and the liquid monomer as the basic ingredients.

Vat polymerization was the first 3D printing technology in the market, and it is typically known by its most common technique, stereolithography (SLA). The SLA technique uses a build plate which moves down in the vat as the polymer is solidified. After solidification of a layer, the build plate descends, allowing more liquid photopolymer to fill on top of the solid. There are three common ways to focus the curing

light for the SLA process, which are vector scan, mask projection, and a two-photon approach. The vector scan is a point scan approach which is the most typically commercially available. Mask production is a layer scan approach which cures a whole layer by a UV lamp at one time. The light is selectively blocked by a mask in order to project the shape of the part. The two-photon approach has two point scans which will enhance the resolution of the final part [168]. The schematics of all three techniques can be seen in Figure 2.25. The advantages and disadvantages for the SL technique are summarized in Table 2.7 [169]:

Table 2.7. Summary of the advantages and disadvantages of the vat polymerization additive manufacturing technique [169].

Vat Polymerization	
Advantages	Disadvantages
Fast build times	Support structures needed
Smooth surfaces	Parts can easily warp
Good tolerances	Photopolymer resins are hazardous

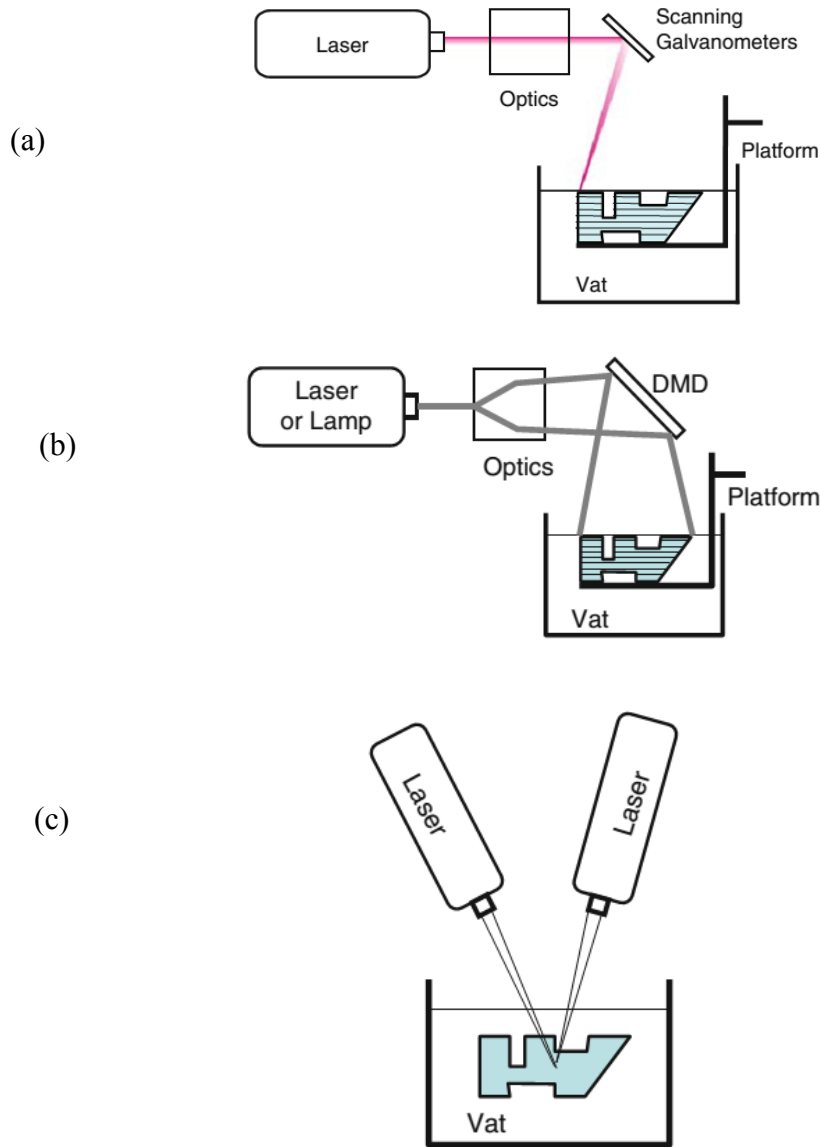


Figure 2.25. Schematics of the curing techniques used in the SL technology. Vector scan (a), mask projection (b) and a two-photon (c) [167].

2.5.3 Sheet Lamination

Sheet lamination manufacturing involves layering sheets of any material on top of each other. The sheets are glued together by a variety of methods. The first sheet lamination technique that was commercialized was called Laminated Object

Manufacturing (LOM) by Helysis [170]. In this process the layers are bonded together by a thermal adhesive coating. A spool of thin sheet material, typically 0.080-0.250 mm thick, is spread onto the build area (see Figure 2.26). Subsequently, a heated roller sets the adhesive to glue the part together, and CO₂ laser cuts the object out on that specific layer. The sheet material is cut off, the stage lowers, and the process repeats. The material that is not being used in the part is cut with a cross hatching pattern in order to be easily removed [171].

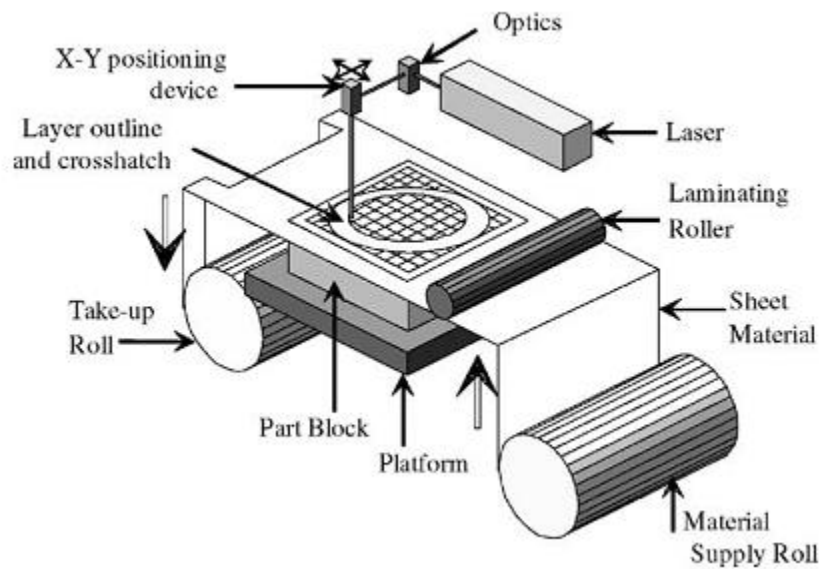


Figure 2.26. Schematic of the laminated object manufacturing technique. The material is rolled into the build area where the laminating roller sets the adhesive. The laser cuts the part out of the sheet material. The platform lowers and the process continues [171].

Typically, the adhesive is used for paper and wood based products. Metal sheets are usually held together by mechanical fasteners or brazing [172]. It is worth mentioning that the weak adhesion from glue and brazing will result in anisotropic properties on the final parts. This aspect will need to be considered when choosing the orientation of the

part being created [171]. The biggest advantage of the LOM process is its fast build times [173]. A list of the all the advantages and disadvantages are listed in Table 2.8 [169, 174].

Table 2.8. Summary of the advantages and disadvantages of the sheet lamination additive manufacturing technique [169, 174].

Sheet Lamination	
Advantages	Disadvantages
Fast build times	Waste of material
No supporting structures needed	Low surface definition
Can manufacture large parts	Anisotropic properties
Low cost	Complex internal cavities can be hard to build
No deformation or phase change	Complex parts can be hard to remove

2.5.4 Powder Bed Fusion

Powder bed fusion is described as any process that uses thermal energy to selectively fuse regions of a powder bed [164]. This process was originally developed at the University of Texas at Austin for plastic prototypes, which was called selective laser sintering (SLS). The process now has been modified to be used on metals and ceramics [175]. The different processes of powder bed fusion are all very similar, only a few variables differ. During this process a layer of powder is spread evenly over a build plate. An energy source, typically a laser or electron beam, is selectively moved across the powder bed in the shape of the part described in the CAD file (see Figure 2.27). The particles are locally melted, or sintered, to create solid part. The energy source must be powerful enough to penetrate and melt all the particles in the layer thickness to ensure bonding between the layers. The variables of laser power, spot size, speed, layer thickness, and scan spacing

all have an effect on the density of the part and mechanical properties [176]. The powder can be melted in four different mechanisms: solid state sintering, chemically-induced sintering, liquid-phase sintering, and full melting. Solid state sintering and full melting are the same mechanism, only differing in the amount of energy that is incorporated into the powder system. During both of these mechanism, only the source of energy is used to locally melt the solid powder. In the case of the solid state sintering mechanism, the energy required is between $T_{melt}/2$ and T_{melt} , where T_{melt} is the melting temperature of the powder [177]. Solid state sintering will achieve a neck formation between two particles leaving large amounts of porosity in the final composite. The benefits of solid state sintering are its fast build times and the ability to use multiple materials in one machine [167]. In contrast, full melting uses energy that is equal to or larger than T_{melt} . Full melting processes were designed to achieve full density parts.

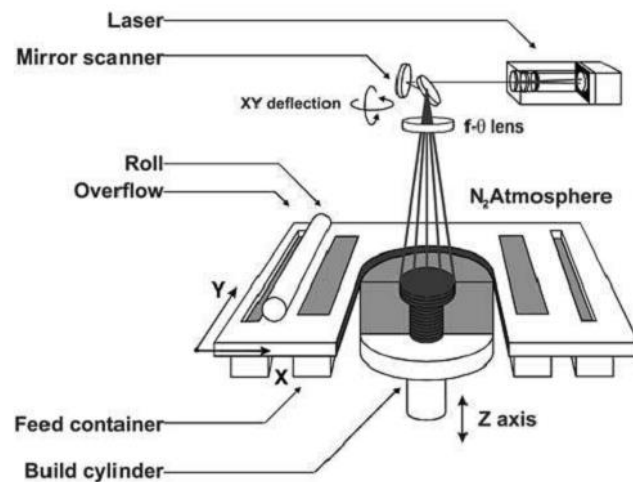


Figure 2.27. Schematic of a typical powder bed fusion process. A laser is focused and deflected off of mirrors to locally melt particles in the powder bed. After a layer is finished, the build plate lowers, more powder is spread on top, and the process continues

[177].

The other two powder bed fusion methods have different mechanisms than melting the powder. The chemically induced binding mechanism takes advantage of a chemical reaction between the powder and a gas that is introduced to the system. For example, aluminum powder will react with a nitrogen atmosphere to form aluminum nitride (AlN) when heated with a laser [178]. Silicon carbide is also used in this mechanism, where the SiC breaks down to form Si and C. The created Si reacts with oxygen in the atmosphere to form SiO₂. The SiO₂ acts as a binder for the SiC particles [177]. Similar to this process, is the liquid-phase sintering mechanism that uses other chemicals, such as plastics, as the binding agent to create parts. The binder materials can be mixed in with the powder or can be used to coat the powder before melting. The processes of chemically induced sintering and liquid-phase sintering are typically followed by a post-process for densification purposes, such as hot isostatic pressing or metal infiltration [177]. The advantages and disadvantages of the powder bed fusion can be seen in Table 2.9 [169, 174]:

Table 2.9. Summary of the advantages and disadvantages of the powder bed fusion additive manufacturing technique [169, 174].

Powder Bed Fusion	
Advantages	Disadvantages
Parts can be built with no supports	Surface finish is poor
Large variety of materials can be used	Machines take a while to warm up
Good tolerances	Parts can warp
Can recycle unused powder	Atmospheric control is crucial

2.5.5 Material Extrusion

The process of material extrusion is the most commonly used, and the cheapest to purchase of all types of additive manufacturing. Plastic extrusion printers is a fused deposition modeling (FDM) technique that uses a thread of plastic as the feed material. The plastic thread is pushed through a nozzle where there is a heater melting the plastic at the tip of the nozzle. The nozzle lays down material on the build plate in the X and Y directions. When the layer is complete the build plate lowers and more material is laid on top of the previous layer (see Figure 2.28) [167]. The material comes out of the nozzle in a molten state, and is hardened upon cooling. The plastic must be able to slightly re-melt the layer below it, to create a new bond.

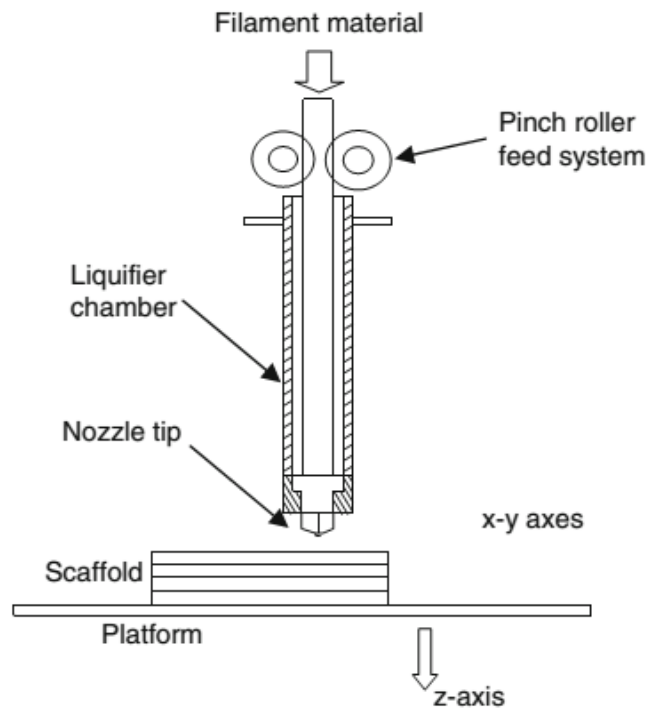


Figure 2.28. A schematic of the fused deposition modeling process. Polymer thread is forced through a nozzle, where it is melted and deposited onto the build platform [167].

The FDM technique is typically used for modelling and prototyping, not for structural materials, therefore the outside of the shape being printed is typically all that is needed. The inside of the shape is filled with only a few passes of material for support. The amount of internal filling can be changed in most FDM printers [167]. One of the drawbacks of FDM, is that parts cannot support steep angles and floating appendages without support. Typically, the support material is made of a weaker polymer that is deposited through a different nozzle than that printing the main part. After completion of the part, the support material is broke off or dissolved away using an etchant [169].

The material extrusion process is mostly performed with polymers such as polycarbonate (PC), acrylonitrile butadiene styrene (ABS), and polyphenylsulfone (PPSF), but other research groups have been working on extrusion processes for ceramic materials [179]. B. Khoshnevis, from the University of Southern California, invented Contour Crafting, a system that extrudes cement based ceramics to build large structures [180]. The additives on the mixture make the printed cement set in minutes with a capability of supporting hundreds of pounds [181]. Other ceramic extrusion research is being performed by research groups at the University of Rutgers, which included the printing of lead zirconate titanate (PZT) [182] and bio-ceramics materials [183]. The advantages and disadvantages of the FDM process are mentioned in Table 2.10 [169, 174].

Table 2.10. Summary of the advantages and disadvantages of the material extrusion additive manufacturing technique [169, 174].

Material Extrusion	
Advantages	Disadvantages
No post-processing of the part is needed	Support structures are needed
No resins for curing needed	Poor surface finish
Machines are cheap to purchase	Process is slow on large mass parts
Stock material is cheap	Printed parts are anisotropic in strength
Variety of materials can be used	

2.5.6 Directed Energy Deposition

Directed energy deposition is described as any process that uses thermal energy to fuse materials together by melting them as they are simultaneously being deposited [164]. Directed energy deposition processes are found in the market as Laser Engineered Net Shaping (LENS), Directed Light Fabrication (DLF), Directed Metal Deposition (DMD), 3D Laser Cladding, Laser Generation, Laser Based Metal Deposition (LBMD), Laser Freeform Fabrication (LFF), and Laser Direct Casting. All of these processes are very similar, with some differences such as laser power, laser spot size, laser type, powder delivery method, inert gas delivery method, or feedback control systems [167]. In general, a thermal source (laser) and a material feed nozzle are focused on a singular point on the build plate (see Figure 2.29). The thermal source instantly melts the feed material onto the build plate. The material can be delivered to the build plate as a powder

(most commonly used) or as a filament wire. The directed energy processes can lead to full density parts similar to those achieved through the SLS technology [167].

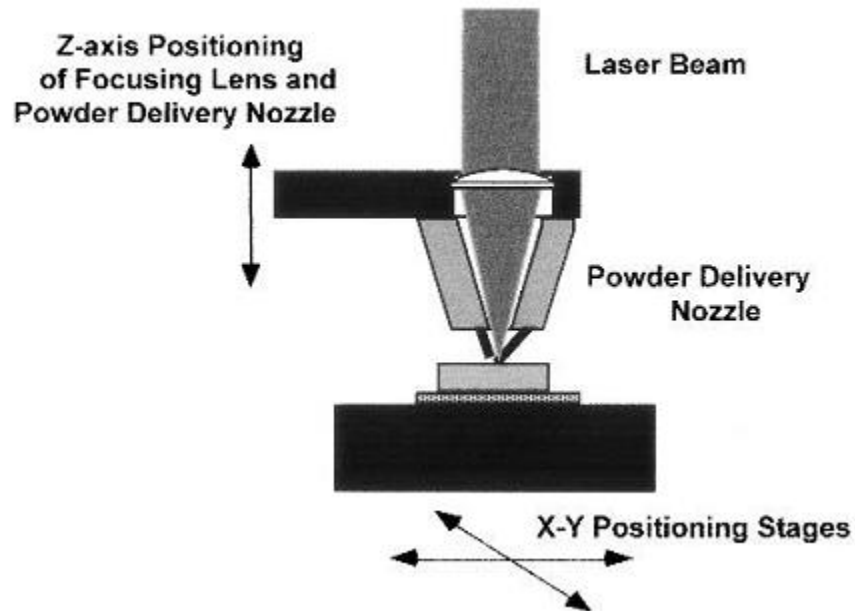


Figure 2.29. Schematic representation of the directed energy deposition technique. The laser and powder feed are focused on a moving point as the material is delivered, melted, and solidified to create an individual layer [184].

Typically, directed energy deposition techniques are used to create metallic parts, but they are also useful in creating MMCs and functionally graded materials (FGMs) which have both metal and ceramic components. Multiple feed nozzles can be used in order to bond different materials in different phase compositions throughout the printed part. Liu and DuPont [185] created a Ti/TiC FGM by using two different feed nozzles for both materials. They were able to manufacture a composite that is pure Ti on one side and 95:5 % TiC:Ti on the other. The composite had hardness value of 200 on the Vickers hardness scale on the Ti side and 2300 on the TiC side. Directed energy deposition can

also be used to deposit ceramic coatings on metal substrates. For instance, Balla *et al.* [186] was able to deposit a yttria-stabilized zirconia (YSZ) coating on a stainless steel structure.

The directed energy deposition technique offers a lot of promise as a manufacturing technique to create MMCs and FGMs. A full list of its advantages and disadvantages can be seen in Table 2.11 [167, 174].

Table 2.11. Summary of the advantages and disadvantages of the directed energy deposition additive manufacturing technique [169, 174].

Directed Energy Deposition	
Advantages	Disadvantages
Can be used to repair parts	Poor surface finish
Can create multiphase materials	Slow build times
Can produce single crystal materials	Supports needed to produce complex parts

2.5.7 Binder Jetting

2.5.7.1 Introduction

The AM technique of binder jetting was used in this research project and it is therefore discussed in much more detail than the other AM techniques. Binder jetting is described as the process of using a liquid bonding agent to selectively deposit and join powder materials [164]. The process was originally developed by E. Sachs at the Massachusetts Institute of Technology (MIT) in the early 1990's [187]. The process works by evenly spreading the feed powder across a build plate. Current binder jetting machines spread the powder with a counter rotating roller or with a traversing doctor blade. After the spreading step, the print head selectively lays binder down to locally

“glue” the powders together to create the image of a sliced CAD file. When the binder is deposited, the build plate lowers in the Z direction (the height of specified layer thickness), and fresh powder from the feed stock is spread onto the build plate (see Figure 2.30). The printing process repeats again until the entire CAD file is printed on the powder bed.

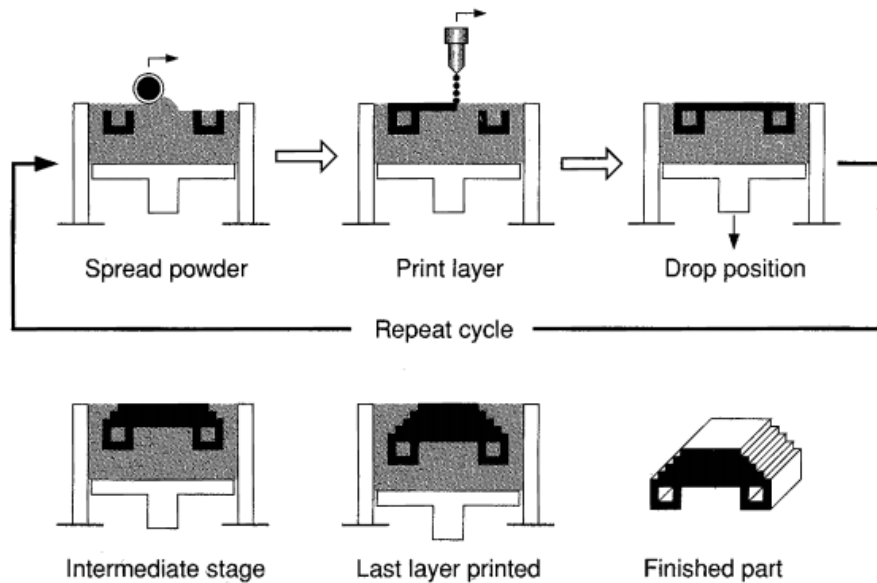


Figure 2.30. Schematic of the binder jetting process. The powder is spread, binder is deposited, the build plate lowers and the process is repeated [188].

After the printing process is complete, the part remains in the excess powder for support purposes while the binder is cured. The curing stage of the binder allows the printed parts to be handled without breaking. To achieve its final dense state, the part is sintered, achieving bonding between the individual particles. The binder jetting process was originally created to print ceramic materials. Yoo *et al.* [189] found that printing alumina powder, with a particle size distribution of 75-150 μm with an acrylic copolymer resin as the binder, will lead to a sintered density of 62.5 %. Improved densities were achieved

by using an isostatically pressing process. Here, the printed parts were pressed before sintered, resulting in better sintered densities. Cold isostatic pressing (CIP) and warm isostatic pressing (WIP) yielded densities of 95.9 % and 97.8 % of the theoretical density, respectively. Yoo *et al.* [189] acknowledges that binder jet printing will not achieve fully dense parts (solid state diffusion to occur during sintering), without using post processing techniques, unless the un-sintered or “green density” is approximately 60% dense. This is a challenge because a proper particle size distribution must be achieved for a high packing density [190], and presence of binder accounts for significant volume fraction of the printed sample [191]. Besides isostatic pressing, the infiltration of another material into the printed part can make it completely dense. Currently, Ex One™ offers a 316 and 420 stainless steel powder which is subsequently infiltrated with a bronze alloy. The resulting composite is an IPC of both materials. The microstructure of this IPC can be seen in Figure 2.31.

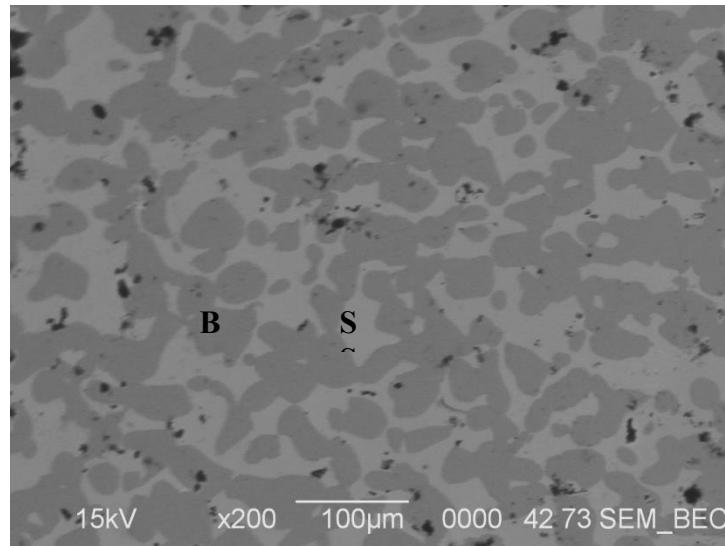


Figure 2.31. Scanning electron micrograph of a binder jetted stainless steel part, which was infiltrated with bronze. The bronze (Br) is the lighter color phase, the stainless steel (SS) is the darker color phase, and the black spots are the porosity.

Other research groups have also investigated the binder jetting process with subsequent infiltration of multiple materials as a means of creating composite materials. For instance, the stainless steel/bronze combination that is sold by Ex One™ was studied and modelled by Wegner and Gibson [28, 192-194]. The infiltration of bronze through stainless steel was found to happen naturally and can take place against gravity. The composites manufactured by Wegner and Gibson were made of two different volume fractions of stainless steel and bronze (60:40 and 80:20). For comparison, the stainless steel backbones were also infiltrated with a low strength resin. The fracture of the stainless steel/resin composite showed crack bridging between the two phases even though the resin offers little structural strength to the composite. The overall strength of the composites were maximized when the more ductile phase (infiltrate) was minimized. This technique seems to be an appropriate way to create near net-shaped composites with intricate designs. The general advantages and disadvantages of binder jetting can be seen Table 2.12 [167, 169].

Table 2.12. Summary of the advantages and disadvantages of the binder jetting additive manufacturing technique [167, 169].

Binder Jet Printing	
Advantages	Disadvantages
Shorter build times	Printed parts are fragile
Inexpensive and reusable raw materials	Poor surface finish
No support structures are needed	Low dimensional accuracy
	Post processing is needed

2.5.7.2 Process Parameters

Although binder jetting process is an easy technology to use, its process parameters of particle size, particle shape, spread speed, layer thickness, binder material, and binder saturation need to be optimized based on the material being printed. It is widely known that a small particle size increases the mechanical strength of commonly manufactured metals and ceramics [195-196]. However, due to the large Van der Waals forces in the small particles (<5 μm), it has been observed, that they do not tend to spread well. In fact, small particles tend to stick together, leaving uneven spreading and large porosity gaps in the final part. Smaller particles can also be affected by the force of the binder being injected onto the powder, and erosion, during the binder deposition [196]. Thus, the particle size of a printed material is a critical parameter in the 3D process, since it can influence the sinterability, surface roughness, pore size, and the surface area of the manufactured component. In contrast, larger particle sizes will spread easier than smaller, but will lead to an increased porosity and a weak mechanical strength of the final product [195]. A mixture of large and small particles has been shown to increase the density of the green precursors significantly. The mixture allows the large particles to be spread easily and the smaller particles to fill the voids left by the large particles. When using large and small particles, it was found that there was a maximum volume percent of small particles that can be used in the mixture before the green density decreases [197]. It has also been reported that a finer powder results in an increased sinterability, smaller features, and thinner layers of the printed component [196]. It has been also found that

the preferred particle size should be larger than 20 μm , with a particle size distribution of 15-40 μm (i.e. 15-30 or 10-50 μm) [198].

One way to avoid the poor spreading of small particles during the 3D printing process is to spread the material wet. The powder is mixed with dispersants which helps the material spread evenly. The dispersants are removed by heating the sample through either infrared light, warm air, or microwaves [198]. Another technique involves spray drying small particles which creates larger spherical particles, where the smaller particles are held together with a binding agent.

The particle shape also affects the spreading of the material. Faceted and anisotropic particles will stick to each other, creating more friction compared to spherical particles. Although spherical particles have better flow characteristics, such geometrical requirement is not needed for 3D printing [199]. The flow characteristics directly affects the density of the final part. If a powder does not spread well, it does not pack well, resulting in a lower density. This can be avoided by mechanically compressing the powder with a roller. After the powder is spread, the stage can be raised and the roller can go over the powder a second time with the roller spinning in the opposite direction [199]. The powder can also be mechanically pressed by a secondary stage that fits into the build box, and presses the powder down. Subsequently the stage will rise to the top to account for the compressed powder [200].

Regarding the layer thickness, the particle size of the printed material must be smaller than the printed layer thickness. Unlike particle size, it has been found that the lowest layer thickness is not optimal. At a certain thickness, specific to the particle size, lower layer sizes result in low surface quality, and uniformity of the final product [201-202]. Lu

and Reynolds suggest that the layer thickness should be two times greater than the particle size [201].

Also, the variable of powder spreading speed is an important parameter for each individual material. The spreading speed is mostly dependent on the flowability of the powder. In general, the better flow characteristics, the faster the spreading speeds.

Binder selection is another important parameter in 3D printing. Commonly used binders include organic binders such as butyral resins, polymeric resins, furfuryl resins, and various polyvinyls [203-204]. Also, the binder can be premixed with the powder bed, and a solvent is printed to locally dissolve the binder in the powder bed. Maltodextrin and sucrose are the typical binders used in the powder bed. When the solvent penetrates the bed, the binder spreads in a localized area and the volatile liquid evaporates. Other less commonly used techniques for binding involve hydration based systems, preceramic polymers, acid-base systems, inorganic binders, and metal salts [203]. A large number of variables effect the way that the binder reacts with the powder such as: surface tension, viscosity, molecular weight, conductivity, and material compatibility. It is important to select a proper binder since it ultimately determines the printing resolution, surface finish and dimensional control. The decomposition of the binder must also be considered. Typically, high molecular weight polymers will leave more residual mass in the final sintered part [204]. In order to correctly identify a binder system that works, bench top tests are recommended to be performed. This enables the user to have an idea of the powder-binder interaction before cleaning and loading the printer with experimental binders. One bench top experiment can be completed by dispensing droplets of a binder on a small sample of packed powder using a syringe. Quick absorption of the binder and

the formation of “pebbles” (bound material) are considered positive results [205]. Another bench top experiment involves the mixing of specific powder with different binder ratios to find the proper amount of binder needed to achieve the proper green strength. The mixtures are cast and then dried for examination. The parts should hold edge definition and should break cleanly without crumbling [206].

Saturation of the binder is also an important printing parameter that can be adjusted by the following equation:

$$S = \frac{V_{binder}}{V_{air}} \times 100 \quad (2.5)$$

Where S is the saturation, V_{binder} is the volume of the binder deposited, and V_{air} is the volume of porosity in the powder. V_{air} can be found by determining the powder’s tap density, where the tap density is the bulk density of the loose powder after “tapping” the container. Here, if the volume of the binder equals the volume of the open space in the powder, the binder saturation is 100 % [207]. Binder saturation has a direct correlation to the strength of the cured state of the printed part, since more binder is being deposited. However, this does not have a correlation to the strength of the sintered part, in fact it could have a negative effect, since more residual binder could be left in the system. Also by increasing the binder saturation level, the dimensional accuracy can be affected [201].

When testing a new material in binder jetting, there are no exact parameters that will work for all materials, but there are some general trends for optimization of the printing parameters. A summary of these trends are:

- Spherical particles have better spreading characteristics.

- Particle sizes in the range of 10-100 μm have better printing qualities.
- Use of a layer thickness greater than two times the particle size.
- Choice of a binder system with relatively good wetting conditions for the investigated powder.
- Use of the smallest amount of binder saturation that allows handling of the sample in its cured state.

2.5.7.3 Infiltration of Printed Ceramic Structures

As previously mentioned, the infiltration of binder jet printed materials seems to be an appropriate way to achieve densification. Here, the infiltrate material must have a lower melting point than the printed material to ensure that the part keeps its shape. This is one reason why a ceramic-metal composite system can benefit from this manufacturing process. It is beneficial to find an infiltrate that has good wetting conditions, high mobility, and a low viscosity to freely fill the porosity of the printed material since pressure infiltrating chambers can be difficult to build [192].

A system that has been studied through the infiltration process is the $\text{Al}_2\text{O}_3/\text{Cu}$ IPC [118, 120]. Here, the wetting angle of copper on alumina was decreased with the addition of Cu_2O to the infiltrating alloy, giving the alloy an oxygen content of 3.2 wt%. Melcher *et al.* [120] was able to create sintered parts with porosity as low as 33%. It was also found that these composites behaved isotopically after infiltration despite the layering process. Another infiltrated system that has been studied, are structures based on a ceramic-glass composition by printing alumina and infiltrating it with lanthanum-

aluminosilicate glass [208]. This process has been possible because the glass material has a melting temperature (1100°C) lower than that of alumina (2072°C). Other composite systems have also been created through the reaction that takes place during the infiltration process. In fact, it is common to use carbon or add it as a carbon based binder (which turns to carbon during the firing process) to the powder bed to react with the infiltrate in order to produce MMCs. Fu *et al.* [117] was able to create a Si/SiC by using a mixture of Si and SiC as the printed body. Subsequently, the green part was infiltrated with a silicone resin (polymethylphenylhydrogensilsesquioxane) and cured. Some carbon from the silicone resin was left in the printed part during the sintering process, which reacted with the infiltrated silicon to form the final composite with porosities of 5% and lower. Moon *et al.* [207] was able to create a similar Si/SiC composite by printing carbon powder and infiltrating it with silicon.

Titanium based composite systems have also been investigated. Rambo *et al.* [209] printed a cellulose-starch material and infiltrated it with a TiCu (50:50) molten alloy. The final composite had phases of TiC and Ti-Cu alloys. Although some parts of the composites were reacted and showed a two phase composite, there was a large amount (roughly 25%) of unreacted material. Yin *et al.* [123, 210] printed a mixture of TiC, TiO₂, and dextrin, which was subsequently infiltrated with aluminum. The final composite result in the creation of a ternary carbide Ti₃AlC₂ (see Figure 2.32a). Ternary carbides have a periodic planar stacking of TiC₆ octahedra and close packed Al crystals. This structure is thought to be a good grain boundary for the ceramic-metal interface due to its elevated toughness and formability [210]. Nan *et al.* [121] tried to create ternary carbides by printing a mixture of TiC and dextrin. This mixture was then infiltrated with

silicon to form Ti_3SiC_2 . The final composite had phases of TiC , SiC , Ti_3SiC_2 and TiSi_2 (see Figure 2.32b). Zhang *et al.* [211] was also able to create a $\text{NbAl}_3/\text{Al}_2\text{O}_3$ composites by infiltrating aluminum into a printed body of Nb_2O_5 and carbon. The composite initially had a NbC phase, but it was removed using a reductive annealing technique.

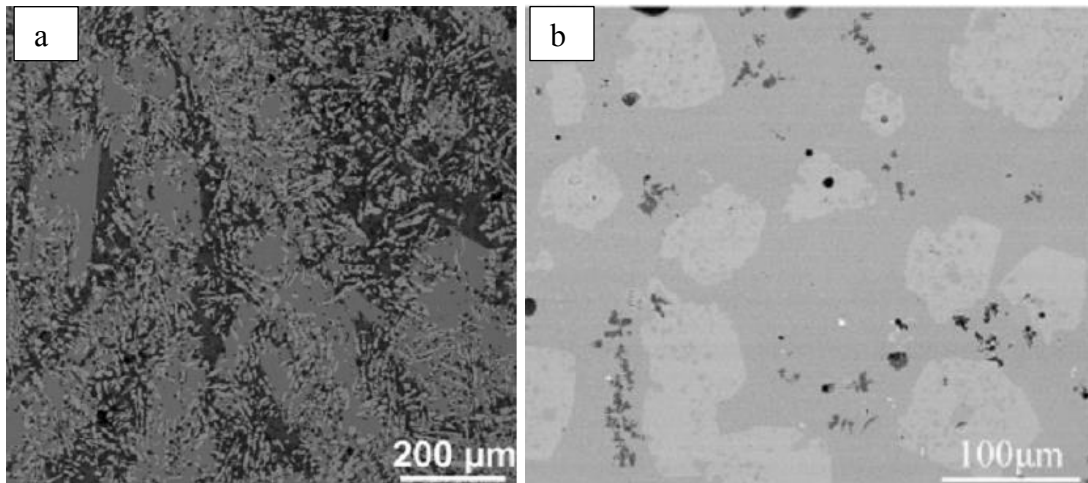


Figure 2.32. Microstructure of infiltrated binder jetted ceramic bodies that formed ternary carbides. a) The smallest plate like phase with the brightest contrast is Ti_3AlC_2 , the gray phase is TiAl_3 , the round dark particles are Al_2O_3 , and the dark matrix phase is Al [210]. b) The white phase is Ti_3SiC_2 , the continuous gray phase is TiSi_2 , the black phase is SiC , and the white-gray phase is TiC [121].

The porosity left in the sample from the binder jet printing process can also be of interest to different applications. In fact, this porosity is being investigate as an open network for applications that need high surface area, such as the biomedical field. For instance, glass and glass-ceramic materials have attracted attention as a possible bone and tissue replacement material for unloaded conditions [212]. Biocompatible materials such as calcium phosphate and other oxides of the type $6\text{Na}_2\text{O}-12\text{K}_2\text{O}-5\text{MgO}-20\text{CaO}-4\text{P}_2\text{O}_5-53\text{SiO}_2$ can be printed and infiltrated with biodegradable fillers [212-213].

Another application of porous printed ceramics is electromagnetic wave-transparent materials with good dielectric properties. An effective way to increase dielectric properties is to increase the porosity in a material (typically over 35%). Li *et al.* [214] was able to print Si₃N₄ and then use a chemical vapor infiltration technique to infiltrate more Si₃N₄ to enhance its mechanical strength. The final part had excellent dielectric properties with an increased mechanical strength after the infiltration process.

References

1. Callister, W. D. (2003). *Materials Science and Engineering an Introduction*. New York: Wiley.
2. Pollack, H. W. (1973). *Materials Science and Metallurgy*. Reston, VA: Reston Publishing Company.
3. Askeland, D. R., Fulay, P. P., & Wright, W. J. (2011). *The Science and Engineering of Materials* (6th ed.). Stamford, CT: Cengage Learning.
4. Gersten, J. I., & Smith, F. W. (2001). *The Physics and Chemistry of Materials*. New York, NY: John Wiley & Sons.
5. Shackelford, J. F. (2009). *Introduction to Materials Science for Engineers* (7th ed.). Upper Saddle River, NJ: Pearson Prentice Hall.
6. Weller, M. T. (1994). *Inorganic Materials Chemistry*. New York, NY: Oxford University Press.
7. Ionic Crystals. Retrieved March 18, 2016, from http://www.tf.uni-kiel.de/matwis/amat/def_en/kap_2/basics/b2_1_6.html

8. Smith, W. F., & Hashemi, J. (2010). *Foundations of Materials Science and Engineering* (5th ed.). New York, NY: McGraw-Hill.
9. Anderson, J. C., Leaver, K. D., Leever, P., & Rawlings, R. D. (2003). *Materials Science for Engineers* (5th ed.). Cheltenham, UK: Nelson Thornes.
10. Bradt, R. C., Munz, D., Sakai, M., & White, K. W. (2005). *Fracture Mechanics of Ceramics*. New York, NY: Springer.
11. Dowling, N. E. (1999). *Mechanical Behavior of Materials* (2nd ed.). Upper Saddle River, NJ: Prentice-Hall.
12. ASTM C1161-13, (2103) Standard Test Method for Flexural Strength of Advanced Ceramics at Ambient Temperature, ASTM International, West Conshohocken, PA, www.astm.org
13. Mackenzie, J. K. (1950). The elastic constants of a solid containing spherical holes. *Proceedings of the Physical Society*. Section B, 63(1), 2.
14. Gladysz, G. M., & Chawla, K. K. (2014). *Voids in Materials: From Unavoidable Defects to Designed Cellular Materials*. Elsevier.
15. Kalpakjian, S., & Schmid, S. R. (2008). *Manufacturing Processes for Engineering Materials* (5th ed.). Upper Saddle River, NJ: Prentice-Hall.
16. Young, J. F., & Shane, R. S. (1985). *Materials and Processes Part B: Processes* (3rd ed.). New York, NY: Marcel Dekker.
17. Black, J. T., & Kohser, R. A. (2012). *Materials and Processes in Manufacturing* (11th ed.). Hoboken, NJ: John Wiley & Sons.

18. West, A. R. (1984). *Basic Solid State Chemistry*. New York, NY: John Wiley & Sons.
19. Brick, R. M., & Pense, A. W. (1977). *Structure and Properties of Engineering Materials* (4th ed.). New York, NY: McGraw-Hill.
20. Rosenthal, D., & Asimow, R. M. (1971). *Introduction to Properties of Materials* (2nd ed.). New York, NY: Van Nostrand Reinhold Company.
21. Cahn, R. W., Haasen, P., & Kramer, E. J. (1991). *Materials Science and Technology* (Vol. 15). New York, NY: VCH.
22. Material Selection and Processing. Retrieved March 18, 2016, from <http://www-materials.eng.cam.ac.uk/mpsite/default.html>
23. Introduction to Deformation Processes. Retrieved March 18, 2016, from <http://www.doitpoms.ac.uk/tlplib/metal-forming-2/printall.php>
24. Bansal, N. P., & Lamon, J. (2015). *Ceramic Matrix Composites: Materials, Modeling and Technology*. Hoboken, NJ: John Wiley & Sons.
25. Mitchell, B. S. (2004). *An Introduction to Materials Engineering and Science for Chemical and Materials Engineers*. Hoboken, NJ: John Wiley & Sons.
26. Chawla, N., & Chawla, K. K. (2006). Metal-matrix composites in ground transportation. *The Journal of The Minerals, Metals & Materials Society*, 58(11), 67-70.
27. Rosso, M. (2006). Ceramic and metal matrix composites: Routes and properties. *Journal of Materials Processing Technology*, 175(1), 364-375.

28. Wegner, L. D., & Gibson, L. J. (2001). The fracture toughness behaviour of interpenetrating phase composites. *International journal of mechanical sciences*, 43(8), 1771-1791.
29. Hashim, J., Looney, L., & Hashmi, M. S. J. (1999). Metal matrix composites: production by the stir casting method. *Journal of Materials Processing Technology*, 92, 1-7.
30. Harnby, N., Edward, M. F., & Nienow, A. W. (1985). *Mixing in Process Industries*. London: Butterworths.
31. Thomas, D. G. (1962). Transport characteristics of suspensions: Part VI. Minimum transport velocity for large particle size suspensions in round horizontal pipes. *American Institute of Chemical Engineers Journal*, 8(3), 373-378.
32. Prabu, S. B., Karunamoorthy, L., Kathiresan, S., & Mohan, B. (2006). Influence of stirring speed and stirring time on distribution of particles in cast metal matrix composite. *Journal of Materials Processing Technology*, 171(2), 268-273.
33. Stefanescu, D. M., Ahuja, S., Dhindaw, B. K., & Phalnikar, R. (1992). Modeling of Particle Distribution in Equiaxed-Grains Metal Matrix Composites. *Processing of Semi-Solid Alloys and Composites*, 406-416.
34. McDanel, D. L. (1985). Analysis of stress-strain, fracture, and ductility behavior of aluminum matrix composites containing discontinuous silicon carbide reinforcement. *Metallurgical transactions A*, 16(6), 1105-1115.

35. Aghajanian, M. K., Rocazella, M. A., Burke, J. T., & Keck, S. D. (1991). The fabrication of metal matrix composites by a pressureless infiltration technique. *Journal of Materials Science*, 26(2), 447-454.
36. Binner, J., Chang, H., & Higginson, R. (2009). Processing of ceramic-metal interpenetrating composites. *Journal of the European Ceramic Society*, 29(5), 837-842.
37. Song, J. I., & Han, K. S. (1997). Mechanical properties and solid lubricant wear behavior of Al/Al₂O₃/C hybrid metal matrix composites fabricated by squeeze casting method. *Journal of Composite Materials*, 31(4), 316-344.
38. Prielipp, H., Knechtel, M., Claussen, N., Streiffer, S. K., Müllejans, H., Rühle, M., & Rödel, J. (1995). Strength and fracture toughness of aluminum/alumina composites with interpenetrating networks. *Materials Science and Engineering: A*, 197(1), 19-30.
39. Breval, E., Aghajanian, M. K., & Luszcz, S. J. (1990). Microstructure and composition of alumina/aluminum composites made by directed oxidation of aluminum. *Journal of the American Ceramic Society*, 73(9), 2610-2614.
40. Sindel, M., Travitzky, N. A., & Claussen, N. (1990). Influence of Magnesium-Aluminum Spinel on the Directed Oxidation of Molten Aluminum Alloys. *Journal of the American Ceramic Society*, 73(9), 2615-2618.
41. Antolin, S., Nagelberg, A. S., & Creber, D. K. (1992). Formation of Al₂O₃/Metal Composites by the Directed Oxidation of Molten Aluminum-Magnesium-Silicon

Alloys: Part I, Microstructural Development. *Journal of the American Ceramic Society*, 75(2), 447-454.

42. Chou, W. B., & Tuan, W. H. (1995). Toughening and strengthening of alumina with silver inclusions. *Journal of the European Ceramic Society*, 15(4), 291-295.
43. Shamsuddin, S., Jamaludin, S. B., Hussain, Z., & Ahmad, Z. A. (2010). The effects of Al₂O₃ amount on the microstructure and properties of Fe-Cr matrix composites. *Metallurgical and Materials Transactions A*, 41(13), 3452-3457.
44. Mazen, A. A., & Ahmed, A. Y. (1998). Mechanical behavior of Al-Al₂O₃ MMC manufactured by PM techniques part I—scheme I processing parameters. *Journal of Materials Engineering and Performance*, 7(3), 393-401.
45. Breslin, M. C., Ringnalda, J., Xu, L., Fuller, M., Seeger, J., Daehn, G. S., Otani, T., & Fraser, H. L. (1995). Processing, microstructure, and properties of co-continuous alumina-aluminum composites. *Materials Science and Engineering: A*, 195, 113-119.
46. Yurcho, A. M. (2011). *Microstructural Investigation of Al/Al-Fe alloy-Al₂O₃ Interpenetrating Phase Composites Produced by Reactive Metal Penetration* (Masters Thesis, Youngstown State University).
47. Henri, G. (1955). *U.S. Patent No. 2,702,750*. Washington, DC: U.S. Patent and Trademark Office.
48. Breslin, M. C. (1993). *U.S. Patent No. 5,214,011*. Washington, DC: U.S. Patent and Trademark Office.

49. Saiz, E., Foppiano, S., MoberlyChan, W., & Tomsia, A. P. (1999). Synthesis and processing of ceramic–metal composites by reactive metal penetration. *Composites Part A: Applied Science and Manufacturing*, 30(4), 399-403.
50. Sobczak, N., Stobierski, L., Radziwill, W., Ksiazek, M., & Warmuzek, M. (2004). Wettability and interfacial reactions in Al/TiO₂. *Surface and Interface Analysis*, 36(8), 1067-1070.
51. Avraham, S., & Kaplan, W. D. (2005). Reactive wetting of rutile by liquid aluminium. *Journal of Materials Science*, 40(5), 1093-1100.
52. Fahrenholtz, W. G., Ewsuk, K. G., Loehman, R. E., & Tomsia, A. P. (1996). Formation of structural intermetallics by reactive metal penetration of Ti and Ni oxides and aluminates. *Metallurgical and Materials Transactions A*, 27(8), 2100-2104.
53. Avraham, S., Beyer, P., Janssen, R., Claussen, N., & Kaplan, W. D. (2006). Characterization of α -Al₂O₃–(Al–Si)₃Ti composites. *Journal of the European Ceramic Society*, 26(13), 2719-2726.
54. Shen, P., Fujii, H., & Nogi, K. (2006). Wettability of polycrystalline rutile TiO₂ by molten Al in different atmospheres. *Acta Materialia*, 54(6), 1559-1569.
55. Myers, K. M. (2012). *Investigation of Novel Precursor Routes for Incorporation of Titanium Alloys and Nano-Sized Features into Ceramic-Metallic Composites Formed via the TCON Process* (Masters Thesis, Youngstown State University).

56. Loiacona, D. (2011). *Synthesis of β -Alumina-Type Compounds and Their Transformation via the TCON Process* (Masters Thesis, Youngstown State University).
57. Hosson, J. T. M. D., & Kooi, B. J. (2001). Metal/ceramic interfaces: a microscopic analysis. *Surface and Interface Analysis*, 31(7), 637-658.
58. Pavese, M., Valle, M., & Badini, C. (2007). Effect of porosity of cordierite preforms on microstructure and mechanical strength of co-continuous ceramic composites. *Journal of the European Ceramic Society*, 27(1), 131-141.
59. Liu, W., & Köster, U. (1996). Criteria for formation of interpenetrating oxide/metal-composites by immersing sacrificial oxide preforms in molten metals. *Scripta Materialia*, 35(1), 35-40.
60. Chidambaram, P. R., Edwards, G. R., & Olson, D. L. (1992). A thermodynamic criterion to predict wettability at metal-alumina interfaces. *Metallurgical Transactions B*, 23(2), 215-222.
61. Mattern, A., Huchler, B., Staudenecker, D., Oberacker, R., Nagel, A., & Hoffmann, M. J. (2004). Preparation of interpenetrating ceramic-metal composites. *Journal of the European Ceramic Society*, 24(12), 3399-3408.
62. Coupard, D., Goni, J., & Sylvain, J. F. (1999). Fabrication and squeeze casting infiltration of graphite/alumina preforms. *Journal of Materials Science*, 34(21), 5307-5313.

63. Kalazhokov, K. K., Kalazhokov, Z. K., & Khokonov, K. B. (2003). Surface tension of pure aluminum melt. *Technical Physics*, 48(2), 272-273.
64. Macke, A., Schultz, B. F., & Rohatgi, P. (2012). Metal matrix composites offer the automotive industry an opportunity to reduce vehicle weight, improve performance. *Advanced Materials & Processes*, 170(3), 19-23.
65. Ibrahim, I. A., Mohamed, F. A., & Lavernia, E. J. (1991). Particulate reinforced metal matrix composites—a review. *Journal of Materials Science*, 26(5), 1137-1156.
66. Macke, A., Schultz, B. F., Rohatgi, P. K., & Gupta, N. (2013). Metal matrix composites for automotive applications. *Advanced Composite Materials for Automotive Applications: Structural Integrity and Crashworthiness*, 311-344.
67. Palleti, H. K. T., Gurusamy, S., Kumar, S., Soni, R., John, B., Vaidya, R., Bhoge, A., & Naik, N. K. (2012). Ballistic impact performance of metallic targets. *Materials & Design*, 39, 253-263.
68. Hazell, P. J., Roberson, C. J., & Moutinho, M. (2008). The design of mosaic armour: The influence of tile size on ballistic performance. *Materials & Design*, 29(8), 1497-1503.
69. Pandya, K. S., Pothnis, J. R., Ravikumar, G., & Naik, N. K. (2013). Ballistic impact behavior of hybrid composites. *Materials & Design*, 44, 128-135.

70. Zhou, Z., Wu, G., Jiang, L., Li, R., & Xu, Z. (2014). Analysis of morphology and microstructure of B₄C/2024Al composites after 7.62 mm ballistic impact. *Materials & Design*, *63*, 658-663.
71. Radhakrishna Bhat, B. V., Somaraju, K., Venkataraman, B., & Bhanuprasad, V. V. (1998). Metal Matrix Composites as Potential Armour Materials.
72. Karamiş, M. B., Cerit, A. A., & Nair, F. (2006). Surface characteristics of projectiles after frictional interaction with metal matrix composites under ballistic condition. *Wear*, *261*(7), 738-745.
73. Karamis, M. B., Nair, F., & Tasdemirci, A. (2004). Analyses of metallurgical behavior of Al–SiCp composites after ballistic impacts. *Composite Structures*, *64*(2), 219-226.
74. Guo, Q., Sun, D. L., Jiang, L. T., Han, X. L., Chen, G. Q., & Wu, G. H. (2012). Residual microstructure associated with impact craters in TiB₂/2024Al composite. *Micron*, *43*(2), 344-348.
75. Karamiş, M. B., Cerit, A. A., & Nair, F. (2008). Mutual action between MMCs structure and projectile after ballistic impact. *Journal of Composite Materials*, *42*(23), 2483-2498.
76. Karamis, M. B., Nair, F., & Cerit, A. A. (2009). The metallurgical and deformation behaviours of laminar metal matrix composites after ballistic impact. *Journal of Materials Processing Technology*, *209*(10), 4880-4889.

77. Vaziri, R., Delfosse, D., Pageau, G., & Poursartip, A. (1993). High-speed impact response of particulate metal matrix composite materials—an experimental and theoretical investigation. *International Journal of Impact Engineering*, 13(2), 329-352.
78. Grujicic, M., Bell, W. C., Pandurangan, B., Yen, C. F., & Cheeseman, B. A. (2011). Computational investigation of structured shocks in Al/SiC-particulate metal-matrix composites. *Multidiscipline Modeling in Materials and Structures*, 7(4), 469-497.
79. Chang, H., Binner, J., Higginson, R., Myers, P., Webb, P., & King, G. (2011). Preparation and characterisation of ceramic-faced metal–ceramic interpenetrating composites for impact applications. *Journal of Materials Science*, 46(15), 5237-5244.
80. Chang, H., Binner, J., Higginson, R., Myers, P., Webb, P., & King, G. (2011). High strain rate characteristics of 3-3 metal–ceramic interpenetrating composites. *Materials Science and Engineering: A*, 528(6), 2239-2245.
81. Prasad, S. V., & Asthana, R. (2004). Aluminum metal-matrix composites for automotive applications: tribological considerations. *Tribology letters*, 17(3), 445-453.
82. Transparency Market Research “Metal Matrix Composites (MMC) Market for Ground Transportation, Electronics/Thermal Management, Aerospace and Other End-users - Global Industry Analysis, Size, Share, Growth, Trends and Forecast,

2013 – 2019” (May 2014). <http://www.transparencymarketresearch.com/metal-matrix-composites.html>.

83. Blau, P. J., & Meyer, H. M. (2003). Characteristics of wear particles produced during friction tests of conventional and unconventional disc brake materials. *Wear*, 255(7), 1261-1269.
84. Mosleh, M., Blau, P. J., & Dumitrescu, D. (2004). Characteristics and morphology of wear particles from laboratory testing of disk brake materials. *Wear*, 256(11), 1128-1134.
85. Natarajan, N., Vijayarangan, S., & Rajendran, I. (2006). Wear behaviour of A356/25SiC p aluminium matrix composites sliding against automobile friction material. *Wear*, 261(7), 812-822.
86. Natarajan, N., Vijayarangan, S., & Rajendran, I. (2007). Fabrication, testing and thermal analysis of metal matrix composite brake drum. *International Journal of Vehicle Design*, 44(3-4), 339-359.
87. Howell, G. J., & Ball, A. (1995). Dry sliding wear of particulate-reinforced aluminium alloys against automobile friction materials. *Wear*, 181, 379-390.
88. Uyyuru, R. K., Surappa, M. K., & Brusethaug, S. (2007). Tribological behavior of Al–Si–SiC p composites/automobile brake pad system under dry sliding conditions. *Tribology International*, 40(2), 365-373.
89. Laden, K., Guerin, J. D., Watremez, M., & Bricout, J. P. (2000). Frictional characteristics of Al–SiC composite brake discs. *Tribology Letters*, 8(4), 237-247.

90. Shorowordi, K. M., Haseeb, A. S. M. A., & Celis, J. P. (2004). Velocity effects on the wear, friction and tribochemistry of aluminum MMC sliding against phenolic brake pad. *Wear*, 256(11), 1176-1181.
91. Zhang, S., & Wang, F. (2007). Comparison of friction and wear performances of brake material dry sliding against two aluminum matrix composites reinforced with different SiC particles. *Journal of Materials Processing Technology*, 182(1), 122-127.
92. Valente, M., & Billi, F. (2001). Micromechanical modification induced by cyclic thermal stress on metal matrix composites for automotive applications. *Composites Part B: Engineering*, 32(6), 529-533.
93. Straffelini, G., Pellizzari, M., & Molinari, A. (2004). Influence of load and temperature on the dry sliding behaviour of Al-based metal-matrix-composites against friction material. *Wear*, 256(7), 754-763.
94. Akay, A., Giannini, O., Massi, F., & Sestieri, A. (2009). Disc brake squeal characterization through simplified test rigs. *Mechanical Systems and Signal Processing*, 23(8), 2590-2607.
95. Kennedy, F. E., Balbahadur, A. C., & Lashmore, D. S. (1997). The friction and wear of Cu-based silicon carbide particulate metal matrix composites for brake applications. *Wear*, 203, 715-721.
96. Daoud, A., & El-khair, M. A. (2010). Wear and friction behavior of sand cast brake rotor made of A359-20vol% SiC particle composites sliding against automobile friction material. *Tribology International*, 43(3), 544-553.

97. Vencel, A., Rac, A., & Bobic, I. (2004). Tribological behaviour of Al-based MMCs and their application in automotive industry. *Tribology in Industry*, 26(3-4), 31-38.
98. Daehn, G. S., & Breslin, M. C. (2006). Co-continuous composite materials for friction and braking applications. *The Journal of The Minerals, Metals & Materials Society*, 58(11), 87-91.
99. Hemrick, J. C., Hu, M. Z., Peters, K. M., & Hetzel, B. (2010). Nano-Scale Interpenetrating Phase Composites (IPC's) for Industrial and Vehicle Application. *ORNL/TM-2010/80* Oak Ridge, TN.
100. Wang, H., Wang, S., Liu, G., & Wang, Y. (2013). AlSi11/Si3N4 interpenetrating composites Tribology properties of aluminum matrix composites. *Advances in Materials Physics and Chemistry*, 2(4), 130.
101. Williams, J. C., & Starke, E. A. (2003). Progress in structural materials for aerospace systems. *Acta Materialia*, 51(19), 5775-5799.
102. Anderson, J.D. (2002). *The Airplane, a history of its technology*. Reston, VA, American Institute of Aeronautics and Astronautics.
103. Yan, C., Lifeng, W., & Jianyue, R. (2008). Multi-functional SiC/Al composites for aerospace applications. *Chinese Journal of Aeronautics*, 21(6), 578-584.
104. Steyer, T. E. (2013). Shaping the future of ceramics for aerospace applications. *International Journal of Applied Ceramic Technology*, 10(3), 389-394.

105. Hand, M. L., Chakrabarti, B., Lehman, L. L., & Mathur, G. P. (2011). *U.S. Patent No. 8,043,690*. Washington, DC: U.S. Patent and Trademark Office.
106. Leiser, D. B., Churchward, R., Katvala, V., Stewart, D., & Balter, A. (1989). Advanced Porous Coating for Low-Density Ceramic Insulation Materials. *Journal of the American Ceramic Society*, 72(6), 1003-1010.
107. Heng, V., Hinkle, K. A., & Santos, M. A. (2004). *U.S. Patent No. 6,716,782*. Washington, DC: U.S. Patent and Trademark Office.
108. Stewart, D., & Leiser, D. (2007). Lightweight Thermal Protection System for Atmospheric Entry.
109. Glass, D. E. (2008). Ceramic matrix composite (CMC) thermal protection systems (TPS) and hot structures for hypersonic vehicles. In *15th AIAA space planes and hypersonic systems and technologies conference*, 1-36.
110. Opeka, M. M., Talmy, I. G., & Zaykoski, J. A. (2004). Oxidation-based materials selection for 2000 C+ hypersonic aerosurfaces: theoretical considerations and historical experience. *Journal of materials science*, 39(19), 5887-5904.
111. Fahrenholtz, W. G., Hilmas, G. E., Talmy, I. G., & Zaykoski, J. A. (2007). Refractory diborides of zirconium and hafnium. *Journal of the American Ceramic Society*, 90(5), 1347-1364.
112. Silvestroni, L., Sciti, D., Melandri, C., & Guicciardi, S. (2010). Toughened ZrB₂-based ceramics through SiC whisker or SiC chopped fiber additions. *Journal of the European Ceramic Society*, 30(11), 2155-2164.

113. Rouxel, T., & Laurent, Y. (1998). Fracture characteristics of SiC particle reinforced oxynitride glass using chevron-notch three-point bend specimens. *International Journal of Fracture*, 91(1), 83-101.
114. Taya, M., Hayashi, S., Kobayashi, A. S., & Yoon, H. S. (1990). Toughening of a Particulate-Reinforced Ceramic-Matrix Composite by Thermal Residual Stress. *Journal of the American Ceramic Society*, 73(5), 1382-1391.
115. Günther, R., Klassen, T., Dickau, B., Gärtner, F., Bartels, A., & Bormann, R. (2001). Advanced Alumina Composites Reinforced with Titanium-Based Alloys. *Journal of the American Ceramic Society*, 84(7), 1509-1513.
116. Chen, Y., & Chung, D. D. L. (1996). Aluminium-matrix silicon carbide whisker composites fabricated by pressureless infiltration. *Journal of Materials Science*, 31(2), 407-412.
117. Fu, Z., Schlier, L., Travitzky, N., & Greil, P. (2013). Three-dimensional printing of SiSiC lattice truss structures. *Materials Science and Engineering: A*, 560, 851-856.
118. Melcher, R., Martins, S., Travitzky, N., & Greil, P. (2006). Fabrication of Al₂O₃-based composites by indirect 3D-printing. *Materials Letters*, 60(4), 572-575.
119. Travitzky, N. A., & Shlayan, A. (1998). Microstructure and mechanical properties of Al₂O₃/Cu-O composites fabricated by pressureless infiltration technique. *Materials Science and Engineering: A*, 244(2), 154-160.

120. Melcher, R., Travitzky, N., Zollfrank, C., & Greil, P. (2011). 3D printing of $\text{Al}_2\text{O}_3/\text{Cu-O}$ interpenetrating phase composite. *Journal of Materials Science*, 46(5), 1203-1210.
121. Nan, B., Yin, X., Zhang, L., & Cheng, L. (2011). Three-Dimensional Printing of Ti_3SiC_2 -Based Ceramics. *Journal of the American Ceramic Society*, 94(4), 969-972.
122. Wang, L., Yin, X., Fan, X., Greil, P., & Travitzky, N. (2014). $\text{Ti}_3\text{Si}(\text{Al})\text{C}_2$ -based ceramics fabricated by reactive melt infiltration with Al 70 Si 30 alloy. *Journal of the European Ceramic Society*, 34(6), 1493-1499.
123. Yin, X., Travitzky, N., & Greil, P. (2007). Near-Net-Shape Fabrication of Ti_3AlC_2 -Based Composites. *International Journal of Applied Ceramic Technology*, 4(2), 184-190.
124. San Marchi, C., Kouzeli, M., Rao, R., Lewis, J. A., & Dunand, D. C. (2003). Alumina–aluminum interpenetrating-phase composites with three-dimensional periodic architecture. *Scripta Materialia*, 49(9), 861-866.
125. Wang, Q., Min, F., & Zhu, J. (2013). Microstructure and thermo-mechanical properties of SiCp/Al composites prepared by pressureless infiltration. *Journal of Materials Science: Materials in Electronics*, 24(6), 1937-1940.
126. Pech-Canul, M. I., & Makhlouf, M. M. (2000). Processing of Al-SiCp metal matrix composites by pressureless infiltration of SiCp preforms. *Journal of Materials Synthesis and Processing*, 8(1), 35-53.

127. Aghajanian, M. K., Macmillan, N. H., Kennedy, C. R., Luszcz, S. J., & Roy, R. (1989). Properties and microstructures of Lanxide® Al₂O₃-Al ceramic composite materials. *Journal of Materials Science*, 24(2), 658-670.
128. Chen, C., Yang, J., & Chu, C. (2011). Effect of MgO content on the microstructure and mechanical properties of Fe–Cr–Ni/MgO composites produced by reactive hot pressing. *Materials Science and Engineering: A*, 528(6), 2995-2998.
129. Fahrenholtz, W. G., Ellerby, D. T., & Loehman, R. E. (2000). Al₂O₃–Ni composites with high strength and fracture toughness. *Journal of the American Ceramic Society*, 83(5), 1279-1280.
130. Fahrenholtz, W. G., Loehman, R. E., & Ewsuk, K. G. (2002). Reactive Hot Pressing of Alumina-Molybdenum Disilicide Composites. *Journal of the American Ceramic Society*, 85(1), 258-260.
131. Guichard, J. L., Tillement, O., & Mocellin, A. (1997). Preparation and characterization of alumina–iron cermets by hot-pressing of nanocomposite powders. *Journal of Materials Science*, 32(17), 4513-4521.
132. Guichard, J. L., Tillement, O., & Mocellin, A. (1998). Alumina-chromium cermets by hot-pressing of nanocomposite powders. *Journal of the European Ceramic Society*, 18(12), 1743-1752.
133. He, S. S., Yin, X. W., Zhang, L. T., Li, X. M., & Cheng, L. F. (2009). Ti₃AlC₂-Al₂O₃-TiAl₃ composite fabricated by reactive melt infiltration. *Transactions of Nonferrous Metals Society of China*, 19(5), 1215-1221.

134. Hong, C., Han, J., Zhang, X., Meng, S., & Du, S. (2008). Thermal ablation resistance of melt-infiltrated titanium diboride-(copper, nickel) composites. *Journal of Alloys and Compounds*, 460(1), 400-408.
135. La Vecchia, G. M., Badini, C., Puppo, D., & D'Errico, F. (2003). Co-continuous Al/Al₂O₃ composite produced by liquid displacement reaction: Relationship between microstructure and mechanical behavior. *Journal of Materials Science*, 38(17), 3567-3577.
136. Loehman, R. E., Ewsuk, K., & Tomsia, A. P. (1996). Synthesis of Al₂O₃-Al Composites by Reactive Metal Penetration. *Journal of the American Ceramic Society*, 79(1), 27-32.
137. Manfredi, D., Pavese, M., Biamino, S., Fino, P., & Badini, C. (2009). Preparation and properties of NiAl (Si)/Al₂O₃ co-continuous composites obtained by reactive metal penetration. *Composites Science and Technology*, 69(11), 1777-1782.
138. Manfredi, D., Pavese, M., Biamino, S., Antonini, A., Fino, P., & Badini, C. (2010). Microstructure and mechanical properties of co-continuous metal/ceramic composites obtained from reactive metal penetration of commercial aluminium alloys into cordierite. *Composites Part A: Applied Science and Manufacturing*, 41(5), 639-645.
139. Pavese, M., Fino, P., Valle, M., & Badini, C. (2006). Preparation of C4 ceramic/metal composites by reactive metal penetration of commercial ceramics. *Composites Science and Technology*, 66(2), 350-356.

140. Scherm, F., Völkl, R., Neubrand, A., Bosbach, F., & Glatzel, U. (2010). Mechanical characterisation of interpenetrating network metal–ceramic composites. *Materials Science and Engineering: A*, 527(4), 1260-1265.
141. Travitzky, N., Kumar, P., Sandhage, K. H., Janssen, R., & Claussen, N. (2003). Rapid synthesis of Al₂O₃ reinforced Fe–Cr–Ni composites. *Materials Science and Engineering: A*, 344(1), 245-252.
142. Wittig, D., Aneziris, C. G., Graule, T., & Kuebler, J. (2009). Mechanical properties of three-dimensional interconnected alumina/steel metal matrix composites. *Journal of Materials Science*, 44(2), 572-579.
143. Yun, Y. H., Hong, S. W., & Choi, S. C. (2002). Metal penetration processing and mechanical properties of Al/Al₂O₃ composite system. *Journal of Materials Science Letters*, 21(16), 1297-1299.
144. Grey, G. T. (2002). *High-Strain-Rate Testing of Materials: The Split-Hopkinson Pressure Bar*. New York, NY: John Wiley & Sons.
145. Sjoblom, P. O., Hartness, J. T., & Cordell, T. M. (1988). On low-velocity impact testing of composite materials. *Journal of Composite Materials*, 22(1), 30-52.
146. Safri, S. N. A., Sultan, M. T. H., Yidris, N., & Mustapha, F. (2014). Low Velocity and High Velocity Impact Test on Composite Materials—A review. *The International Journal of Engineering and Science*, 3, 50-60.

147. Shen, Z. (2014). *Characterisation of Low Velocity Impact Response in Composite Laminates* (Doctoral dissertation, School of Engineering and Technology, University of Hertfordshire).
148. Fard, K. M., Khalili, S. M. R., Forooghi, S. H., & Hosseini, M. (2014). Low velocity transverse impact response of a composite sandwich plate subjected to a rigid blunted cylindrical impactor. *Composites Part B: Engineering*, *63*, 111-122.
149. Bull, D. J., Spearing, S. M., & Sinclair, I. (2015). Investigation of the response to low velocity impact and quasi-static indentation loading of particle-toughened carbon-fibre composite materials. *Composites Part A: Applied Science and Manufacturing*, *74*, 38-46.
150. Markaki, A. E., & Clyne, T. W. (2000). Characterisation of impact response of metallic foam/ceramic laminates. *Materials Science and Technology*, *16*(7-8), 785-791.
151. Villanueva, G. R., & Cantwell, W. J. (2004). The high velocity impact response of composite and FML-reinforced sandwich structures. *Composites Science and Technology*, *64*(1), 35-54.
152. Singh, A. K., Davidson, B. D., Hasseldine, B. P., & Zehnder, A. T. (2015). Damage resistance of aluminum core honeycomb sandwich panels with carbon/epoxy face sheets. *Journal of Composite Materials*, *49*(23), 2859-2876.
153. Jung, A., Lach, E., & Diebels, S. (2014). New hybrid foam materials for impact protection. *International Journal of Impact Engineering*, *64*, 30-38.

154. Pernas-Sánchez, J., Pedroche, D. A., Varas, D., López-Puente, J., & Zaera, R. (2012). Numerical modeling of ice behavior under high velocity impacts. *International Journal of Solids and Structures*, 49(14), 1919-1927.
155. Chichili, D. R., & Ramesh, K. T. (1995). Dynamic failure mechanisms in a 6061-T6 Al/Al₂O₃ metal—matrix composite. *International Journal of Solids and Structures*, 32(17), 2609-2626.
156. San Marchi, C., Cao, F., Kouzeli, M., & Mortensen, A. (2002). Quasistatic and dynamic compression of aluminum-oxide particle reinforced pure aluminum. *Materials Science and Engineering: A*, 337(1), 202-211.
157. Owolabi, G. M., Odeshi, A. G., Singh, M. N. K., & Bassim, M. N. (2007). Dynamic shear band formation in aluminum 6061-T6 and aluminum 6061-T6/Al₂O₃ composites. *Materials Science and Engineering: A*, 457(1), 114-119.
158. Tan, Z. H., Pang, B. J., Gai, B. Z., Wu, G. H., & Jia, B. (2007). The dynamic mechanical response of SiC particulate reinforced 2024 aluminum matrix composites. *Materials Letters*, 61(23), 4606-4609.
159. Li, Y., Ramesh, K. T., & Chin, E. S. C. (2004). The mechanical response of an A359/SiC p MMC and the A359 aluminum matrix to dynamic shearing deformations. *Materials Science and Engineering: A*, 382(1), 162-170.
160. Kalambur, A., & Hall, I. W. (1997). Dynamic compressive behavior of a SiC w/Al composite. *Scripta Materialia*, 37(2), 193-198.

161. Vogt, R., Zhang, Z., Huskins, E., Ahn, B., Nutt, S., Ramesh, K. T., ... & Schoenung, J. M. (2010). High strain rate deformation and resultant damage mechanisms in ultrafine-grained aluminum matrix composites. *Materials Science and Engineering: A*, 527(21), 5990-5996.
162. Zhu, D., Wu, G., Chen, G., & Zhang, Q. (2008). Dynamic deformation behavior of a high reinforcement content TiB₂/Al composite at high strain rates. *Materials Science and Engineering: A*, 487(1), 536-540.
163. Ivanova, O., Williams, C., & Campbell, T. (2013). Additive manufacturing (AM) and nanotechnology: promises and challenges. *Rapid Prototyping Journal*, 19(5), 353-364.
164. ASTM F2792-12a, Standard Terminology for Additive Manufacturing Technologies: (Withdrawn 2015), ASTM International, West Conshohocken, PA, 2012, www.astm.org
165. Berman, B. (2012). 3-D printing: The new industrial revolution. *Business Horizons*, 55(2), 155-162.
166. Pham, D. T., & Gault, R. S. (1998). A comparison of rapid prototyping technologies. *International Journal of Machine Tools and Manufacture*, 38(10), 1257-1287.
167. Gibson, I., Rosen, D. W., & Stucker, B. (2010). *Additive Manufacturing Technologies: Rapid Prototyping to Direct Digital Manufacturing*. New York, NY: Springer.

168. Jacobs, P. F. (1996). *Stereolithography and other RP&M technologies*. Dearborn, MI: Society of Manufacturing Engineers.
169. Upcraft, S., & Fletcher, R. (2003). The rapid prototyping technologies. *Assembly Automation*, 23(4), 318-330.
170. Feygin, M. (1988). *U.S. Patent No. 4,752,352*. Washington, DC: U.S. Patent and Trademark Office.
171. Wimpenny, D. I., Bryden, B., & Pashby, I. R. (2003). Rapid laminated tooling. *Journal of Materials Processing Technology*, 138(1), 214-218.
172. Himmer, T., Techel, A., Nowotny, S., & Beyer, E. (2003). Recent developments in metal laminated tooling by multiple laser processing. *Rapid Prototyping Journal*, 9(1), 24-29.
173. Guo, N., & Leu, M. C. (2013). Additive manufacturing: technology, applications and research needs. *Frontiers of Mechanical Engineering*, 8(3), 215-243.
174. Wong, K. V., & Hernandez, A. (2012). A review of additive manufacturing. *ISRN Mechanical Engineering*, 2012.
175. Huang, S. H., Liu, P., Mokasdar, A., & Hou, L. (2013). Additive manufacturing and its societal impact: a literature review. *The International Journal of Advanced Manufacturing Technology*, 67(5-8), 1191-1203.
176. Kamath, C., El-dasher, B., Gallegos, G. F., King, W. E., & Sisto, A. (2014). Density of additively-manufactured, 316L SS parts using laser powder-bed fusion

- at powers up to 400 W. *The International Journal of Advanced Manufacturing Technology*, 74(1-4), 65-78.
177. Kruth, J. P., Mercelis, P., Van Vaerenbergh, J., Froyen, L., & Rombouts, M. (2005). Binding mechanisms in selective laser sintering and selective laser melting. *Rapid Prototyping Journal*, 11(1), 26-36.
178. Sercombe, T. B., & Schaffer, G. B. (2003). Rapid manufacturing of aluminum components. *Science*, 301(5637), 1225-1227.
179. Grida, I., & Evans, J. R. (2003). Extrusion free forming of ceramics through fine nozzles. *Journal of the European Ceramic Society*, 23(5), 629-635.
180. Khoshnevis, B., Hwang, D., Yao, K. T., & Yeh, Z. (2006). Mega-scale fabrication by contour crafting. *International Journal of Industrial and Systems Engineering*, 1(3), 301-320.
181. Contour Crafting. Retrieved March 21, 2016, from <http://www.contourcrafting.org/>
182. Jafari, M., Han, W., Mohammadi, F., Safari, A., Danforth, S. C., & Langrana, N. (2000). A novel system for fused deposition of advanced multiple ceramics. *Rapid Prototyping Journal*, 6(3), 161-175.
183. Bandyopadhyay, A., Panda, R. K., McNulty, T. F., Mohammadi, F., Danforth, S. C., & Safari, A. (1998). Piezoelectric ceramics and composites via rapid prototyping techniques. *Rapid Prototyping Journal*, 4(1), 37-49.

184. Unocic, R. R., & DuPont, J. N. (2004). Process efficiency measurements in the laser engineered net shaping process. *Metallurgical and Materials Transactions B*, 35(1), 143-152.
185. Liu, W., & DuPont, J. N. (2003). Fabrication of functionally graded TiC/Ti composites by laser engineered net shaping. *Scripta Materialia*, 48(9), 1337-1342.
186. Balla, V. K., Bandyopadhyay, P. P., Bose, S., & Bandyopadhyay, A. (2007). Compositionally graded yttria-stabilized zirconia coating on stainless steel using laser engineered net shaping (LENS™). *Scripta Materialia*, 57(9), 861-864.
187. Sachs, E., Cima, M., Williams, P., Brancazio, D., & Cornie, J. (1992). Three dimensional printing: rapid tooling and prototypes directly from a CAD model. *Journal of Engineering for Industry*, 114(4), 481-488.
188. Jee, H. J., & Sachs, E. (2000). A visual simulation technique for 3D printing. *Advances in Engineering Software*, 31(2), 97-106.
189. Yoo, J., Cima, M. J., Khanuja, S., & Sachs, E. M. (1993). Structural ceramic components by 3D printing. In *Solid Freeform Fabrication Symposium* (pp. 40-50).
190. Ahmed, S., & Jones, F. R. (1990). A review of particulate reinforcement theories for polymer composites. *Journal of Materials Science*, 25(12), 4933-4942.

191. Lewis, J. A., & Cima, M. J. (1990). Diffusivities of dialkyl phthalates in plasticized poly (vinyl butyral): impact on binder thermolysis. *Journal of the American Ceramic Society*, 73(9), 2702-2707.
192. Wegner, L. D., & Gibson, L. J. (2000). The mechanical behaviour of interpenetrating phase composites—I: modelling. *International Journal of Mechanical Sciences*, 42(5), 925-942.
193. Wegner, L. D., & Gibson, L. J. (2000). The mechanical behaviour of interpenetrating phase composites—II: a case study of a three-dimensionally printed material. *International Journal of Mechanical Sciences*, 42(5), 943-964.
194. Wegner, L. D., & Gibson, L. J. (2001). The mechanical behaviour of interpenetrating phase composites—III: resin-impregnated porous stainless steel. *International Journal of Mechanical Sciences*, 43(4), 1061-1072.
195. Lu, K., Hiser, M., & Wu, W. (2009). Effect of particle size on three dimensional printed mesh structures. *Powder Technology*, 192(2), 178-183.
196. Sachs, E. M., Cima, M. J., Caradonna, M. A., Grau, J., Serdy, J. G., Saxton, P. C., Uhland, S. A., & Moon, J. (2003). *U.S. Patent No. 6,596,224*. Washington, DC: U.S. Patent and Trademark Office.
197. Liu, J., & Ryneson, M. L. (2006). *U.S. Patent No. 7,070,734*. Washington, DC: U.S. Patent and Trademark Office.
198. Sachs, E. M. (2000). *U.S. Patent No. 6,036,777*. Washington, DC: U.S. Patent and Trademark Office.

199. Cima, M., Sachs, E., Fan, T., Brecht, J. F., Michaels, S. P., Khanuja, S., ... & Tuerck, H. (1995). *U.S. Patent No. 5,387,380*. Washington, DC: U.S. Patent and Trademark Office.
200. Dion, S., Balistreri, J., & Reed, A. (2013). *U.S. Patent No. 8,475,946*. Washington, DC: U.S. Patent and Trademark Office.
201. Lu, K., & Reynolds, W. T. (2008). 3DP process for fine mesh structure printing. *Powder Technology, 187*(1), 11-18.
202. Vaezi, M., & Chua, C. K. (2011). Effects of layer thickness and binder saturation level parameters on 3D printing process. *The International Journal of Advanced Manufacturing Technology, 53*(1-4), 275-284.
203. Utela, B., Storti, D., Anderson, R., & Ganter, M. (2008). A review of process development steps for new material systems in three dimensional printing (3DP). *Journal of Manufacturing Processes, 10*(2), 96-104.
204. Moon, J., Grau, J. E., Knezevic, V., Cima, M. J., & Sachs, E. M. (2002). Ink-Jet Printing of Binders for Ceramic Components. *Journal of the American Ceramic Society, 85*(4), 755-762.
205. Brecht, J. F., Clark, S., & Gilchrist, G. (2006). *U.S. Patent No. 7,087,109*. Washington, DC: U.S. Patent and Trademark Office.
206. Utela, B., Anderson, R. L., & Kuhn, H. (2006, August). Advanced ceramic materials and processes for three-dimensional printing (3DP). In *Solid Freeform Fabrication Symposium Proceedings (17)* 290-303.

207. Moon, J., Caballero, A. C., Hozer, L., Chiang, Y. M., & Cima, M. J. (2001). Fabrication of functionally graded reaction infiltrated SiC–Si composite by three-dimensional printing (3DP™) process. *Materials Science and Engineering: A*, 298(1), 110-119.
208. Zhang, W., Melcher, R., Travitzky, N., Bordia, R. K., & Greil, P. (2009). Three-Dimensional Printing of Complex-Shaped Alumina/Glass Composites. *Advanced Engineering Materials*, 11(12), 1039-1043.
209. Rambo, C. R., Travitzky, N., Zimmermann, K., & Greil, P. (2005). Synthesis of TiC/Ti–Cu composites by pressureless reactive infiltration of TiCu alloy into carbon preforms fabricated by 3D-printing. *Materials Letters*, 59(8), 1028-1031.
210. Yin, X., Travitzky, N., & Greil, P. (2007). Three-Dimensional Printing of Nanolaminated Ti₃AlC₂ Toughened TiAl₃–Al₂O₃ Composites. *Journal of the American Ceramic Society*, 90(7), 2128-2134.
211. Zhang, W., Travitzky, N., & Greil, P. (2008). Formation of NbAl₃/Al₂O₃ composites by pressureless reactive infiltration. *Journal of the American Ceramic Society*, 91(9), 3117-3120.
212. Winkel, A., Meszaros, R., Reinsch, S., Müller, R., Travitzky, N., Fey, T., ... & Wondraczek, L. (2012). Sintering of 3D-Printed Glass/HAp Composites. *Journal of the American Ceramic Society*, 95(11), 3387-3393.
213. Khalyfa, A., Vogt, S., Weisser, J., Grimm, G., Rechtenbach, A., Meyer, W., & Schnabelrauch, M. (2007). Development of a new calcium phosphate powder-

binder system for the 3D printing of patient specific implants. *Journal of Materials Science: Materials in Medicine*, 18(5), 909-916.

214. Li, X., Zhang, L., & Yin, X. (2012). Effect of chemical vapor infiltration of Si₃N₄ on the mechanical and dielectric properties of porous Si₃N₄ ceramic fabricated by a technique combining 3-D printing and pressureless sintering. *Scripta Materialia*, 67(4), 380-383.

Chapter 3 Experimental

The purpose of this research work is to study the structure-property relationship of ceramic-metallic composites by using a binder jetting technology. Using this technology, ceramic preforms are manufactured via the 3D printing and subsequently infiltrated through a reactive metal penetration technique. The resulting composites were structurally and mechanically tested, and therefore, the binder jetting process, the structural analysis, and the mechanical property testing is described in the following sections.

3.1 Binder Jetting of Ceramic Precursors

Fused silica powders with the mesh size of -100, -200, -325 (150, 74, and 44 μm respectively) were purchased from CE Minerals (Greeneville, TN). The -100 powder was subsequently sieved through a 170 mesh (90 μm) to assure that all particles were below 100 μm . These powder blends have d_{50} particle sizes of 65, 48, and 8 μm respectively. A GP-3I powder blend was also purchased from Harbison Walker International (Cleveland, OH) which has a d_{50} of 4 μm , therefore, the powders will be described as the particle sizes of 65, 48, 8, and 4 μm respectively. The particle size distributions of each powder were classified with a d_{10} , d_{50} , and d_{90} particles sizes using a fourth root two series sieve analysis, where the 10, 50 and 90 are the particle sizes that represent the cumulative percent finer than [1].

The binder jetting printers that were used for the manufacturing process of the ceramic precursors were the X1-Lab and the M-Flex from Ex-One (Irwin, Pennsylvania). The X1-lab printer has a build volume of 60 x 40 x 35 mm (2.3 x 1.5 x 1.3 in.)

corresponding to depth x width x height, respectively, while the M-Flex is 400 x 250 x 250 mm (15.7 x 9.8 x 9.8 in.) (see Figure 3.1). Although the powder is dispensed differently in each of the printers, the spreading of powder and binder deposition are the same in both printers.



Figure 3.1. Images of the Ex One binder printers X1-Lab (left) and the M-Flex (right).

3.1.1 Powder Feeding Systems

Regarding the X1-Lab printer, the powder is dispensed from a feeding box which must be filled before printing. During the printing process, the feed box raises and a roller spreads the powder across the build box where the part is being printed (see Figure 3.2a). Alternatively, the M-Flex has a hopper system that can be continuously filled while the print is running. The hopper drops powder onto the build box and is spread with a roller system. The hopper controls the flow of the powder as its being laid on the bed with a “snaking” channel system in which the width of the channels can be changed with different particle shapes and sizes. In both machines, after a layer is printed the build volume lowers and another layer of powder is spread on top and the process repeats again.

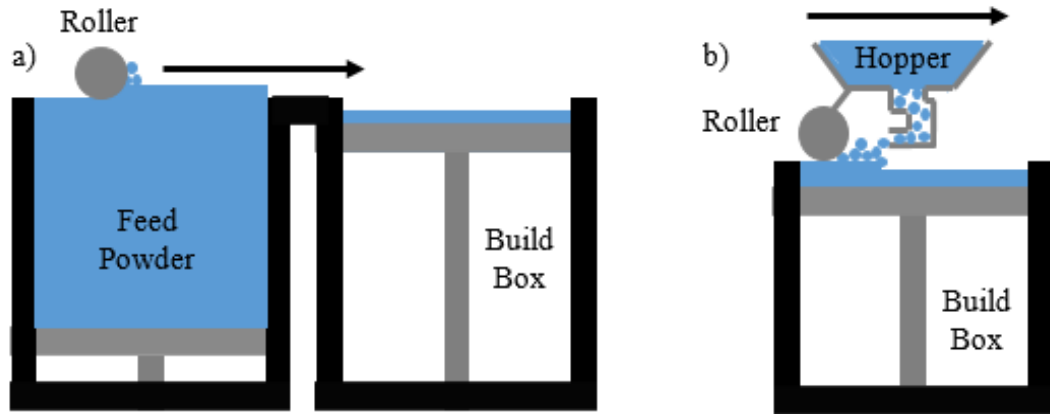


Figure 3.2. Schematic feeding systems of the X1-Lab (a) and the M-Flex (b) printers. The X1-Lab uses a feed powder system, while the M-Flex uses a hopper system.

3.1.2 Printhead Systems

The binder agent in the 3D printers can be dispensed out of the printhead in two methods: continuous stream (CS) or drop-on-demand (DOD). The CS method delivers a constant stream of binder which is then broken up into droplets due to a Rayleigh instability. The droplet formation can be regulated by applying a vibration to the printhead as it dispenses the binder (see Figure 3.3a) [2]. The biggest advantage of the CS binder deposition is its high binder dispensing rates. In contrast, the DOD deposition methods directly creates the droplets in the nozzle. Typically the printhead works by taking advantage of the piezoelectric effect for the droplet formation (see Figure 3.3b) [2].

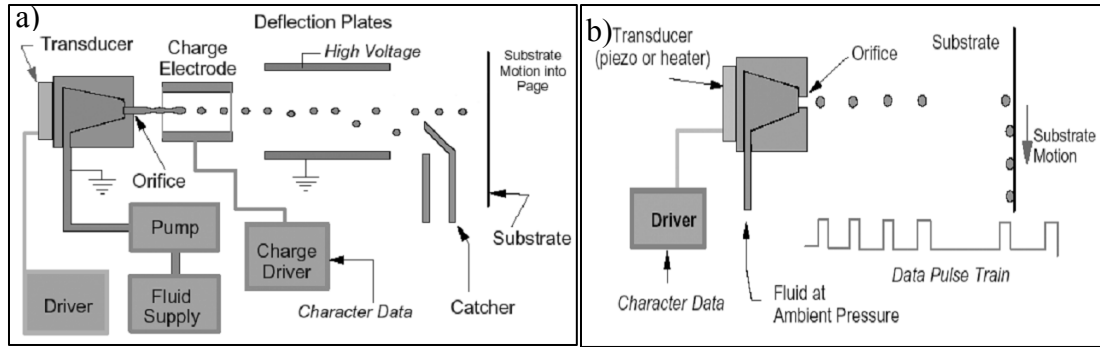


Figure 3.3. The schematics of the continuous stream (left) and droplet on demand (right) deposition method for binder jetting [2].

Here, the droplet forms by applying a current to the piezoelectric ceramic, which makes the ceramic bend, resulting in the ejection of a droplet of binder (see Figure 3.4). The droplet formation can be performed by using a simple positive square wave or can be as complex as using a positive-negative wave that varies in amplitude and duration [3]. The X1-Lab used in the current research work has a DOD deposition printhead while the M-Flex has a CS deposition printhead. Also, the binder used here is a water-based glycol binder that is proprietary to Ex One.

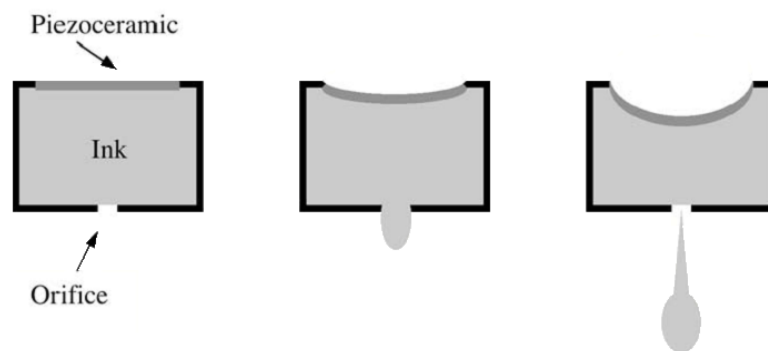


Figure 3.4. Schematic of a piezoelectric nozzle used in a droplet on demand binder printing [2]. The piezoelectric ceramic bends to eject the droplet of binder onto the material.

3.1.3 CAD File

The model drawing files (.stl) that were used in this research project were created using the SolidWorks CAD software. Simple shapes of a cylinder, cube, rectangle, and plate were printed for various tests (see Figure 3.5).

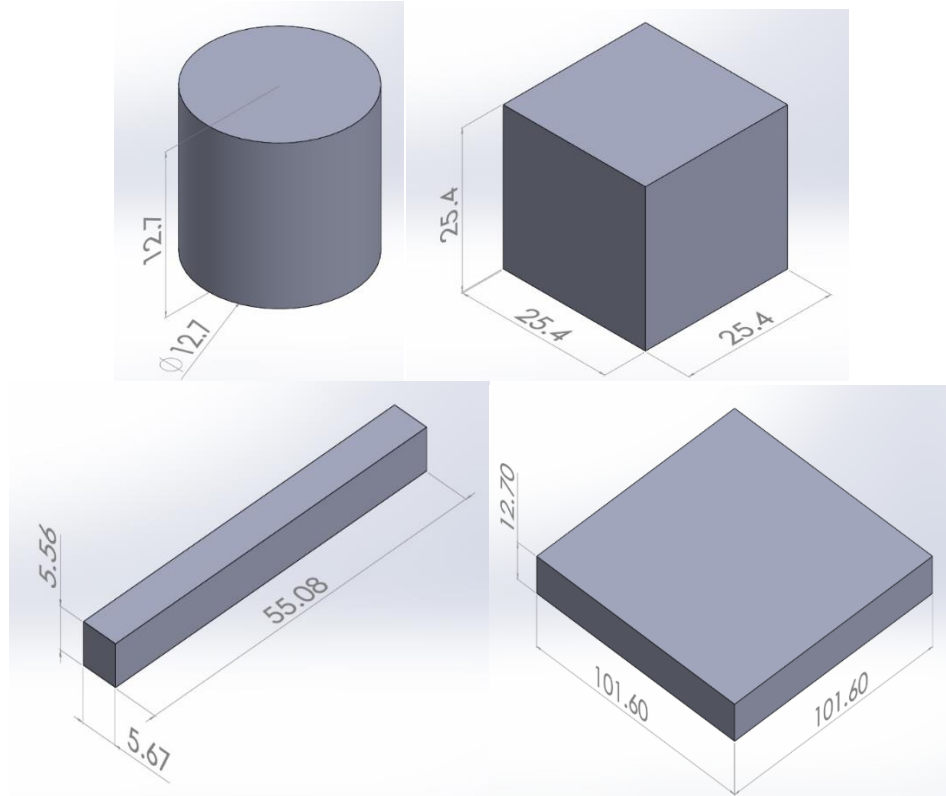


Figure 3.5. Actual CAD drawing of the geometries used in this research work: a) cylinder, b) cube, c) rectangle, and d) plate. Dimensions are given in millimeters.

3.1.4 Curing and Sintering

After the part is printed, the specimens are placed into a curing oven to thermally set the binder. The excess powder is left next to the printed part for stability during this

step. In this work, the samples were cured between 180-190°C for 2-8 hours depending on the thickness of the specimen. Subsequently, the parts were removed from the oven and the excess powder was brushed away with a paint brush to retrieve the cured part. At this point, the particles were only bonded together by the cured thermoset plastic binder. To achieve a dense part, the samples were post processed by a sintering cycle. During this stage, the binder was burned off to leave a consolidated specimen. At temperatures over 650°C the water-based binder was completely removed with minimal carbon residue. A support material, non-reactive alumina for example, can be added around the part to minimize drooping and warping of the sintered part. The silica parts that were printed in this research work were sintered at temperatures between 1200-1500°C and held in this range for 4 hours. The sintering process was performed in an open atmosphere in a Thermolyne 46200 high temperature furnace.

3.2 Reactive Metal Penetration of Printed Silica Parts

The infiltration of the silica composites was carried out by a reactive metal penetration technique. The sintered silica parts were immersed under an excess amount of molten aluminum or aluminum alloys and held approximately 16 hours at 1200°C. The aluminum used was a 99.7% grade (P1020) ingot. The molten metal was held in high temperature crucibles (alumina based) that were manufactured by Fireline Inc. (Youngstown, OH). A separate crucible was used as a sample holder for the sintered silica part. The sample holder had large enough openings to allow liquid metal to enter, but small enough to prevent the samples from floating out. The reaction was performed in a 27.94 x 40.64 cm (diameter x height) induction kiln manufactured by LL Kilns (see Figure 3.6). During the whole transformation time, the molten metal is under a constant

flow of argon to prevent oxidation of the metal. After the desired transformation time, the composite parts are removed and allowed to cool to room temperature. Some of the intricate parts were cleaned using compressed air to blow away any excess of undesired molten skin on the outside section of the transformed parts.

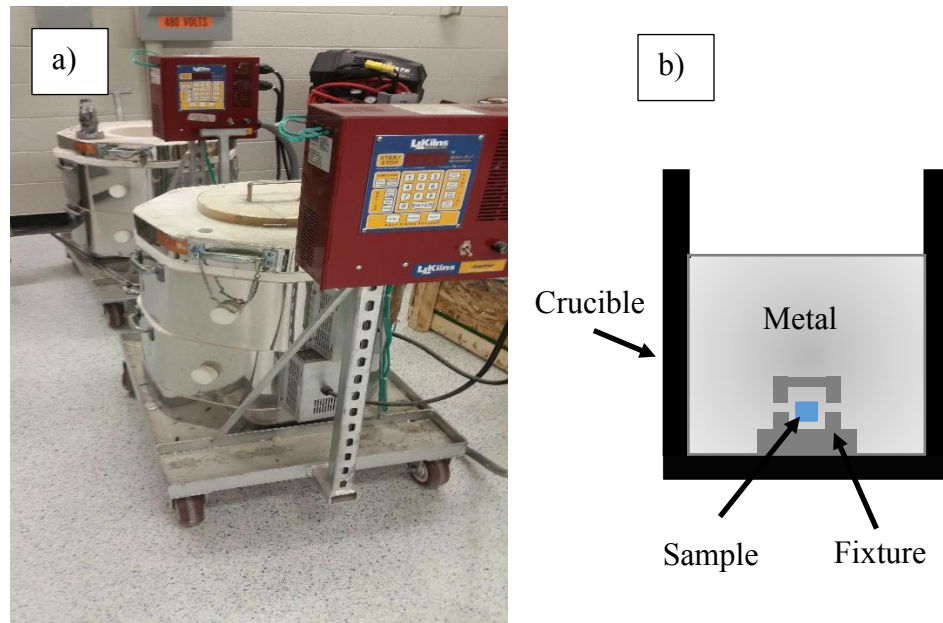


Figure 3.6. Image of the induction kilns used for the transformation process (a) and a schematic of the crucibles, metal, fixtures, and samples during the transformation process (b).

3.3 Optical and Analytical Characterization of the Printed Ceramic and Composite Materials

The microstructure, crystal structure, and chemical composition of all the cured, sintered, and transformed samples were characterized using an optical and electron microscope, as well as an X-Ray diffractometer.

3.3.1 Grinding and Polishing

All specimens intended for microscopy were subjected to a grinding and polishing process to achieve a representative image of the microstructure. Initially, grinding was performed on a rotating wheel with a magnetically attached diamond embedded grinding disk while using water as the lubricant and coolant agent. Preliminary grinding is carried out using a 120 grit pad and then continued with a 600 and 1200 grit pads. Each individual grinding pad was used for approximately 2 minutes. Mechanical polishing is then performed using a diamond suspension on a cloth until a finish of 1 micron is achieved. All samples were cleaned with soap and water between each step to prevent cross contamination. The whole grinding and polishing procedure is summarized in Table 3.1.

Table 3.1. Procedure of the grinding and polishing steps used in the studied materials for the optical and electron beam microscopy analysis.

Step	Disk Type	Suspension	Lubrication
Grinding 1	Struers Diamond Piano 120 grit	None	Water
Grinding 2	Struers Diamond Piano 600 grit	None	Water
Grinding 3	Struers Diamond Piano 1200 grit	None	Water
Polish 1	Struers MD-Plan Cloth	Struers 6 μm diamond DP Paste	Struers DP-Lubricant Blue
Polish 2	Struers MD-Dac Cloth	Struers 3 μm diamond DP Paste	Struers DP-Lubricant Blue
Polish 3	Struers MD-Nap Cloth	Struers 1 μm diamond DP Paste	Struers DP-Lubricant Blue

3.3.2 Optical Microscopy

All the polished samples were initially investigated by optical microscopy. The microscope used to investigate the microstructure of the specimens was a ZEISS Axiophot compound light microscope assisted with a PixeLink® CCD camera to acquire digital images. All photos taken in this research work were brightfield images, meaning that the reflected light used to make the images was not altered. The optical microscopy was performed to initially evaluate the binding of the printed specimens in the cured state. Additionally, the sintered specimens were investigated to evaluate the degree of bonding between the individual particles. The composite specimens were investigated with the purpose of determining if the precursor had transformed through recognition of the presence of multiple phases, as well as to characterize the homogeneity of a composite. Even though no chemical or crystallographic information can be determined by optical microscopy, it is an important step in the analysis of a sample to identify phases or characteristics of the material for further analysis.

3.3.3 X-ray Diffraction (XRD)

Following the initial characterization of the specimens via optical microscopy, selected samples were analyzed using powder X-ray diffraction (PXRD) for phase identification. Powder XRD patterns were collected using the Bruker D8 Advance diffractometer, which uses Cu-K_α radiation for pattern collection (see Figure 3.7). The Bruker D8 diffractometer uses sample cups of sufficient depth to accommodate samples that have a height around 5 mm after cutting and polishing. Each sample was mounted in

an open sample cup using paraffin wax. Diffraction patterns were collected at room temperature in reflective mode with the Bragg-Brentano geometry. Each sample was set to run for 5 hours spanning a range of $10\text{-}90^\circ$ in 2θ . Each sample is set to spin for the entire duration of the measurement to optimize the X-ray interaction with all possible crystal orientations, and to partially average effects from preferred orientation of crystallites in the samples.



Figure 3.7. Image of the Bruker D8 diffractometer used in this research work.

The Bragg-Brentano arrangement is the typical arrangement for PXRD. This arrangement is unique for symmetry of the angles of the incident and reflected X-rays (see Figure 3.8). This is achieved by aligning the slits of the X-ray source and the X-ray detector at the same angle of the sample [4]. As the sample moves through the 2θ scale, either the source or the detector will move to match the angle.

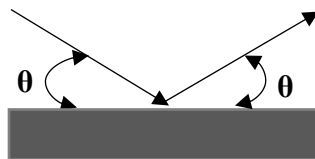


Figure 3.8. Schematic of the Bragg-Brentano (symmetric) geometry used in PXRD,

where the angles, θ , of the incident and reflected X-rays are equal.

X-ray beams are created by the X-ray tube and then are diffracted by a bent monochromator crystal creating a focused beam of monochromatic X-rays. The monochromator focuses the Cu-K_α radiation to pass through a slit to cut off the outer parts of the focusing beam. The X-ray beam then reaches the sample and diffraction takes place. Diffraction can be easily explained by looking at the first few layers of the crystal system. The incident X-rays are diffracted through constructive and destructive interference following interaction with the electrons in the crystal lattice. Diffracted X-rays will leave the sample at different angles. The X-rays that are detected are those that are being scattered by their interaction with atoms located at O, P, and R points (see Figure 3.9).

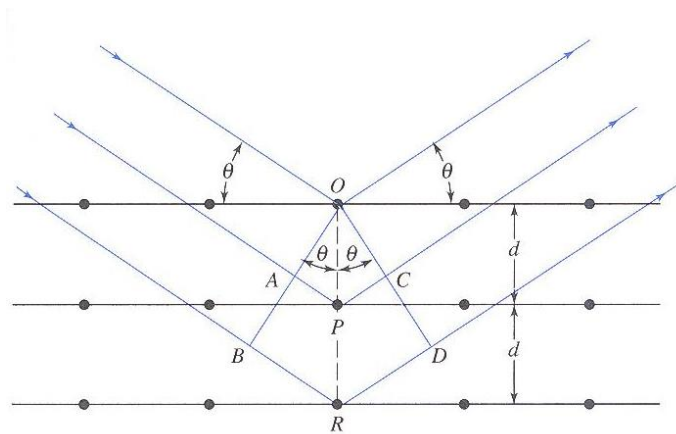


Figure 3.9. The diffraction of X-rays of a single crystal showing Bragg's law [5].

Bragg's law of diffraction can be initially derived by the following equations:

$$AP + PC = n\lambda \quad (3.1)$$

Where n is an integer, and λ is the wavelength of the monochromatic X-ray. The scattered X-rays will all be in phase along the line OCD (see Figure 3.9). Additionally, the

scattered X-rays are in relation to the angle of the incidence-diffraction theory by the following equation:

$$AP = PC = d \sin \theta \quad (3.2)$$

Where d is the interplanar distance of the crystal. Therefore, the conditions for X-rays that have constructive interference are:

$$n\lambda = 2d \sin \theta \quad (3.3)$$

where Equation 3.3 is the Bragg's law equation [5]. Here, the detector will only receive the X-rays that are reflected by the d -spacing that is associated with a specific angle. A diffraction pattern is then plotted as the intensity of the signal versus 2θ .

The resulting PXRD patterns are analyzed using the software of Diffract.EVA version 3.1 software (Bruker AXS, Madison, WI). The patterns are compared to over 700,000 compounds in the database published by the International Center for Diffraction Data (ICDD) using their PDF-2 2015 and PDF-4+ 2015 databases. Indeed, every crystalline material has a unique diffraction pattern due to its specific combination of crystal lattice, unit cell parameters, and structure. Therefore, the XRD analysis allows for the identification of all the phases present in each specimen investigated.

3.3.4 Scanning Electron Microscopy (SEM)

Any sample that was analyzed via SEM was performed using a JEOL JIB 4500 multibeam system and a JEOL JSM-IT 300 variable pressure microscope (see Figure 3.10). Here, the specimens were held in place by using a sample holder and a two-sided non-conductive carbon tape. Conductive copper tape was used to bridge the holder and

sample to improve the conductivity of the sample. The sample holder was inserted into the microscope through a vacuum lock into the sample chamber, and both secondary and backscattered electron micrographs, as well as point EDS and EDX mapping, were acquired for detailed analysis.

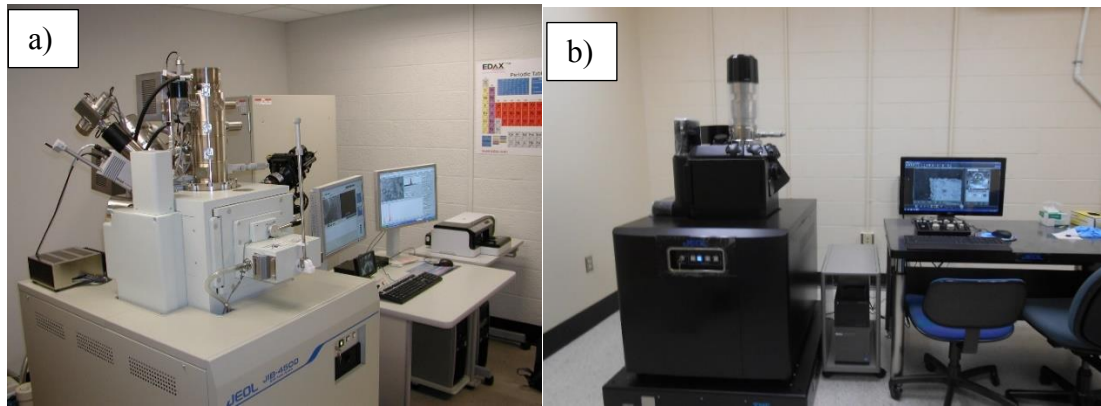


Figure 3.10. Image of the JEOL JIB 4500 multibeam system (a) and the JEOL JSM-IT 300 (b) scanning electron microscopes used in this research work.

The electrons for imaging and analysis in the SEM are created by means of an electron gun, and are focused by an electromagnetic field. The electron source is a filament that is typically made of tungsten (W) or lanthanum boride (LaB_6). The electrons are pulled off of the filament and accelerated to an energy between 1 and 30 keV [5]. The electron beam is focused with a series of magnetic condenser lenses (CL) and objective lenses (OL) (see Figure 3.11) [6]. The lens system will reduce the spot size of the beam to a diameter of 2-10 nm as it reaches the sample. The beam is able to scan the sample by using the scan coils. The scan coils can deflect the beam in the x and y direction by an electrical signal. The electrical signal varies the beam deflection as a function of time, allowing for different scanning speeds [5].

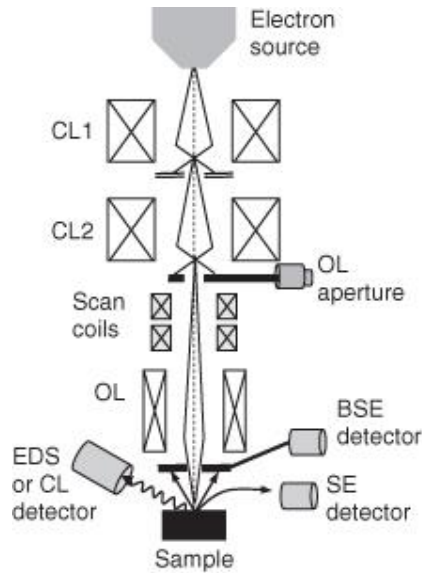


Figure 3.11. Schematic of an electron beam column in a scanning electron microscope. The beam is focused by condenser and objective lenses, which is then rastered by the scanning coils. The electrons interact with the sample creating secondary electrons, backscattered electrons and X-rays, which are subsequently detected to create a detailed image of the analyzed sample [6].

The image is generated in response to the scattering interaction at the sample surface. As the electron beam interacts with the sample, the electrons can either be scattered in an inelastic or elastic manner (see Figure 3.12). The inelastically scattered electrons are the secondary electrons (SE) which can be detected and used for imaging. They are called secondary electrons because they are not from the original electron beam, but from the sample itself. Backscattered electrons (BSE) originate from elastic collisions as electrons from the beam interact with nuclei of atoms in the sample, and are elastically scattered back towards the detector. This technique is useful because the electron that scatters by an element, is proportional to the atom's atomic weight. In other words, the higher the atomic weight the brighter the backscatter image is. In the case of a non-

elemental compound, the backscattering effect is averaged amongst all of the elements present in one area [5]. Thus, in an alumina/aluminum composite, the backscattered image would result in Al_2O_3 grains appearing darker than Al. The detectors in the SEM can also take advantage of cathodoluminescence, auger electrons, and characteristic X-rays that are emitted by the sample. The signals utilized in this research work are the secondary and backscattered electrons for imaging, and characteristic X-rays for energy dispersive spectroscopy (EDS).

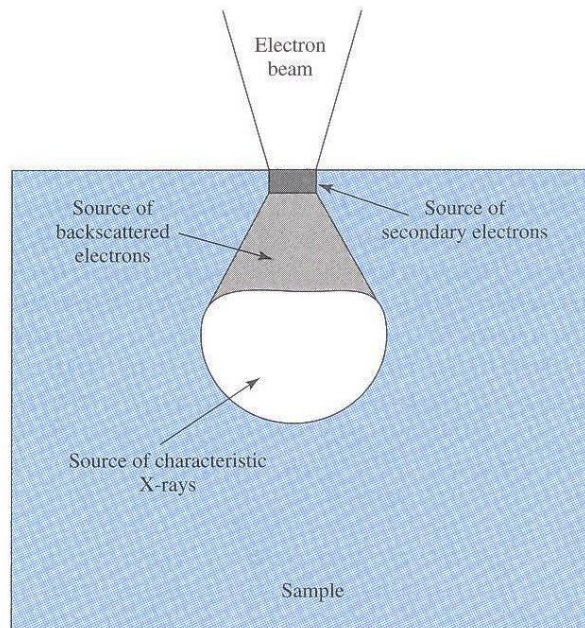


Figure 3.12. A representation of the interaction of an electron beam with a sample, depicting the areas of which the secondary electrons, backscattered electrons and characteristic X-rays are created [5].

The images captured by the SEM analysis can have a magnification range between $\times 10$ and $\times 300,000$. It should be noted that the low energy secondary electrons originate from the top layer, are the electron source commonly used for SEM imaging. In contrast, the

higher energy electrons are detected from greater depths, and a larger fraction of them are therefore absorbed by the material. Thus, the signal from the high-energy backscattered electrons needs to be enhanced, which lowers the resolution of the produced images [7].

3.3.5 Energy Dispersive Spectroscopy (EDS)

In this research work the EDS analysis was used for measuring the chemical compositions and the distributions of compounds within the studied composites. An EDAX™ Apollo SDD EDS detector was used in the JEOL JIB-4500 multi beam system for the analysis.

As mentioned in the SEM section, characteristic X-rays are emitted by bombarding the sample with electrons. The Auger electron is another type of source that can also be obtained from the interaction of an electron beam and a sample. The electron beam can knock out inner K-shell electrons (Auger electrons) from atoms near the surface of the material. This leaves the atom in an excited state which leads to a relaxation of outer shell electrons from the L-shell (or other higher energy shells) to fill the lower vacancy. As a result, the energy given off from the electron relaxation comes out in the form of characteristic X-rays [6]. A schematic of this phenomenon is shown in Figure 3.13.

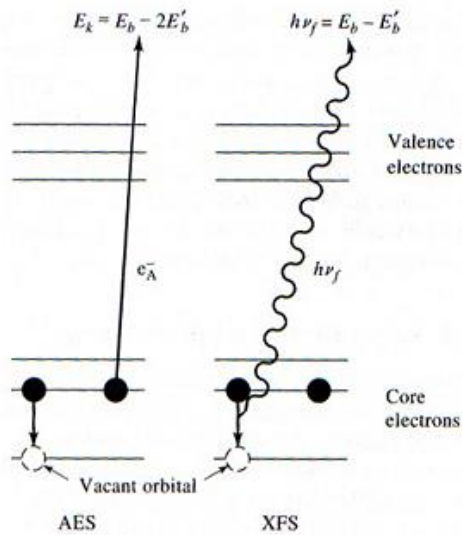


Figure 3.13. A representation of the source of Auger electron emission (left) and X-ray fluorescence (right) that takes place during electron microscopy [7].

The wavelengths of the x-rays given off and the ratios of the different x-rays are characteristic for each element, which are then used to accurately identify elements. This identification enables the EDS to create an elemental map of the investigated sample. The elemental map shows a distribution of elements for a specific area by identifying the unique elemental x-rays.

3.4 Mechanical Testing

The samples manufactured in the cured, sintered, and transformed state were all characterized by mechanical testing. The mechanics and desired properties of each test are described as follows.

3.4.1 Compression Testing (Quasi-Static Loading Rate)

Cylindrical samples of 12.7 x 12.7 mm and 12.7 x 6.35 mm (diameter x height) were subjected to a quasi-static compression testing using an universal Instron machine, which collects data in the form of displacement and force. Here, the specimens were tested based on the ASTM C1424, where the cylindrical specimen was placed between two flat platforms and the compression test was performed at displacement rates of either 0.1 or 0.5 mm/min (see Figure 3.14).

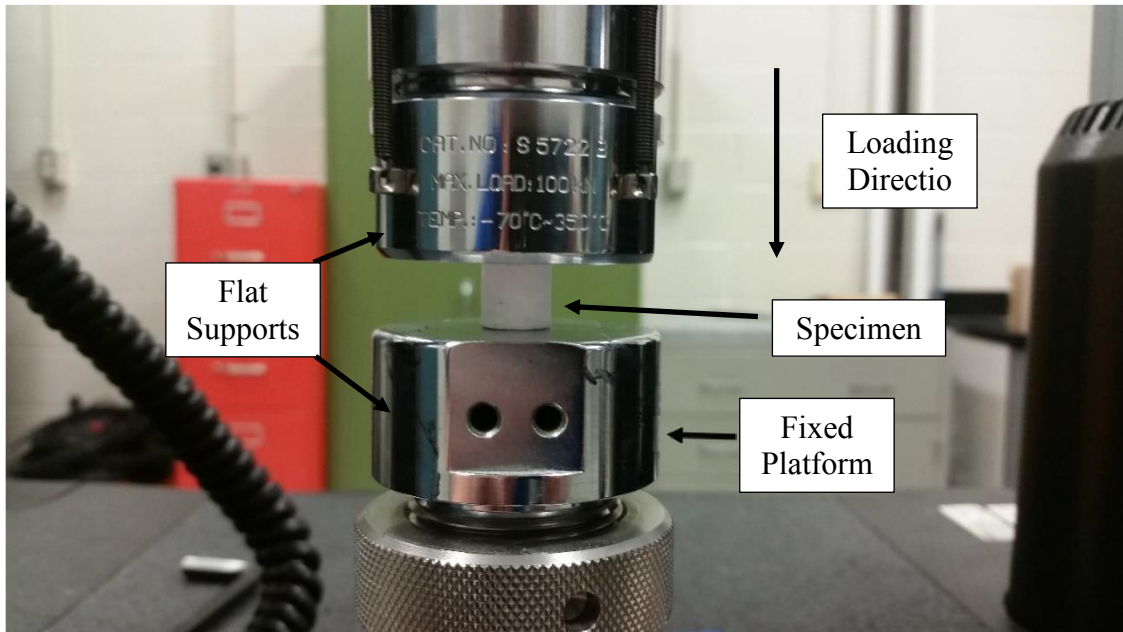


Figure 3.14. Image of the universal Instron machine used for compression testing. Two flat platforms were used to compress the sample.

The load-displacement output data was recorded by a Bluehill 3 software (developed by Instron). Here, the force data was converted into a stress (σ) using Equation 3.4.

$$\sigma = \frac{F}{A} \quad (3.4)$$

Where F is the force recorded by the load cell, and A is the original cross sectional area of the sample before compression. From the test, a maximum compression stress is found by taking the largest stress value before failure occurs.

The Young's modulus of the composite specimen was found via the compression testing of a 25.4 x 25.4 x 25.4 mm specimen by taking the slope of the stress-strain relationship in the elastic region using the following equation:

$$E = \frac{\sigma}{\varepsilon} \quad (3.5)$$

Where E is the Young's modulus, σ is the stress, and ε is the strain. The strain (ε) can be calculated by the ratio of the change in length of a sample (Δl) and its original length (l_0):

$$\varepsilon = \frac{\Delta l}{l_0} \quad (3.6)$$

The strain measured in this work was recorded using OMEGA strain gauges glued to each side of the sample, with a parallel orientation to the direction of the compression test. Each gauge was integrated as a quarter-bridge type I (see Figure 3.15), and was connected to a Micro-Measurements P3 strain indicator.

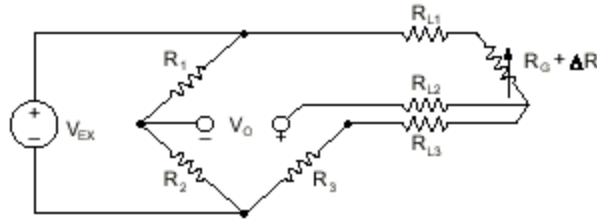


Figure 3.15. Schematic of the circuit of the three wire quarter bridge used for the quasi-static compression testing. Here, R_1 , and R_2 are the half-bridge completion resistors, R_3 is the quarter-bridge completion resistor, R_{L1-3} are lead resistors, and $R_G + \Delta R$ is the variable resistance data provided by the strain gauge.

3.4.2 Flexural Testing (Quasi-Static Loading Rate)

A three-point bending flexural testing was also completed using a universal Instron machine. The flexural tests were performed based on the ASTM C1161-13 standard (see Figure 3.16). Here, rectangular shapes with the dimensions of 5.67 x 5.556 x 55.08 mm (height x width x length) were manufactured for testing. The flexural test was carried out at either 0.1 or 0.5 mm/min in order to ensure quasi-static loading rates.

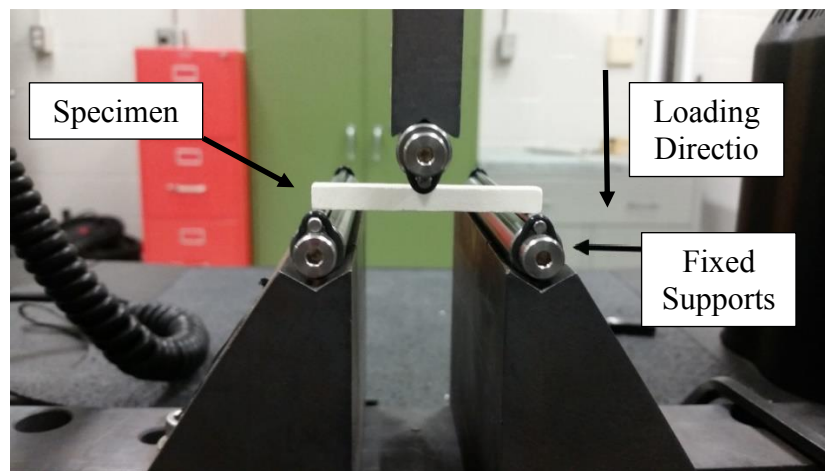


Figure 3.16. Image of the universal Instron machine used for the three point bending flexural testing.

Similar to the compression testing, a Bluehill 3 software was used to collect the data. The data outputs of force and displacement were used in this test. In this testing, the force was converted to a stress value using the following relationship:

$$\sigma = \frac{3FL}{2bd^2} \quad (3.7)$$

Where F is the force, L is the length of the support span, b is the width of the sample, and d is the thickness of the sample. A maximum flexural stress was found by taking the largest stress value before failure occurred.

3.4.3 High Strain Rate Compression Testing

The high strain rate testing is commonly used to display a materials response under dynamic conditions (i.e. explosion, ballistic, and vehicle impacts). In this research work a Split Hopkinson Pressure Bar (SHPB), originally known as a Kolsky bar was used. The testing was accomplished by placing the samples in between two bars, and using a striker to create an incident pulse through the system. The rectangular pulse wave travels through the incident bar and then interacts with the sample. The pulse is sent through the sample as well as to the transmission bar, which also reflects the pulse back through the incident bar (see Figure 3.17).

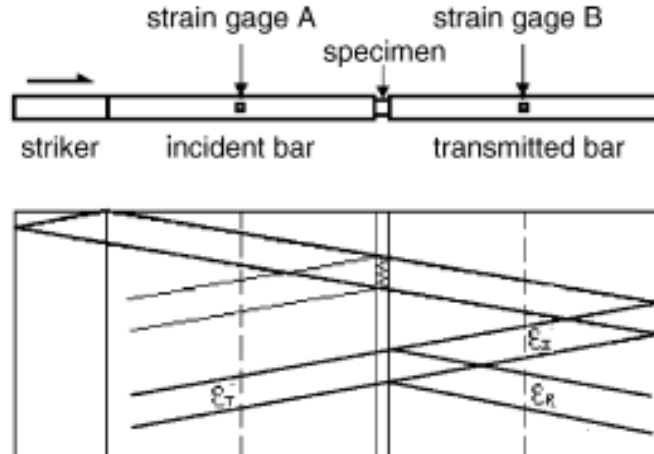


Figure 3.17. A schematic representation of the split Hopkinson pressure bar (top) and the wave propagation through the system (bottom) [8].

The incident and transmission bars both had strain gauges attached to them at equal distances away from the sample. The strain gauges record the wave propagation, and the stress and strain of the tested sample can be determined by the following relationships [9]:

$$\sigma_{sample} = E \left(\frac{A}{A_s} \right) \epsilon_T \quad (3.8)$$

$$\epsilon_{sample} = \frac{-2C_0}{L} \int_0^t \epsilon_R dt \quad (3.9)$$

Where E , A , and C_0 are the elastic modulus, the cross-sectional area, and the longitudinal wave speed of the incident and transmission bars respectively. The variables of L , A_s , ϵ_T , and ϵ_R are the length and cross-sectional area of the sample, and the strain of the transmitted and reflected strains respectively.

The SHPB used in this work was purchased from REL Inc. (Calumet, MI). The data was collected and analyzed by REL's proprietary SurePulse software. Both the incident and the transmission bars were made of a C-350 maraging steel with a Young's modulus of 195 GPa. The length and diameter of the bars were 1.8 m and 19.05 mm, respectively. A 76.2 mm long striker bar was projected at the incident bar using a pressure chamber filled with compressed air. The generated pulse signals were acquired through a signal conditioning amplifier and subsequently collected by a PicoScope oscilloscope. The maximum stress value was taken from the highest recorded stress value of the stress-strain curve for each sample, and the compression modulus was determined by the slope of the first 1000 data points recorded. The samples used in the SHPB analysis had the same dimensions of the cylinders used in the quasi-static compression tests.

References

1. Dinger, D. R. (2001). *Particle Calculations for Ceramists*. Kearny, NE: Morris Publishing.
2. Margolin, L. (2006). *Ultrasonic droplet generation jetting technology for additive manufacturing: an initial investigation*. (Masters Thesis, Georgia Institute of Technology).
3. Basaran, O. A. (2002). Small-scale free surface flows with breakup: Drop formation and emerging applications. *American Institute of Chemical Engineers Journal*, 48(9), 1842-1848.

4. Hammond, C. (2009). *The Basics of Crystallography and Diffraction* (3rd ed.). Oxford, UK: Oxford University Press.
5. Skoog, D. A., Holler, F. J., & Crouch, S. R. (2007). *Principles of Instrumentation* (6th ed.). Belmont, CA: Thomson Brooks/Cole.
6. Bell, D. C., & Erdman, N. (2013). *Low Voltage Electron Microscopy: Principles and Applications*. West Sussex, UK: John Wiley & Sons.
7. Skoog, D. A., Holler, F. J., & Nieman, T. A. (1998). *Principles of Instrumentation Analysis* (5th ed.). Philadelphia, PA: Saunders College Publishing.
8. Lee, O. S., & Kim, M. S. (2003). Dynamic material property characterization by using split Hopkinson pressure bar (SHPB) technique. *Nuclear Engineering and Design*, 226(2), 119-125.
9. Lee, O. S., & Kim, G. H. (2000). Thickness effects on mechanical behavior of a composite material (1001P) and polycarbonate in split Hopkinson pressure bar technique. *Journal of Materials Science Letters*, 19(20), 1805-1808.

Chapter 4 Mechanical Property Simulation

The considerable increase in computational hardware and software has provided the ability to simulate the mechanical response of composite materials in order to accurately predict their performance. Certainly, this task can be challenging due to the random microstructures of multiple, three dimensional phases present in composite systems. In this research work, a homogenization technique was used to predict the elastic modulus of a two-phase ceramic-metallic composite system that was manufactured via the binder jet printing of SiO₂, with subsequent infiltration of molten aluminum. Before a detailed description of the homogenization technique used in this research work, a brief background of simulation techniques for composites is initially provided.

4.1 Mechanical Property Simulation Techniques for Composites

One of the original and easiest techniques to evaluate the mechanical properties of composite materials is the rule of mixtures [1]. The rule of mixtures is essentially the arithmetic average of a property of interest, and the contribution of each phase on the property. Hence, the upper bound for the Young's modulus of a two-phase composite is calculated by:

$$E_c = E_a X_a + E_b X_b \quad (4.1)$$

where E_a , E_b , and E_c are the elastic modulus of the phase a, phase b, and the composite respectively, and X_a and X_b are the volume fraction of each individual phase. While the lower bound is the harmonic average, given by:

$$E_c = \frac{E_a E_b}{E_a X_a + E_b X_b} \quad (4.2)$$

This technique can be used for linear relationships such as transversal modulus as well as non-linear relationships such as strength [2]. These bounds typically over and under estimate the properties of a material. The most well-known bounds on describing the elastic modulus of a composite system are those created by Hashin and Shtrikman [3]. These bounds are based on variation principles of linear elasticity and are formulated from a “polarization tensor”. Here, the bounds apply to any phase-geometry where the composite is considered to be homogeneous and isotropic when the specimen’s dimensions are much larger than the microstructural features. The bounds described by Hashin and Shtrikman [3] are the most accurate without incorporating microstructural information in the calculations.

An additional self-consistent model has been created to show the mechanical effects of inclusions in a composite matrix. A simple version of this model was created to model fiber matrix composites [4]. The theory of this model works by embedding a spherical or elliptical inclusion that has a known effective property (see Figure 4.1). Riley and Whitney use a hollow fiber embedded in a spherical matrix. The volume fraction of the fiber and matrix is chosen to represent the volume fraction of the overall composite system, although this assumption can lead to unreliable values because the matrix material may not coat the entire fiber, creating voids [4]. The self-consistent model

depends on accurately describing the phase distribution, the gradient of inclusion, and the shape of inclusion to achieve accurate results [5]. It has been found that the self-consistent model is not accurate for moderate and large phase contrast materials [6].

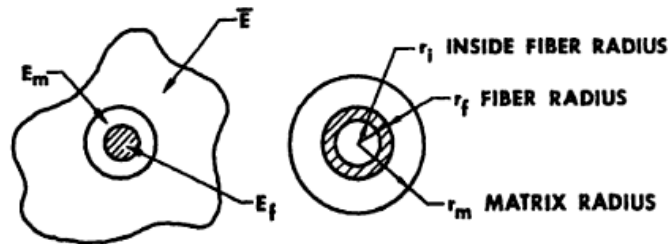


Figure 4.1. Schematic of a microstructure used for a basic self-consistent model described by Riley and Whitney, where E_m and E_f represent the elastic modulus of the matrix and fiber, respectively [7].

Improved theories have been developed that include a probability function $S_n(x^n)$, where S_n is the probability of finding n -points at positions $x_n \equiv x_1, \dots, x_n$ in one of the phases present in the sample [1]. Through this approach, three and four point bounds have been used to compute the elastic modulus of various composites [8]. Although the use of higher order points offers a benefit in the accuracy, they can be problematic for specific materials. For example, a three or four point bound can result in the simulated modulus diverging to infinity if one phase has a much larger modulus than the other [1]. In fact, only lower order probability functions are available in practice, which leads to the creation of bounds and not an exact solution [9].

On the other hand, unit cell methods have also been investigated to more accurately describe the microstructure of a randomly oriented or interpenetrating microstructures. The creation of unit cells is mostly tied with the finite element method (FEM). Here, a 3D unit cell is created to represent the microstructure of a two phase or multiphase composite, which is subsequently used in the FEM. For instance, Wegner and Gibson [9-10] created a unit cell by arranging intersecting and uniform spheres in a hexagonal closed packed structure, where the spheres and interstitial space represented the stainless steel/bronze composite (see Figure 4.2). The hexagonal closed packed unit was selected due to the nature of the microstructure obtained from the 3D printing of spherical stainless steel particles. The FE model was found to be well suited by exhibiting data which correlated to the experimental results.

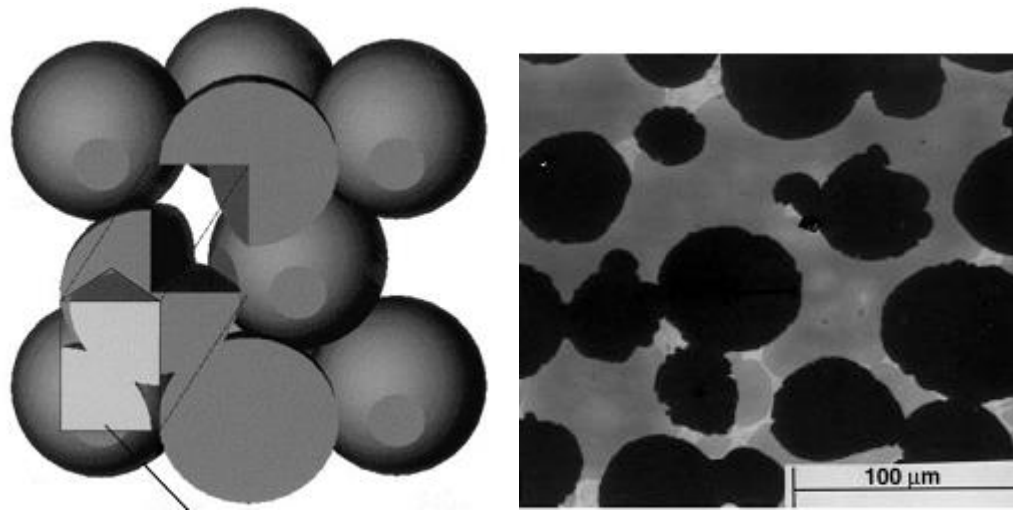


Figure 4.2. The unit cell representation (left) of a 3D printed stainless steel/bronze composite which was used to characterize the actual microstructure (right) [9-10].

Feng *et al.* [11] also used a unit cell method to model a multiphase composite where some phases were continuous and some were isolated as particles throughout the system

(see Figure 4.3). The unit cell, alongside the Mori-Tanaka method [12], proved to accurately model a $B_4C/Al/AlB_2/Al_4BC$ composite, where B_4C and Al were the continuous phases and AlB_2 and Al_4BC the isolated particles.

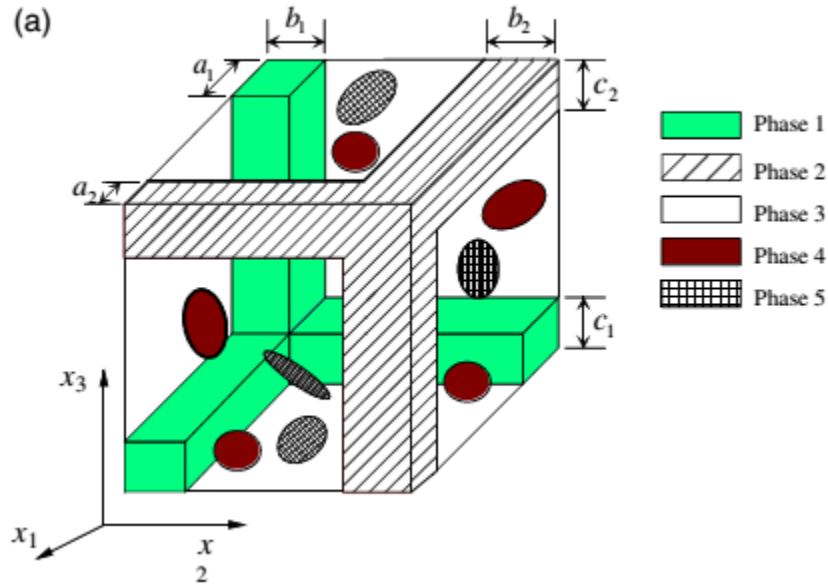


Figure 4.3. Unit cell representation created by Feng *et al.* [11] to describe a multiphase composite. In this representation phases 1-3 are continuous and 4-5 are isolated particles.

Poniznik *et al.* [13] created a voxel unit cell system to describe a microstructure. Here, a known phase distribution was randomly generated in a 3D unit cell consisting of a smaller cubes (voxels) to match the desired phase distribution (see Figure 4.4). The size of the smaller cubes was determined by prescribing a number of voxels to be on the edge of the unit cell. Indeed, the more voxels required on the edge of the unit cell the more accurate the simulation results (although an increase in the computing time is required). Poniznik *et al.* also decided that 10 voxels/edge were sufficient to have a small enough deviation in the outputted elastic modulus. The results from this method were compared

to FEM simulations of the actual composite, which was X-ray CT-scanned (see Figure 4.4), showing that this method was accurate in describing a composite's effective elastic properties. The authors also claimed that random voxel method should be more accurate than the method described by Feng *et al.* [11] since it has a better resolution on a random microstructure.

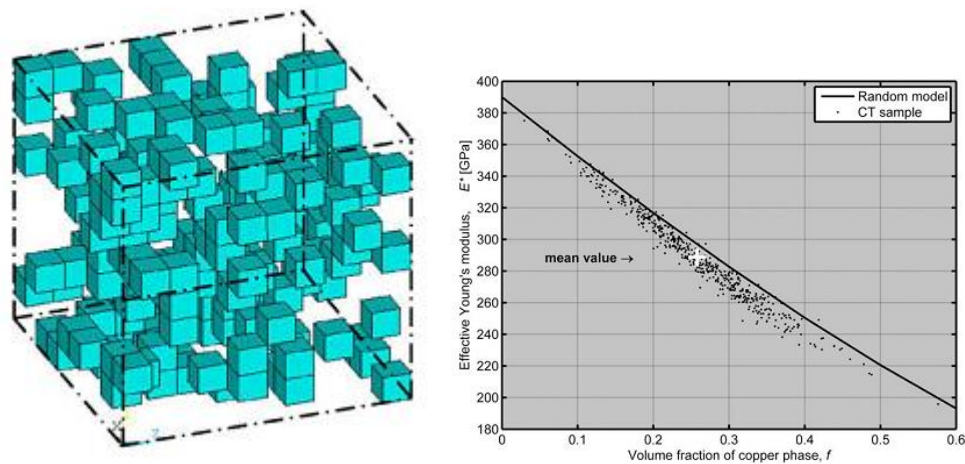


Figure 4.4. Randomized voxel unit cell representing a two-phase composite, set to 10 voxels/edge (left), and its comparison to a CT-scanned FEM analysis (right) [13].

Certainly, there are many different techniques that have been used to simulate the elastic modulus of materials as variations of the methods previously mentioned. Typically, these techniques are created to work for unique materials with specific microstructures. Although these methods may be accurate, they can be computationally expensive and may not work for every single composite. Recently, there has been a driving effort in the simulation field to create unique ways to model composite materials accurately and quickly, to a variety of different microstructures. Agarwal *et al.* [14] created a method that uses a 2D unit cell technique with an elemental free Galerkin method (EFGM) in

MATLAB, for simulating the mechanical properties of a metal-ceramic IPC. The authors consider the EFGM method to be more advantageous in finding numerical solutions than the FEM due to the random geometry of IPC materials, since it does not require conformal meshing. The testing was performed with different variances in metal interpenetration described as low, medium, and high (see Figure 4.5). It was found that this method accurately described the elastic modulus of the composite in approximately 15 minutes of computational time.

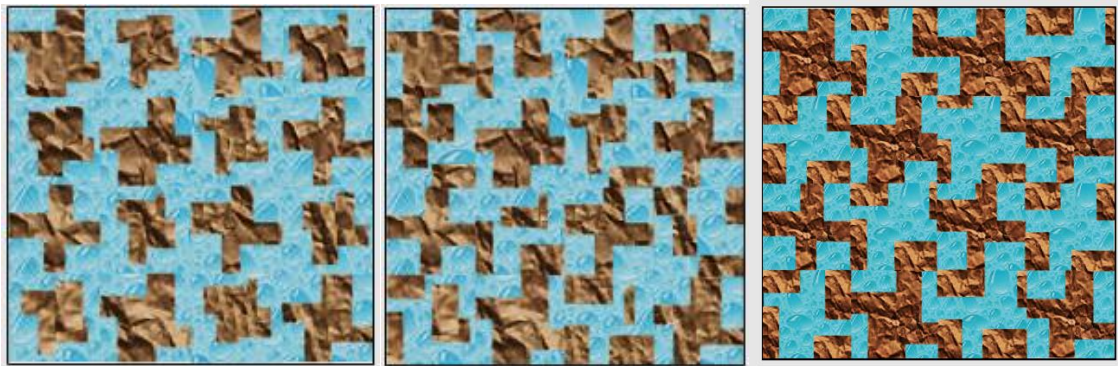


Figure 4.5. Unit cell representations of low, medium, and high degrees of interpenetration (left, center, right) in a metal-ceramic composite [14].

To apply a more accurate description of microstructures, researchers have used computer softwares to take 2D real-time micrographs and convert them into a computational gray scale for phase identification [15]. Here, the real microstructure can be converted into at FEM software for simulations. Wang *et al.* [16] used a computer software to distinguish the two different phases in an Al/SiC IPC. The authors were able to take the image and convert it into ANSYS for FEM analysis. The composite was simulated in the flexural testing mode and the crack initiation and propagation was compared to experimental results. The ANSYS model showed that the crack would initiate in the ceramic matrix

due to tensile forces (see Figure 4.6). These models were able to accurately describe the Al/SiC in flexural testing, and the fracture mechanism was confirmed by micrographs.

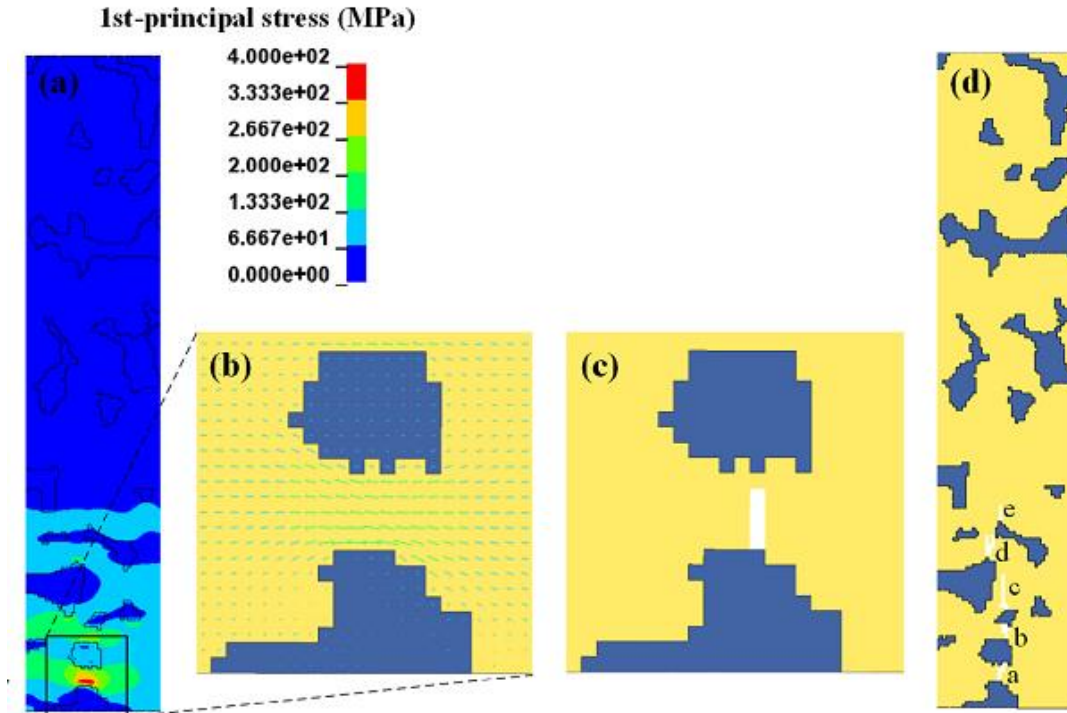


Figure 4.6. Calculated stress contours of a SiC/Al composite (a), stress vectors showing tensile behavior of ceramic phase (b), crack initiation in the SiC phase (c), and further crack propagation sights through the ceramic matrix (d) [16].

Andreassen and Andreasen [17] created a MATLAB code that uses a homogenization technique to find the elastic tensor of a two phase composite. A small and self-contained MATLAB code was implemented to lower the barrier of the daunting task of using numerical homogenization. The authors utilize MATLAB to find the elastic modulus of a two-phase system, with extensions for three phase materials, thermal

expansion, and thermal conductivity. For the bi-phase composite, the MATLAB code inputs a matrix (of 1's and 2's) to represent the microstructure. Here, a randomized 200x200 matrix was inputted in the homogenization code and the elastic tensor was obtained in a few seconds. Although the homogenization technique was shown to yield fast results, it was applied to a virtual microstructure. Therefore, in this present research work, the aforementioned homogenization code was expanded to accurately predict the elastic tensor of a manufactured Al/Al₂O₃ IPC.

4.2 Homogenization Technique

Composite materials such as solid foams, bone, and ceramic matrix composites (CMCs), consist of multiple, distinct phases. While each phase has its own individual physical and mechanical properties, the composite properties are formed by the sum, of all the phases in the heterogeneous material. Most heterogeneous materials exhibit a random arrangement of phases present throughout its continuum structure. The prediction of the mechanical properties of these materials can be performed through the micro-mechanics theory. This theory commonly makes use of a representative volume element (RVE), or a statistical volume element (SVE). The homogenization technique works when there is a clear separation between the macro and micro length scales. A RVE is the smallest volume of a structure which still represents the macroscopic properties of the structure, while a SVE is smallest volume of a structure that statistically represents the macroscopic properties of the structure [18-19]. The RVE and SVE are very similar in theory, where both intend to capture the macroscopic properties, but each technique differs by their mechanism. The present work defines the RVE as the smallest volume of a structure which contains the required information under a chosen numeric scheme to

represent the macroscopic properties of the structure. In heterogeneous materials, forming a RVE for all phases within the continuum is the process of homogenization. The main benefit of homogenization is that the physical and the mechanical properties can be analytically determined without need to test the material. This is especially important in composites materials, since statistically relevant testing of the numerous variables applicable to composites could be challenging, and time consuming.

Two prominent homogenization methods for the homogenization of a multiphase composites are the method of cells, or unit cell method, and Hashin spheres. Hashin and Shtrikman [3] used a variational approach and multilayer spheres, where the spheres form the RVE for the multiphase material. The unit cell method, depending on which definition is taken, is synonymous of the RVE approach, and in practice, the two concepts are interchangeable. Both of these methods discretize a material into a periodic repeating structure, but may be visualized using different shapes. The quality of the result of homogenization is directly tied to the quality of the RVE and how it represents the true microstructure. The unit cell approach of Andreassen and Andreassen [17] shows to be advantageous due to the ability to incorporate micrographs to create unique unit cells which are used to represent the composite on the microscale.

According to the theory of homogenization, the macroscopic elasticity tensor for two distinct periodic phases is given by Equation 4.3 [19];

$$C_{ijkl}^H = \frac{1}{|V|} \int_V C_{pqrs} \left(\varepsilon_{pq}^{0(ij)} - \varepsilon_{pq}^{(ij)} \right) \left(\varepsilon_{rs}^{0(kl)} - \varepsilon_{rs}^{(kl)} \right) dV \quad (4.3)$$

Where V is the volume of the unit cell, C_{ijkl}^H is the homogenized elasticity tensor, and C_{pqrs} , which is a function of position, is the local elasticity tensor. Here, C_{pqrs} can be obtained by

$$C_{pqrs}(\mathbf{x}) = C_{pqrs}^{mat.1} \beta^{mat.1}(\mathbf{x}) + C_{pqrs}^{mat.2} \beta^{mat.2}(\mathbf{x}) \quad (4.4)$$

where $\beta(\mathbf{x})$ is an indicator function to determine the phase (mat.1 = material 1 and mat.2 = material 2) for a given position, and $\varepsilon_{pq}^{0(ij)}$ is the macroscopic strain field. In this case, $\varepsilon_{pq}^{(ij)}$ represents the local strain fields and it is expressed by

$$\varepsilon_{pq}^{(ij)} = \frac{1}{2} \left(\frac{\partial u_p^{(ij)}}{\partial x_q} + \frac{\partial u_q^{(ij)}}{\partial x_p} \right) \quad (4.5)$$

Therefore, Equation 4.3 can be found by solving the elasticity equation,

$$\int_V C_{ijpq} \varepsilon_{ij}(v) \varepsilon_{pq}(u^{kl}) dV = \int_V C_{ijpq} \varepsilon_{ij}(v) \varepsilon_{pq}^{0(kl)} dV \quad (4.6)$$

where v is the virtual displacement within the unit cell, which is calculated by weighted residuals or finite element techniques.

4.3 Simulation Work

In the present research work, the MATLAB code of Andreassen and Andreasen [17] was extended to model the Al/Al₂O₃ IPC with random microstructures. The composites were manufactured via binder jetting of fused silica parts, which were subsequently infiltrated with molten aluminum. Microstructural images of the printed parts are used for the computational analysis. The present work has implemented an extension to the code created by Andreassen and Andreasen which consists of using

photographs of the microstructure of the composite as the homogenization platform. The computational results were compared to the experimental results, which were found using quasi-static compression testing of the printed part.

For the homogenization process to work, the code first prompts the user to enter the name of both phases, as well as its elastic modulus and Poisson's ratio for each component of the composite in order to calculate the individual Lamé parameters (Equations 4.7- 4.9). The dimensions of the printed sample along with its orientation to the compression load, placed the experimental sample in plane stress conditions. Therefore, the Lamé parameters for plane stress (λ , μ , and $\hat{\lambda}$), were calculated for the simulation. These Lamé parameters relate the elastic and shear modulus of a homogeneous and isotropic material as follows:

$$\lambda = \frac{\nu E}{(1 + \nu)(1 - 2\nu)} \quad (4.7)$$

$$\mu = \frac{E}{2(1 + \nu)} \quad (4.8)$$

$$\hat{\lambda} = \frac{2\mu\lambda}{\lambda + 2\mu} \quad (4.9)$$

Subsequently, the program asks for the quantity of samples. The modified code allows input from multiple images in order to achieve statistical relevance. The extension for each image can be inputted into the MATLAB program, and can be subsequently displayed. The program then prompts the user to crop the image to remove any defects in the image. The images are cropped by using the built-in MATLAB function “imcrop”, as well as turned into a square image by using the smaller of the two lengths in pixels. A

square image is used because the homogenization function requires a square matrix for calculation purposes. The photographs are then converted into a binary image by first setting the image to a grey scale, where each pixel is assigned a value from 0-1 depending on its contrast. The “graythresh” function determines a threshold value to evaluate whether the pixel is a 0 or 1, which is completed by the Otsu’s method [20]. A purely black and white “binary” version of the image is then produced using the command “im2bw”. A dialog box then follows and prompts the user to adjust the image contrast, if necessary (to best capture the microstructure while mitigating possible image defects). The resulting image represents a matrix of 1’s and 0’s, which is used in the homogenization function. An example of the original inputted image used in this research work, and its binary image can be seen in Figure 4.7.

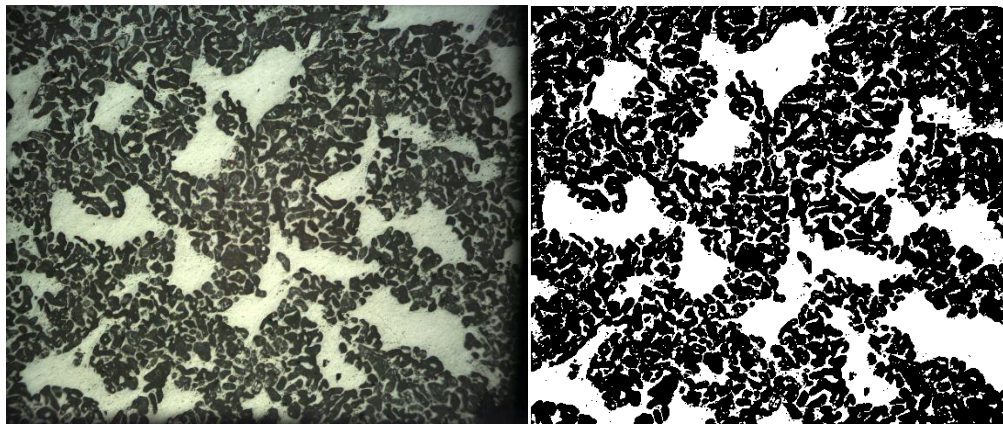


Figure 4.7. Original microstructure image of an Al₂O₃/Al composite (left), and its computational converted binary image (right).

It is worth mentioning that the MATLAB code created by Andreassen and Andreassen [17] provides a random matrix for the integers 1 and 2, for a 200 x 200 matrix. Therefore, the binary matrix was changed into 1’s and 2’s to fit the original existing code. Also, the

binary matrix needs to have a specific numerical value which was performed by using the command “double”, which gives the matrix an appropriate data structure. This data is then incorporated into the MATLAB program, which in turn calculates the elastic tensor and also the phase distribution of the composite from the inputted image. The phase distribution of the sample is calculated by using the area of the square cropped image. The code counts the number of 1’s in the matrix, and divide them by the total number of pixels in the image. This provides the phase distribution of both phases in the system. In order to collect the phase distribution of multiple samples, a new variable was created for each image for the black and white phases. The final outputted value of each phase distribution is the averaged phase distribution across all images used.

The homogenization code established by Andreassen and Andreasen [17], also requires six inputs to run. The first two inputs are the length and width of the unit cell. For this work, the generic value of 1 was used for both inputs. The third and fourth inputs are the individual Lamé parameters ($\hat{\lambda}$ and μ) for each component, which as mentioned before, were calculated by the Young’s modulus and Poisson’s ratio of the two investigated materials. In this work, the Lamé constants were calculated using values of 69 GPa and 0.3 for aluminum’s Young’s modulus, and Poisson’s ratio, respectively. For alumina, the values of 375 GPa and 0.22 for the Young’s modulus and Poisson’s ratio were used respectively. The fifth input is the angle, ϕ , which is considered the angle between the horizontal axis and the left wall of the unit cell. Andreassen and Andreasen [17] stated that the angle ϕ can be between 45-135° to represent a repeatable parallelogram of the unit cell. For the present research work, the angle was set to 90°. The final input is the matrix representing the microstructure of the two phase system. In

this study, the matrix was the square binary image of the $\text{Al}_2\text{O}_3/\text{Al}$ system. Following the entrance of the previous six inputs, the homogenization technique runs automatically. When the program is finished, the elastic tensor and the phase distribution percent of the composite, (which is averaged across all of the inputted samples) is obtained.

4.4 Experimental

Fused silica (from CE Minerals) was sieved through a 90 μm screen and used in the binder jetting process. The 3D printing was accomplished using an X1-Lab (Ex One) machine. The parts were designed as simple rectangular boxes in SolidWorks CAD software, and the dimension were made large enough to fit a strain gauge for later testing. The printed part had dimensions of 8.58 x 13.37 x 22.38 mm (representing the width x thickness x height respectively). During the printing, the silica powder was spread at a 0.1 mm/sec speed. The binder was a water based solution proprietary to Ex One. After printing the silica parts, they were cured at 190°C for 4 hours and subsequently sintered at 1500°C for 4 hours. The sintered parts were then infiltrated by submerging them in a molten aluminum bath. The final composites were then ground and polished for optical microscopy. The images used in the homogenization technique were taken with a Zeiss Axiphot microscope at 200x magnification. The experimental modulus was found using a universal compression testing machine with a loading rate of 0.1 mm/min.

4.5 Results and Discussion

Two different samples were used for the homogenization technique. Both of which were created by printing a simple cube shape using the fused silica powder. The first sample was sintered at 1500°C and then metal-infiltrated. At the sintering temperature of 1500°C, the sample showed no drooping or warping of the printed shape. The second sample, which was sintered at 1650°C, showed drooping and warping from the original dimensions due to the high sintering temperature. Therefore, experimental quasi-static testing was not performed in these parts due to warping, and only the homogenization analysis was carried out. The modeling results of this second sample were instead compared to literature data. It should be noted that lower sintering temperatures results in samples with higher volume fraction of the metal phase, which is the result of the lower sintering density of the printed silica.

Ten images from both samples were taken with an optical microscope with a 200x magnification. Three images from Sample 1 can be seen in Figure 4.8, where the white phase in the images is the aluminum, and the dark phase is the alumina.

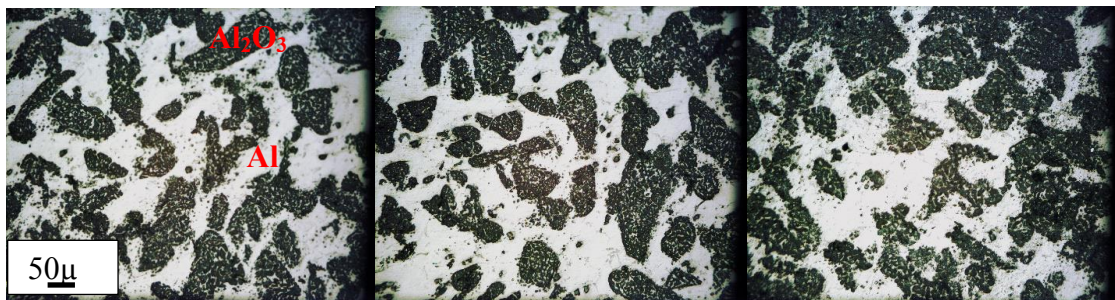


Figure 4.8. Representative example of the images used in the homogenization technique of the $\text{Al}_2\text{O}_3/\text{Al}$ composite.

Here, 10 images for Sample 1 were inputted into the MATLAB code for analysis. The elastic tensor for each image was calculated and then averaged together. The elastic

tensor was then calculated by the homogenization technique using the 10 images, and it can be seen in Equation 4.10.

$$C = \begin{bmatrix} C_{11} & C_{12} & C_{16} \\ C_{21} & C_{22} & C_{26} \\ C_{61} & C_{62} & C_{66} \end{bmatrix} = \begin{bmatrix} 1.6106 & 0.4608 & 0.0068 \\ 0.4608 & 1.6028 & 0.0050 \\ 0.0068 & 0.0050 & 0.5635 \end{bmatrix} * 1.0 \times 10^{11} \quad (4.10)$$

Subsequently, the elastic tensor was used to calculate the elastic modulus E_x assuming plane stress conditions by:

$$\begin{bmatrix} \sigma_x \\ \sigma_y \\ \sigma_{xy} \end{bmatrix} = \begin{bmatrix} C_{11} & C_{12} & C_{16} \\ C_{21} & C_{22} & C_{26} \\ C_{61} & C_{62} & C_{66} \end{bmatrix} \begin{bmatrix} \varepsilon_x \\ \varepsilon_y \\ \varepsilon_{xy} \end{bmatrix} = \frac{1}{1 - \nu_{yx}\nu_{xy}} \begin{bmatrix} E_x & E_x\nu_{yx} & 0 \\ E_y\nu_{xy} & E_y & 0 \\ 0 & 0 & G_{xy} \end{bmatrix} \begin{bmatrix} \varepsilon_x \\ \varepsilon_y \\ \varepsilon_{xy} \end{bmatrix} \quad (4.11)$$

Where ν_{xy} and ν_{yx} were calculated by:

$$\nu_{xy} = \frac{C_{21}}{C_{22}} \quad (4.12)$$

$$\nu_{yx} = \frac{C_{12}}{C_{11}} \quad (4.13)$$

And subsequently E_x was calculated by Equation 4.14:

$$E_x = C_{11}(1 - \nu_{yx}\nu_{xy}) \quad (4.14)$$

The calculated values for ν_{xy} , ν_{yx} , and E_x for the 10 images of Sample 1 were found to be 0.287, 0.286, and 147.8 GPa respectively. In contrast, the sample yielded an experimental elastic modulus of 167 GPa. This represents a theoretical-experimental deviation of 11.5%. Here, it was found that Sample 1 has a phase distribution of 49.7% Al_2O_3 and 50.3% Al. For comparison 20 images were analyzed for Sample 1. The calculated values for ν_{xy} , ν_{yx} , and E_x for the 20 images of Sample 1 were found to be 0.289, 0.287, and

144.6 GPa respectively, with a deviation of 13.4%. From the simulated results, it can be observed that the addition of 10 more images in the analysis process has a negligible difference (see Figure 4.9).

It is possible to achieve a deviation in the elastic tensor that is computed from an individual image due to the contrast changing, random cropping of the image, and the program cropping the data to form a square matrix. To evaluate this deviation, the homogenization technique was run 10 times, using the same 10 images, cropping a random portion of the image, and selecting the most appropriate phase contrasts. The resulting average had the elastic modulus at 145.7 GPa with a standard deviation of 0.75 GPa. This suggests that there is a very minimal deviation from using the same images on multiple occasions.

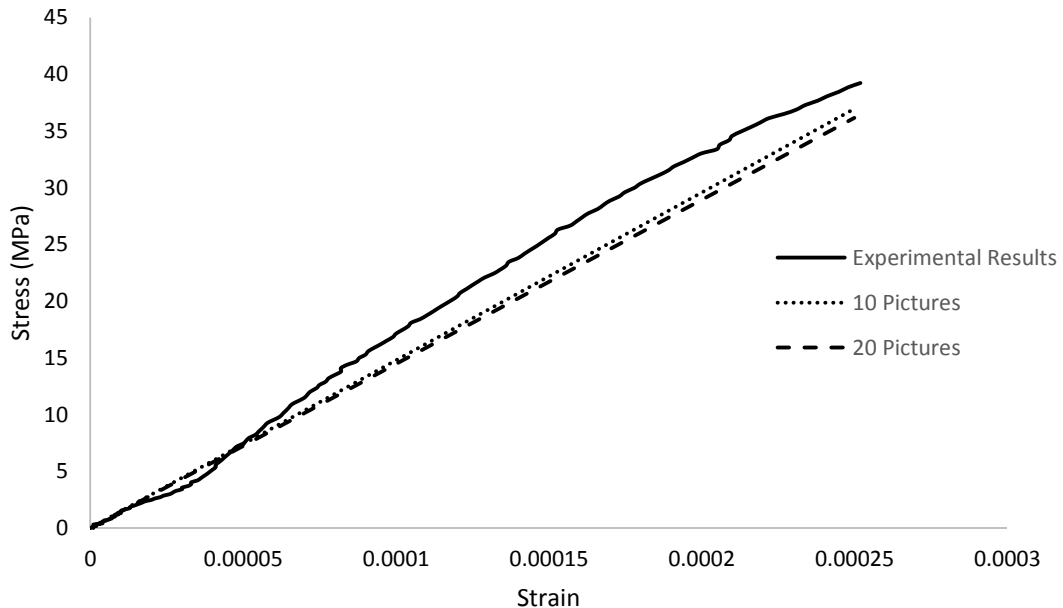


Figure 4.9. Stress-strain curve from the experimental and homogenization results.

All of the images used in the homogenization process were taken from the same plane of the cubic sample. The microstructure of the other two orthogonal planes showed similar random heterogeneous phase distribution, suggesting that the results in the other planes would yield similar elastic moduli in the simulation. The microstructures of all three planes can be seen in Figure 4.10.

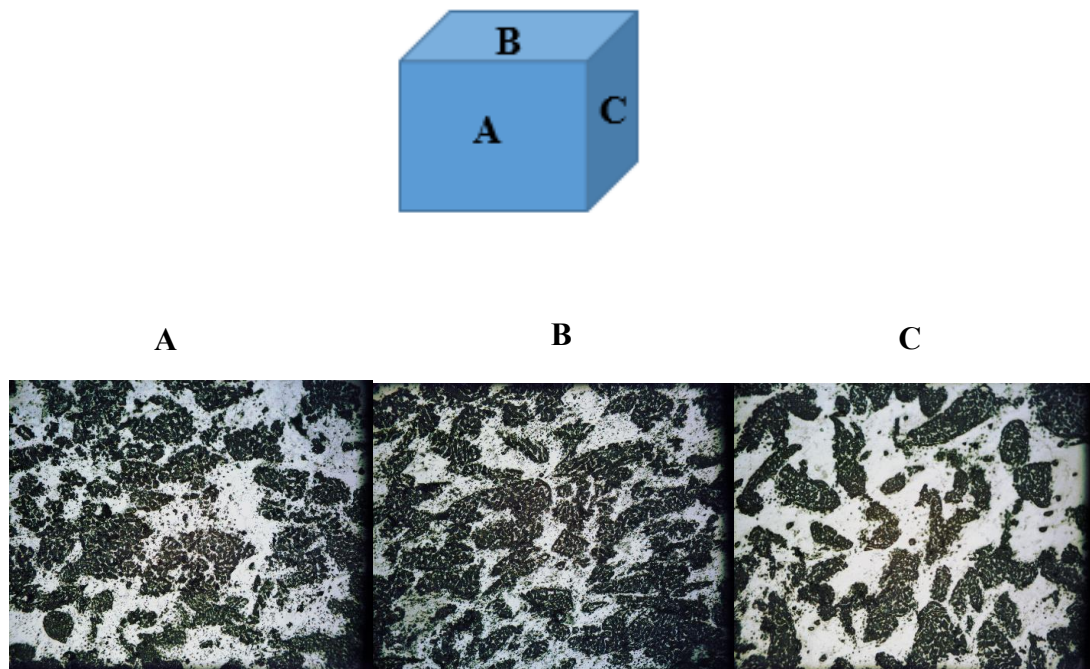


Figure 4.10. Microstructure of all three planes of sample 1.

Figure 4.11 shows some of the images taken from Sample 2 for its homogenization analysis. Indeed, due to the higher sintering temperature (1650°C), which resulted in a denser structure, the code calculated a higher volume fraction of ceramic phase than in the first sample. Here, the calculated average phase distribution for Sample 2 was 61.1% Al₂O₃ and 38.9% Al.

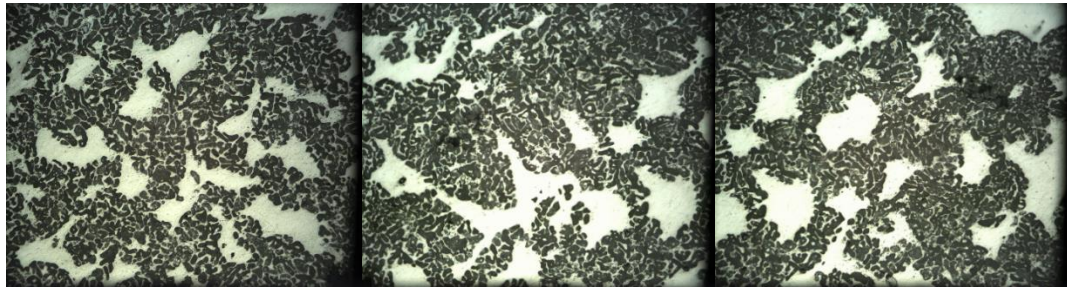


Figure 4.11. Images that were used in the homogenization technique of the Al₂O₃/Al (Sample 2).

For Sample 2, ten images were used in the homogenization technique, which yielded an elastic modulus E_x equal to 180.8 GPa. Breslin *et al.* [21] reports their C4 Al₂O₃/Al to have an elastic modulus of 215 GPa (15.9% difference). However, their investigated C4 material was approximately 65% Al₂O₃ and 35% Al. In contrast, the averaged phase distribution for the simulated specimen (Sample 2) has less volume fraction of the ceramic phase (61.8% Al₂O₃). This slightly lower amount of the Al₂O₃ phase in Sample 2, caused the predicted elastic modulus to be below than the reported by Breslin *et al.* A summary of all the simulation results can be seen in Table 4.1.

Table 4.1. Summary of the simulated elastic modulus and Poisson's ratio and the experimental data from the investigated samples.

Sample	Number of Images	Simulated ν_{xy}	Simulated ν_{yx}	Simulated E_x	Experimental E_x
1	10	0.287	0.286	147.8	167
1	20	0.289	0.287	144.6	167
2	10	0.276	0.273	180.8	215*

*The experimental data for sample 2 was taken from Breslin *et al.* [21].

It should be noted that both samples used in the homogenization technique have a small degree of porosity through the sample. The presence of porosity can result in an error during the modeling process, since the porosity is black in the images being used, and the program can recognize these pixels as part of the darker phase (in this case, as the ceramic Al_2O_3). Therefore, the modeled homogenized modulus could result in an increased error of the elastic modulus due to a misidentification of phases. Figure 4.12 shows how the MATLAB program recognizes porosity as an actual phase. Here, the porosity is highlighted in a red box in both images. In the actual micrograph of the sample (left), the porosity can be easily seen by its pure black color, which is darker than the Al_2O_3 phase. Whereas in the binary image (right), it is shown that the porosity is recognized as the dark (ceramic) phase in the image. It is suggested that increasing the magnification of the images used will allow the program to detect smaller differences in the microstructure of composite materials.

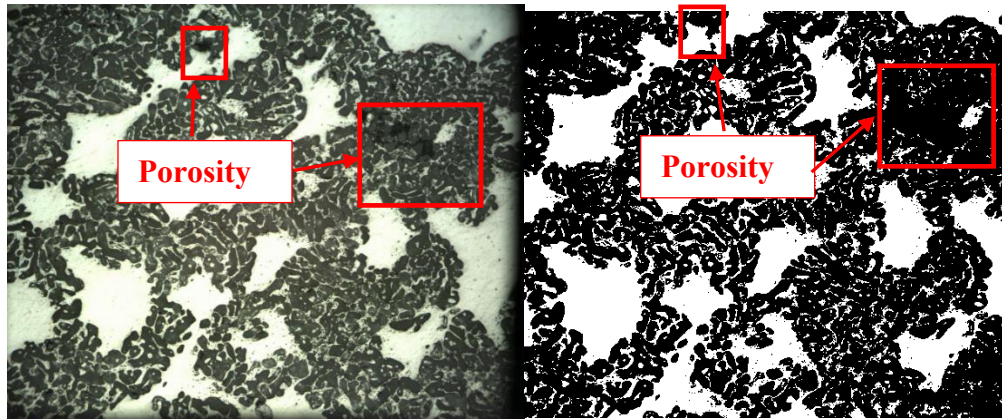


Figure 4.12. Micrograph of an Al₂O₃/Al composite highlighting the porosity (left), and the resulting binary image used in the homogenization technique (right).

4.6 Conclusions

A MATLAB code created by Andreassen and Andreassen was here expanded by transforming a micrograph of a two phase system into a binary matrix, which was subsequently used in a homogenization technique. Ten micrographs of an Al₂O₃/Al composite were used to have a representative average phase distribution of the sample. The elastic tensor was found for the composite using 10 and 20 different images for comparison. The results show little deviation between themselves. The simulation using 10 images resulted in an elastic modulus of 147.8 GPa, which is a value of approximately 13.4% lower than that obtained experimentally. A second Al₂O₃/Al composite with a different phase distribution and microstructure was also modeled, resulting in a predicted modulus of 180.8 GPa, which was 15.9% lower than the reported in the literature. The homogenization of 10 images, analyzed only once, in the MATLAB program extension was preformed in under 1.5 hours, proving that this technique is a rapid and reliable way to find the elastic modulus of a two phase system.

References

1. Torquato, S. (2000). Modeling of physical properties of composite materials. *International Journal of Solids and Structures*, 37(1), 411-422.
2. Hashin, Z. S. H. T. R., & Shtrikman, S. (1962). A variational approach to the theory of the elastic behaviour of polycrystals. *Journal of the Mechanics and Physics of Solids*, 10(4), 343-352.
3. Hashin, Z., & Shtrikman, S. (1963). A variational approach to the theory of the elastic behaviour of multiphase materials. *Journal of the Mechanics and Physics of Solids*, 11(2), 127-140.
4. Riley, M. B., & Whitney, J. M. (1966). Elastic properties of fiber reinforced composite materials. *American Institute of Aeronautics and Astronautics Journal*, 4(9), 1537-1542.
5. Hill, R. (1965). A self-consistent mechanics of composite materials. *Journal of the Mechanics and Physics of Solids*, 13(4), 213-222.
6. Torquato, S. (1998). Morphology and effective properties of disordered heterogeneous media. *International Journal of Solids and Structures*, 35(19), 2385-2406.
7. Jones, R. M. (1998). *Mechanics of Composite Materials* (2nd ed.). New York, NY: Brunner-Routledge.
8. Torquato, S. (1991). Random heterogeneous media: microstructure and improved bounds on effective properties. *Applied Mechanics Reviews*, 44(2), 37-76.

9. Wegner, L. D., & Gibson, L. J. (2000). The mechanical behaviour of interpenetrating phase composites–I: modelling. *International Journal of Mechanical Sciences*, 42(5), 925-942.
10. Wegner, L. D., & Gibson, L. J. (2000). The mechanical behaviour of interpenetrating phase composites–II: a case study of a three-dimensionally printed material. *International Journal of Mechanical Sciences*, 42(5), 943-964.
11. Feng, X. Q., Mai, Y. W., & Qin, Q. H. (2003). A micromechanical model for interpenetrating multiphase composites. *Computational Materials Science*, 28(3), 486-493.
12. Mori, T., & Tanaka, K. (1973). Average stress in matrix and average elastic energy of materials with misfitting inclusions. *Acta Metallurgica*, 21(5), 571-574.
13. Poniznik, Z., Salit, V., Basista, M., & Gross, D. (2008). Effective elastic properties of interpenetrating phase composites. *Computational Materials Science*, 44(2), 813-820.
14. Agarwal, A., Singh, I. V., & Mishra, B. K. (2013). Evaluation of elastic properties of interpenetrating phase composites by mesh-free method. *Journal of Composite Materials*, 47(11), 1407-1423.
15. Wei, S., Fu-chi, W., Qun-bo, F., Zhuang, M., & Xue-wen, Y. (2011). Finite element simulation of tensile bond strength of atmospheric plasma spraying thermal barrier coatings. *Surface and Coatings Technology*, 205(8), 2964-2969.
16. Wang, L., Fan, Q., Li, G., Zhang, H., & Wang, F. (2014). Experimental observation and numerical simulation of SiC 3D/Al interpenetrating phase

composite material subjected to a three-point bending load. *Computational Materials Science*, 95, 408-413.

17. Andreassen, E., & Andreasen, C. S. (2014). How to determine composite material properties using numerical homogenization. *Computational Materials Science*, 83, 488-495.

18. Nemat-Nasser, S., & Hori, M. (2013). *Micromechanics: overall properties of heterogeneous materials*. Elsevier.

19. Torquato, S. (2002). *Random Heterogeneous Materials: Microstructure and Macroscopic Properties*. New York, NY: Springer.

20. Otsu, N. (1975). A threshold selection method from gray-level histograms. *Automatica*, 11(285-296), 23-27.

Breslin, M. C., Ringnalda, J., Xu, L., Fuller, M., Seeger, J., Daehn, G. S., Otani T., & Fraser, H. L. (1995). Processing, microstructure, and properties of co-continuous alumina-aluminum composites. *Materials Science and Engineering: A*, 195, 113-119.

Chapter 5 Binder Jetting Results and Discussion

The following chapter will present and discuss all of the data collected on the manufacturing process of ceramic-metallic composites based on the binder jetting of fused silica parts and their subsequent infiltration of molten aluminum. One of the main goals of this research work was to manufacture a fully dense, two phase composite. Hence, multiple powders with different particle size distributions were evaluated for their ability to be printed. The process parameters for the Ex One Lab printer were optimized

to create the densest printed part. After printing, the ceramic parts were infiltrated with aluminum to investigate their composite state. Also, additional methods were investigated as alternate routes to create fully dense composite systems. Throughout each processing step, the samples were physically, chemically, and mechanically characterized.

5.1 Fused Silica Powder Investigation

Four SiO₂ powders with varying mesh sizes and particle size distributions were investigated in this research work. The largest three powder blends purchased from CE Minerals (Greeneville, TN) were made by mesh sizes of -100, -200, and -325 screens, while the smallest blend was purchased from Harbison Walker International and was titled as “GP-3I” by the manufacturer. The -100 mesh powder was further sieved with a 170 mesh (90 μm) to assure that all particles were below 100 μm. The particle size distribution of all the powders were analyzed by their d₁₀, d₅₀, and d₉₀, where the numeral subscripts correspond to the percentage of the overall mass below that particle size. The particle size distributions of the powders can be seen in Table 5.1.

Table 5.1. The d₁₀, d₅₀, and d₉₀ of the four powders used in the binder jetting.

Powder	d ₁₀	d ₅₀	d ₉₀
-100	39	65	88
-200	26	48	84
-325	2	8	35
GP-3I	1	4	18

Table 5.1 shows that there is a wide range of particle sizes throughout each blend; some of which are not in the recommended particle size range of $20 \pm 15-45 \mu\text{m}$ as suggested by Sachs, for 3D printing [1]. For simplicity, the powder blends will be referred in this work to their d_{50} particle sizes. Thus, the -100, -200, -325, and GP-3I specimens will be associated to the 65, 48, 8, and $4 \mu\text{m}$ sizes respectively. Also, all of the powders used here were faceted and anisotropic in shape (see Figure 5.1). Figure 5.1 shows a variety of shapes and sizes of the particles investigated. For instance, the $65 \mu\text{m}$ powder shows large, sharp edged particles around the scale of $100 \mu\text{m}$, while the $4 \mu\text{m}$ powders shows much smaller particles smaller than $10 \mu\text{m}$. The particle shape and size have a great influence on the quality of the printed part. Thus, the spreadability of the powder was the first step of the investigation on new powders in the binder jetting process.

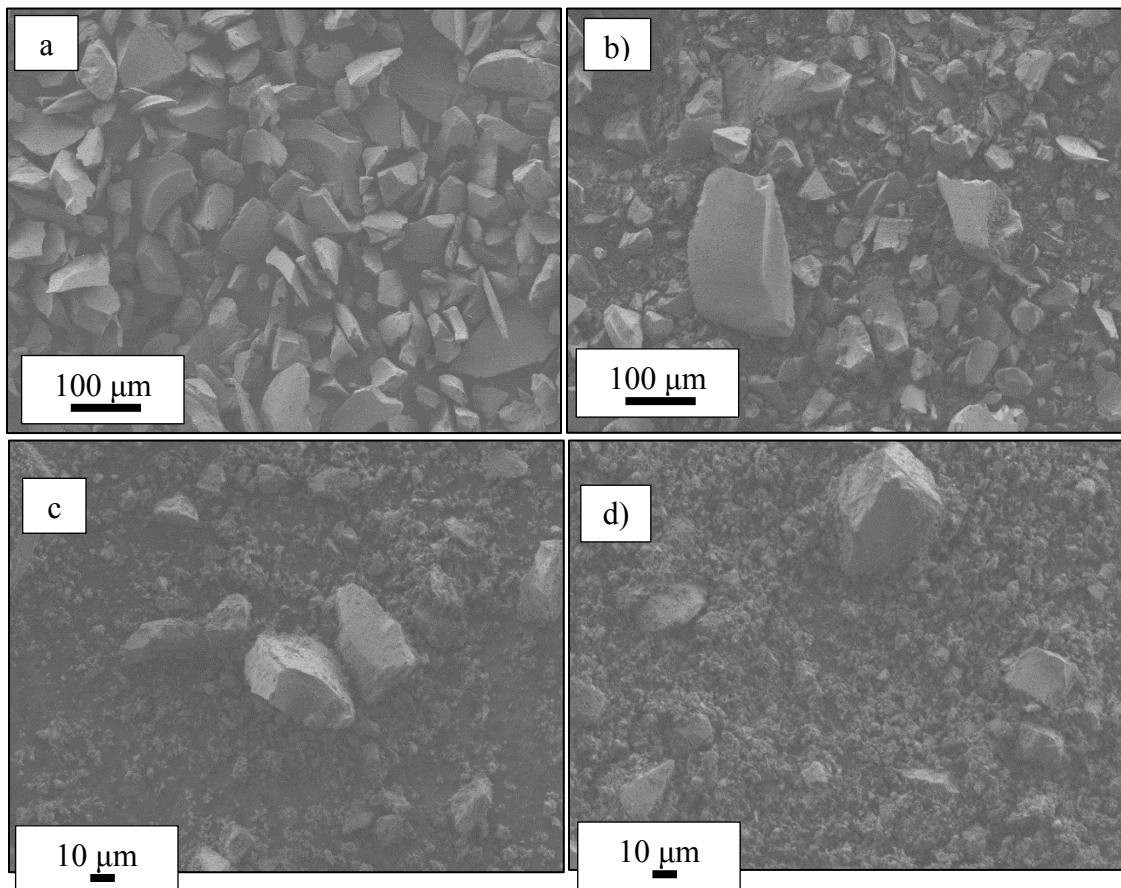


Figure 5.1. SEM images of all four powders used in this work. a) 65 μm , b) 48 μm , c) 8 μm , and d) 4 μm .

For the binder jetting process, the variables of layer thickness and binder saturation were set at 100 μm and 60%, respectively, as the printing standard. Initially, cylindrical parts with dimensions of 12.7 x 6.35 mm (diameter x height) were printed with the cross-sectional area of the part in the x-y plane of the printer (see Figure 5.2)

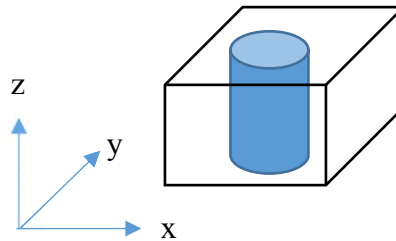


Figure 5.2. Diagram of the cylinder shapes used for testing the process parameters of the binder jetting of fused silica powders.

All four particle size distributions were printed with the aforementioned layer thickness and binder saturation, settings and then evaluated based on the speed at which the printer could spread them without any visual problems. Spread speeds of 10.0, 5.0, and 0.5 mm/min were investigated for this test. It was found that the smaller the particle size distributions (8 and 4 μm), the lower the quality of the spreading due to large gaps in the printed parts. These large gaps were formed from the powder sticking to the rolling device, leaving uneven spreading (see Figure 5.3). It has been reported that the van der

Waals interactions of the 5 μm particles and below, lead to powder sticking, and poor spreading characteristics [2].

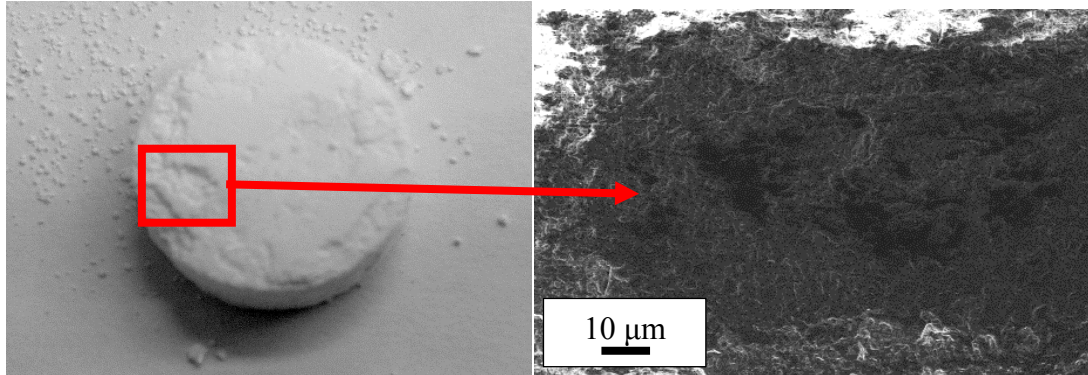


Figure 5.3. Images of the 8 μm printed fused silica showing large gap formations due to van der Waals interactions during the spreading process.

Even though the 8 and 4 μm powder have some larger particles than that of its d_{50} size (see Figure 5.2c and d), which could result in some degree of quality spreading, there are also finer powders below 2 μm , shown by the d_{10} (see Table 5.1), which resulted in the aforementioned “sticky” spreading performance. Additionally, the faceted nature of the ceramic powders added further “stickiness” to the particles due to surface matching and locking. Due to the poor spreadability of the 8 and 4 μm powders, they were no longer investigated in this research work. In contrast, the 65 and 48 μm particles were both successfully printed at all three aforementioned spread speeds with no observable gaps or sticking profile. While using the 65 and 48 μm powders, parts were printed at different

spread speeds and investigated as a function of the cured density. It was found that the density increased by decreasing the spread speed for the 48 μm powder, but not for the 65 μm (see Figure 5.4).

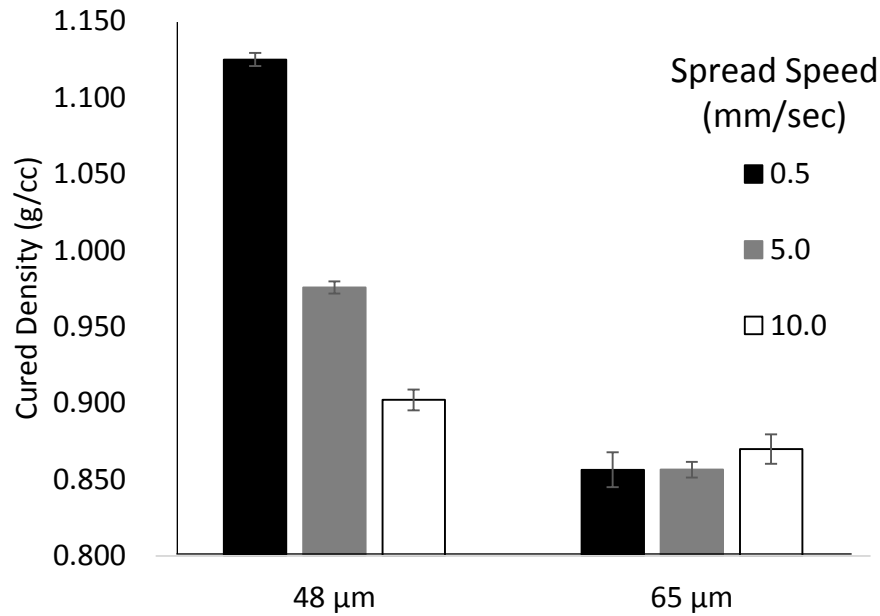


Figure 5.4. Measured densities of the cured parts based on different printing spreading speeds (printing conditions: particle size = 48 μm , binder saturation = 60%, layer thickness = 100 μm).

Figure 5.4 shows that the density of the 48 μm cured sample increased from 0.902 to 1.125 g/cc when the spread speed was slowed from 10.0 to 0.5 mm/min respectively. It seems that the increased time for spreading the powder allowed for more particle compaction from the rolling mechanism, resulting in an increased density. Other

compaction techniques have been used to increase the density of printed parts, such as re-compressing the powder via running the roller over the powder in the opposite direction (of the rolling process) and by mechanically compressing the newly deposited layer with a metal plate [3-4]. The overlapping standard error of the density for the 65 μm powder infers that there was a minimal compaction during the slowest spread speed. The absence of compaction could be due to the larger particles in the powder blend which are similar to the layer thickness used during the printing process (100 μm). Based on these results, the optimization of the binder saturation, layer thickness, and sintering temperature were performed at a spreading speed of 0.5 mm/min with the 48 μm particle size powder as the constant factor on the parametric analysis for the density and compression strength of the sintered parts.

5.2 Optimization of the Printing Parameters and Sintering Temperature to Maximize Density and Compression Strength of the Sintered Ceramic Structures

The parameters of binder saturation, layer thickness, and sintering temperature were varied to find the maximum density and compression strength of the sintered parts. Here, the values used for the binder saturation, layer thickness, and sintering temperature were 60%, 100 μm , and 1400°C respectively. These values were chosen based on preliminary studies showing the feasibility and the printing quality of the 48 μm silica powder. For each test, one variable at a time was investigated above and below the established reference point, while the other parameters remained constant (see Table 5.2). Eight cylinders with the dimensions of 12.7 x 12.7 mm (diameter x height) were printed in the same orientation as shown in Figure 5.2 for each test parameter. Following the

curing stage, the samples were subjected to a sintering process in order to bind the particles together and yield solid structures for the subsequent infiltration to form metal-ceramic composites.

Table 5.2. A list of the values used in the variable analysis of binder saturation, layer thickness, and sintering temperature.

Test	Binder Saturation (%)	Layer Thickness (μm)	Sintering Temperature ($^{\circ}\text{C}$)
1	40	100	1400
2	60	100	1400
3	80	100	1400
4	100	100	1400
5	120	100	1400
6	60	75	1400
7	60	125	1400
8	60	150	1400
9	60	100	1300
10	60	100	1350
11	60	100	1450
12	60	100	1500

5.2.1 Binder Saturation

The values of 40, 60, 80, 100, and 120% binder saturation were used for this test and the layer thickness and sintering temperature were kept constant at 100 μm and 1400 $^{\circ}\text{C}$ respectively. From the results, it was observed that the binder saturation of 60% yielded the highest sintered density of 1.387 g/cc, while 100% had the lowest at 1.234 g/cc (see Figure 5.5).

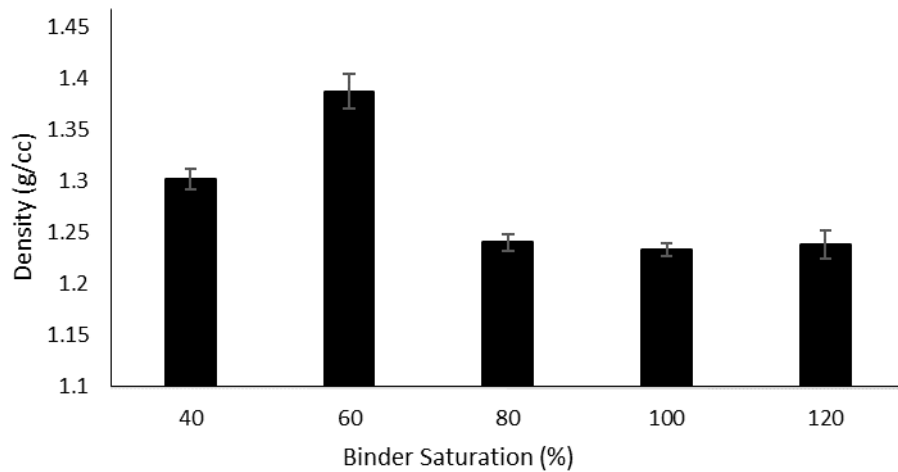


Figure 5.5. Resulting sintered densities based on the variation of the binder saturation during the printing process.

It was also observed that the parts manufactured with 40 and 60% binder saturation showed great definition and accuracy, while the parts with 80, 100, and 120% show large expansion (barrel deformation) in the x-y plane (see Figure 5.6). Figure 5.6 is a picture of printed parts using 60, 100 and 120% binder saturation; where it is displayed that those samples based on 100 and 120% saturation show a clear barrel deformation in the x-y plane. Here, the z-direction is the direction of layer building. These increased dimensions suggest that the additional binder expands the designed printing proportion, where the over-saturation and diffusion of excess binder is most abundant in the x-y plane. Also, the extra binder appears to lead into a decrease in the density of the printed parts due to the movement of the tightly packed particles created from the slow spreading speed. Vaezi et al. [5] has also showed that increasing the binder saturation led to less uniform printed parts.

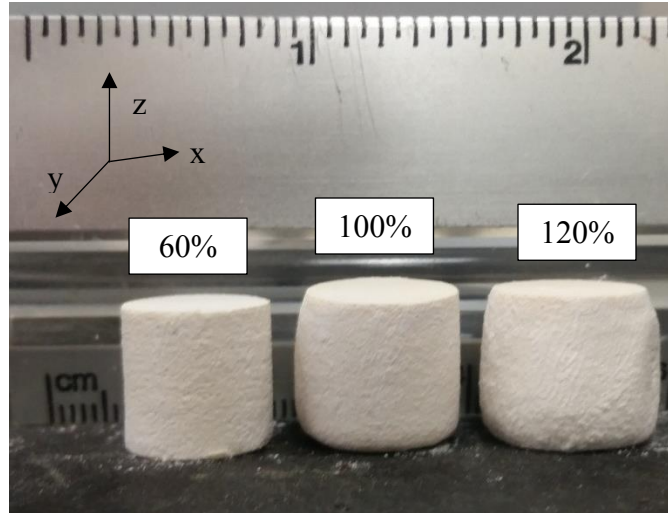


Figure 5.6. Printed cylinders that were manufactured with 60, 100 and 120 % binder saturation levels respectively. The binder saturations of 100 and 120 % show barrel deformation in the x-y plane.

The density of the sintered parts seems to have a direct relationship to the compression strength of the sintered samples (see Figure 5.7). The figure suggests a direct correlation between the highest compressive strength (10.00 MPa) and the highest density (a binder saturation of 60%). Vaezi et al. [5] showed that there is an increase in strength with binder saturation, but they correlated the increased strength to the cured state, not to the sintered state. The authors acknowledged the strength increase due to a larger amount of binder in the system, which is the matrix phase of the printed part; a phase that contributes to the strength of the cured state. However, an opposite trend is observed in the sintered state, where the increase of binder saturation level resulted in deformed parts with a lower sintered density, and consequently lower compressive strength. The creation of porosity from the removal of binder during the sintering process directly correlates to the decrease of sintered state compressive strength [6].

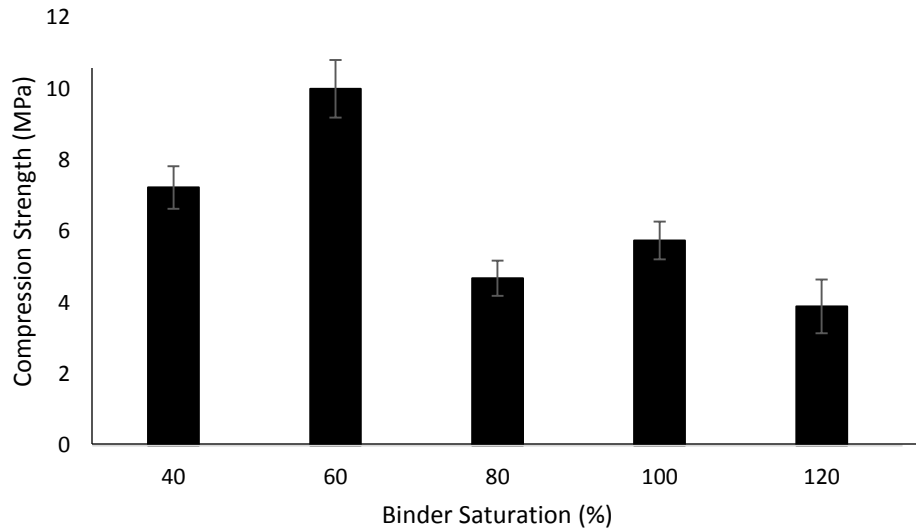


Figure 5.7. Relationship of the compressive strength of the sintered 48 μm printed powder parts with different binder saturation levels.

5.2.2 Layer Thickness

The values of 75, 100, 125, and 150 μm layer thickness were investigated in this test, using the 48 μm powder, while the spread speed, binder saturation, and sintering temperature were kept constant at 0.5 mm/sec, 60 %, and 1400°C respectively. The results showed that the layer thickness of 100 μm yielded the highest density of 1.387 g/cc, while the 150 μm had the lowest at 1.247 g/cc (see Figure 5.8).

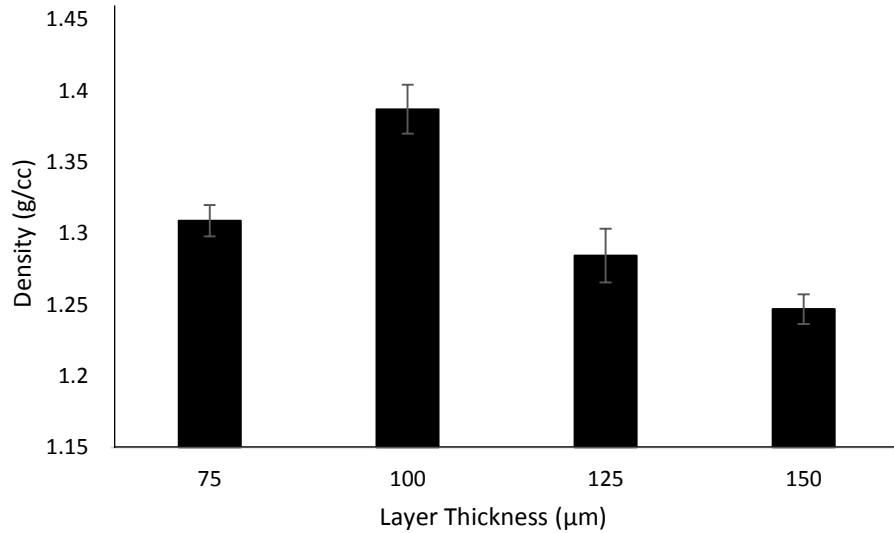


Figure 5.8. Resulting sintered densities as function of the layer thickness during the printing process.

Lu *et al.* [7] stated that the optimal layer thickness should be at least two times the size of the average particle size of the printed powder to achieve minimal deviation in the printed dimensions (cured state). No major deviations in the part dimensions were noticed for any layer thickness that were investigated here. The data displayed in Figure 5.8 shows that having a layer thickness two times the average particle size (d_{50} of $48 \mu\text{m}$) also correlates to the highest density. In fact, the figure also shows that there is an optimal layer thickness zone at $100 \mu\text{m}$ (approximately two times the average particle size), where the values above and below decrease the packing ability of the powder to form dense parts. The $75 \mu\text{m}$ layer thickness resulted in a lower sintered density than the $100 \mu\text{m}$ due to the size similarities between the particle size ($48 \mu\text{m}$) and the printing layer thickness ($75 \mu\text{m}$). Here, the larger particles (d_{90} of $84 \mu\text{m}$) of the $48 \mu\text{m}$ powder had less

opportunity to be compressed, resulting in a decreased density of the printed part. The limited ability for compaction was also observed in the spread speed test of the 65 μm powder when using the 100 μm layer thickness.

The compression strength of the sintered samples was also investigated as a function of the layer thickness. The results showed that the 100 μm layer thicknesses yielded the highest compression strength of 10.00 MPa (see Figure 5.9). The correlation of the sintering density with compressive strength can also be seen with every layer thickness that was tested. It should be noted that the variation of the layer thickness had the smallest impact deviation on the final density (0.14 g/cc) and compressive strength (3.22 MPa) of the sintered parts, compared to the deviations observed by varying the binder saturation and sintering temperature.

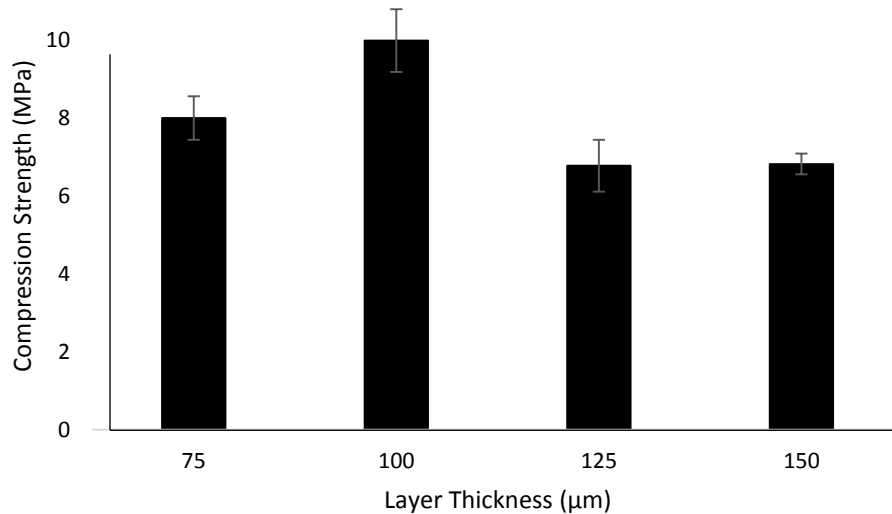


Figure 5.9. Relationship of the compressive strength of the sintered 48 μm printed powder parts as a function of different layer thickness.

5.2.3 Sintering Temperature

The density of the sintered parts was also investigated as a function of different sintering temperatures. Here, the cured printed samples were subjected to sintering temperatures of 1300, 1350, 1400, 1450, and 1500°C, while the binder saturation and layer thickness were kept constant at 60% and 100 μm , respectively. The sintering temperature was found to have the largest deviation on the density of printed parts, which also yielded the sintered parts with the highest density in this study (see Figure 5.10). From the figure, it was observed that the sintered density is an approximately linear increase by increasing the sintering temperature. The figure also shows that the sintered parts with the highest density (1.631 g/cc) were sintered at 1500°C, and the lowest (1.223 g/cc) at 1300°C. The increase of density is due to the reduction of porosity by increasing the sintering temperature. An effect widely shown in a large number of research works. The aforementioned temperature range was selected because at temperatures below 1300°C, the samples showed a “flakey” profile due to a partial sintering, and above 1500°C, they exhibited a “warping” profile, due to the temperature approaching the melting point (see Figure 5.11).

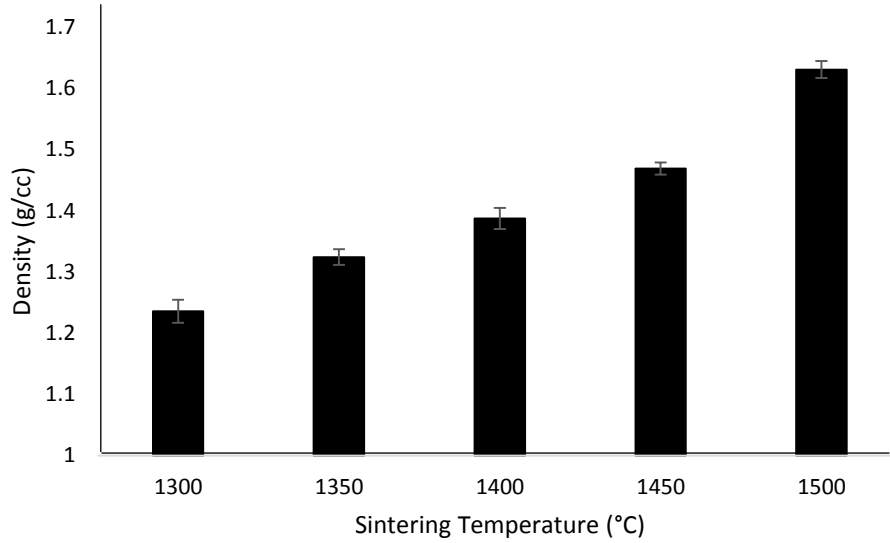


Figure 5.10. Resulting sintered densities as a function of the sintering temperature after the printing process.

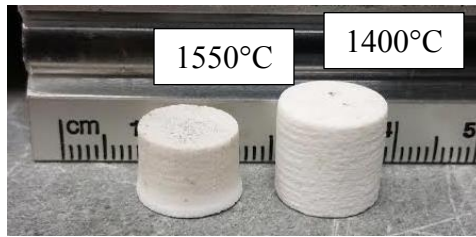


Figure 5.11. Printed cylinders that were sintered at 1400°C (right) and 1550°C (left), illustrating the “warping” effect caused when the sintering temperature is higher than 1500°C. This photo also illustrates the significant amount of densification (shrinkage) from the increase in sintering temperature.

The compression strength of the sintered parts, as a function of the sintering temperature, was also investigated. Figure 5.12 shows that the highest compressive strength was recorded from the samples sintered at 1500°C (27.9 MPa) and the lowest from the samples sintered at 1300°C (3.9 MPa).

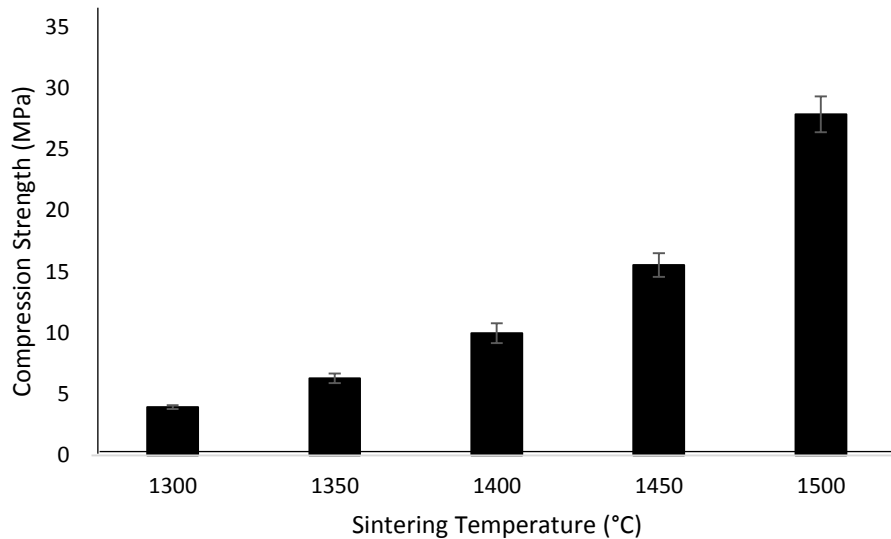


Figure 5.12. Relationship of the compressive strength of the sintered 48 µm printed powder parts as a function of different sintering temperatures.

Figure 5.12 shows an exponential increase in the compression strength by increasing the sintering temperature. It has been reported that sintering SiO_2 at temperatures of 1275°C and higher can form the cristobalite crystalline phase [8]. Breneman and Halloran [9] have shown that when fused silica is devitrified, the alpha-cristobalite crystals can produce micro-cracking in these particles at room temperature. This micro-cracking can lead to a decrease in strength comparative to the beta-cristobalite phase, which is stable at 350°C. Although micro-cracks typically result in a decrease in strength, Breneman and Halloran state that a comparison of the amorphous and crystalline systems can be

difficult because the two phases have different densities and porosities. When only comparing the maximum strength of the two systems, the presence of cristobalite shows an increase in strength to the silica system, which is also seen in this work. Cristobalite is a polymorph structure of SiO_2 that is stable at temperatures over 1450°C , although, it can crystallize in small amounts at lower temperatures [8]. The crystalline phase of cristobalite was found in various amounts in all of the sintered samples, shown by the PXRD (see Figure 5.13). Figure 5.13 shows an amorphous starting powder with no crystalline structure as well as the cristobalite phase after each sintering temperature. A closer examination of the largest peak associated to the cristobalite phase, reveals that each sample shows the crystalline phase with different intensity amounts (see Figure 5.14). This intensity can be used as a direct relationship to the concentration of cristobalite in the sample [10]; however, it can only be used in a qualitative manner due to the analysis of a small sample comparative to the whole printed part, as well as not being able to quantify the amount of amorphous phase still present in the sintered samples. From Figure 5.14, it can also be seen that the samples sintered at 1350°C and 1300°C have the lowest intensity peaks of cristobalite respectively. In fact, the micro-cracking associated with cristobalite formation can be seen in the samples sintered at 1450°C (see Figure 5.15). Although the samples sintered at 1500°C have the formation of micro-cracks, the particle bonding during the sintering appears to be a superior feature due to the notable compression strength increase comparatively to all other sintering temperatures. The temperature phase diagram of silica can be seen in Figure 5.16 for verification. It should be noted that none of the crystalline phases of silica were detected by PXRD.

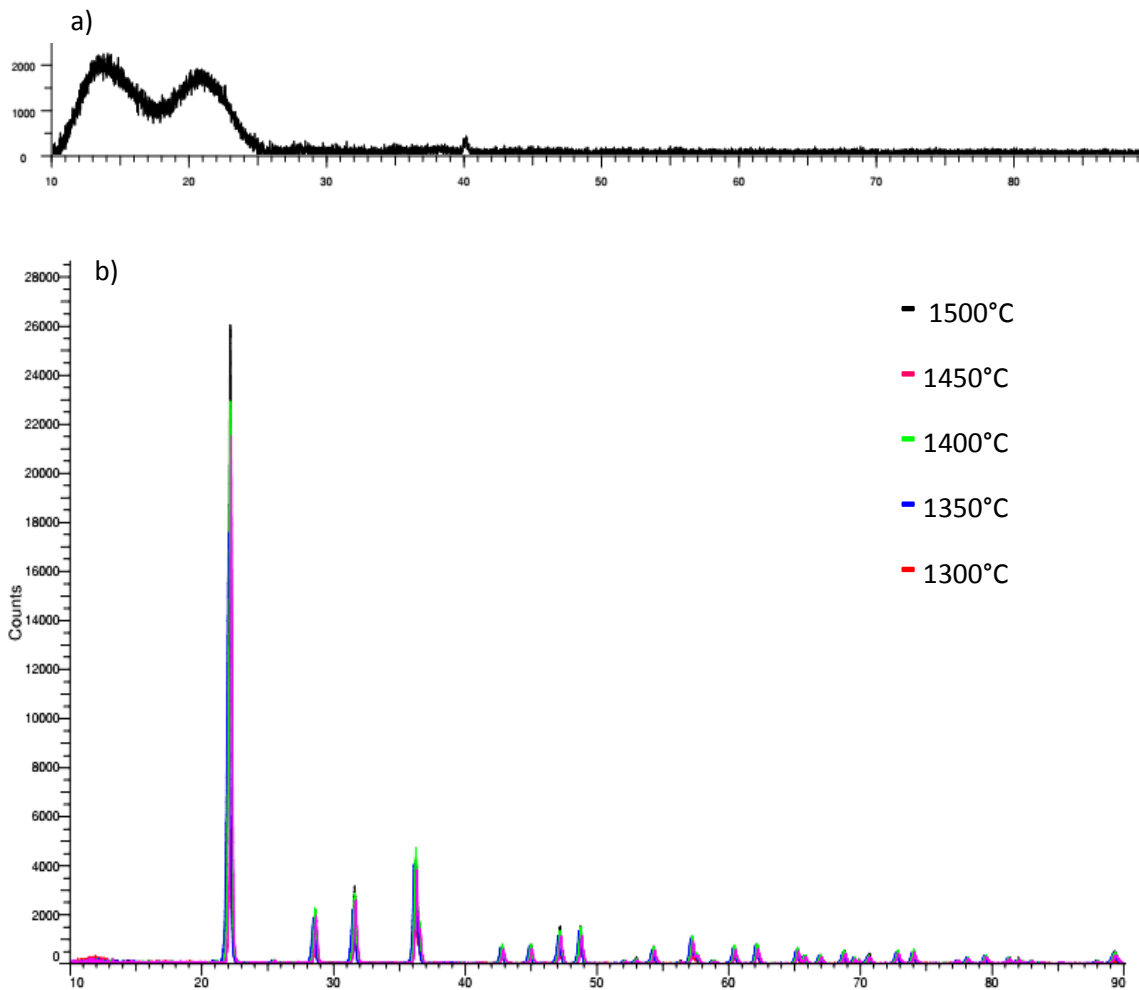


Figure 5.13. PXR D analysis of the amorphous raw 48 μm powder (a), and subsequent binder jetting parts sintered at 1300, 1350, 1400, 1450, and 1500°C (b), showing the presence of the cristobalite crystal structure.

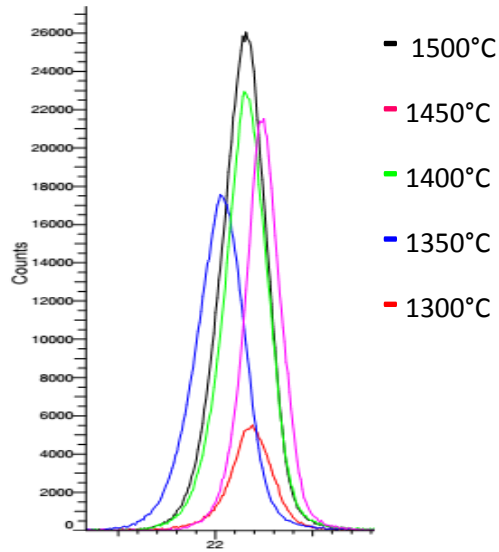


Figure 5.14. Magnification of the PXR D analysis of parts sintered at temperatures of 1300, 1350, 1400, 1450, and 1500°C.

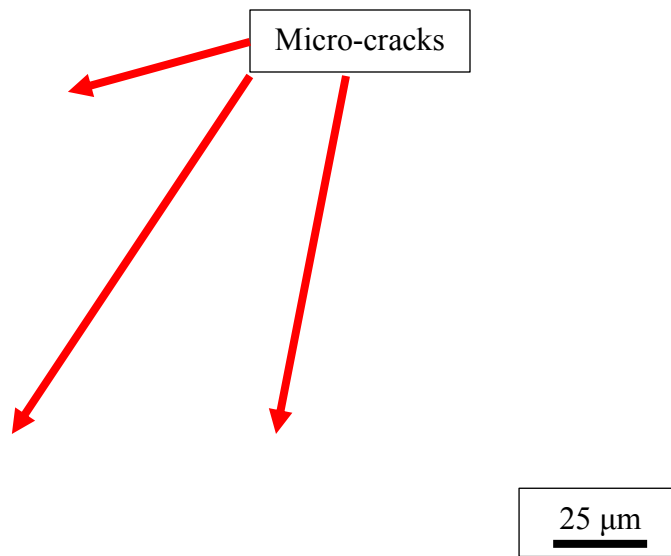


Figure 5.15. SEM image of the 48 μm powder sintered at 1450°C showing the presence of micro-cracking.

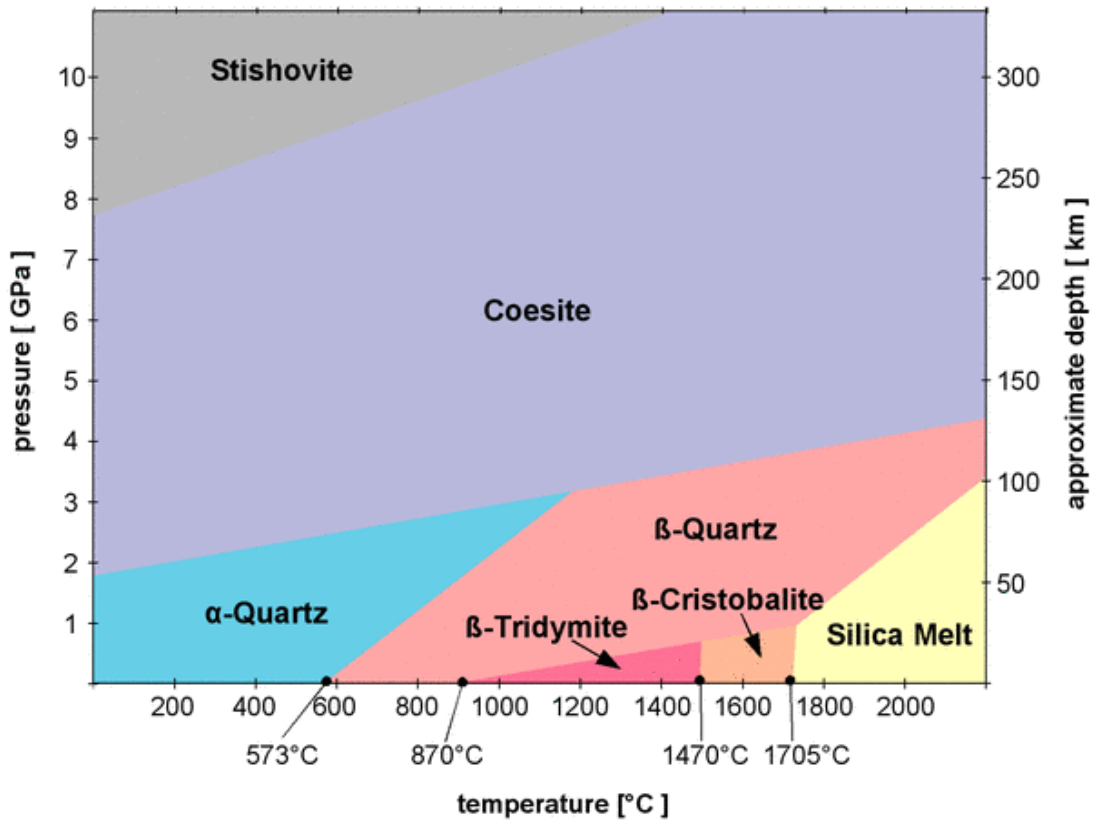


Figure 5.16. Temperature and pressure phase diagram of silica [11].

5.2.4 Printing Parameters

The results of this research work show that using the 48 μm powder, at a spreading speed of 0.5 mm/sec, a layer thickness of 100 μm , a binder saturation of 60%, and a sintering temperature 1500°C resulted in the highest density and subsequent highest compressive strength of the printed parts. A summary of these results can be seen in Figure 5.17.

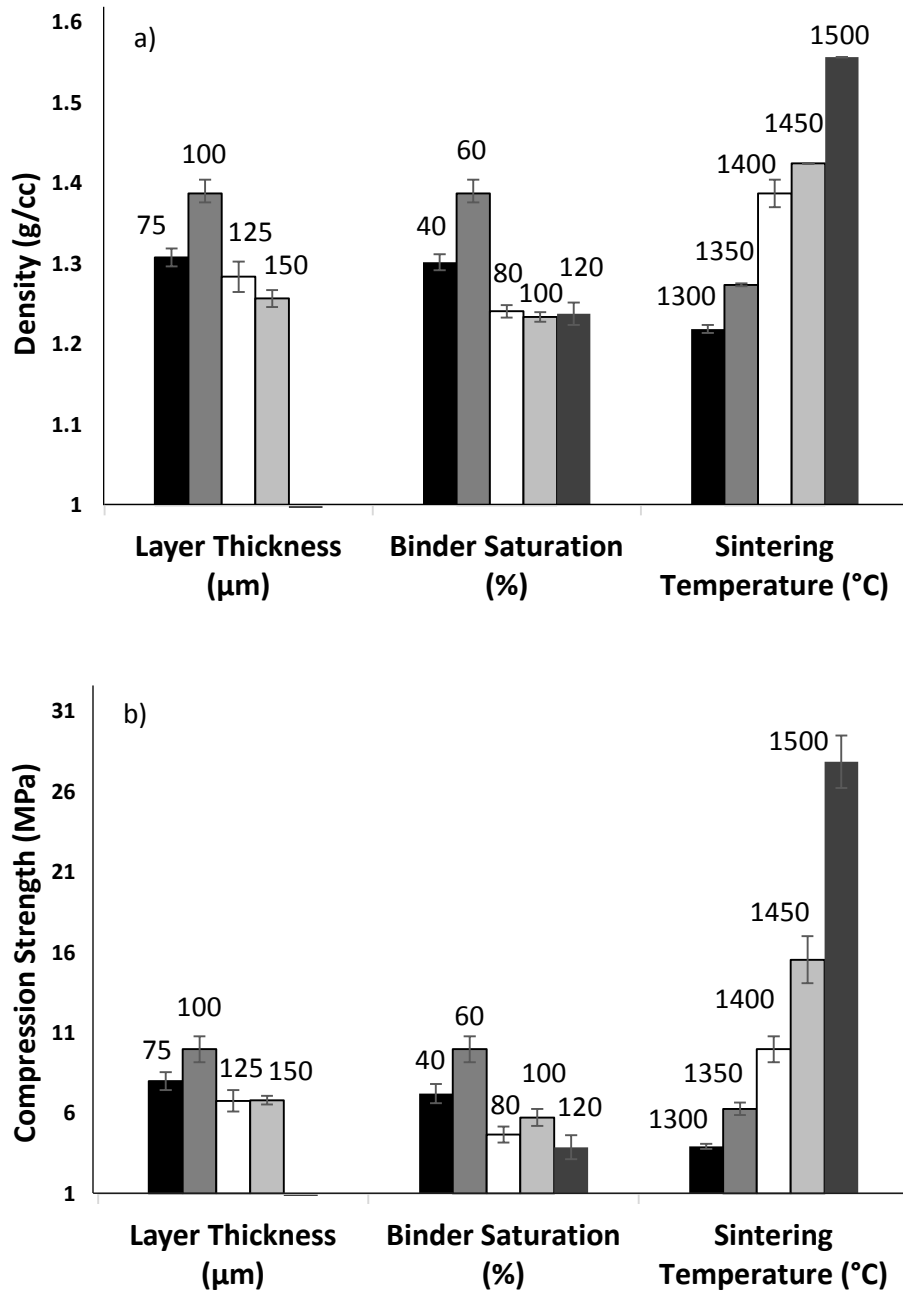


Figure 5.17. Summary of the sintered density (a), and compression strength (b) of the 48 μm printed powder as a function of the layer thickness, binder saturation, and sintering temperature.

Although the best printing and processing parameters were established for the printing process of fused silica parts, the resulting porosity of printed samples displays an opportunity to manufacture metal-ceramic composites with different phase distributions. Theoretically, the open porosity of the sintered parts could be filled with a metal phase, allowing the physical and mechanical properties of the final composite to be adjusted to fit a specific application. Therefore, the 48 and 65 μm powder was printed with the optimal printing parameters and sintered at 1450 and 1500°C to investigate the level of porosity that can be created (see Table 5.3).

Table 5.3. Resulting densities of parts printed with the 65 and 45 μm powders, which were sintered at 1450 and 1500°C. The value indicated in parenthesis, represents the percent density comparative to cristobalite (2.33 g/cc), which is the highest density that SiO_2 can achieve.

	1450°C	1500°C
65 μm	0.92 (39%)	1.08 (46%)
48 μm	1.48 (64%)	1.68 (72%)

The resulting densities of the sintered parts as a function of different particle sizes in correlation with sintering temperatures are shown in Table 5.3, where it is observed that a higher sintered temperature yielded a denser part in both powder sizes, with the density of the 65 μm powder being considerably lower than that of the 48 μm . The results can be associated to the larger ceramic particles, which can create a more natural porosity during the compaction of the sample, providing a lower surface area during the sintering stage. Included in the table is the ratio of the investigated samples to the density of cristobalite (2.33 g/cc). In this work, XRD analyses were carried out on the 65 and 48 μm samples,

and it was found that cristobalite was present in both of them. According to these calculations, metal-ceramic composites could potentially be manufactured with a metal volume between approximately 28-61%.

The microstructures of the different sintered ceramic parts can be seen in Figure 5.18, which illustrates the differences in porosity as function of the sintering temperature. The figure shows large particles with sharp edges for images c, d, e, and f, while a and b show a continuous microstructure where small amounts of individual particles can be identified.

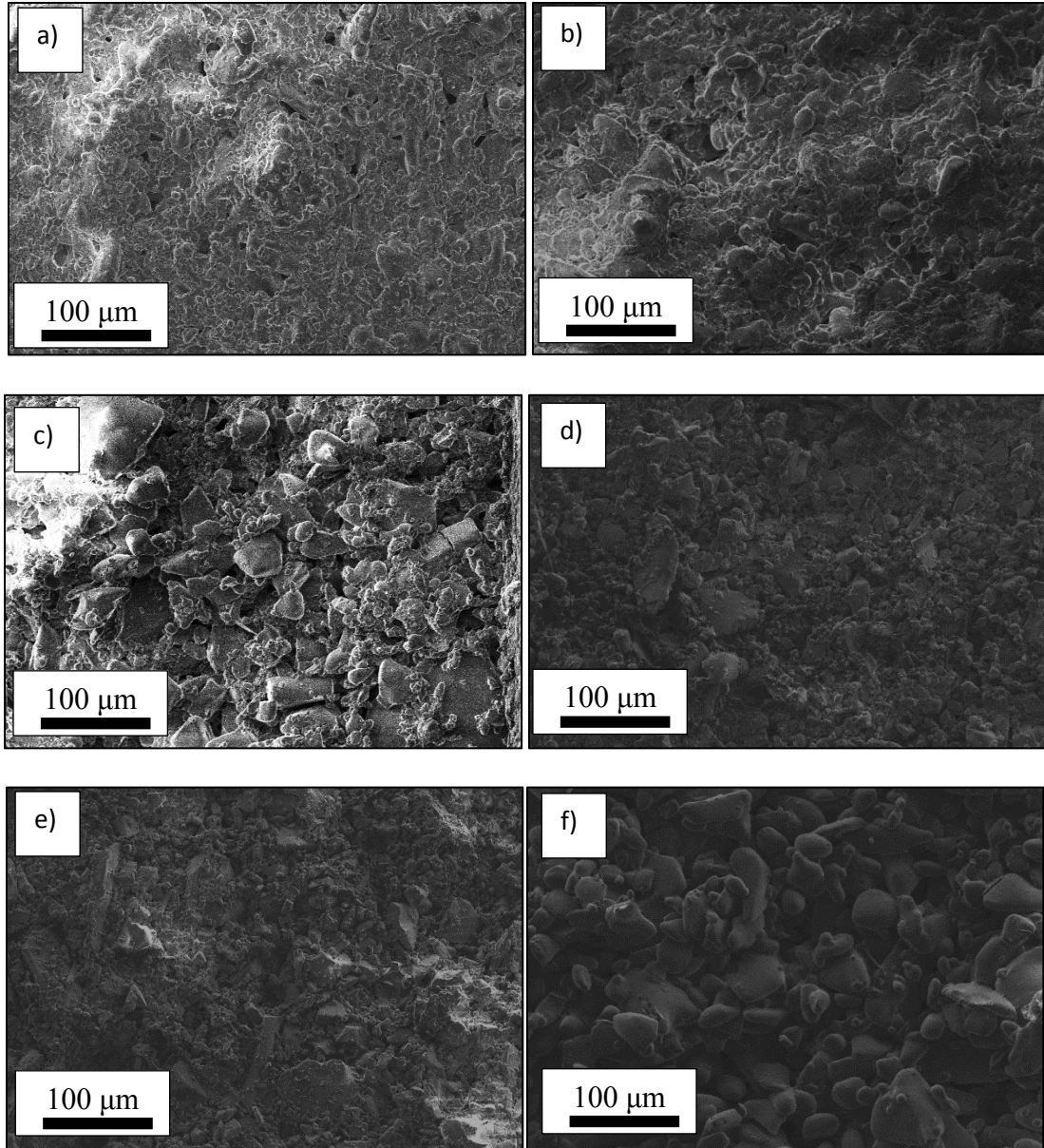


Figure 5.18. SEM images of the silica parts based on different particle size powders and sintering temperatures: a) 48 μm - 1500°C, b) 48 μm - 1450°C, c) 48 μm - 1400°C, d) 48 μm - 1350°C, e) 48 μm - 1300°C, and f) 65 μm - 1500°C.

5.3 Investigation of the Infiltration Process of Sintered Silica Parts for the Manufacturing of Metal-Ceramic Interpenetrating Phase Composites (IPCs)

For the infiltration process, sintered silica parts were immersed under molten aluminum at 1200°C for approximately 16 hours. Initially, the 65 μm sample that was sintered at 1500°C was infiltrated with molten aluminum to produce an IPC. The microstructure of the composite created from the 65 μm powder shows that the reaction between Al and SiO_2 to form Al_2O_3 did take place; however, it was not a large enough driving force for the molten aluminum to fill the open porosity of the network (see Figure 5.19).

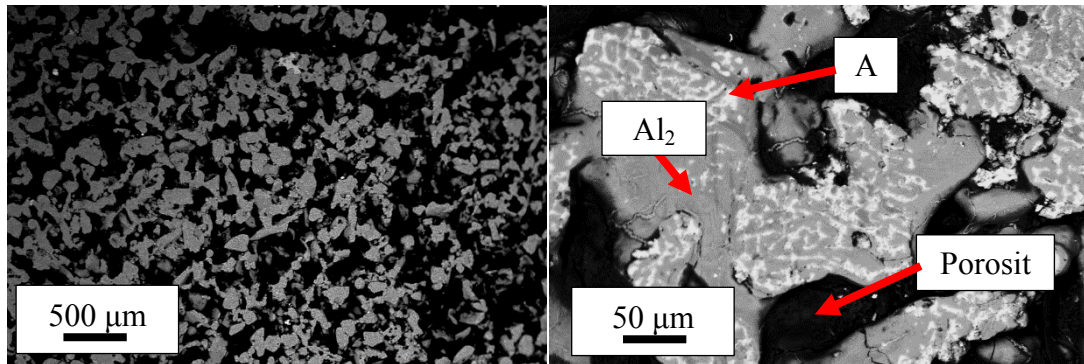


Figure 5.19. SEM images of the infiltrated sintered silica (65 μm) manufactured via binder jetting. The lighter phase is aluminum and the gray phase is alumina. The black zones in the images represent the open porosity network, which was not infiltrated by the molten aluminum. Left (low-magnification), and right (high-magnification).

In contrast, the microstructures of the IPCs manufactured from the 48 μm powder show more infiltration and less porosity gaps compared to the 65 μm powder, although there were still some gaps of porosity present in the sample (see Figure 5.20).

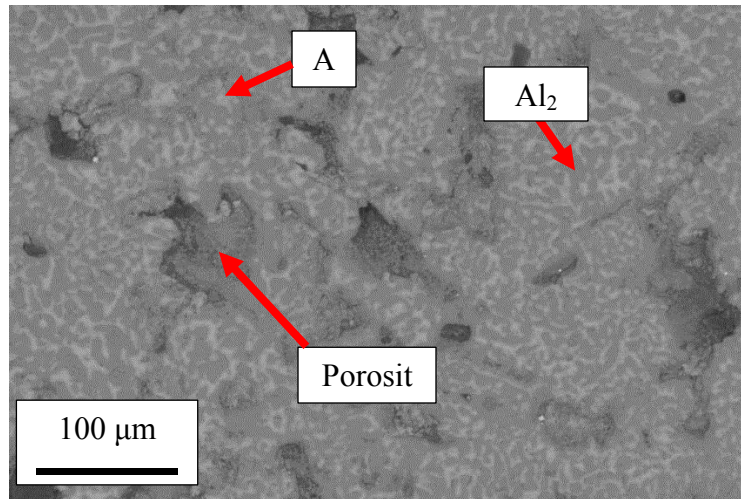


Figure 5.20. SEM image of an infiltrated composite from the binder jetted 48 μm SiO_2 powder, sintered at 1450°C, and subsequently infiltrated. The lightest phase is aluminum, while the darker phase is the alumina, and the darkest contrast is the porosity.

It is widely known that molten aluminum has poor wetting conditions on alumina. Typically, a non-wetting metal is infiltrated using external pressures [12-14]. In a non-wetting system, a threshold pressure must be met to initiate the capillary infiltration. Mattern *et al.* [12] developed a relationship between external pressure and infiltrated pore diameter of the aluminum/alumina system showing an inverse correlation between the two. In that model, a threshold pressure of 1 MPa was needed to fill a pore on the size of a few microns, while pressures around 100 MPa would be needed to fill pores of around 20 nm [12]. Commonly, near fully dense composites are created from a dense fused silica preform, which results in metal grains that are smaller than 10 μm when examining crosscut sections, implying that the metal infiltration due to the thermodynamics of the reaction has a limitation based on the pore size [15-16]. This demonstrates that an external pressure would be needed for the full infiltration of the ceramic parts printed in this work.

The density of the infiltrated composites as well as their compressive strength were investigated as a function of the particle size and the sintering temperature. This analysis was performed by comparing the densities and strengths from the two powder systems which were the closest in density (1450°C with 48 µm powder and at 1500°C with 65 µm powder) (see Table 5.4). From the table, it can be observed that the composite manufactured by the 65 µm powder resulted in a density of 1.80 g/cc, while the 48 µm powder yielded a density of 2.64 g/cc. Also, Table 5.4 shows that the initial compression results of the composite materials display show a large increase in strength when using the 48 µm powder.

Table 5.4. Relationship of sintered and composite densities as well as the composite compressive strength.

Powder Size (µm)	Sintered Temperature (°C)	Sintered Density (g/cc)	Composite Density (g/cc)	Composite Compression Strength (MPa)
65	1500	1.08	1.80	26.9
48	1450	1.48	2.64	270.6

From the results shown in Table 5.4, it is seen that the increase in density of the sintered parts initially shows a direct correlation to the density of the composite as well as to the compressive strength. Therefore, a more in depth investigation of the sintering temperature was performed on the 48 µm powder.

5.4 Effect of the Sintering Temperature on the Compressive Strength of Composites Manufactured from the 48 μm Powder

The effect of the sintered temperature on the composite compressive strength of the IPCs was investigated in more detail by printing additional samples and testing them at the sintering temperatures of 1300, 1350, 1400, 1450, and 1500°C. For this test, forty samples made of five batches, consisting of eight samples per batch, were printed on the X1-Lab system. From the forty samples, eight random samples were chosen to be sintered at each of the aforementioned temperatures to dampen any randomness of the printing process. Indeed, it has been observed in this work that even with the best printing parameters, the printing process can yield significant variability in the porosity of the printed parts. After sintering the printed parts, all samples were measured for density calculations, and one sample of each group was used for XRD analysis. The XRD analysis showed similar results to that shown in Figure 5.14, where every sintering temperature used showed peaks for the cristobalite phase. For the infiltration process, all five batches were infiltrated at the same time and in the same molten metal bath to avoid discrepancies in infiltration time, temperature, or melt chemistry. During the infiltration process, the samples were separated using specially designed containers that allowed the molten metal infiltration, as well as for an easy identification of the samples. (see Figure 5.21).



Figure 5.21. Special fixture used for a simultaneous infiltration of the 48 μm specimens sintered at different temperatures simultaneously.

After the infiltration processes, one sample of each run was also held back for microstructural SEM investigation, leaving six samples from each sintering test to correlate the compressive strength of the infiltrated composite parts. The samples for this test were printed as 12.7 x 12.7 x 15.875 mm cubes (with the largest dimension in the z-direction). The cube shape was chosen over the cylinder shape to ensure an easy cleaning and a grinding of the excess of aluminum from the surface of the part after infiltration. The compression testing was performed by applying the load in the z-direction for all samples. From the results, it was observed that the 1500°C sintering temperature yielded the highest composite density and compressive strength (see Table 5.5).

Table 5.5. Physical and mechanical properties of the sintered and composite parts based of the binder jetted of 48 μm fused silica sintered at different temperatures.

Sintered Temperature ($^{\circ}\text{C}$)	Sintered Density (g/cc)	Composite Density (g/cc)	Composite Compression Strength (MPa)
1300	1.264	1.911	41.5
1350	1.330	1.935	49.1
1400	1.418	1.990	58.6
1450	1.498	2.194	109.8
1500	1.618	2.325	126.4

Table 5.5 shows a clear relationship between the sintering density, composite density and the composite compression strength. The composite sintered at 1500°C showed the highest composite compression strength and density (126.4 MPa and 2.325 g/cc, respectively). From this table, it is apparent that there is a discrepancy between the composite densities shown in Tables 5.4 and 5.5. Based on the presented results, it can be inferred that more metal was retained in the composites shown in Table 5.4 (density 2.64 g/cc). A discussion of this density variability is explained later in this chapter.

An optical examination of the macrostructures of the tested samples shows a gradual increase in the amount of molten aluminum retained in the composite as the sintering temperature increased (see Figure 5.22). It is interesting to note that an edge affect was present in every infiltrated sample, a feature easily observed by optical examination.

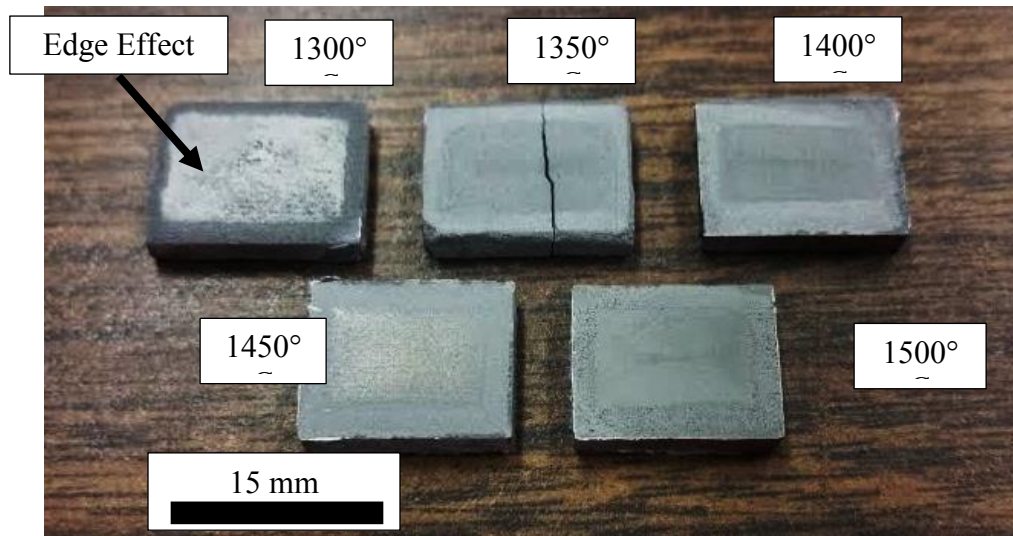


Figure 5.22. Image of the cross-cut section of the composites, sintered at different temperatures (displaying a noticeable edge affect).

The macrostructure of both noticeable regions observed in the composites showed less porosity (black spots) as the sintering temperature increased. SEM images of the top left corner of each cross-section can be seen in Figure 5.23, where the darkest phase is the Al_2O_3 ceramic phase, the lighter phase is the area where Al is retained and an $\text{Al}_2\text{O}_3/\text{Al}$ network is present, and the black phase is the porosity. Higher magnification SEM images of the composite that was sintered at 1300°C shows that in the outer zone, the Al_2O_3 ceramic grains are mostly out of focus within the plane of scanning (see Figure 5.24a). This infers that there are large amounts of porosity in the outer zone of the sample. In contrast, the center of this composite shows an interpenetrating plane, inferring a denser composite at the center of part (see Figure 5.24b).

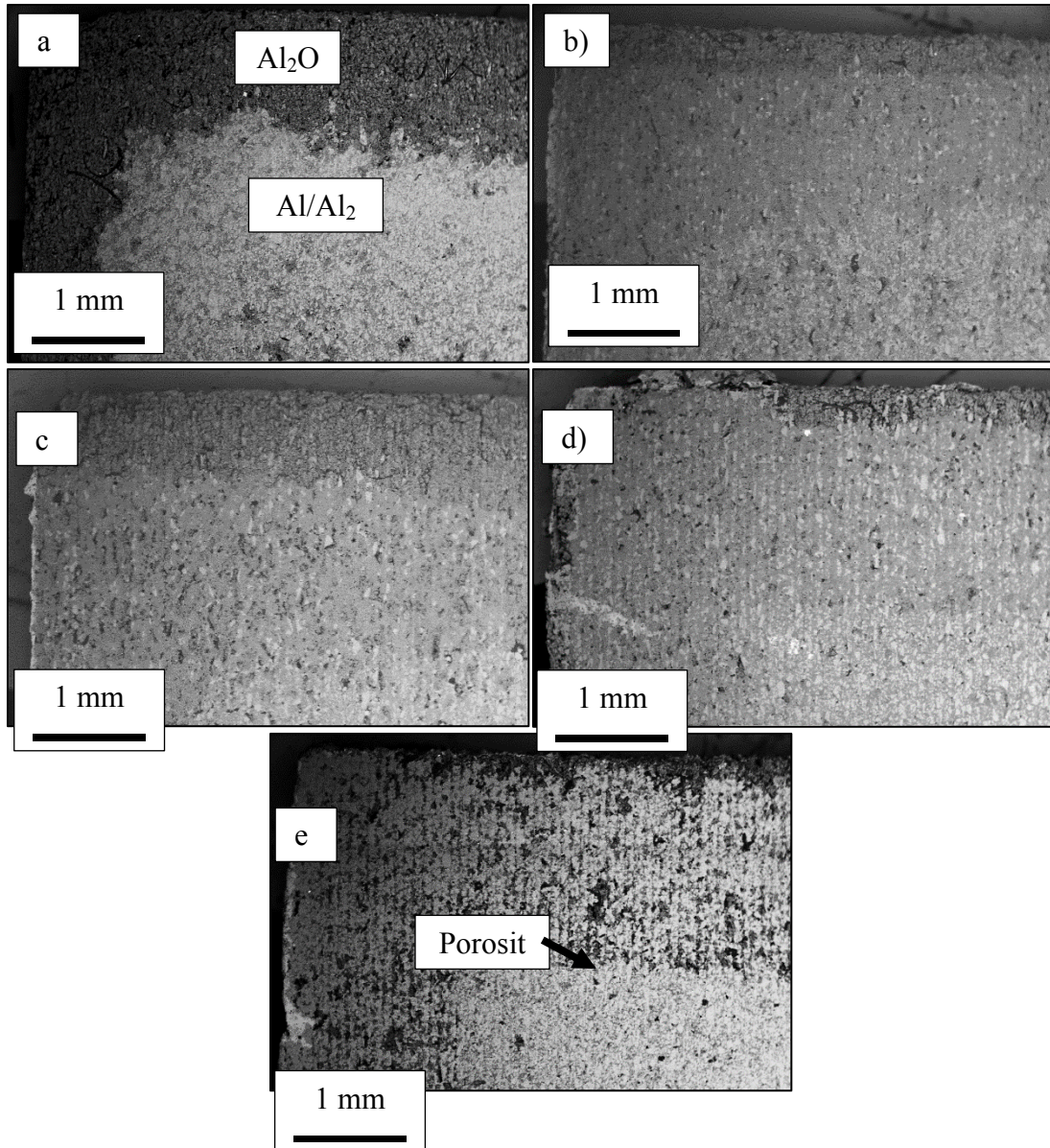


Figure 5.23. SEM images of the corner of each composite sample illustrating the different porosity zones in each sample, and the increasing metal retention by increasing the sintering temperature. a) 1300, b) 1350, c) 1400, d) 1450 and e) 1500°C.

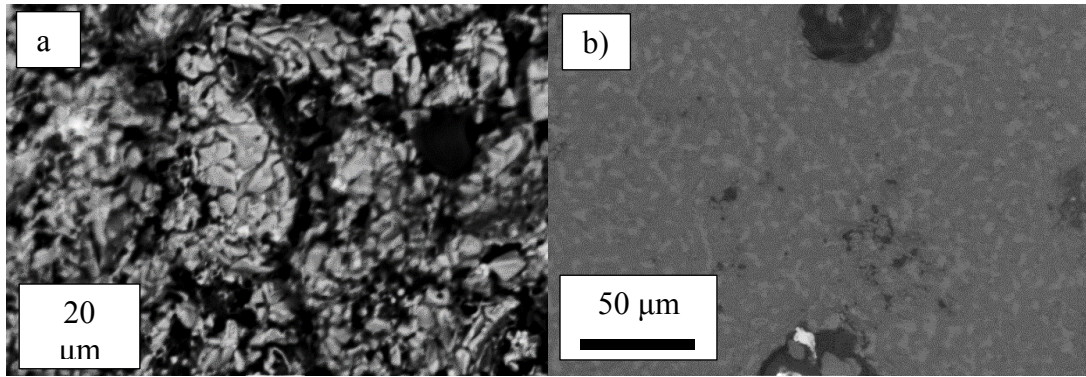


Figure 5.24. SEM images of the a) outside edge and b) the center region of the infiltrated composite created from a printed part sintered at 1300°C.

Conversely, the composite that was sintered at 1500°C shows a planer interpenetrating network on both the outer and inner parts (see Figure 5.25). Figure 5.25 shows the intersection of the outer and inner sections, where the outer region has a clear defining line with extra porosity. A further examination of the inner section of the 1500°C-sintered/infiltrated sample shows the interpenetration network but still with some degree of porosity (see Figure 5.26).

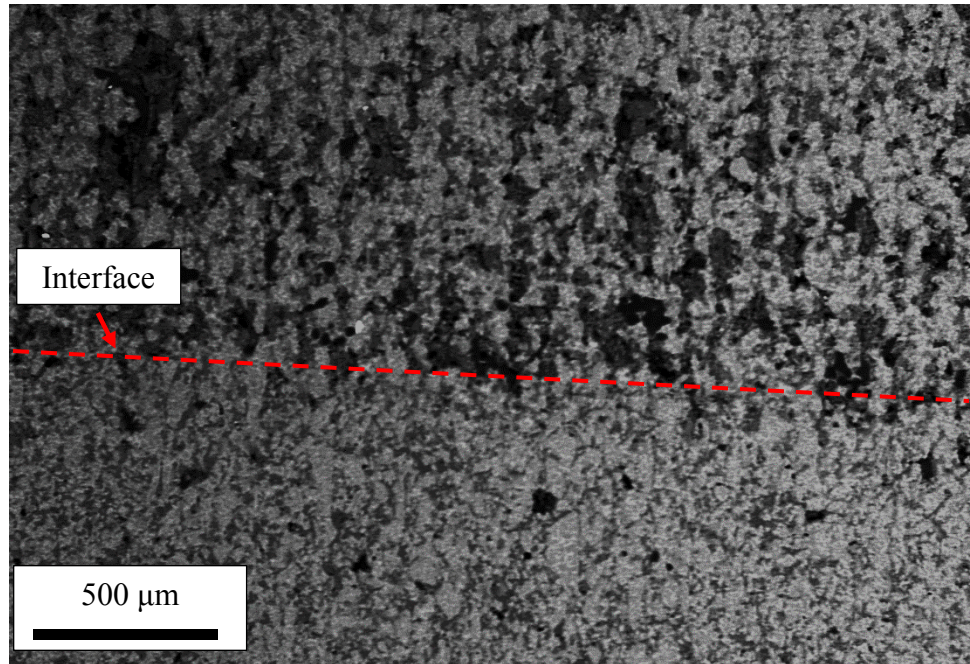


Figure 5.25. SEM image of the outer and inner sections of the composite manufactured from the printed part sintered at 1500°C.

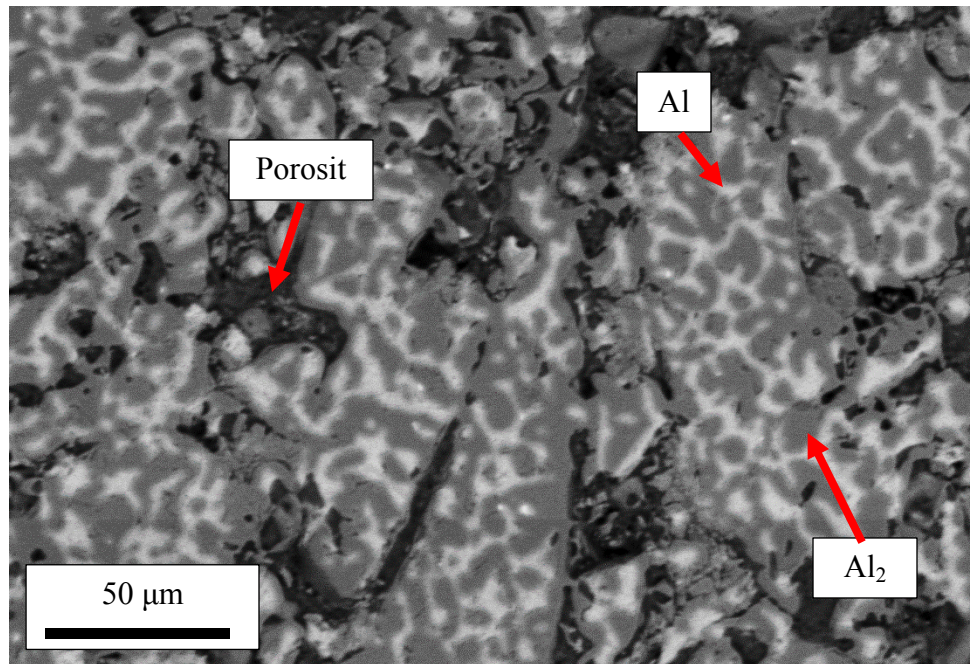


Figure 5.26. High magnification SEM image of the inner section of the infiltrated composite manufactured from the printed part sintered at 1500°C.

The aforementioned variation in density, and inherent porosity, shown in Tables 5.4 and 5.5 could be associated to the powder spreading process. It has been found in this work that single layers can leave large artifacts of porosity during the printing process (see Figure 5.27). Here, large gaps can be found in the final composite due to random layers that have uneven powder spreading and packing. This absence of material can be attributed to particle sticking during the spreading of the powder. Indeed, external influences such as the humidity in the air, affect the way the powder is spread. The experiments conducted in this research work were not performed in a climate controlled room. Therefore, the spreadability of the powders can vary dramatically as the weather changes. Without any additional compression methods, a different spreading mechanism, or improvement in the ability of the powder to flow, these artifacts cannot be easily controlled during the printing process of ceramic powders. The artifact considerable affect the density and strength of each printed batch. A situation clearly shown in the two aforementioned tables, despite the printing and sintering variables being constant.

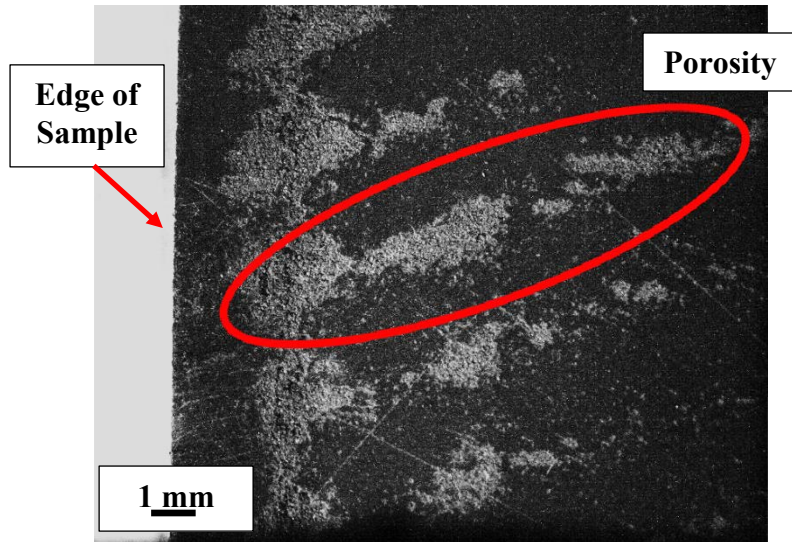


Figure 5.27. Optical image of a crosscut section of an infiltrated composite that was binder jetted using the 48 μm powder, and sintered at 1400°C. The brighter contrast shows random porosity throughout the cross cut section of the composite.

Another aspect that can alter the density of the composite system is the infiltration process. The infiltration process is difficult to keep consistent due to variables such as temperature, time, melt volume, melt chemistry, the placement of the sample in the melt, and the fixtures used to hold the sample. Thus, it was difficult to have all conditions exactly the same for each infiltration performed in this research work. For example, the sample shown in Figure 5.28, displays a large porosity that was filled with molten metal. In this sample, even though the density of the sintered ceramic body was approximately 38% dense, the molten aluminum was able to infiltrate gaps larger than 200 μm , a condition which was only reproducible with very few samples that were printed with the 65 μm powder. It is possible that the minimal pressure required to achieve densification

due to large porosity gaps, as described by Mattern *et al.* [12], was achieved in these infiltrations.

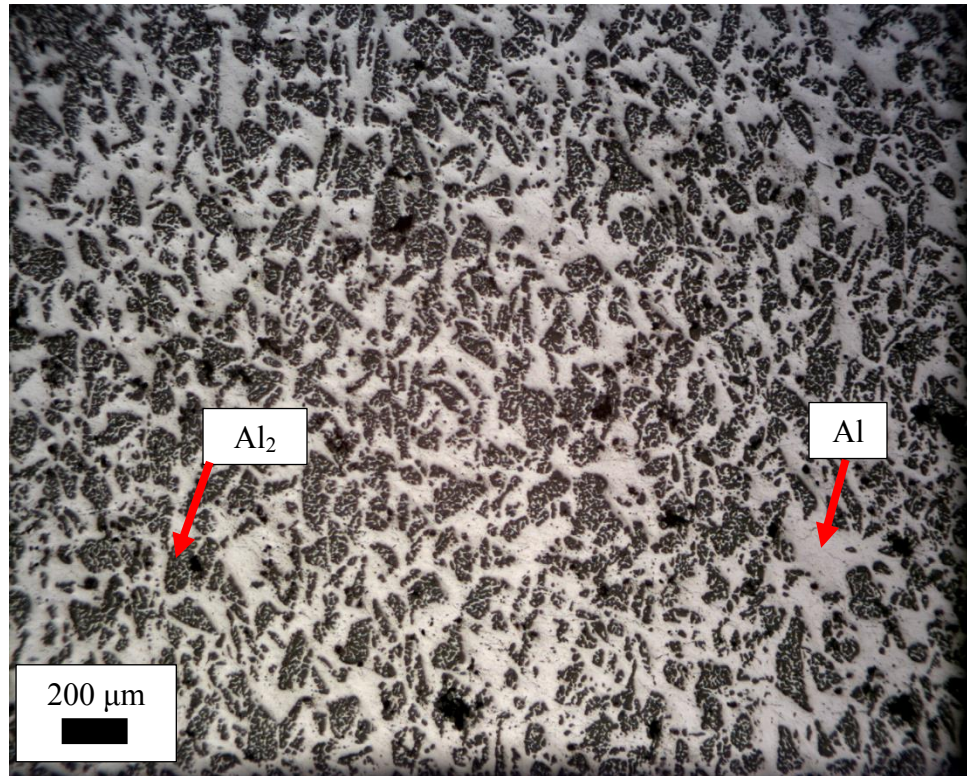


Figure 5.28. Optical micrograph of a fully infiltrated composite from the 65 μm printing of powder, sintered at 1650°C.

5.5 Dimensional Accuracy and Reproducibility

As previously mentioned, it is possible to print samples that have inherent large porosity gaps due to powder sticking and non-uniform spreading. Therefore, it is beneficial to characterize the accuracy and reproducibility of the printing process with the optimized printing parameters. Here, the physical dimensions of the printed parts have been thoroughly investigated in the cured and sintering states to characterize the accuracy

of the print comparative to the dimensions of the CAD file, and the shrinkage that occurs during the sintering process.

For this investigation, five different prints of eight pellets each were completed with 100 μm layer thickness, 60% binder saturation, 0.5 mm/sec spread speed, and then sintered at 1500°C with both the 65 and 48 μm powders for comparison. It was found that the height of the printed cylinder (z-direction) was larger than the designed height in the CAD file for every sample. Conversely, the diameter, printed in the x-y plane, was found to be smaller in some samples and larger in others. The expansion in the height can be associated to the printing process as it reaches completion. Here, any difference in the height between the designed shape and that of the STL file results in the addition of a full printed layer. Also, the printing always starts on an excess of powder below the first layer, and if an excess of binder is also added to the part, bleeding of the binder into this excess powder can occur. Therefore, the tolerance in z-direction depends on finding the appropriate binder saturation and layer thickness for each powder. On the other hand, the tolerance in the x and y-directions are dependent of the quality of the print head. The Ex One binder jet printer deposits binder on an internal grid where either none or one drop is deposited in any given cell. The internal grid is made to the appropriate size to have the droplet enter the powder and expand to connect to an adjacent cell. The print head for the X1-Lab printer has square holes that are 55 x 55 μm for binder extrusion, which create a certain drop volume. The internal grid is then created as a function of the process parameters of the layer thickness and the binder saturation:

$$S = \frac{V_b}{\left(1 - \frac{PR}{100}\right) * X_s * Y_s * LT} \quad (5.1)$$

where s is the binder saturation, V_b is the volume of the binder droplet, PR is the packing rate of the powder, X_s and Y_s are the spacings created in the internal grid pattern for the binder deposition, and LT is the layer thickness. The printing software allows for inputs of the layer thickness, binder saturation, packing rate, and droplet volume, while the x and y spacings are calculated. If there is an incomplete overlap from the part and the grid spacing, the droplet is still deposited on the sample, causing discrepancies between the STL file and the printed part. It should be noted that the internal standard for the packing rate of the X1-lab was 60 and was not changed in this research work. Although, this is not the actual packing rate of the silica powders used here, it was held constant for all printing cases after determining that these parameters work well. These values lead to the x and y drop spacing of 72.571 and 73.923 μm respectively. The results of the dimensional accuracy test can be seen in Table 5.6. The table displays the average change in height and diameter of the printed part to the dimensions on the STL file comparatively for each batch of eight printed parts. Since some of the printed dimensions were smaller than the STL dimensions, the absolute value of the difference was used. The average density for each batch is also given for comparison. It was found that z direction of the larger powder had the largest deviation of approximately 300 μm . This is due to the larger particles adding height to the part as the binder expands in that direction. The deviation of the smaller powder was found to be around 90 μm in both the x - y plane and the z direction, as well as the larger powder in the x - y plane. The average density of the cured state for the 65 μm powder was calculated to be 0.856 g/cc. In comparison, the 48 μm powder's density was calculated to be 1.129 g/cc, showing a 0.273 g/cc increase in density from the 65 μm powder.

Table 5.6. Dimensional accuracy results from the cured state of the 65 and 48 μm powders.

Batch	Powder (μm)	Δ Height (mm)	Error (mm)	Δ Diameter (mm)	Error (mm)	Density (g/cc)	Error (g/cc)
1	65	0.21	0.0075	0.05	0.0135	0.857	0.0057
2	65	0.26	0.0063	0.08	0.0194	0.854	0.0051
3	65	0.34	0.0112	0.07	0.0142	0.869	0.0041
4	65	0.34	0.0131	0.12	0.0107	0.847	0.0044
5	65	0.30	0.0122	0.05	0.0099	0.851	0.0047
1	48	0.03	0.0100	0.09	0.0182	1.134	0.0061
2	48	0.07	0.0177	0.09	0.0146	1.131	0.0035
3	48	0.12	0.0388	0.06	0.0156	1.130	0.0026
4	48	0.11	0.0308	0.10	0.0160	1.121	0.0030
5	48	0.13	0.0308	0.11	0.0102	1.128	0.0018

The same samples were then tracked during the sintering process to characterize the shrinkage for each powder. All samples were sintered at 1500°C for this test, and subsequently the change in height and diameter were measured, and the density was calculated (see Table 5.7). It was discovered that each powder showed a small degree of anisotropic shrinkage of different magnitudes. The 65 μm powder shrank on average 8.86 and 9.77 % in the x-y plane, and z direction respectively, while the 48 μm powder shrank 10.71 and 13.03 %. The 48 μm powder achieved larger sintering degree due to its increased surfaced area contact. Larger shrinkages demonstrated by the 48 μm powder are also evident in the sintered density, showing 44.4 % density increase comparatively to 31.2 % of the 65 μm powder. The change in density was calculated using a corrected density value of the cured state. Here, the mass of the sintered sample was used with the volume of the cured sample, since it is assumed that all of the binder is burned off during

sintering, and no chemical reaction takes place with the atmosphere leaving only the mass of the silica powder. The final average sintered density for the 65 and 48 μm powders was 1.08 and 1.58 g/cc respectively.

Table 5.7. Averaged shrinkage measurements from the 65 and 48 μm powders sintered at 1500°C.

Batch	Powder (μm)	Δ Height (%)	Error (%)	Δ Diameter (%)	Error (%)	Density (g/cc)	Error (g/cc)
1	65	9.76	0.2074	8.59	0.3457	1.07	0.0047
2	65	10.01	0.1467	9.05	0.1741	1.09	0.0037
3	65	9.33	0.2058	8.57	0.3888	1.09	0.0054
4	65	9.96	0.2111	8.84	0.4663	1.07	0.0089
5	65	9.82	0.1049	9.26	0.3822	1.08	0.0062
1	48	12.68	0.0857	10.47	0.1618	1.58	0.0049
2	48	13.13	0.1041	10.92	0.1150	1.60	0.0051
3	48	13.31	0.0640	11.18	0.0727	1.61	0.0050
4	48	13.17	0.0937	10.63	0.1326	1.58	0.0024
5	48	12.85	0.1006	10.38	0.1125	1.57	0.0045

5.6 Investigation of the Physical and Mechanical Isotropic Properties of Sintered Parts

Additive manufacturing can lead to parts that have anisotropic properties due to the layer by layer addition of material. The layering effect of AM shows similar anisotropic properties to those observed in laminated materials, which has been modeled using classic laminate theory [17]. Yoo *et al.* [18] has shown that the binder jet process can show anisotropic sintering effects, but the degree of anisotropy can be reduced by reducing the amount of binder being deposited. Any excess binder in the system can expand the printed part dimensions, as shown in the barrel deformation in Figure 5.6.

Also, the excess binder can move particles away from each other, lowering the surface contact, which would result in lower sintering effectiveness. This shows that finding the appropriate manufacturing process settings is crucial for creating an isotropic material. Multiple researchers have shown isotropic shrinking of binder jetted ceramics [18-22], but only a few have reported isotropic mechanical properties of the infiltrated composite [21-22]. Therefore, an investigation of the mechanical strength of the sintered and infiltrated composite was completed here.

For this study, eight cylindrical shapes of the 48 μm powder were printed in two different directions (see Figure 5.29). Only two directions were investigated (x or y, and z), since the x and y direction are the same layering sequence in the final printed part. The printing parameters of 0.5 mm/sec, 100 μm , 60 %, and 1500°C were used for the spread speed, the layer thickness, the binder saturation, and the sintering temperature respectively for all the tests. Four of the eight samples were used for the sintered compression test, while the other four were subsequently infiltrated and then tested. The direction of the compression load is also shown in Figure 5.29.

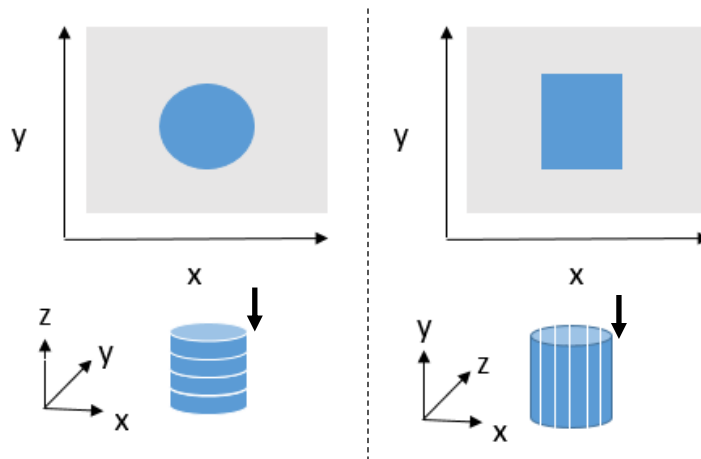


Figure 5.29. Schematic of the two different printing directions used for isotropic testing.

- a) The z-direction has the compressive load applied perpendicular to the layered structure, and b) the y-direction has the load applied parallel to the layered structure.

The results of the sintered samples showed that there is a minor anisotropy in the compressive strength of the tested samples (see Table 5.8). It was found that the parts produced with the face of the cylinder in the y-axis (Figure 5.29b) were stronger than those tested in the z-axis. These results seem to be an opposite trend of what is typically observed in the laminate theory, where the compressive strength in the z-direction (perpendicular to laminate) has a higher strength [23]. It was found here, that the parts printed in the y-axis failed vertically along the printed layers, which made a clean break in the direction of the compression force. Conversely, the parts printed in the z-axis had a shearing failure through the center of the part (see Figure 5.30).

Table 5.8. Density and compression strengths of the sintered (1500°C) and compiste samples from the 48 μm SiO_2 powder.

Print Direction	Density (g/cc)	Compression Strength (MPa)
Y-axis Sintered	1.60	36.3
Z-axis Sintered	1.63	27.9
Y-axis Composite	2.34	166.3
Z-axis Composite	2.32	126.4

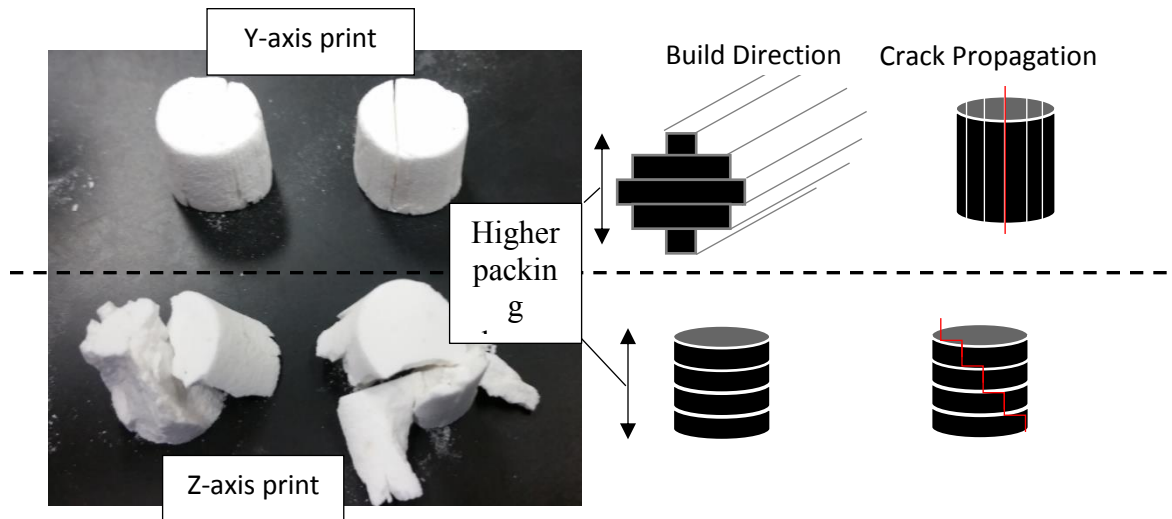


Figure 5.30. Sintered samples of 48 μm SiO_2 , which were printed in the y-axis (top) and z-axis (bottom), after compression testing. A schematic of the failure mechanism is also provided in the crack propagation figures.

The failure mechanism can be explained by a closer examination of the printing process. It can be argued that the particle packing in the z-direction (from the compression force of the spreading roller) is greater than that in the x-y plane due to a higher degree of

shrinkage. The higher degree of shrinkage is a direct correlation to surface area contact of the particles during the sintering process. Typically, laminated ceramics exhibit higher degree of shrinkage in the traversing direction due to a higher solids content (opposite of trend found here). For example, laminated alumina ceramics created by tape casting exhibit a higher degree of shrinkage, in what would be considered the x-y plane (traverse direction). This shrinkage can be over 10 times higher than that of the z-direction (casting direction) [24]. Although the anisotropic sintering trend of tape casting is opposite of that shown here, the concept of higher solids content creating larger degrees of shrinkage can be applied. It is possible that there is a higher solids content in the z-direction from the spreading mechanism of the binder jetting process. Hence the superior mechanical performance of the y-axis printed samples could be associated to the presence of vertical columns on the sample, which after the interlayer delamination, they are still capable to support stress. In the case of the z-direction the shear initially propagates in the interlaminar region (again due to the high porosity and limited particle contact) to subsequently being affected by the loading shear, to continue its shearing failure profile. Since the supporting area is severely reduced, it resulted in a lower compression strength. Farzadi *et al.* [25] found that there is an anisotropic strength to binder jetted bio-compatible ceramic materials. This work showed higher compression strengths in both the x and y-directions comparatively to the z-direction. Although Farzadi *et al.* showed similar results to this work, their testing was performed in the cured state.

The anisotropic nature favoring the y-axis direction was also found in the composite state (see Table 5.8). Here, the composites printed in the y-direction were found to have the higher compression strength of those printed in the z-axis. The

composites created in y-axis have an increase of almost 40 MPa, comparative to the z-axis, with no overlap of the deviations. The failure mechanism for both printing direction showed similar shear bands during failure but the y-direction composites resulted in stronger specimens. Unlike the sintered parts, there was no observable delamination and/or the formation of columns in the infiltrated composite. This is most likely due to densification of the sintered bodies with metal during the infiltration process, creating a stronger bond between each printed layer and 3D nature of the IPC.

5.7 High Strain Rate Compression Testing of Composite Parts

Due to the lightweight – high strength features of IPCs, these materials are of interest to the aerospace, automotive, and military fields where the composites can be exposed to high strain rate impact conditions. Therefore, it is necessary to test the high strain rate capabilities of the composites manufactured in this research work. Here, a split Hopkinson pressure bar was used to test cylindrical samples printed with the dimensions of 12.7 x 12.7 mm (height x diameter). For this test, the 48 μm powder was used, and printed considering the following parameters: 100 μm layer thickness, 60 % binder saturation, and 0.5 mm/sec spreading speed. The temperatures of 1500 and 1400°C were used, and subsequently infiltrated. For the compression test, a 76.2 mm (3 in) striker bar launched by a pressure chamber set to 0.14 MPa (20 psi) was used for each test. The selected pressure resulted in an average strain rate of 850.1 and 769.4 1/sec for the composite samples which were sintered at 1400 and 1500°C respectively. After each high-strain rate test, the data was analyzed by the SurePulse Software provided by REL

Inc. The software initially selects three points related to the “begin reflected pulse”, “end reflected pulse”, and “begin transmission pulse” in order to calculate the stress-strain response of the material (see Figure 5.31). Figure 5.31a shows how the impulse wave (blue) travels across the bar, hits the sample, and reflects down the same bar with an opposite phase. At the same time, the impulse wave travels through the sample and across the transmission bar (red). The analysis is completed by specifying those three points in the area of the first reflected and transmitted impulses (see Figure 5.31b). Figure 5.32c also shows the stress-strain response of a typical infiltrated sample. The stress-strain relationship shows a linear elastic profile followed by a maximum stress and a decay of stress in the plastic zone, which is similar to other results seen in the dynamic testing of aluminum based MMCs [26].

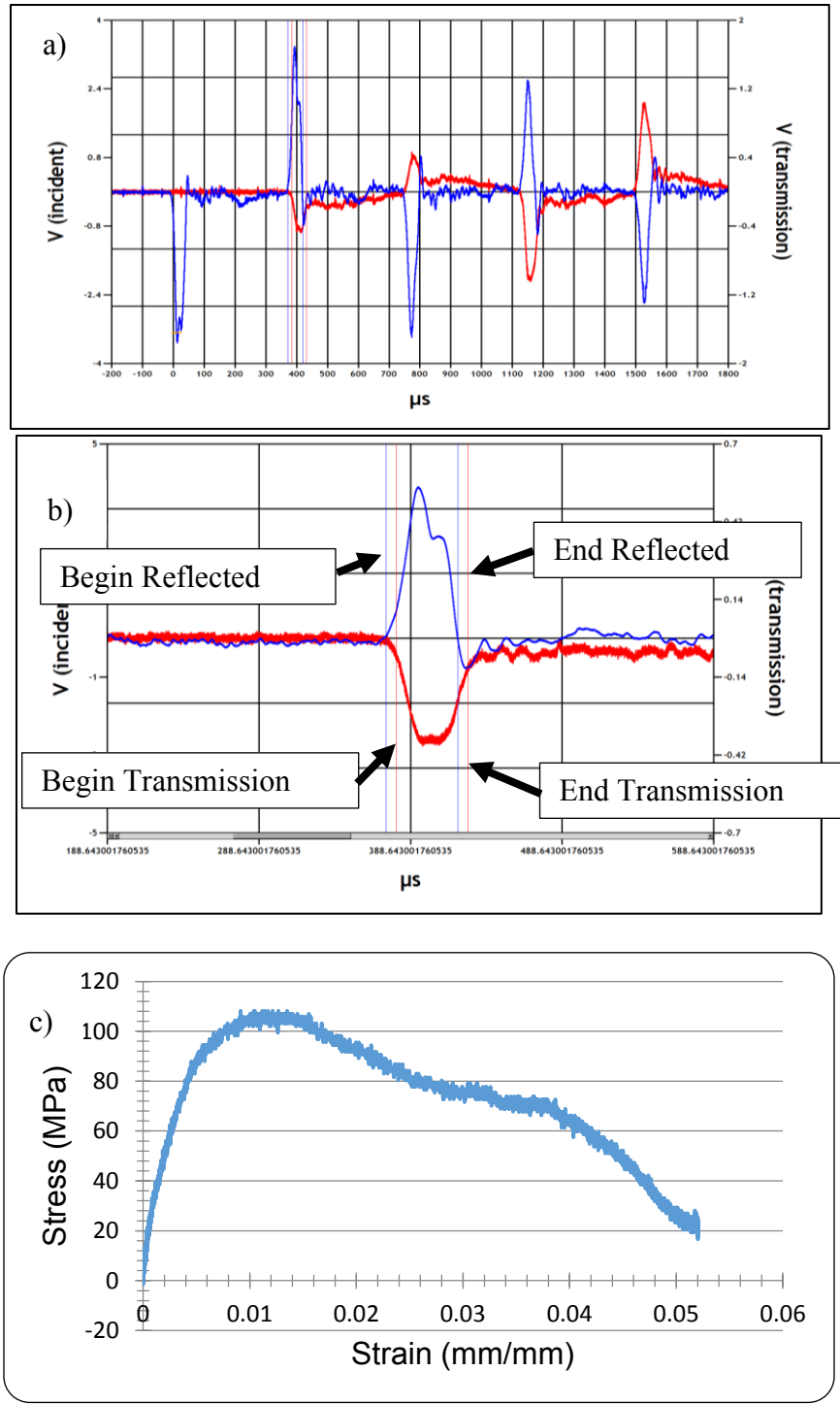


Figure 5.31. Split Hopkinson pressure bar response of an IPC composite manufactured via binder jetting of the 48 μm powder, sintered at 1400°C a-b), and its stress-strain relationship c).

It is interesting to note that it is possible to manually select these pulse points as well; however, minor changes in the selection of the pulses can modify the elastic modulus value of the tested sample (see Figure 5.32). Therefore, the modulus was not reported, and only the maximum compressive strength was analyzed, which was compared to the quasi-static compressive strengths.

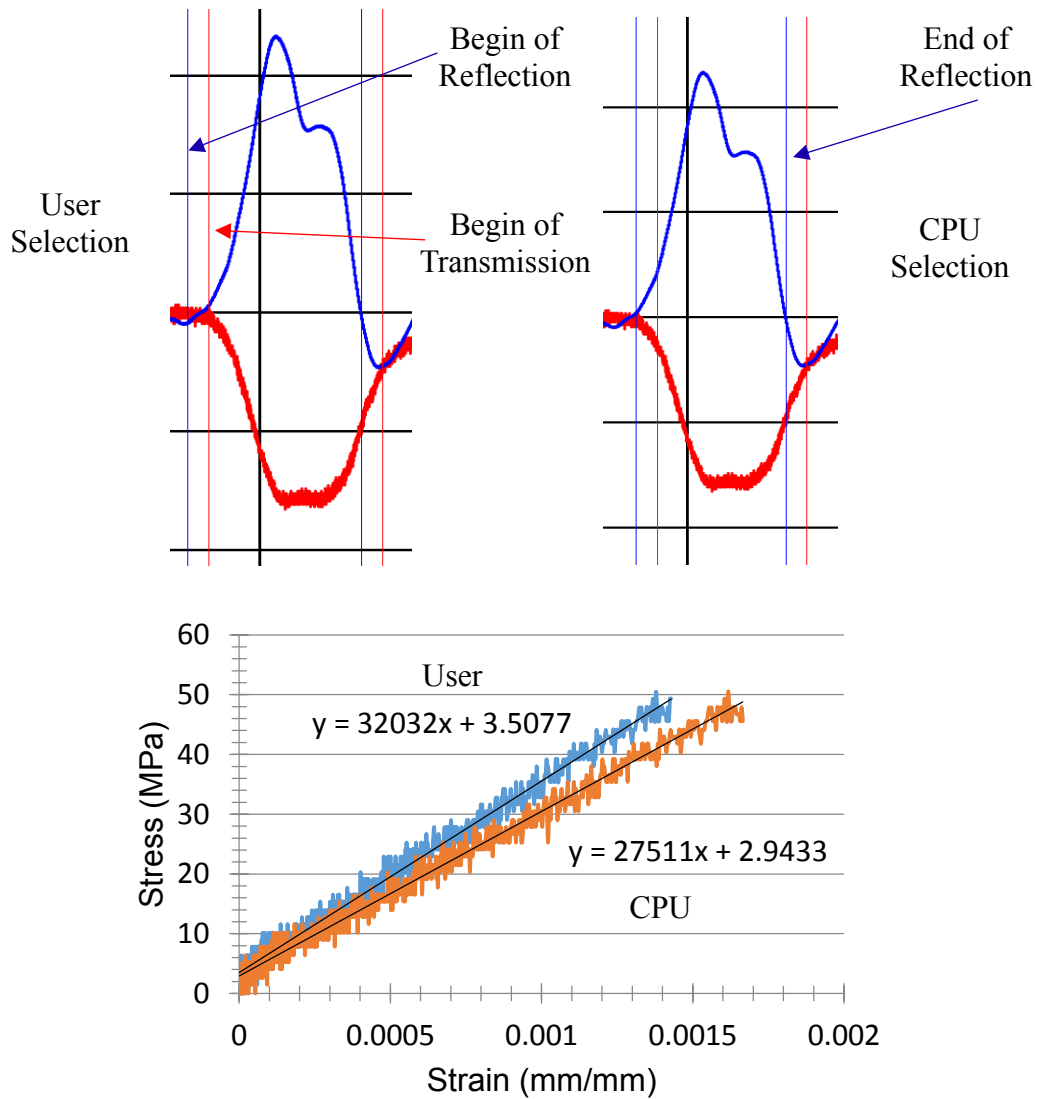


Figure 5.32. Analysis of the elastic modulus. a) automatic and user selected points of the waves pulses, and b) the resulting elastic modulus values.

The compressive strength results of the split Hopkinson testing can be seen in Table 5.9. It was found that the composite system that was sintered at 1400°C exhibited a strain rate sensitivity, since the strengths under the high strain rate increased the overall max strength from 58.6 (quasi-static) to 108.7 MPa. The strain rate sensitivity has also been shown in aluminum foam and composite materials with the 10-30% peak strength increase with high strain rate testing [27]. The strain rate dependency was not noticed by the composite that was sintered at 1500°C. This can be explained by a closer examination at the post high strain rate impacted composites (see Figure 5.33). After a single impulse from the split Hopkinson bar, the composite “flakes” off the outer region of high porosity that was described in Section 5.4. This phenomenon was not observed during the testing of the composites sintered at 1400°C, where those samples completely failed and mostly fractured to dust. The flaking in the 1500°C sample shows that only the porous exterior part in the composite fails during the instantaneous loading, whereas the same load was enough to fracture the whole composite sintered at 1400°C. The similar high strain rate compression strengths (108.7 and 118.4 MPa) of both composites show the stress capacity for force that is created by loading the gas gun of the split Hopkinson to 20 psi. A larger pressure would be required to completely fracture the composite sintered at 1500°C, which would result in a higher maximum compression strength and consequently in a strain rate dependent profile. The strain rate dependency is typically shown by the matrix or most abundant phase. For ceramics, the strain rate dependency is reasoned by the inhibition of the propagation of micro-flaws caused by inertial effects. An additional explanation is that ceramics can exhibit a micro-plasticity during dynamic loading conditions [28].

Table 5.9. Quasi-static and dynamic compression strengths of the composite materials sintered at 1400 and 1500°C.

Sintering Temperature (°C)	Composite Density (g/cc)	Quasi-Static Compression Strength (MPa)	SHPB Compression Strength (MPa)
1400	2.191	58.6	108.7
1500	2.325	126.40	118.4



Figure 5.33. Composites samples, which were sintered at 1500°C, after split Hopkinson testing. The samples display “flaking” nature of the outer porous region.

5.8 Manufacturing of Scaled-Up Parts for Industrial Purposes

For manufacturing larger plates for impact testing, the larger build box of the M-Flex was used here. As mentioned in Chapter 3, the M-Flex has a different powder dispensing mechanism than X1-Lab. The M-Flex was initially loaded with the 48 μm powder to reproduce the conditions of the previous testing. In the M-Flex, the powder

must travel through a “S” shape channel in the recoater to dispense the powder into the build box. A vibrating apparatus is used to assist the movement of the powder through the recoater and into the build box. The recoater dispenses powder by utilizing the flow rate of the powder through the channel for a given specific vibration rate. The channels in the recoater and the vibration frequency are adjustable to accommodate different size and shape powders. It was found that the anisotropic nature and stickiness of the fine particles hindered the flowability of the powder through the “S” channel in the recoater. After maximizing the channel width and frequency, the powder clumped up and clogged the channel allowing minimal spreading into the build box. It was determined that this dispensing mechanism would not work for the 48 μm powder. Therefore, to achieve larger printed parts in the M-Flex, the 65 μm powder was used. It should also be noted that that the 65 μm powder was not sieved with the 90 μm mesh due to the large amount of time needed to separate 100 lbs of powder to fill the volume of the build box and hopper of the M-Flex. Without the extra screening process, the d_{50} particle size increases to 82 μm . With the increased powder size, the layer thickness was increased to 150 μm to ensure that the powder could fit in one layer. The best results for powder flow through the recoater was found when the S channel was opened up to the maximum capacity and the oscillation was set at 2450 Hz. The powder was first dispensed across the build box, and then spread and compacted by the roller with a spread speed of 5 mm/sec and a roller speed of 250 rpm. The binder saturation was set to 60 % for all prints. The M-Flex has the ability to stack multiple parts in the z-direction, therefore, a print was set up with 5 layers with 6 plates in each layer (30 plates in total). After printing, the samples were cured at 190°C for 8 hours to ensure the set of the binding agent. The resulting printed

plates were found to have good feature definition except for the bottom layers of some of the plates (see Figure 5.34). From Figure 5.34, it can be observed that the bottom layers seemed to have been forced out of the established dimensions. The structural deviation stopped when the part had enough mass, from the previous layers, to restrain the pushing force of the rolling system.



Figure 5.34. Image of the binder jetted 101.6 x 101.6 x 12.7 mm plates printed on the M-Flex.

Although there were minor defects on the bottom of some of the printed plates, the plates were still used for sintering tests. Initially, one plate was sintered at 1500°C for 4 hours. The resulting plate was found to have some small cracks and were considered to be “flakey” due a minimal sintering. Additional sintering tests were completed at 1650°C for 16 hours. The resulting plates were still found to be flakey in some spots and major cracks were present through the plates (see Figure 5.35). The initiation of thermal cracks in the sintered parts resulted in the abandonment of using of the M-Flex in this research work.



Figure 5.35. Image of a sintered 101.6 x 101.6 x 12.7 mm plate which initiated large cracks during the sintering process.

After the technical constraints on the manufacturing process of larger parts in the M-Flex printer, the build volume of the X1-Lab was maximized to create the largest possible plate (that was 60 x 40 x 12.7 mm) for testing. The plates were printed using the 48 μm powder, with a 0.5 mm/sec spread speed, 100 μm layer thickness, and 60% binder saturation. The parts were initially sintered at 1500°C to maximize the density of the composite system. The resulting sintered parts showed cracking due to thermal stressing during the sintering process which caused delamination (see Figure 5.36). The delamination which occurs during sintering is due to the non-homogeneous parts that are created during the printing process which led to anisotropic shrinking during the sintering. Additional plates were printed and then sintered at 1450 and 1400°C to investigate the cracking process. Each sintered plate investigated showed large cracks

across the length of the plate. The large cracking makes the printed plates unusable for impact testing and emphasizes the need to find a way to print dense and homogeneous parts.

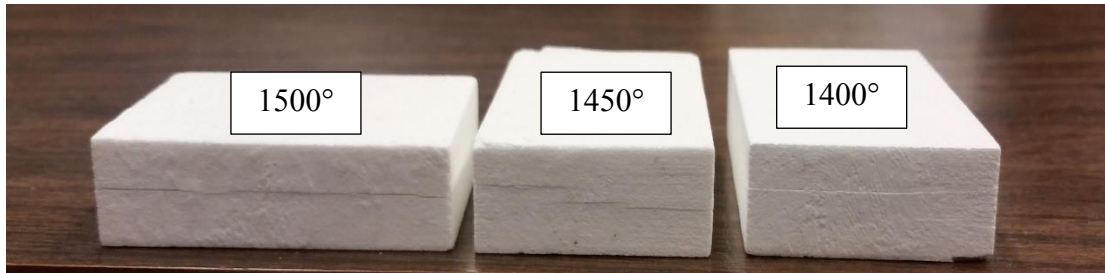


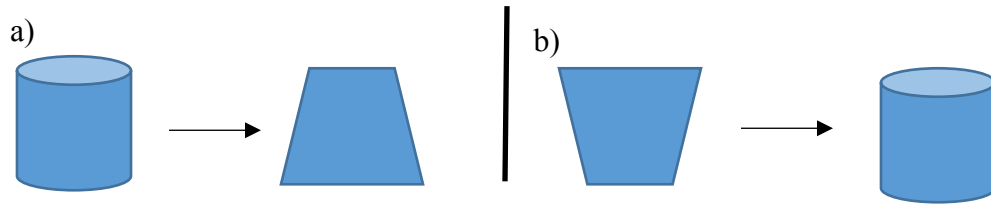
Figure 5.36. The largest possible plates that were printed for impact testing in the X1-lab after sintering at different temperatures. Each plate shows delamination after the sintering process.

5.9 Densification Techniques.

The results of this research work have shown that there might be a need a secondary process that needs to be used in conjunction with the binder jetting to create a fully dense composite part. This can be achieved in several ways, including: redesigning of parts, external pressure, agglomeration techniques, and lowering the surface tension of molten aluminum. All of these techniques were explored as possible future research routes to create dense Al/Al_2O_3 composites from the binder jet printing of fused silica parts.

5.9.1 Redesigning of Parts

The redesigning of molds or parts to allow for shrinkage or expansion in manufacturing techniques is a common practice. For this research, it was discovered that the sintering of silica parts over 1500°C would result in the warping of the designed part.



This was observed by the increased diameter at the base of the cylinder during the sintering resulting in a downwards taper deformation. Designing a part with an upwards taper, could remove the deformity of final sintered part over 1500°C (see Figure 5.37).

Figure 5.37. Schematic of the warping affect after the sintering process of fused silica over 1500°C a), and the proposed upwards taper of the designed part for yielding a parallel part after sintering b).

Hence, a cylindrical part was designed with a 5-degree upwards taper, where the top and bottom diameters were 13.8 and 12.7 mm respectively. The parts were printed with the 48 μm silica powder, 100 μm layer thickness, 60 % binder saturation, 0.5 mm/sec spread speed and subsequently sintered at 1650°C. It should be noted that the sintering temperature of 1650°C was the highest available temperature in this research work. The results showed that the newly designed part with a 5-degree taper overcompensated the warping since measurements of the top and bottom diameter of the sintered part were found to be 12.63 and 11.06 mm respectively (see Figure 5.38). The data shows that the 5-degree taper was probably too large to compensate for warping created during sintering

at 1650°C. Thus, a smaller taper would be needed to manufacture a sintered part with similar size diameters on the top and bottom of the part.



Figure 5.38. Image of the 1650°C sintered part that was designed with a 5-degree taper.

The sintering temperature of 1650°C was shown to have an increase on the compression strength of both the sintered and composite state samples (see Table 5.10). The sintered part compressive strength was increased to 67.76 MPa from the 27.87 MPa which was reported by the parts sintered at 1500°C. The increased strength found in the 1650°C sintered parts follows the same trend shown on the aforementioned strength-density relationship. Here, the 1650°C sintered parts have the highest density of all tested parts in this work (1.73 g/cc). The composite microstructure shows minimal porosity and high metal infiltration throughout the sample (see Figure 5.39). The increased infiltration leads to one of the highest composite density and compression strengths found in this research work of 2.71 g/cc and 191.39 MPa, respectively.

Table 5.10. Compression strength data for the sintered and composite states of the tapered silica parts that were sintered at 1650°C.

Sample	Density (g/cc)	Compression Strength (MPa)
Sintered	1.73	67.76
Composite	2.71	191.39

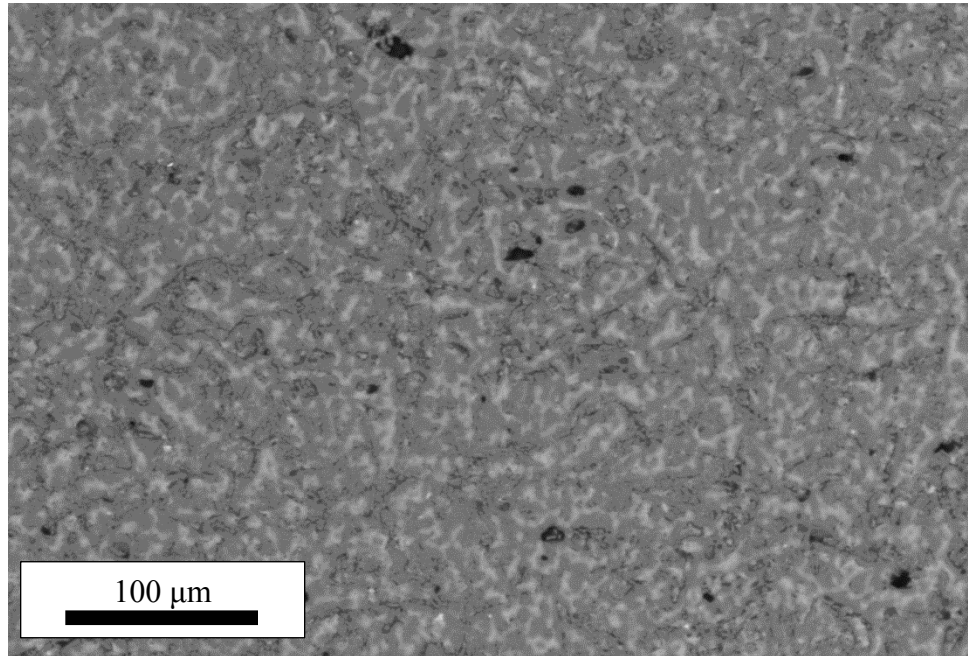


Figure 5.39. Microstructure of a tapered part that was sintered at 1650°C and subsequently infiltrated with molten aluminum. The darker phase is Al₂O₃, the lighter phase is Al, and the black phase is porosity.

5.9.2 External Pressure

The addition of pressure can be utilized in the form of hot isostatic pressing (HIP) during the sintering process, as well as pressure during the infiltration process of the molten metal. Thus, a HIPing process was performed at Quintus Technologies (Columbus, OH) with two different process settings. For the HIPing process, the samples were printed with the 48 μm powder, using a 100 μm layer thickness, a 60 % binder saturation, and a 0.5 mm/sec spreading speed. After the printing stage, the samples were presintered at 1300°C for 4 hours, in order to remove all of the binder from the samples.

The HIPing process consisted of dwelling the sintered samples at either 1050 or 1400°C, at 103.42 MPa of pressure, for 2 or 4 hours (see Table 5.11). Also included in Table 5.11 is the density and compressive strengths of both the sintered and infiltrated parts after the HIPing. It can be seen that the use the HIP process shows no density increase of sintered parts with the conditions here studied. It is interesting to note that HIPing at 1050 and 1400°C both resulted in density of 1.20 g/cc, which is equal to that completed under atmospheric conditions sintered completed 1300°C (1.23 g/cc). In comparison to the atmospheric sintered parts, the ceramic parts that were HIPed at 1050°C showed a compression strength of 3.79 MPa, which is equal to the atmospheric sintered at 1300°C (3.95 MPa see Figure 5.12). Although, the HIPing at 1400°C showed no density increase, a compression strength increase was found, but it matched the strength of the non-pressurized sintered ceramic parts. The same trend for density and compression strength of the composite systems were also found here (see Table 5.5). The composite which was HIPed at 1050°C showed similar results to the composites to which the precursors were atmospheric sintered at 1300°C. Also, the non-HIPed and HIPed composite parts had similar densities and compression strengths. These results show that an external pressure of 103.42 MPa (15 ksi) has no effect on compaction of these 3D printed silica parts.

Table 5.11. Density and compression results of hot isostatic pressing on printed silica parts and composite materials.

Sample	HIP Temperature (°C)	HIP Pressure (MPa)	HIP Time (hour)	Density (g/cc)	Compression Strength (MPa)
HIP-1	1050	103.42	2	1.20	3.79
HIP-2	1400	103.42	4	1.20	9.36
Composite-1	1050	103.42	2	1.70	10.75
Composite-2	1400	103.42	4	2.05	63.06

Another alternative to the external pressure process, would be the introduction of pressure during the infiltration step. Here, external pressure is added to the system in the form of a gas. A sintered sample was loaded into a pressure chamber with a small aluminum ingot above it. For this testing, a vacuum was incorporated in the chamber and the temperature was elevated above the melting temperature of the aluminum. After reaching the desired temperature, argon was backfilled to a desired pressure to force the molten aluminum into the open porosity of the sintered part. The pressure infiltration experiments were completed at Budapest University of Technology and Economics (Budapest, Hungary). The process of pressure infiltration of binder jetted ceramics has potential for customization of mechanical properties and density, by controlling the porosity in the ceramic part. By modifying the printing parameters, and sintering conditions, a ceramic part with a wide range of porosity can be printed and subsequently infiltrated. In this work, four cylinders were printed with the 48 μm silica powder, and infiltrated with pure aluminum in an argon induced pressure chamber (see Figure 5.40). The chamber was heated to 700°C and an external pressure of 3.45 MPa (500 psi) forced the molten aluminum into the porosity of the sintered parts. The parts dwelled at this temperature and pressure for 0.5 minutes, followed by a pressure release, and a cooling down stage to room temperature.



Figure 5.40. Pressure chamber used for infiltrating molten aluminum into sintered silica parts.

Initially, the resulting composites appeared to be fully infiltrated by optical examination. However, further microscopic analysis showed that the silica (shown by the white ceramic phase in the composite) as well as porosity was still present in the composite. It seems that the silica did not have enough time to react with the molten aluminum to create alumina and fully infiltrate the 12.7 x 12.7 mm (height x diameter) sintered samples. The low dwell time used here was selected at the discretion of the engineers using the pressure chamber, in fear of damaging the system. It is expected that longer dwelling times would have allowed for the transformation and full infiltration of the printed sintered specimens. The results are encouraging for alternative systems that do not require a long reaction time, such as CerMets.

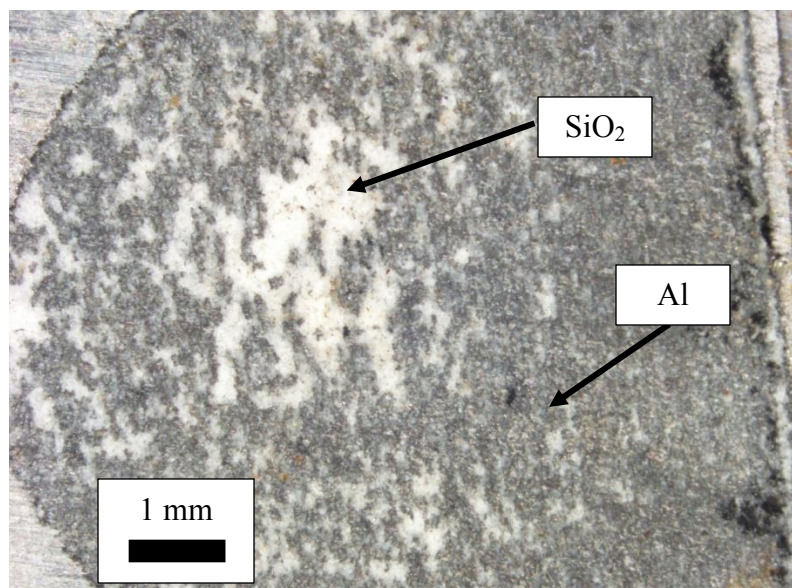


Figure 5.41. Optical image of the printed SiO₂ cylinders that were infiltrated in a pressure chamber. The white phase is the unreacted SiO₂ and dark grey is the infiltrated aluminum. Phase conformation was performed by EDS analysis.

Therefore, a 48 μm (-200 mesh) SiC powder was printed with the process parameters of 100 μm layer thickness, 60% binder saturation, and 0.5 mm/sec spread speed. The SiC cylinders were sintered at a minimal temperature and time in an open atmosphere in order to ensure minimal SiO₂ growth on the surface of the SiC particles. The growth of the SiO₂ phase was used as a sintering aid, to allow the part to be physically handled. It was found that a sintering temperature of 1200°C with a 1-hour dwell time was enough to create stable SiC parts with minimal SiO₂ growth. The SiC cylinders were then infiltrated with 3.45 MPa of pressure at 750°C with a 0.5 minute dwelling time. The results display that the microstructure of the SiC/Al composite showed minimal porosity on the outside of the composite (see Figure 5.42). Although the outside of the composite system was infiltrated, the dwell time was not long enough to fully infiltrate the entire sample,

therefore no mechanical testing was completed. The low infiltration temperature and time benefit the SiC/Al system by not allowing the reaction of SiC with Al to form Al_4C_3 . Indeed, aluminum carbide can readily react with moisture in the air to cause degradation of the composite part [29].

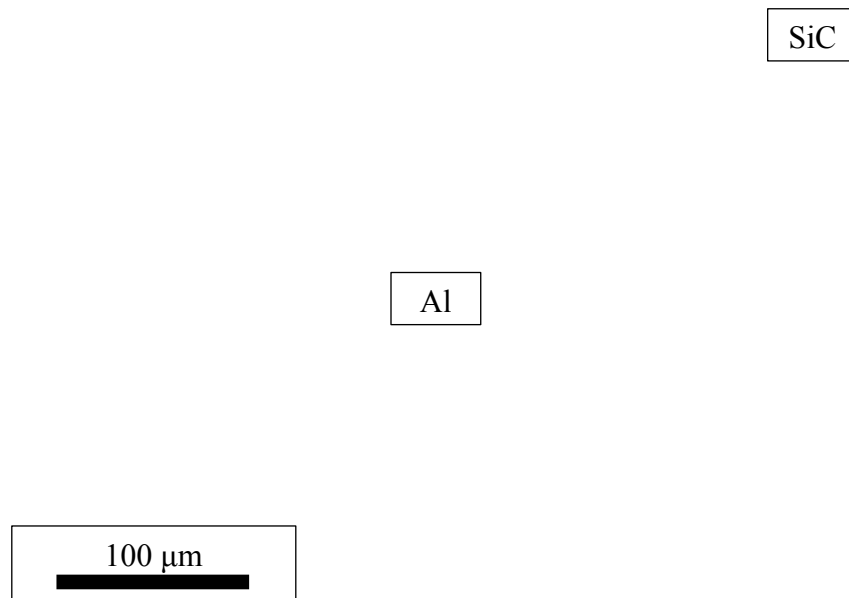


Figure 5.42. SEM image of the SiC/Al composite system where a binder jet printed SiC part that was infiltrated via external pressure.

5.9.3 Agglomerated Powder

The agglomeration process of smaller powders has been utilized in powder injection molding since the 1970s, when it was developed for the metal industry [30]. Agglomeration works by using a polymer or wax-based binder to blend and create larger, typically spherical particles starting with powders that are less than 10 μm . The increased surface area of the smaller particles achieves high sintering densities that have great

dimensional tolerances and mechanical properties close to wrought parts for metals. The major limitation of the agglomeration process is the availability and high cost of fine powders [30].

For this research work, the 4 μm (GP-3I) silica powder was agglomerated with two different binders, which were a 1 vol% solution of polyvinyl alcohol and a 1 vol% solution dextrin in water. The powder was agglomerated by Eirich, a process engineering company located in Gurnee, IL, using a large scale mixer. The received powders were then sieved through a 74 μm mesh to try to match the particle size distribution of the 48 μm powder previously used. The resulting powders were found to be mostly spherical and constituted by multiple particles per agglomerate (see Figure 5.43).

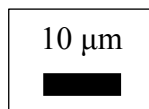


Figure 5.43. SEM image of the 4 μm powder agglomerated with a 1 vol% PVA.

The agglomeration process dramatically increased the flowability of the 4 μm powder, allowing it to be spread at 10 mm/sec with no visual problems. After the printing process, the powders were cured at 190°C for 4 hours. After the curing stage, the printed parts showed a full collapse, suggesting that an alternative binder system was required to match the PVA and dextrin agglomerated SiO_2 particles. Hence, determining an appropriate binder system that works well with agglomerated powders would be beneficial for creating dense binder jet printed parts.

5.10 Cured State Mechanical Properties

In order to manufacture ceramic parts via binder jet printing for subsequent sintering and metal infiltration, the cured state is typically overlooked because the cured parts only need to be strong enough to be transferred to a sintering oven. Although the mechanical strength of the cured state was not specifically investigated in this work, it could be useful for other applications. Therefore, the flexural and compression strength of the cured state was analyzed as a function of the spreading speed, layer thickness, and binder saturation. As before, the standard printing parameters were set at 0.5 mm/sec, 100 μm , and 60% for the spread speed, layer thickness, and binder saturation, respectively. For each test, only one parameter was modified at a time, while the others were held constant. A summary of the testing results can be seen in Table 5.12.

Table 5.12. Summary of the density, compression strength, and flexural strength of the cured state from varying the spread speed, layer thickness, and binder saturation. The standard parameters were highlighted in bold for easy comparison.

Binder	LT	SS	Density	Error	Comp	Error	Flex	Error
60	100	10.0	0.9021	0.0068	1.29	0.04	1.10	0.09
60	100	5.0	0.9756	0.0040	1.83	0.04	1.27	0.09
60	100	0.5	1.1246	0.0043	3.68	0.06	1.94	0.07
60	75	0.5	1.0689	0.0147	1.65	0.17	1.03	0.08
60	125	0.5	1.1413	0.0034	5.15	0.30	2.78	0.18
60	150	0.5	1.1555	0.0053	6.69	0.18	3.99	0.18
40	100	0.5	1.0749	0.0053	1.23	0.10	0.62	0.03
80	100	0.5	1.1183	0.0057	4.49	0.11	2.83	0.27
100	100	0.5	1.1250	0.0052	5.75	0.22	4.13	0.07
120	100	0.5	1.1279	0.0084	8.69	0.25	5.17	0.07

LT – Layer Thickness (μm), SS – Spread Speed (mm/sec), Comp – Compression Strength (MPa), Flex – Flexural Strength (MPa).

Table 5.12 shows that the strongest cured state sample was a result of the highest binder saturation (120). For the parameters of layer thickness and binder saturation, there is a direct inverse relationship to the strength of the cured state and the sintered state (i.e. higher cured state strength results in lower sintered state strengths). This is because changing the binder saturation and layer thickness directly affects the droplet spacing. The increased binder saturation and layer thickness decrease the drop spacing to ensure the appropriate amount of binder saturation and dispersion through the layer thickness. The increased binder droplets add additional strength and density to the cured state, but led to a higher porosity and a decrease in strength in the sintered state. Table 5.12 also shows that by increasing the spreading speed, the density and mechanical properties of the cured samples decreased, most likely due to a fast spreading, which limits the particle compaction from the rolling mechanism.

References

1. Sachs, E. M. (2000). *U.S. Patent No. 6,036,777*. Washington, DC: U.S. Patent and Trademark Office.
2. Sachs, E. M., Cima, M. J., Caradonna, M. A., Grau, J., Serdy, J. G., Saxton, P. C., Uhland, S.A., & Moon, J. (2003). *U.S. Patent No. 6,596,224*. Washington, DC: U.S. Patent and Trademark Office.
3. Cima, M., Sachs, E., Fan, T., Brecht, J. F., Michaels, S. P., Khanuja, S., Lauder, A., Lee, S.J., Brancazio, D., Curodeau, A., & Tuerck, H. (1995). *U.S. Patent No. 5,387,380*. Washington, DC: U.S. Patent and Trademark Office.
4. Dion, S., Balistreri, J., & Reed, A. (2013). *U.S. Patent No. 8,475,946*. Washington, DC: U.S. Patent and Trademark Office.
5. Vaezi, M., & Chua, C. K. (2011). Effects of layer thickness and binder saturation level parameters on 3D printing process. *The International Journal of Advanced Manufacturing Technology*, 53(1-4), 275-284.
6. Chen, X., Wu, S., & Zhou, J. (2013). Influence of porosity on compressive and tensile strength of cement mortar. *Construction and Building Materials*, 40, 869-874.
7. Lu, K., & Reynolds, W. T. (2008). 3DP process for fine mesh structure printing. *Powder Technology*, 187(1), 11-18.

8. Wang, L. Y., & Hon, M. H. (1995). The effect of cristobalite seed on the crystallization of fused silica based ceramic core—A kinetic study. *Ceramics International*, 21(3), 187-193.
9. Breneman, R. C., & Halloran, J. W. (2015). Effect of Cristobalite on the Strength of Sintered Fused Silica Above and Below the Cristobalite Transformation. *Journal of the American Ceramic Society*, 98(5), 1611-1617.
10. Norrish, K., & Taylor, R. (1962). Quantitative analysis by X-ray diffraction. *Clay Miner. Bull*, 5(28), 98-109.
11. The Silica Group. Retrieved April 11, 2016, from http://www.quartzpage.de/gen_mod.html
12. Mattern, A., Huchler, B., Staudenecker, D., Oberacker, R., Nagel, A., & Hoffmann, M. J. (2004). Preparation of interpenetrating ceramic–metal composites. *Journal of the European Ceramic Society*, 24(12), 3399-3408.
13. Prielipp, H., Knechtel, M., Claussen, N., Streiffer, S. K., Müllejans, H., Rühle, M., & Rödel, J. (1995). Strength and fracture toughness of aluminum/alumina composites with interpenetrating networks. *Materials Science and Engineering: A*, 197(1), 19-30.
14. Coupard, D., Goni, J., & Sylvain, J. F. (1999). Fabrication and squeeze casting infiltration of graphite/alumina preforms. *Journal of Materials Science*, 34(21), 5307-5313.

15. Breslin, M. C., Ringnalda, J., Xu, L., Fuller, M., Seeger, J., Daehn, G. S., ... & Fraser, H. L. (1995). Processing, microstructure, and properties of co-continuous alumina-aluminum composites. *Materials Science and Engineering: A*, 195, 113-119.
16. del Rio, E., Nash, J. M., Williams, J. C., Breslin, M. C., & Daehn, G. S. (2007). Co-continuous composites for high-temperature applications. *Materials Science and Engineering: A*, 463(1), 115-121.
17. Sayre III, R. (2014). *A Comparative Finite Element Stress Analysis of Isotropic and Fusion Deposited 3D Printed Polymer* (Doctoral dissertation, Rensselaer Polytechnic Institute).
18. Yoo, J., Cima, M. J., Khanuja, S., & Sachs, E. M. (1993). Structural ceramic components by 3D printing. In *Solid Freeform Fabrication Symposium* (pp. 40-50).
19. Yin, X., Travitzky, N., & Greil, P. (2007). Near-Net-Shape Fabrication of Ti₃AlC₂-Based Composites. *International journal of Applied Ceramic Technology*, 4(2), 184-190.
20. Winkel, A., Meszaros, R., Reinsch, S., Müller, R., Travitzky, N., Fey, T., ... & Wondraczek, L. (2012). Sintering of 3D-Printed Glass/HAp Composites. *Journal of the American Ceramic Society*, 95(11), 3387-3393.
21. Melcher, R., Travitzky, N., Zollfrank, C., & Greil, P. (2011). 3D printing of Al₂O₃/Cu–O interpenetrating phase composite. *Journal of Materials Science*, 46(5), 1203-1210.

22. Fu, Z., Schlier, L., Travitzky, N., & Greil, P. (2013). Three-dimensional printing of SiSiC lattice truss structures. *Materials Science and Engineering: A*, 560, 851-856.
23. Sun, C. T. (2006). *Mechanics of Aircraft Structures* (2nd ed.). Hoboken, NJ: John Wiley & Sons.
24. Raj, P. M., & Cannon, W. R. (1999). Anisotropic Shrinkage in Tape-Cast Alumina: Role of Processing Parameters and Particle Shape. *Journal of the American Ceramic Society*, 82(10), 2619-2625.
25. Farzadi, A., Solati-Hashjin, M., Asadi-Eydivand, M., & Osman, N. A. A. (2014). Effect of layer thickness and printing orientation on mechanical properties and dimensional accuracy of 3D printed porous samples for bone tissue engineering. *PloS one*, 9(9), e108252.
26. Li, Y., Ramesh, K. T., & Chin, E. S. C. (2000). Viscoplastic deformations and compressive damage in an A359/SiC p metal–matrix composite. *Acta Materialia*, 48(7), 1563-1573.
27. Balch, D. K., O'Dwyer, J. G., Davis, G. R., Cady, C. M., Gray, G. T., & Dunand, D. C. (2005). Plasticity and damage in aluminum syntactic foams deformed under dynamic and quasi-static conditions. *Materials Science and Engineering: A*, 391(1), 408-417.
28. Wang, H., & Ramesh, K. T. (2004). Dynamic strength and fragmentation of hot-pressed silicon carbide under uniaxial compression. *Acta Materialia*, 52(2), 355-367.

29. Pech-Canul, M. I., & Makhoulouf, M. M. (2000). Processing of Al–SiCp metal matrix composites by pressureless infiltration of SiCp preforms. *Journal of Materials Synthesis and Processing*, 8(1), 35-53.
30. Kalpakjian, S., & Schmid, S. R. (2008). *Manufacturing Processes for Engineering Materials* (5th ed.). Upper Saddle River, NJ: Prentice-Hall.

6. Conclusions

The binder jetting of fused silica powders was investigated in this research program. 3D printed silica bodies were used for molten metal infiltration to manufacture unique Al/Al₂O₃ interpenetrating phase composites. The combination of additive manufacturing and the pressureless infiltration allows for the manufacturing of high complexity composites due to the near net shape manner of the infiltration process. Although there have been previous studies of binder jetting on similar ceramic bodies for metal infiltration, there have been no previous efforts to study the printing process of SiO₂ to react with molten aluminum to create an Al/Al₂O₃ composite, a system with a large number of industrial applications.

It has been observed that when investigating the printing process of a new powder system, the printing parameters must be optimized to manufacture a part of high quality. Here, the parameters of particle size distribution, powder spread speed, layer thickness, binder saturation, and sintering temperature were analyzed. It was found that smaller powder blends with a d₅₀ of 8 and 4 μm had low spreadability characteristics. A powder blend with a d₅₀ of 65 μm was found to spread easily, although the final sintered part was found to show a high degree of porosity due to the large particles and low surface area contact during sintering. In contrast, a powder blend with a d₅₀ of 48 μm was found to have high spreadability characteristics and the highest printed density of all powders investigated.

The intrinsic parameters of the printer were investigated with a 48 μm powder. It was found that slowing down the powder spread speed would increase the density of the

printed parts, due to an increased compaction time of the rolling apparatus. A layer thickness of 100 μm was shown to manufacture parts with the highest density. From the results, it was recommended that layer thickness should be two times the average particle size of the powder used to ensure maximum powder compaction during the printing spreading stage. The addition of excess binder to the system resulted in an increasing strength of the cured parts, although it had a negative effect on the sintering densities. The excess of binder also resulted in the deformation of the desired dimensions of the printed part due to the diffusion of binder, mostly in the x-y plane. The printing parameters of 0.5 mm/sec spread speed, 100 μm layer thickness, and 60% binder saturation were found to manufacture silica parts with the highest density using the 48 μm powder.

The sintering temperature was found to have the greatest effect on the final density of the silica parts. The temperature range of 1300-1500°C was found to be an acceptable range for the sintering of the 48 μm powder. At temperatures below 1300°C the sintered parts displayed a “flakey” behavior due to a low degree of sintering, and the parts sintered above 1500°C showed a warping behavior due to the temperature approaching the melting point of silica. The sintering temperature of 1500°C was found to achieve the highest density part of 1.631 g/cc. Although the optimal temperature range was found for the printing of 48 μm fused silica, the high sintering temperatures resulted in devitrification of the amorphous fused silica powders. The crystalline phase of cristobalite was detected in all temperatures used in this range.

For all of the variables tested in this research work, the density was calculated and correlated to the inherent compressive strength. It was found that the strongest parts

correlated to highest density, which was created for each individual parameter test. The highest compression strength was found to be 27.9 MPa, which was from the sample set printed with a 0.5 mm/sec spread speed, 100 μm layer thickness, 60% binder saturation, and 1500°C sintering temperature. The sintered state was also correlated to the density and compressive strength of the composite system post-infiltration.

Initial pressureless infiltration of printed silica parts was performed with the intention to create composite systems with variable metal-ceramic phase distributions by taking advantage of the porosity in the sintered parts. The results show that molten aluminum will not fill large porosity gaps in the composite system. The aluminum only follows the ceramic network, while filling in the smallest porosity gaps created by the reaction of the molten aluminum and silica. As the density of the sintered part increased, more aluminum was retained in the final composite. It was also observed that the composite density also had a direct correlation to the compression strength. The highest compression strength was found to be 270.6 MPa with a density of 2.64 g/cc.

A mechanical simulation work using a homogenization technique in Matlab was used to quickly and accurately describe the Young's modulus of the Al/Al₂O₃ two phase interpenetrating phase composite. An extension to a preexisting Matlab code was created to assist the simulation of the investigated systems. The simulation results predicted a Young's modulus of 147.8 GPa in the composite, while the experimental results were found to be 167 GPa. The simulation showed a 11.5% difference to the experimental values which was completed in under 1.5 hours.

The binder jetting of fused silica powders for subsequent molten aluminum infiltration shows promise as a potential manufacturing technique to create intricate

composite systems, but improvements are needed to create fully dense composite parts. The resulting densities of printed parts were found to be inconsistent due to the random porosity artifacts found in ceramic bodies and the anisotropic strengths of the sintered and composite parts. The ability to print a homogenous, isotropic ceramic body is one of solution for creating denser parts, as well as larger parts, which showed delamination during the sintering of the powders studied in this research work.

Alternative routes to create homogenous, isotropic parts were investigated. The agglomeration of particles smaller than 4 μm shows promise due to the an increasing spreadability and particle packing of the spherical powders agglomerates. It is expected that the additional surface area of the smaller powders would increase the sintered density. Although, a proper binder system needs to be investigated to find the ultimate potential of printing agglomerated powder systems. The addition of external pressure during the infiltration also shows promise for creating Al/Al₂O₃ composites with varying phase distributions and mechanical properties. However, the proper dwell time and pressure needs to be investigated in order to ensure a full reaction and minimization of the porosity in the composite.

In summary, the present work has shown that the use of binder jetting could be a viable process for the synthesis of customized metal-ceramic composites. It has been observed that a further densification of the printed system is required to achieve the full potential of additive manufacturing on the creation of IPCs.